

Université de Neuchâtel

Development and Application of a Multifunctional Nanotribological Tool

Thèse

présentée à la Faculté des Sciences
pour obtenir le grade de Docteur ès Sciences

par

Nicholas X. Randall

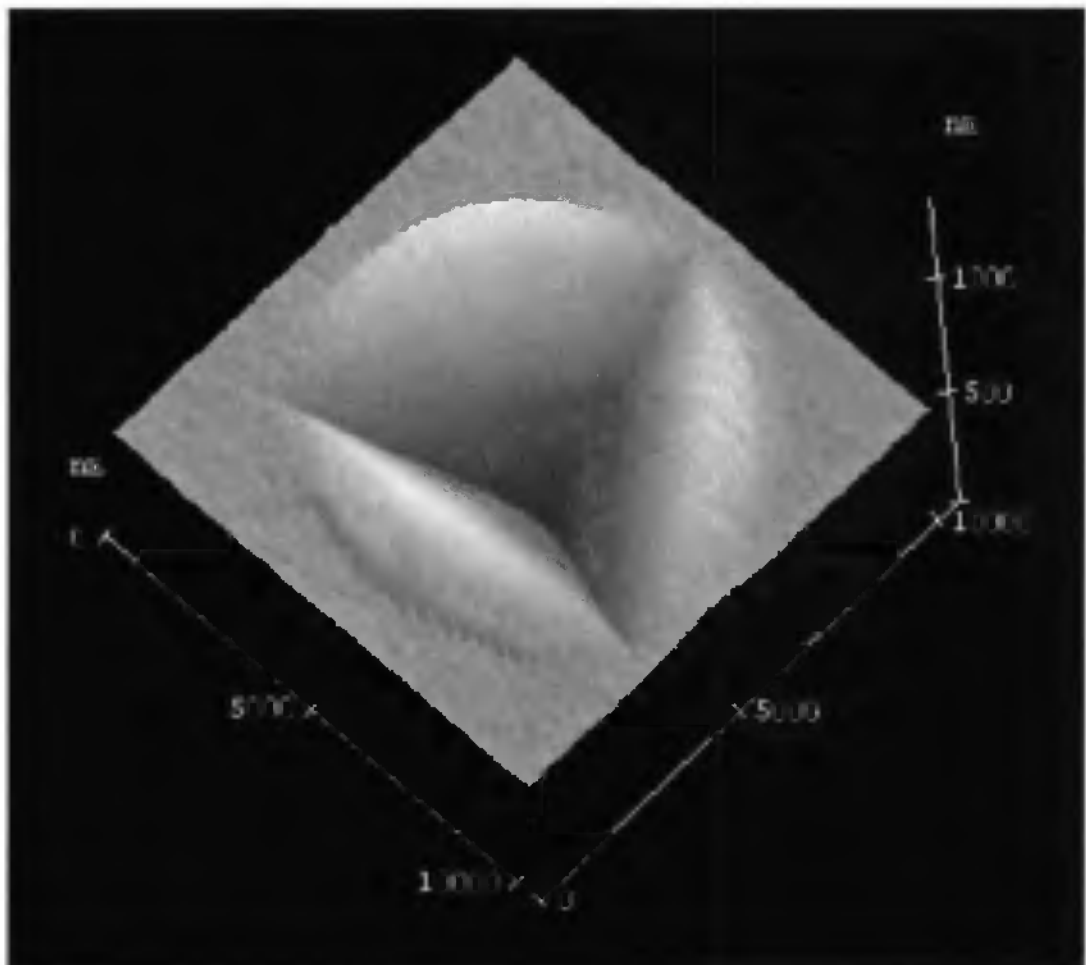
BSc. in Materials Technology and Management
Brunel University, London

Centre Suisse d'Electronique et de Microtechnique (CSEM) S. A.
CH-2007 Neuchâtel, Switzerland

et

Institut de Microtechnique (IMT),
Université de Neuchâtel, Switzerland

1997



Scanning Force Microscopy image of a nanoindentation made through a titanium film (thickness = 200 nm) deposited on a silicon substrate.

IMPRIMATUR POUR LA THÈSE

Development and Application of a Multifunctional Nanotribological Tool

de M. Nicholas Randall

UNIVERSITÉ DE NEUCHÂTEL

FACULTÉ DES SCIENCES

La Faculté des sciences de l'Université de
Neuchâtel sur le rapport des membres du jury,

Mme M. Kudelka-Hep, MM. N. de Rooij (directeur de thèse),
H. E. Hintermann (CSEM, Neuchâtel), B. Bhushan (Ohio, USA)
R. Christoph (ASCOM, Berne) et J. Burger (Bienne)

autorise l'impression de la présente thèse.

Neuchâtel, le 17 novembre 1997

Le doyen:



F. Stoeckli

© *Copyright N. X. Randall 1997*

All rights reserved

'This thesis is dedicated to my mother, who gave me the wood to make the sculpture, and to my father who showed me how to carve it'

Contents

Preface		1
Introduction		3
Chapter 1:	Scanning force microscopy	9
	1.1 The principles of the scanning force microscope	9
	1.2 Friction force microscopy	12
	1.3 The Atomic Scale Tribometer	14
	1.4 Surface roughness and its measurement	16
Chapter 2:	Nanoscale scratching	21
	2.1 Industrial implications	21
	2.2 Experimental instrumentation	22
	2.3 Diamond-coated cantilever tips	24
	2.4 Results	25
	2.4.1 Soft coatings	25
	2.4.2 Hard coatings	30
	2.5 Conclusions	34
Chapter 3:	Nanoindentation	35
	3.1 Historical background	35
	3.2 Indenter geometry	36
	3.3 Analysis of indentation data	39
	3.3.1 The unloading curve	39
	3.3.2 The loading curve	46
	3.3.3 The work of indentation	48
	3.3.4 Cyclic indentation	49
	3.4 The importance of pile-up	50
	3.4.1 Bulk materials	50
	3.4.2 Coated systems	52
Chapter 4:	The SFM approach to nanoindentation	55
	4.1 Nanoscale mechanics	55
	4.2 Instrumental set-up	59
	4.3 Modelling of cantilever displacement	62
	4.3.1 Longitudinal displacement of indenter	63
	4.3.2 Shear force effect	65
	4.4 Results	68
	4.5 Conclusions	75

Chapter 5:	The combined system prototype	77
	5.1 Design constraints	77
	5.2 The electromechanical positioning system	80
	5.3 Software	81
	5.4 Calibration of sample position	81
	5.5 Results	82
	5.6 Conclusions	84
Chapter 6:	Realisation of the Nano Hardness Tester	85
	6.1 The differential-capacitive measurement technique	85
	6.2 System calibration	87
	6.3 Integration of a compact scanning force microscope	89
	6.4 The SIS objective SFM	91
	6.5 Results	93
	6.6 Conclusions	128
Chapter 7:	Published results and applications	129
	7.1 Surface characterisation of bearing components	129
	7.2 Localised micro-hardness measurements with a combined scanning force microscope/nanoindentation system	137
	7.3 Novel nanoindentation method for characterising multiphase materials	145
	7.4 Characterisation of DLC multilayers by nanoindentation and by scanning force and friction microscopy	153
	7.5 Correlation between processing parameters and mechanical properties as a function of substrate polarisation and depth in a nitrided 316L stainless steel using nanoindentation and scanning force microscopy	159
	7.6 Characterisation of IC aluminium bonding pads by nanoindentation and scanning force microscopy	167
	7.7 Nanoindentation and scanning force microscopy as a novel method for the characterisation of tribological transfer films	175
	Summary and Outlook	183
	References	185
	Publications	191
	Acknowledgements	193
	Curriculum Vitae	195

Preface

During the summer of 1993, whilst working at the Centre Suisse d'Electronique et de Microtechnique (CSEM) for a 6-month university work placement, I began discussing the possibilities of developing a new nanotribological system with Dr. Rainer Christoph. The objective was to integrate several different surface analytical techniques into one multifunctional tool for a more complete characterisation of surface mechanical properties. It seemed that the rapidly emerging field of micro- and nanotribology had hatched many new ideas, but no-one as yet had combined them in a simple and user-friendly way. The challenge was there, as was the necessary infrastructure and technical competence to make it a reality. Thus I embarked on a three year research project which would prove exciting, stimulating and which I felt would actively contribute to advances in surface science. However, as with almost all new developments, some problems were encountered and mistakes made along the way which, although frustrating at the time, gave me valuable experience and helped me gain a better understanding of how best to transform a scientific idea into a feasible (and perhaps more commercial) proposition! It is true that making a PhD thesis in a highly competitive and industrial environment is perhaps not the most ideal of situations, but one which has taught me a lot more about the *real world* than I ever could have learnt in an academic establishment.

On a more technical note, this thesis represents only the beginning of what in the future may well become a standardised test method and a common tool in materials science, both at a fundamental level for research into new materials and processes, and at an industrial level for the quality control of increasingly complex structures and coatings. It has been a pleasure for me to work in the field of tribology and I hope that it will continue to develop and evolve with the same vigour with which it has done until now.

Nick Randall

Neuchâtel, Summer 1997

Introduction

The term 'tribology' can be described as the science and technology of two interacting surfaces in relative motion and is derived from the Greek word *tribos* which means rubbing. Although the name tribology has only been in use for some 30 years, the science which it describes dates back to before recorded history and embodies the study of friction, wear and lubrication. The industrial importance of tribological studies cannot be ignored; worldwide surveys have confirmed that at least 1-2% of the gross national product might be saved with minimal further investment in research, and that the potential for even larger savings might exist with further research¹. It is clear that as the relative price of energy continues to rise, and the need to conserve both energy and raw materials becomes more widely appreciated, correct tribological design will become increasingly important.

The more recent development of new techniques to measure surface topography, adhesion, friction and mechanical properties on a micro- and nanometer scale has led to a new field referred to as micro/nanotribology which is concerned with experimental and theoretical investigations of processes occurring from micro scales down to atomic or molecular scales. Such studies are becoming ever more important as the miniaturisation of moving parts and mating surfaces continues to increase. However, as devices and components become smaller, the apparatus required to measure their properties becomes more complicated and the limits of resolution are continually being pushed back. Micro/nanotribological studies are crucial to developing a fundamental understanding of interfacial phenomena occurring at such small scales and are boosted by the various industrial sectors whose livelihood depends on their ability to increase performance, reduce costs and increase efficiency². Such industries include magnetic storage systems, microelectromechanical systems (MEMS), integrated circuits, thin films and coatings, to name but a few.

The invention of the Scanning Tunnelling Microscope (STM) in 1981 by Gerd Binnig and Heini Rohrer at the IBM Zürich Research Laboratory suddenly revolutionised the field of surface science and was awarded the Nobel prize in physics in 1986. This was the first instrument

capable of directly obtaining three-dimensional images of solid surfaces with atomic resolution³ and paved the way for a whole new family of Scanning Probe Microscopies (SPM), e. g., Scanning Force Microscopy (SFM)⁴, Atomic Force Microscopy (AFM)⁵, Scanning Near-field Optical Microscopy (SNOM)⁶, Magnetic Force Microscopy (MFM)⁷, Friction Force Microscopy (FFM)⁸⁻⁹ and others¹⁰⁻¹¹. Although the different types of SPM have their own unique measuring ability, they all have the same principle in common, namely an extremely high local resolution obtained by limiting the interaction range between the probe tip of the microscope and the sample surface to a tiny spatial spot.

SPMs and their modified counterparts can be used over an extreme range of magnifications from 10^3 to 10^9 times in x, y and z directions, meaning that they can image from macro down to atomic dimensions. In addition, such instruments do not require a vacuum environment, nor a conducting sample, and can be used in any sample environment such as ambient air¹², liquid¹³⁻¹⁴, various gases¹⁵, vacuum¹⁶ and at low temperatures¹⁷⁻¹⁸. The most common SPM is probably the SFM, due to its wide range of applications, ease of use and imaging modes (e.g., contact mode, non-contact mode, tapping mode, pulsed-force mode, etc) which enable it to be used for measuring surface topography and roughness, friction, adhesion, elasticity, scratch resistance and for nanolithography and nanomachining. However, at the nanometric scale, certain industries require the accurate and reproducible measurement of other surface mechanical properties such as hardness and elastic modulus, parameters which cannot easily and quantitatively be measured using SFM techniques alone.

This leads us to the field of nanoscale indentation (also referred to as instrumented indentation, or *depth-sensing* indentation) where a tip of known geometry is pressed into the sample whilst simultaneously recording both the force and the displacement. This allows an accurate calculation of hardness, modulus, time-dependent creep, toughness, fatigue and residual stress data for depths as small as <50 nm¹⁹. Such measurements can assess structural heterogeneities on and underneath the surface such as diffusion gradients, precipitates, buried layers, grain boundaries and modifications in surface composition.

Hardness measurements usually fall into three main categories: (i) scratch hardness; (ii) rebound or dynamic hardness; and (iii) static indentation hardness²⁰. Scratch hardness depends on the

ability of one material to scratch another or to be scratched by another solid, and was first put on a semiquantitative basis by Friedrich Mohs in 1822 who selected 10 minerals as standards, beginning with talc and ending with diamond, thus producing the Mohs scale which is still widely used by mineralogists. Modern day solid and thin film surfaces are scratched by a sharp stylus made of a hard material, typically diamond, and either the loads required to scratch or fracture the surface or delaminate the film, or the normal/tangential load-scratch size relationships are used as a measure of scratch hardness and/or interfacial adhesion²¹⁻²³. Rebound or dynamic hardness testing involves the dynamic deformation or indentation of the surface; a diamond-tipped hammer is dropped from a fixed height onto the test surface and the hardness is expressed in terms of the energy of impact and the size of the remaining indentation.

The most widely used method for determining the hardness of materials is the static indentation method which is essentially a measure of the plastic deformation properties and only to a secondary extent the elastic properties. Macrohardness tests are now commonplace and inexpensive instruments have been developed which combine reliability with ease of operation. However, the loads used are still high (of the order 0.5-50 kg) meaning that ultrathin films and coatings cannot be measured with this method. Furthermore, as new surface treatments and thin films are developed, as are used for example in micromechanical applications, new types of instrument have needed to be designed to cope with very shallow indentation depths and low loads (nanonewtons to millinewtons).

In a conventional indentation hardness test, the contact area is determined by measuring the indentation size by an optical microscope after the indenter tip has been unloaded from the sample. For most metals, there is little change in the size of the residual imprint on unloading so that the conventional hardness test is essentially a test of hardness under load, although it is subject to some error due to varying elastic contraction of the imprint²⁴. With depth-sensing indentation hardness tests, the contact area is determined by measuring the indentation depth during the loading/unloading cycle²⁵⁻³⁰, but such depth measurements have a major weakness arising from 'piling-up' and 'sinking-in' of material around the indentation. The measured indentation depth needs to be corrected for the depression (or the hump) of material around the imprint before it can be used for calculation of the hardness³¹⁻³³. The Young's modulus of elasticity is the slope of the stress-strain curve in the elastic regime and is obtained from the slope

of the unloading curve^{32,34}. In addition to measurements of hardness and modulus, static indentation tests have been used for measurements of a wide variety of material properties such as elastic-plastic deformation behaviour³⁵, flow stress²⁰, film-substrate adhesion³⁶, residual stresses³⁷, creep³⁸, stress relaxation³⁹, fracture toughness and brittleness⁴⁰, and fatigue⁴¹.

For the case of very thin films (micron and sub-micron), whose growing industrial importance makes them increasingly common, their intrinsic hardness becomes meaningful only if the influence of the substrate material can be eliminated. Thus the indentation depth should not exceed about one tenth of the total coating thickness and so applied loads in the order of 0.5-50 mN are desirable if the indentation depths are to remain in the nanometer range. In this case, the size of the residual imprint is inferior to the resolution limit of a conventional optical microscope and locating it is almost impossible after removal of the indentation load. Although modern depth-sensing nanoindentation instruments can accurately measure the hardness at such shallow depths, it is of particular interest to visualise the imprint in order to check the depth measurement, characterise the material response in terms of pile-up or sink-in, investigate the surface morphology prior-to and after indentation, and to verify that the measurement has been made in the correct location (particularly important when measuring multiphase materials).

Previous efforts to image residual imprints have included STM/SFM^{42,43}, Scanning Electron Microscopy (SEM)⁴⁴ and Transmission Electron Microscopy (TEM)²⁷ but the problems of accurately relocating the sample in order to place the imprint within the range of the imaging microscope have never really been solved. Furthermore, the need to be able to accurately position indentations at highly localised sites is evermore present as materials become more complex and microstructures more intricate.

The motivation for this work was therefore to satisfy the industrial need to combine a highly accurate nanoindentation system with a high-resolution imaging technique (SFM) in such a way that a specific sample site can be located quickly and easily both before and after an indentation experiment. In addition, the applicability of the SFM technique to alternative modes of operation such as indenting and scratching have been investigated and realised with a hope of producing a complete nanotribological *test-station* in one integrated instrument.

Chapter 1 gives an overview of SFM principles, with emphasis on the use of friction force microscopy and details about the Atomic Scale Tribometer™ which formed the basic instrument from which modifications were made. This instrument was developed and its advantages shown by my predecessor Martin Binggeli in his PhD thesis¹⁴.

In Chapter 2, the principles of nanoscale scratching are described together with their industrial implications, especially in the magnetic hard-disk industry where no other method presently exists for characterising the extremely thin barrier films which are now being used. Some interesting results and the first utilisation of diamond-coated cantilever tips are shown.

The principles of nanoindentation are explained in Chapter 3, after which the SFM approach to nanoindentation is described in Chapter 4, as is the use of such technology for indenting and subsequently imaging with the same diamond tip. The first combined system prototype is presented in Chapter 5 with which nanoindentation and imaging could be carried out in a user-friendly manner. The limitations and restrictions of this system then lead to the development of a more commercially viable solution to the problem, in the form of the Nano Hardness Tester™, which is detailed in Chapter 6. The final section, Chapter 7, lists some published results and applications, confirming the applicability of the system to a whole range of industrial and research problems and demonstrating its potential for future development and more in-depth tribological studies.

Chapter 1

Scanning Force Microscopy

Since its development in 1986 by Gerd Binnig, Cal Quate and Christoph Gerber at Stanford University¹², the scanning force microscope (SFM) has revolutionised the field of surface analysis, allowing three-dimensional imaging up to atomic resolution in almost any sample environment. With an expected annual growth rate of 70%, commercial production of such instruments is expected to become a \$1 billion industry by the year 1998² and it is clear that both research and industrial applications will continue to rapidly expand.

1.1 The principles of the scanning force microscope

The basic principle of the SFM consists of scanning a very sharp tip, which is mounted on a spring or *cantilever* beam, over the sample surface and measuring the tip/sample interaction forces using some kind of deflection sensor. Although a similar principle to conventional stylus profilometers which have been in use for many years, the main innovative feature of the SFM is its feedback control system which allows the contact pressure between the tip and sample to be controlled and adjusted very accurately, in order to image the surface topography with very low contact pressures. In the so-called *contact mode*, the tip and sample are in relative motion whilst being in mechanical contact, meaning that the deflection of the cantilever is proportional to the height variation of the sample and therefore can be recorded with subnanometer height resolution and with force resolution in the order of nanonewtons or smaller⁵. In the *non-contact mode*, the tip is scanned at a very close distance to the sample surface but without in fact coming into contact with it, and force variations due to force gradients of long range interactions are detected¹⁰. This method, although useful for atomic-scale measurements, is not relevant to tribological and normal imaging applications and so is not described further.

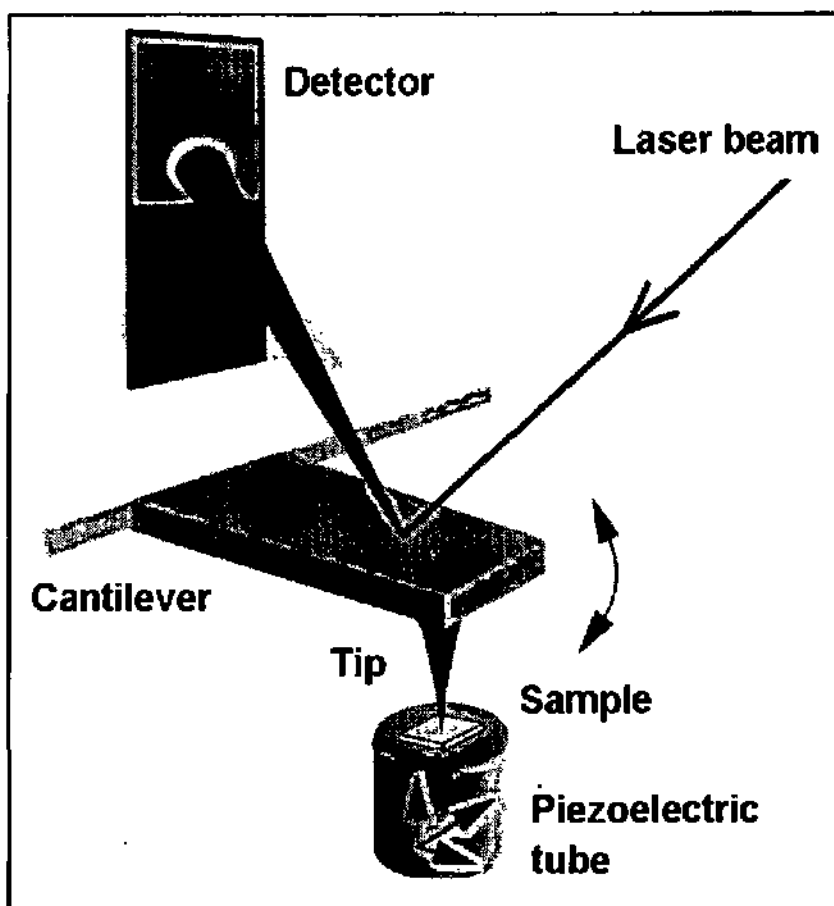


Figure 1: Principle of operation of the scanning force microscope.

In most SFM systems the sample is scanned using a piezoelectric tube which can be actuated in the x , y and z axes and the deflection of the cantilever is measured using a beam deflection technique where a laser beam is focussed onto the reflective backside of the cantilever and is then reflected into a photosensitive detector. The basic principle is depicted in Fig. 1. Other methods for measuring cantilever deflection exist, such as homodyne/heterodyne interferometry⁴⁵, fiber-optic interferometry⁴⁶, capacitive⁴⁷ and piezoresistive⁴⁸ methods, but the beam deflection technique is still the most common. To minimise the effects of lateral forces being applied at the tip during scanning in contact mode, and for measuring the topography of soft surfaces, SFMs can be operated in the so-called *force modulation mode* or *tapping mode*⁴⁹. In this mode, the tip is lifted and then lowered to contact the sample (oscillated at constant amplitude) during scanning over the surface with a feedback loop maintaining a constant average force. This technique eliminates frictional force entirely, the amplitude being kept large enough to prevent the tip from

getting stuck to the sample due to adhesive attractions. In addition, the modulation mode can be used to measure local variations in surface viscoelastic properties⁵⁰.

The tips used for SFM are most commonly microfabricated from silicon or silicon nitride, and are very reproducible if made using modern batch fabrication techniques. The tip forms an integral part of the cantilever beam and can have an apex size with near atomic dimensions. The geometry of the cantilever can be triangular (V-shaped) or rectangular, the former being more suited for topographical measurements, the latter for frictional (lateral force) studies. Fig. 2 shows a typical example of a rectangular cantilever with integrated tip. Cantilevers usually have spring constants in the range 10^{-2} - 10^2 Nm^{-1} and resonant frequencies greater than 10 kHz (but preferably 30-100 kHz) in order to reduce vibrational noise and to increase response time for fast scanning (which is favourable for reduced thermal drift effects).

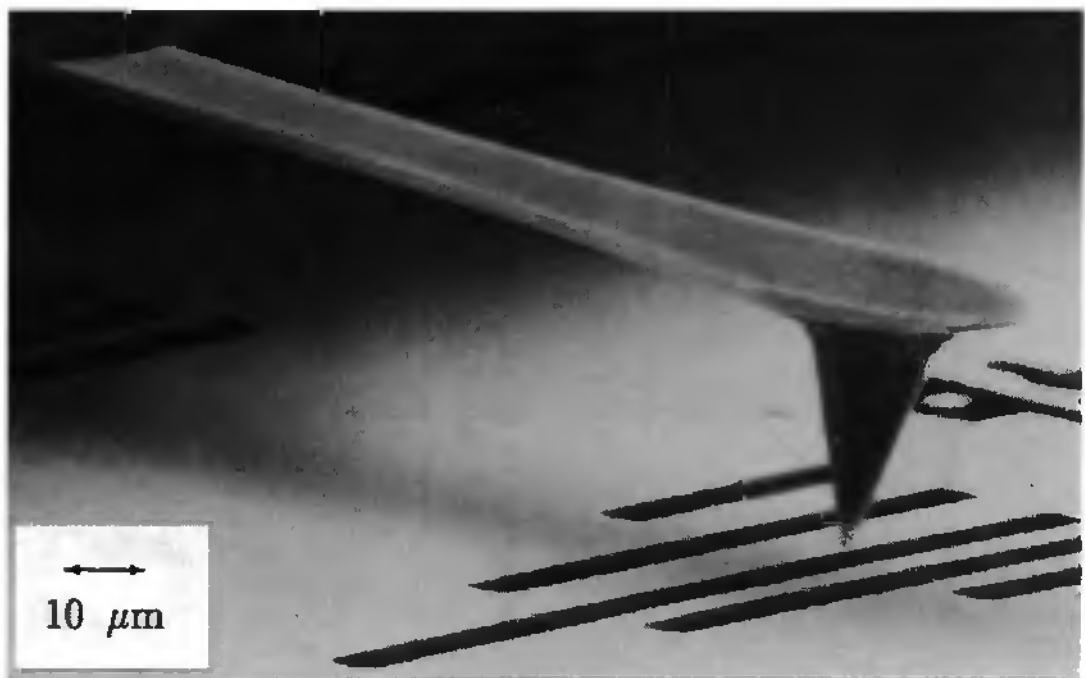


Figure 2: SEM micrograph of a typical micromachined silicon cantilever for SFM (*courtesy of IBM*).

An ideal SFM is a noise-free device that images a sample with perfect tips of known shape and has a perfectly linear scanning piezo. In reality, scanning devices are affected by distortions for which corrections must be made. Such distortions can be either linear or nonlinear. Linear distortions mainly result from imperfections in the machining of the piezoelectric actuators causing cross-talk between the Z-piezo and the X- and Y-piezos and vice versa. Nonlinear distortions mainly result because of the presence of a hysteresis loop in piezoelectric ceramics. Electronic noise may also be present in the system, but can usually be removed with suitable filters.

1.2 Friction force microscopy

By measuring the lateral force on the cantilever tip, or the *torsion*, it is possible to map the frictional properties of the sample surface. This is referred to as Friction Force Microscopy (FFM) or Lateral Force Microscopy (LFM) and is best achieved by using a rectangular cantilever and an optical beam deflection method, such as that shown in Fig. 3. Any angular movement of the cantilever will change the location of the laser spot focussed on the four-quadrant photodiode, and thus the balance of electric current. The intensity difference between the upper and lower segments is proportional to the vertical bending of the cantilever (topography) and the difference between the left and right segments is proportional to the torsion of the cantilever (friction). The advantage of this system is that both normal and lateral forces can be measured simultaneously, allowing *chemical sensitivity* of the surface due to the lateral force being influenced by the chemical properties of the measured material⁵¹. Frictional contrast is obtained experimentally by allowing the normal force to vary whilst scanning, after which a two-dimensional histogram can be plotted of the lateral force as a function of the normal force. Surface regions having different friction coefficients will appear as straight lines on the histogram and can be attributed to different materials depending on their position. Such a procedure eliminates the need to calibrate the zero of the normal force at the contact point, this being difficult in practice owing to the presence of Van der Waals and capillary attractive forces. Coefficients of friction may also be calculated by summing the forward and backward lines of a scan to eliminate any torsion of the cantilever produced by changes in topography.

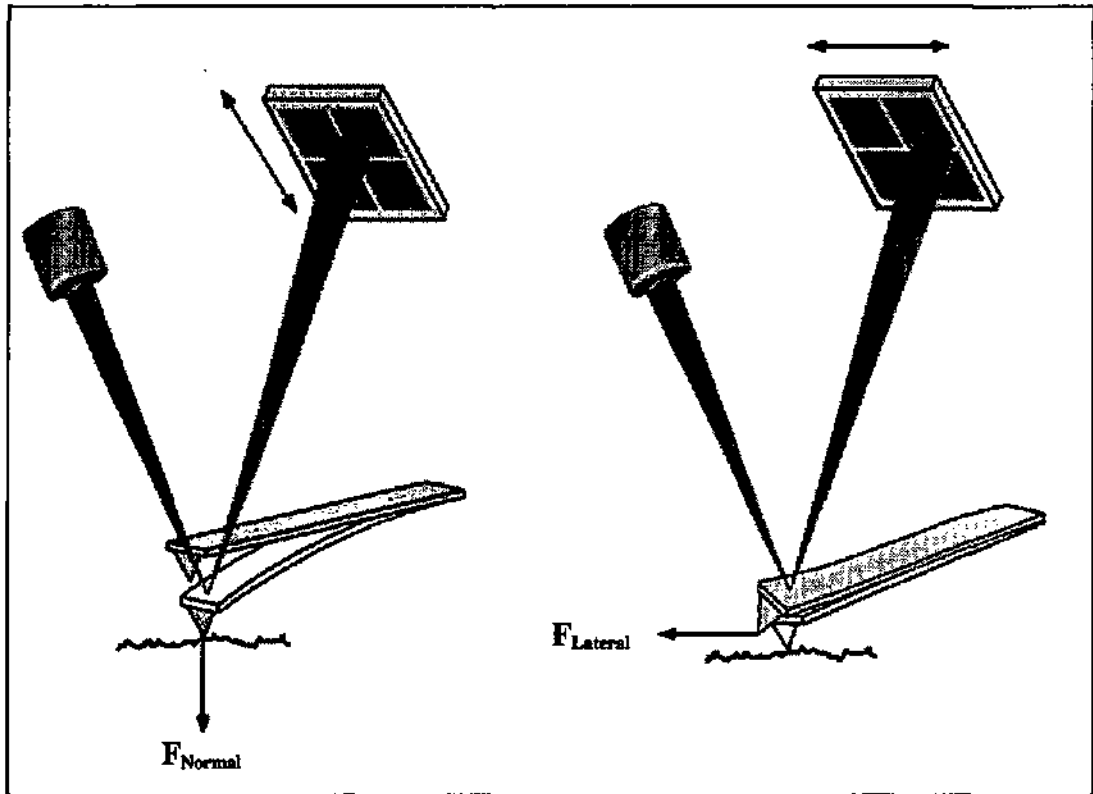


Figure 3: The principle of the two-dimensional beam deflection technique for simultaneous detection of normal and lateral forces acting on the FFM tip.

With regard to nanotribological studies, the FFM is well suited to the simulation of a point contact and can be utilised for a whole host of interesting applications. For a single asperity contact, the dependence of friction on load can be significantly non-linear, this being to the contrary of Amootons' law of friction which states that the coefficient of friction is indepeodent of apparent contact area and normal load. Thus the FFM can be used to study the dependence of shear stress on the mean contact pressure between tip and sample, the results of which have already suggested that microcomponents sliding under lightly loaded conditions should experience very low friction and near-zero wear⁵². Another example is the use of a FFM to move small islands of material by the action of the scanniog tip. The lateral forces are monitored during the manipulation, from which the shear strength at the interface between island and substrate can be accurately measured⁵³.

1.3 The Atomic Scale Tribometer™

The main SFM used in this work was one built by Centre Suisse d'Electronique et de Microtechnique and commercialised under the name *Atomic Scale Tribometer™*(AST). This instrument, developed at the University of Konstanz^{14,54}, merits some further explanation owing to its advantageous design and wide-ranging use.

The instrument is designed as a *stand-alone* measuring head, i.e., the piezoelectric scanner is integrated with the optical beam deflection system in such a way that samples of any size can be imaged. The collinear beam path is depicted in Fig. 4, with a laser diode as the light source. Both normal and lateral forces are measured using a four-quadrant position-sensitive detector (PSD). The laser beam passes through a polarising beam-splitter (BS) and a $\lambda/4$ plate (which rotates the polarisation vector), is reflected off the cantilever, passes undeflected back through the BS due to its polarisation orientation, and is directed into the PSD.

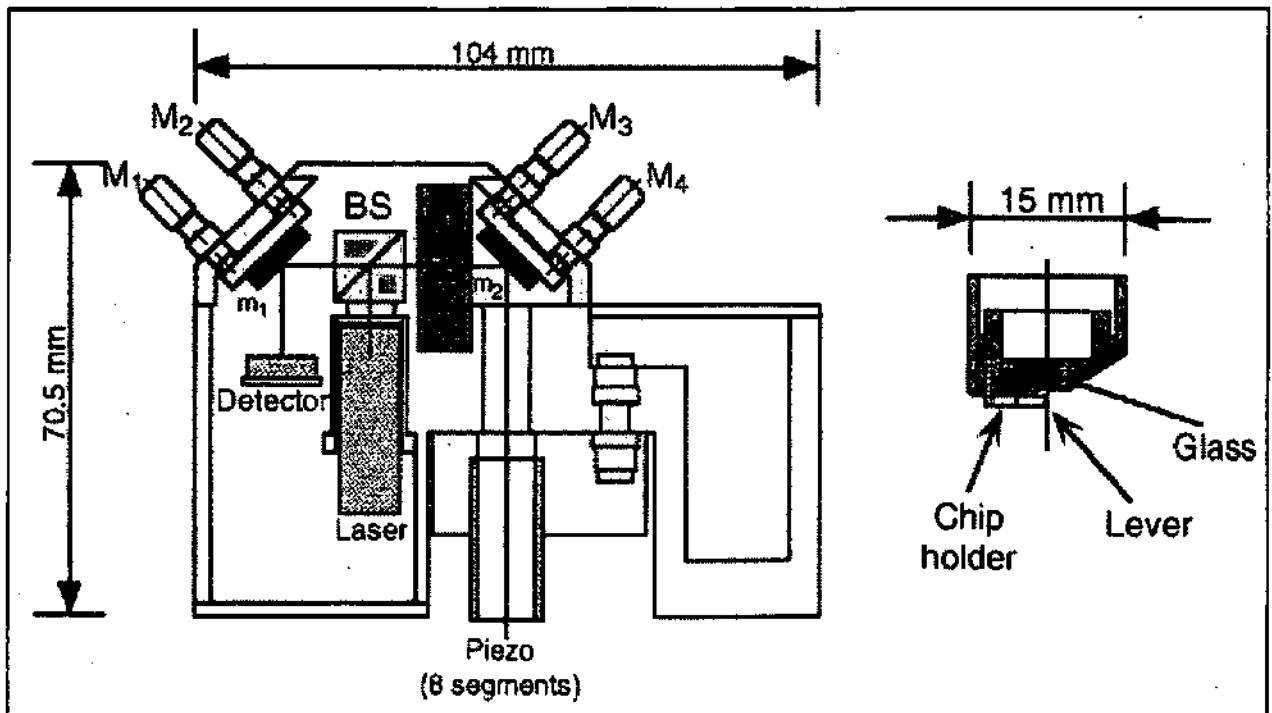


Figure 4: Schematic representation of the collinear detection system used in the Atomic Scale Tribometer™.



Figure 5: The CSEM Atomic Scale Tribometer™ measuring head.

The adjustment of the optical path and force calibration⁵⁵ is performed using two accessible micrometer screws and the measuring head (Fig. 5) includes an automatic coarse and fine approach facility. This instrument has the advantages that both friction and normal forces can be measured simultaneously by using a single laser beam, the measuring head is compact and stand-alone, and the vibrational characteristics are very good. Previous studies have already shown the wide range of applications for which the AST is ideally suited, e.g., *in-situ* electrochemical studies¹⁴, pulsed-force mode imaging of PMMA at varying temperatures⁵⁶, surface characterisation of bearing components⁵⁷, pulsed-force mode imaging of spun PP fibres⁵⁸ and atomic resolution imaging of mica⁵⁵.

1.4 Surface roughness and its measurement

Most tribologists are concerned with what happens when two solid surfaces slide over each other, under either dry or lubricated conditions. Surface texture and roughness parameters are often measured and compared before and after the wear process, as well as at intermediate stages. Understanding the relationship between wear properties and surface texture can lead to the specification of optimised surface properties and manufacturing processes for various surface functional needs. Some theoretical aspects of surface roughness measurements using SFM are now explained regarding their validity with respect to conventional roughness measurements.

There are a great variety of surface parameters, many of which have been developed to characterise the function of engineering surfaces for particular applications. Such parameters can generally be classified as height parameters, wavelength parameters, shape parameters, and combinations of these, known as hybrid parameters. These are all explained in detail in the literature⁵⁹, but when imaging with a SFM, the most common statistical descriptors of surface height are the average roughness, R_a , and the root mean square (RMS) roughness, R_{rms} , which are closely related and can be defined as follows:

$$R_a = \frac{1}{L} \int_0^L |y(x)| dx$$

$$R_{rms} = \left[\frac{1}{L} \int_0^L y^2(x) dx \right]^{\frac{1}{2}}$$

where $y(x)$ is the surface profile, sampled over the length, L . The parameters R_a and R_{rms} are very useful estimates of the average heights and depths of surface profiles. For homogeneous surfaces R_a is very close to R_{rms} , but if the surface is heterogeneous then $R_{rms} > R_a$. Conventionally, such roughness parameters are measured on a microscale using instruments such as the stylus profilometer or the non-contact optical profilometer. The former consists of a sharp, lightly loaded stylus which is drawn at constant speed over the surface to be examined, whereas the latter illuminates the surface with infrared radiation, some of which is scattered back to the instrument, its angular distribution being determined by the surface topography of the sample. Both methods

can measure either a single line profile or an area with a vertical resolution of <10 nm and a lateral resolution of 1 μm . The SFM, in contrast, which has sub-nanometric lateral and vertical resolutions will of course give a far more detailed roughness profile of a given sample area and this will also affect the quantitative roughness value measured. However, the main advantage of three-dimensional imaging is that the surface morphology can be investigated and marked differences observed even if the roughness remains constant. An example of this is shown in Fig. 6 which shows two surfaces of identical R_{rms} but having completely different structure.

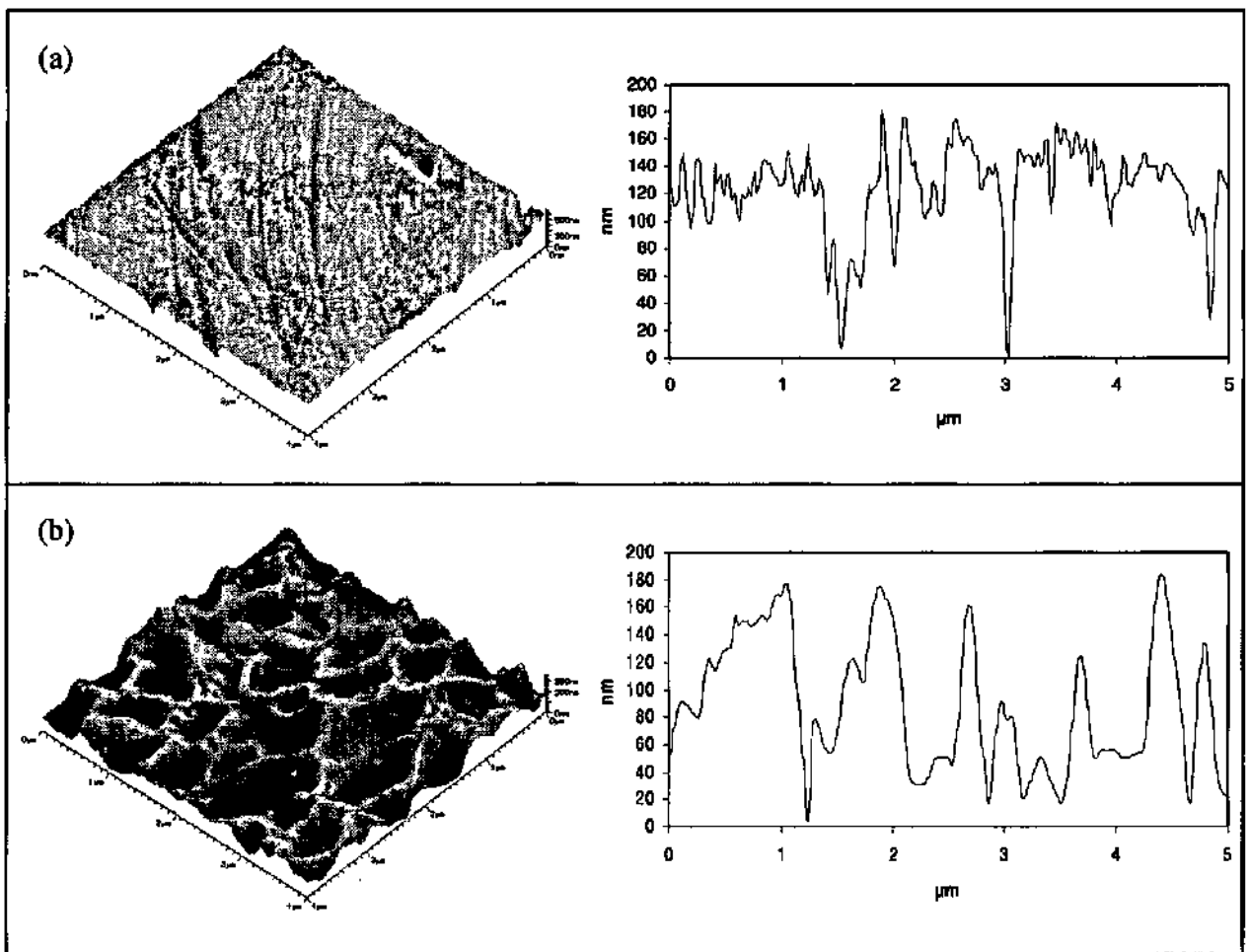


Figure 6: SFM images of two surfaces having the same roughness ($R_{rms} = 54 \text{ nm}$) but completely different structure. Image (a) is a Si_3N_4 bearing ball and (b) a ceramic tool surface. Note the difference between the two typical line profiles (lateral resolution = 20 nm).

A value measured on a micron scale cannot be directly compared with one on a nanoscale so methods are required in order to extrapolate from high resolution SFM images so that comparative roughness values can be calculated in relation to their scale dependence. Fractal analysis, based on Mandelbrot's classic paper of 1967, has been increasingly used to characterise the self-repeating nature of surface roughness^{60,61}, and it has been shown that roughness does appear fractal at nanometer scales⁶². For a small region of a rough surface to statistically resemble a larger region, the enlargement should be done *unequally* in the vertical (z) and lateral (x, y) directions. This is described as a *self-affine* fractal, i.e., the surface scales differently in different directions, and can be characterised by calculating an average roughness for each length scale and plotting it in a log-log plot against the horizontal length scale as shown in Fig. 7.

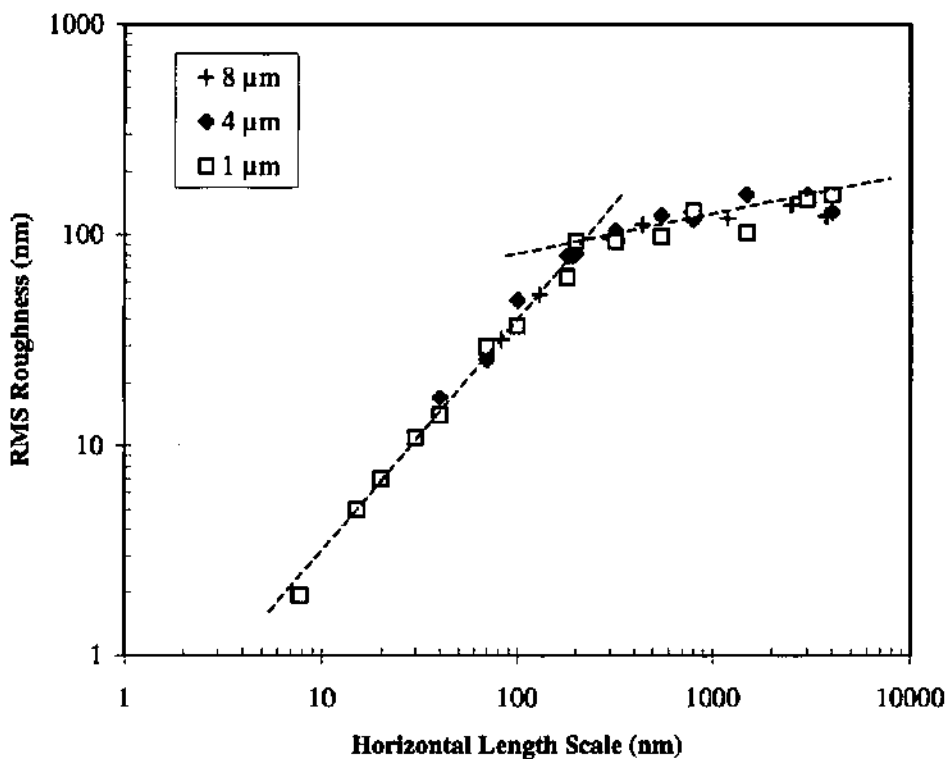


Figure 7: The RMS roughness of the Si_3N_4 bearing ball surface shown in Fig. 6 (a) plotted against the horizontal length scale on a log-log plot. Images of $1 \mu\text{m}^2$, $16 \mu\text{m}^2$ and $64 \mu\text{m}^2$ were subdivided into data parcels from 8 nm up to 4000 nm horizontal scale and an average roughness value calculated for each length scale.

It is observed that the data follows two straight lines of different gradient, depending on the magnitude of the horizontal length scale. Such a linear region over at least two decades is indicative of fractal character. The actual roughness value for the surface is calculated from the gradient of the second slope and therefore this value may be extrapolated in order to obtain a direct roughness comparison with data obtained from conventional profilometers. Many common engineering surfaces exhibit the same phenomenon of fractal behaviour up to a certain critical length scale, L_0 , above which the slope drastically decreases. The value of L_0 can often be attributed to a surface machining or growth process. For polycrystalline surfaces this may be the grain size, whereas for machined surfaces it may correspond to a characteristic tool size. Fractal methods can also be used to extrapolate down to atomic dimensions, although a cut-off point will be reached at which the measurement becomes limited by the geometry of the SFM tip. This has been shown with STM measurements on fracture surfaces⁶³, where the power spectra exhibit fractal characteristics down to a length scale of 12 Å.

Topographical analysis of fractal surfaces from SFM images extends the range of experimental measurement by several orders of magnitude. While fractal dimensions calculated from SFM images cover only perhaps 2-3 decades, they do so in the range of nanometers, in complement to conventional profilometer measurements which typically cover about 3 decades in the range of microns to millimeters. In the cases where both measurement techniques yield equivalent fractal dimensions, it is possible to bridge the gap from atomic up to millimeter scales. In the cases where measurements yield different fractal dimensions, some consideration must be given to the possibility that more than one process has occurred as the surface was being produced, leading to a multifractal structure. This could be further investigated by making a single measurement over the entire range of useful length scales, but present instrumental methods as yet are unable to perform such measurements with adequate resolution over the whole range.

Nanoscale Scratching

Nanoscale scratching and wear studies are a very powerful means of evaluating the mechanical integrity of ultrathin films and coatings. Improvements in experimental techniques and analysis have advanced the study of atomic-level nanotribology on well-defined surfaces, but it is difficult to directly apply these studies to practical surfaces. Almost all sliding surfaces, whether polycrystalline or amorphous, are contaminated, not well-defined and inhomogeneous, and therefore require specially adapted instrumentation for their characterisation.

2.1 Industrial implications

In view of increasing demands for achieving sub-micrometer tolerances without sacrificing the reliability of technologically advanced electromechanical components, such as those used in magnetic recording devices and MEMS, and the rapid emergence of new vacuum techniques for producing ultrathin films with novel microstructures, basic knowledge of the nanoscale mechanical and tribological characteristics of thin films is of both practical and scientific significance. Very lightweight sliding parts are beginning to be used in magnetic storage systems which require wear rates that are almost zero. For magnetic discs with a multilayered thin film structure, any wear of the diamond-like carbon (DLC) overcoat is catastrophic, such wear usually being initiated during each start-stop cycle of the read/write head. Most modern magnetic heads are mounted on a slider which is spring-loaded (typically 30-90 mN) against the disk surface, an air bearing being established at the head-disk interface during the spin-up of the disk. Since such an interface must survive several thousand start-stop cycles during the lifetime of the drive, friction and wear of both the slider and disk become important considerations in the design of the head-disk interface. Current head-disk spacings in magnetic disk drives are of the order of 50 nm, but are being constantly decreased in order to increase the recording density. In the 1960s, typical recording densities were of the order of 5 kbits/inch², whereas densities of up to 1000 Mbits/inch²

are now being achieved. In view of the increasing operational demands on the head-disk interface, the need for a detailed tribological understanding of issues such as surface roughness, wear of the magnetic medium, stiction behaviour and the effects of humidity, contamination and operating environment is becoming ever more important⁶⁴. The magnetic hard disk is but one example of the many modern microdevices whose development can be aided by nanoscale scratching and wear studies.

2.2 Experimental instrumentation

The techniques developed for nanoscale scratching are based on the principles of the scanning force microscope (SFM) described previously in Chapter 1. In order to obtain accurate data in a controlled way it is important to use cantilever tips of known geometry, suitable cantilever beams (i.e., stiff enough to create damage under load, but flexible enough to allow imaging of the surface without causing additional damage), and to calibrate the applied force. As we shall see later, soft materials can be successfully scratched and imaged with commercially available cantilever tips of silicon or Si_3N_4 . However, for harder materials, specially adapted beams and tips are required that will resist damage and to this end the use of diamond, either polished as a solid tip or deposited as a thin film onto an existing Si-based tip, is the logical solution.

In terms of instrumentation, the tip must be moved across the sample either as a single line (*single pass*) or as a series of lines (*multipass*), whilst maintaining a predefined normal load. The integrated piezo of the SFM can be used for this purpose, but only for small scan ranges (<50% of total scan range) otherwise hysteresis effects are no longer negligible. This can be corrected by feedback control of the x- and y-scanner elements but such an option was not available on the SFM used. The second alternative is to use the piezo solely for applying the load, and to move the sample laterally using a separate displacement system. This has the advantage that a much longer scratch can be made and subsequently imaged at certain points along its length. The experimental apparatus shown in Fig. 8 consists of an aluminium uniaxial translation table which has a maximum range of 200 μm and is displaced by a motor-screw assembly. By using a 16-bit programmable function generator it is possible to accurately control the table movement with a lateral step resolution of ~ 3 nm. Table stability in the z-direction is less than 10 nm.

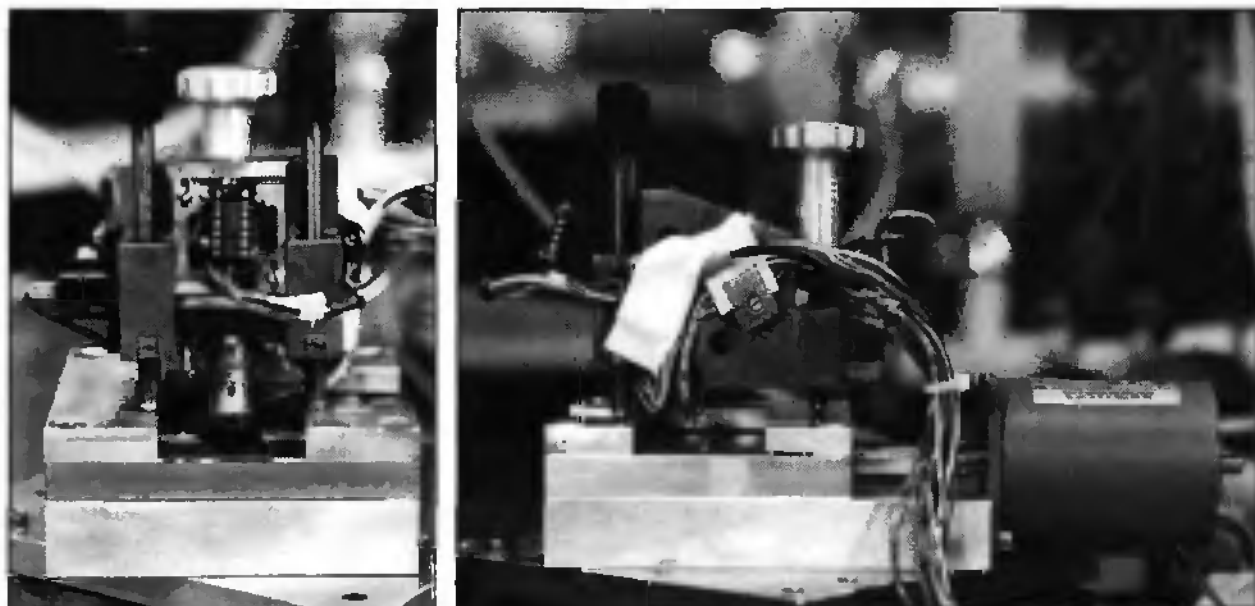


Figure 8 : Apparatus used for nanoscale scratching on PMMA thin films. The SFM head (a predecessor to the Atomic Scale Tribometer™) is shown on the left with its uncovered piezo tube and coarse approach screws. The translation table and motor assembly can be seen on the right.

The SFM head is mounted above the translation table such that the sample displacement direction is 90° to the SFM scanning direction. Thus the scratch can be made and directly imaged at any point along its length. In addition, scratching along the axis of the cantilever beam reduces error due to torsion of the beam. In order to minimise the effects of thermal drift, all measurements were performed in a controlled environment, i.e. $25 \pm 0.5^\circ\text{C}$ and 50% relative humidity ($\pm 5\%$).

Calibration of the applied normal force is performed by multiplying the vertical deflection of the cantilever (measured directly from the photodiode in nm/V) by its force (or spring) constant. If the adhesive force between the sample and tip is large then it should be included in the normal force calculation (see Chapter 4) but this component can be considered to be negligible for the present case of applied forces in the microNewton range. However, precise calibration requires that the cantilever spring constant be accurately known. This can be calculated from the geometry and physical properties of the cantilever material⁴ but the microfabricated Si_3N_4 cantilevers usually used can have significantly different properties to those of the bulk material. Thus, the effective spring constant is often recalculated using a simple procedure described elsewhere².

2.3 Diamond-coated cantilever tips

Recent research at CSEM⁹⁸ has resulted in optimisation of the chemical vapour deposition (CVD) technique for creating polycrystalline diamond thin films which are homogeneous down to thicknesses of 100 nm. Such films can be deposited onto commercial silicon cantilever tips giving an extremely robust surface coating which is ideal for nanoscale scratching of hard materials. In addition, CVD diamond has many material properties close to those of monocrystalline natural diamond. Several of these properties are superlative, and diamond is an attractive tip material owing to its high hardness and stiffness, and low wear. In addition, diamond has no superficial oxide layer and is chemically inert. A typical tip used for nanoscale scratching is shown in Fig. 9, the tip radius being of the order 100 – 150 nm. Such tips were microfabricated on cantilever beams of force constant 10 – 150 Nm⁻¹, in order to achieve the relatively high applied loads required for nanowear studies. Subsequent SFM imaging was possible with high resolution and SEM analysis of tips before and after scratching experiments confirmed that negligible wear had occurred. This demonstrated the applicability of diamond tips and their superior performance when compared to conventional Si and Si₃N₄ tips.

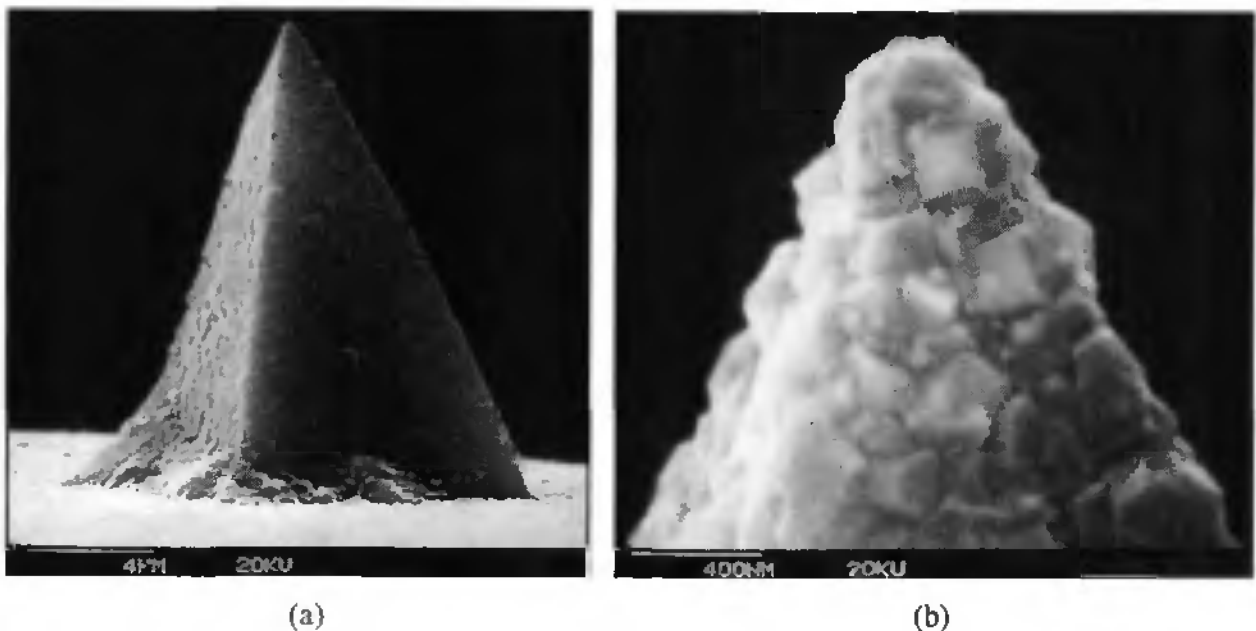


Figure 9 : SEM micrographs of CVD diamond-coated Si cantilever tip ; (a) overview, (b) close-up of tip apex showing the granular structure of the polycrystalline film (thickness = 100 nm).

2.4 Results

In this section some results are presented which effectively demonstrate nanoscale scratching on both soft and hard coating materials which have practical applications. Owing to the different hardnesses of such layers, various cantilever and tip types have been utilised depending on the particular wear characteristics of the measured material.

2.4.1 Soft coatings

Modern polymer-based materials are being increasingly used for very small sliding parts (such as gear wheels, bearings, etc.) because of their low specific gravity and ability to be easily fabricated into high-precision mechanical components. Polymers are also used as the binding medium in magnetic recording media for holding together the magnetic particles. In practice, however, pure polymers are not used due to their lack of adequate properties and are mixed with many kinds of additive to enhance service performance. The tribological properties of such polymer alloys and blends are difficult to accurately investigate because so many different components may influence their behaviour. For this reason, work has begun to characterise the wear resistance of pure polymer materials as well as composites. Bhushan *et al* compared different PET films⁶⁵, polymeric magnetic tapes⁶⁶ and video tapes⁶⁷. The microwear process has also been investigated in other polymers, e.g., polycarbonate⁶⁸, epoxy resin⁶⁹ and polystyrene⁷⁰.

In this study, thin films of polymethyl-methacrylate (PMMA) and polycarbonate (PC) were deposited onto very smooth and flat silicon substrates. The surface roughness of the films was < 1 nm meaning that shallow scratches could be performed without any discrepancies due to local surface variation. Due to the soft nature of these materials, standard Si₃N₄ cantilever tips were used with spring constants of 0.1 - 25 Nm⁻¹.

Fig. 10 shows a series of SFM images taken on a PMMA sample after single pass scratching at various loads using the aforementioned translation table set-up with a speed of 3.33 μm/s. It can be noted that plastic deformation along the sides of the scratch path becomes more marked as the applied load is increased. Similar scratches were carried out with the same applied load but with

varying table speeds and it was found that the scratch depth is lower at higher scratching speeds, probably due to the viscoelastic nature of polymeric materials. The same behaviour was also confirmed for similar experiments on PC. The SFM images were always taken at the same position along the length of the scratch in order to prevent error due to variation of the table in the z-direction. Scanning electron microscopy (SEM) showed that small flakes of wear debris were present along the flanks of the scratches, especially at higher loads, and it seemed that such particles were moved outside the image area during SFM scanning. SEM analysis also confirmed that successive scanning of the tip over the surface results in damage even with the very light loads used and that debris is also pushed into the scratch path by the imaging tip. In addition it was observed that wear particles attached themselves to the surface of the Si cantilever tip.

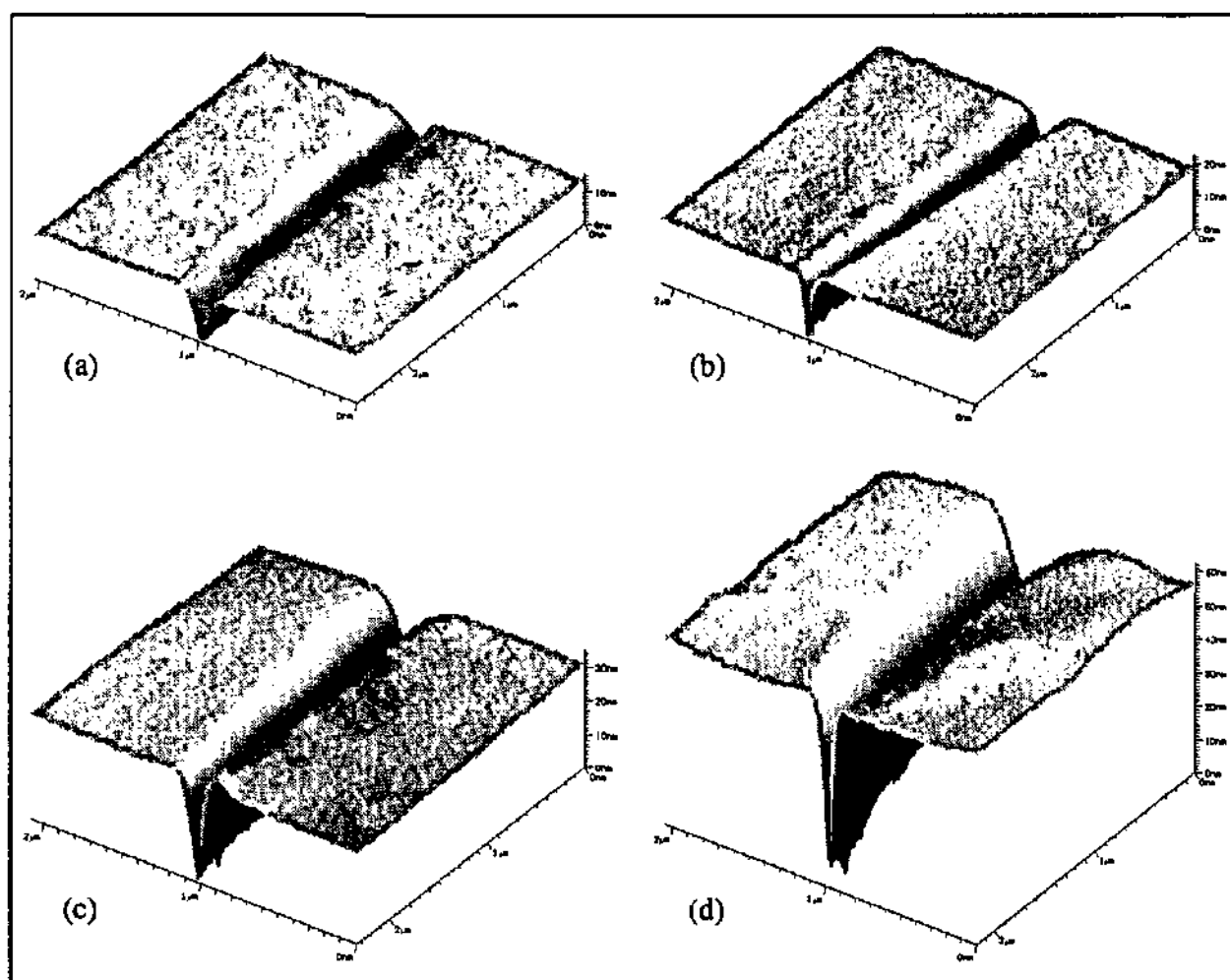


Figure 10 : SFM surface profiles of single pass scratches made on PMMA with a table speed of $3.33 \mu\text{m/s}$, a cantilever of force constant 25 Nm^{-1} and applied normal loads of (a) $2 \mu\text{N}$, (b) $4 \mu\text{N}$, (c) $6 \mu\text{N}$ and (d) $8 \mu\text{N}$.

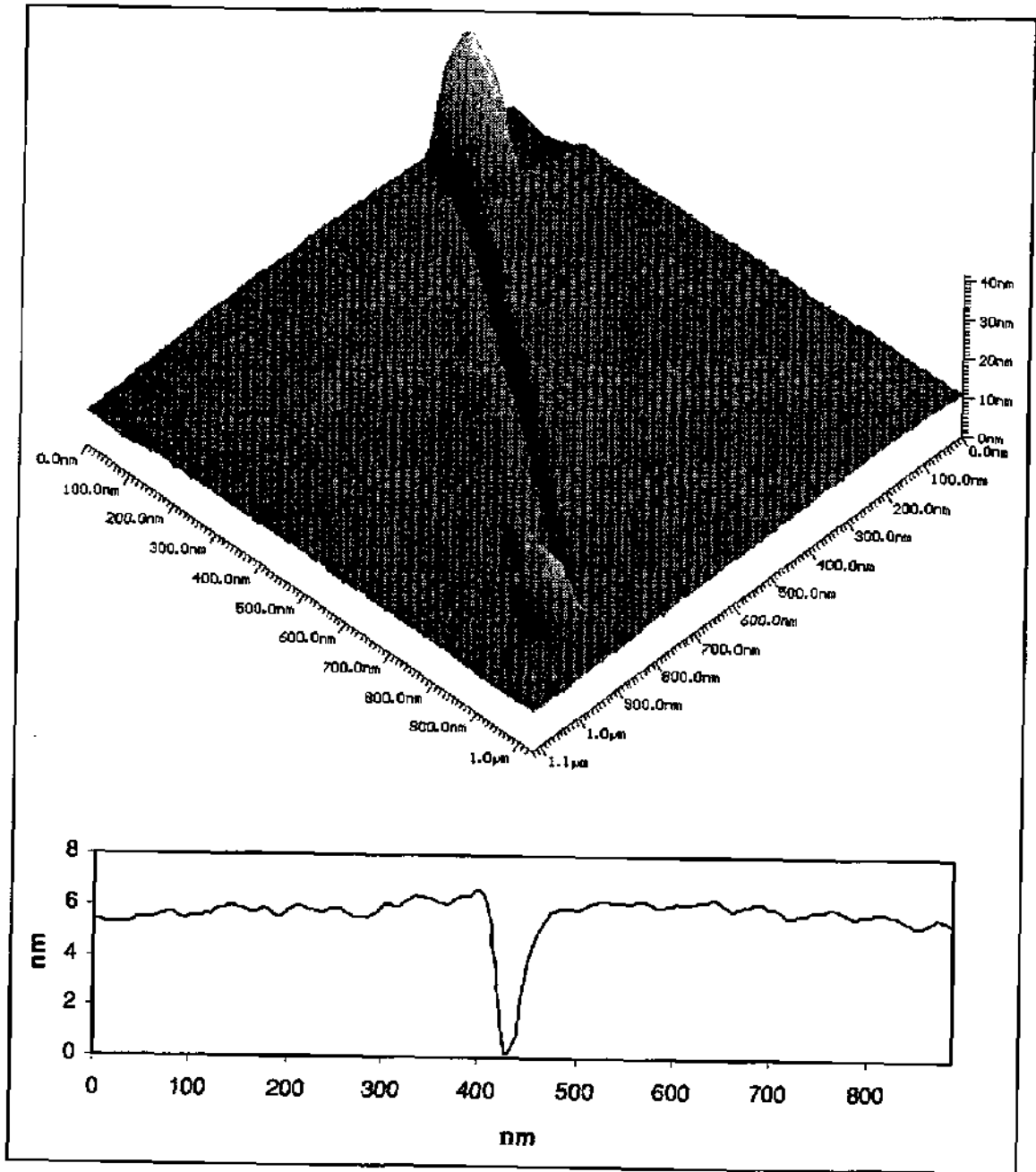


Figure 11 : SFM surface profile and corresponding cross-section of a multipass scratch (10 cycles) made with a cantilever of force constant 0.1 Nm^{-1} and an applied normal load of $1 \mu\text{N}$ on a PMMA thin film of thickness 200 nm.

The effect of a multipass scratch on PMMA is shown in Fig. 11 together with a cross-sectional profile from which the wear depth of $\sim 5 \text{ nm}$ could be measured. Significant pile-up of material is evident at either end of the scratch. Note that the scratch was made at a 45° angle to the

subsequent imaging direction in order to reduce the effects of imaging with the same tip that made the scratch. Similar multipass scratches at higher loads and with a greater number of cycles showed the formation of ridges along the scratch sides and an increasing amount of debris both in and around the scratch path. This phenomenon was observed for both PMMA and PC, the latter having a lower wear rate, although the amount of debris and pile-up seemed to be about the same for a given wear depth.

Apart from single pass and multipass scratching modes, the SFM can also be used for producing arrays of scratches as shown in Fig. 12 (a). In practice the instrument is programmed to scan an image of $6 \times 6 \mu\text{m}$ but with only 8 lines, meaning that an array of scratches is made with a spacing of $\sim 0.8 \mu\text{m}$. This is a particularly useful method for gaining an accurate measure of scratch depth because a simple line profile through the array gives the depth of each scratch from which an average value can be calculated. The example shown also demonstrates the hysteresis of the piezo scanner between the forward and backward line of each scratch, as well as the starting position of the tip under load denoted by a hole near the centre of the array. The tip moves from its rest position to the top left corner before scanning commences.

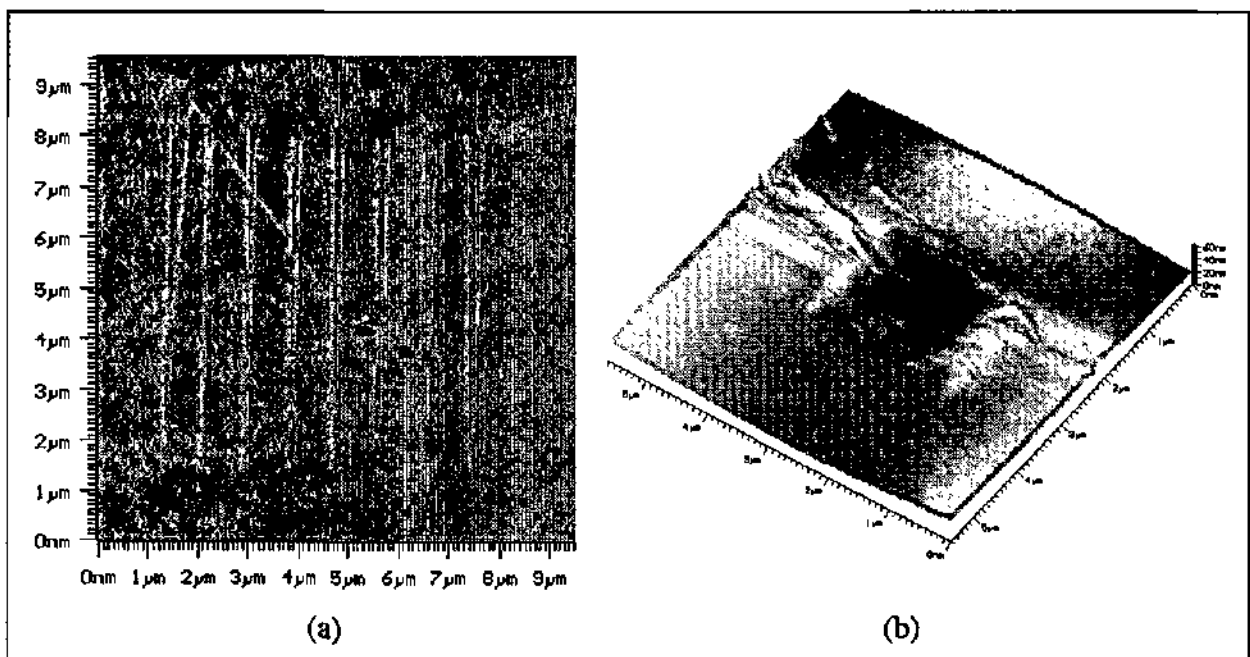


Figure 12 : SFM profiles of scratched polycarbonate (PC) surface after (a) series of 8 multipass (2 cycles) scratches of $6 \mu\text{m}$ length and $0.8 \mu\text{m}$ spacing, and (b) scanning scratching of a central square ($2 \times 2 \mu\text{m}$) with applied force $10 \mu\text{N}$ for 12 cycles.

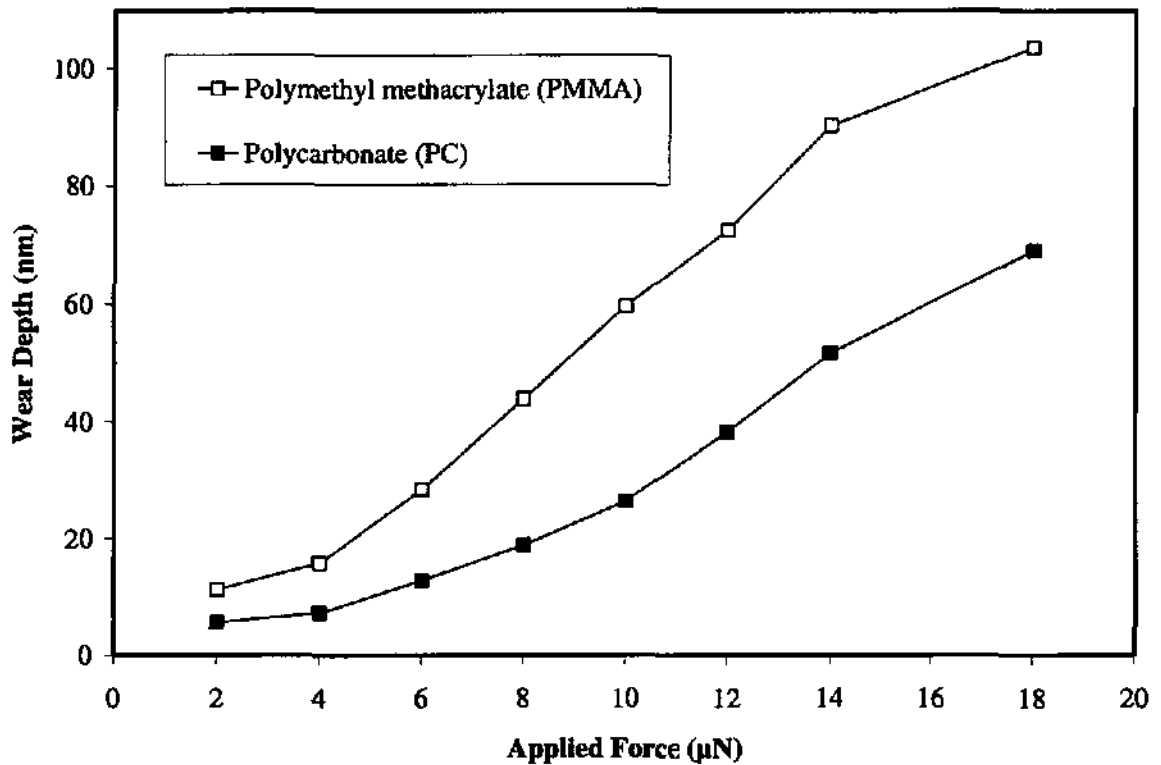


Figure 13 : Wear depth (scratch depth) as a function of applied normal force after a single pass scratch on PMMA and PC thin films.

The SFM also has the capability to scan an area under load after which the load is reduced to a minimum for imaging and the scan size increased so that the worn region can be profiled in three dimensions. An example of this is shown in Fig. 12 (b) where a $2 \times 2 \mu\text{m}$ square has been scanned on a PC film under an applied load of $10 \mu\text{N}$ for 12 cycles. A substantial amount of debris has been pushed to either side of the central worn region by the imaging tip. Continued imaging removes further debris but in practice it is not easy to prevent fouling of the image in this way because debris particles attach themselves to the tip and get redeposited in the worn region. This is particularly evident for soft polymeric materials. With PC it was found that at wear depths greater than approximately 50 nm, the debris clusters begin to have a noticeable effect on the wear process ; this is characterised by the boundaries of the worn region becoming distorted as accumulating debris particles push against the sides and contribute to plastic deformation. For PMMA the effect is even more pronounced with large amounts of debris being produced after the first scanning scratching cycle.

The scratch depth as a function of applied normal force is summarised for the two investigated polymeric materials in Fig. 13. It can clearly be seen that PMMA has a higher wear rate than PC for the same applied load, although both materials have been seen to exhibit a similar microwear process.

The SFM is ideally suited to the quantitative comparison of polymeric coatings by measuring the dimensions of a single scratch made under controlled conditions. It can also provide qualitative information about whether scratching results from brittle fracture or plastic deformation, and the degree to which a scratch can 'heal' via time-dependent relaxation⁷¹. Elastic recovery may be observed on many polymers by imaging a scratch at regular intervals after its fabrication and noticing any reduction in dimensions with time.

2.4.2 Hard coatings

In section 2.1 the importance of characterising hard coatings, especially those used in the magnetic recording industry, was briefly explained. In order to demonstrate the effectiveness of nanoscale scratching on such hard materials, a selection have been studied and compared, consisting of a commercially available hard disk overcoat of diamond-like carbon (DLC), a fluorinated amorphous carbon and a silicon-containing (20%) amorphous carbon overcoat. These three thin film coatings were investigated by the scanning scratching method as outlined in the previous section. Their high hardness meant that conventional Si_3N_4 cantilever tips could not be used as they would be destroyed almost immediately after loading. Thus, some diamond-coated tips were used together with cantilever beams having spring constants of 20 – 150 Nm^{-1} (as described in section 2.3). These stiffer beams were able to apply greater normal forces but at low loads were still found to be flexible enough for high quality imaging.

Fig. 14 shows the evolution of a 2 x 2 μm worn region as a function of number of cycles for a DLC hard disk overcoat of thickness 35 nm. In each case the SFM image is shown as a top view (left) and as a three-dimensional representation (right). The worn square was produced by scanning scratching with one cycle consisting of 256 line scratches of 2 μm length and 8 nm spacing. The scratching speed was 12 $\mu\text{m s}^{-1}$ and the applied force was 40 μN .

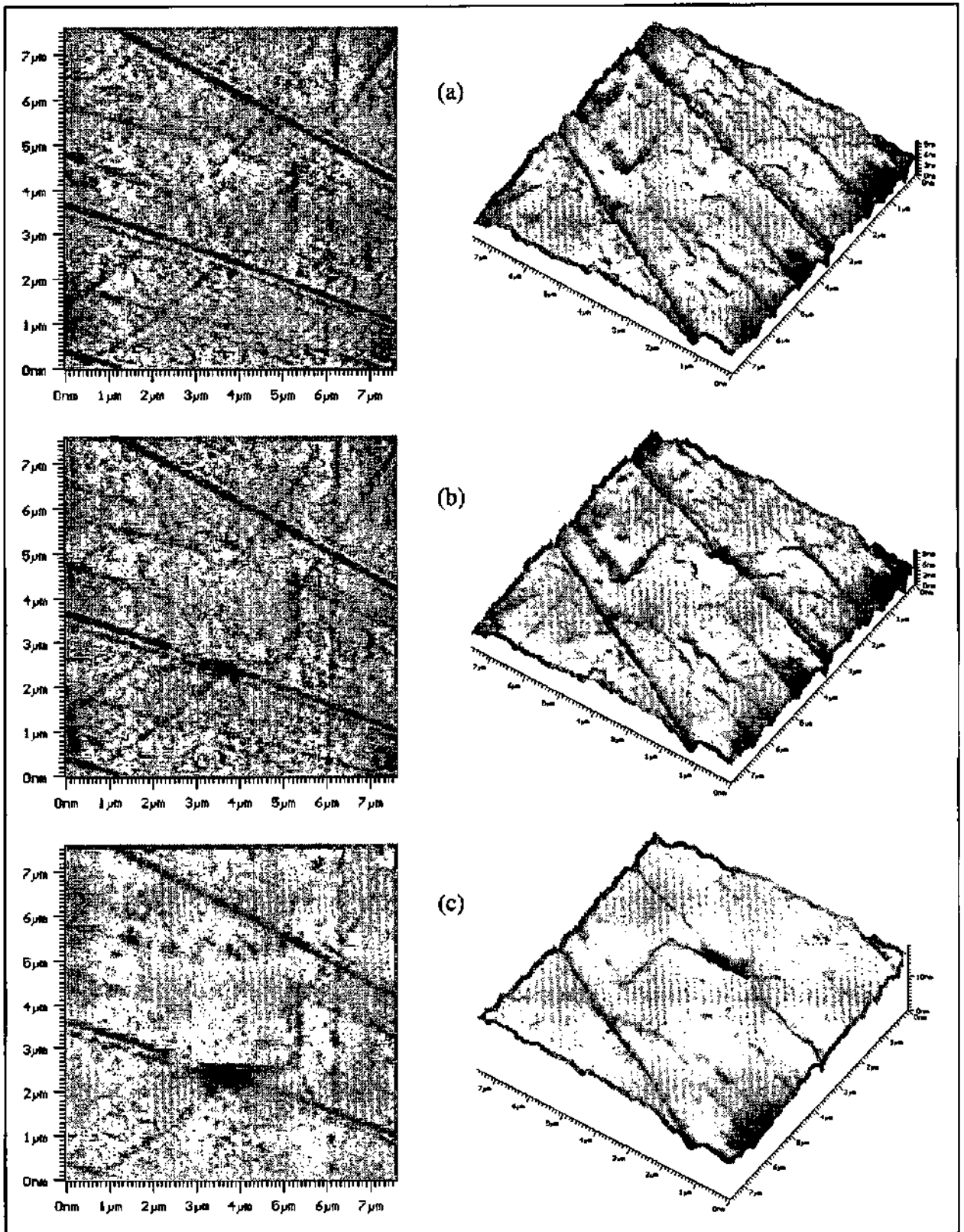


Figure 14: SFM profiles showing the evolution of a central worn region ($2 \times 2 \mu\text{m}$) after scratching with a diamond-coated tip and applied force $40 \mu\text{N}$ for (a) 2 cycles, (b) 4 cycles and (c) 8 cycles. Material is a DLC hard disk overcoat (thickness = 35 nm).

After 2 cycles (Fig. 14 (a)) the worn region is just visible but there has been no significant change in the surface other than a shallow groove around the perimeter. The region becomes more pronounced after 4 cycles (Fig. 14 (b)) with flattening of certain asperities by the loaded tip and build-up of two ridges on either side of the scratched area. The initiation of a hole can also be observed where the tip has moved across a pre-existing surface scratch and gouged out an amount of material. After 8 cycles (Fig. 14 (c)) the worn region has become flatter with any existing bumps being smoothed by the action of the loaded tip. The hole has increased in size and the two ridges have grown. This preferential wear (hole formation) suggests that a hard disk overcoat whose surface is scratched prior to use will fail more readily in service than a smooth unscratched surface.

Fig. 15 compares a $7 \times 7 \mu\text{m}$ area of the same DLC hard disk surface before and after a scanning scratching run of 20 cycles. Slight upheaval of the worn region has occurred together with deep grooving around the perimeter and ridge formation on either side of the plateau. Continued cycling (not shown) results in removal of the ridge material after approximately 35 cycles, leading to severe wear behaviour after 50 cycles. The observed material upheaval is thought to be related to plastic deformation phenomena (ridge formation) and subsequent shearing of material by the loaded tip. A similar effect has been observed with silicon (100) surfaces⁷².

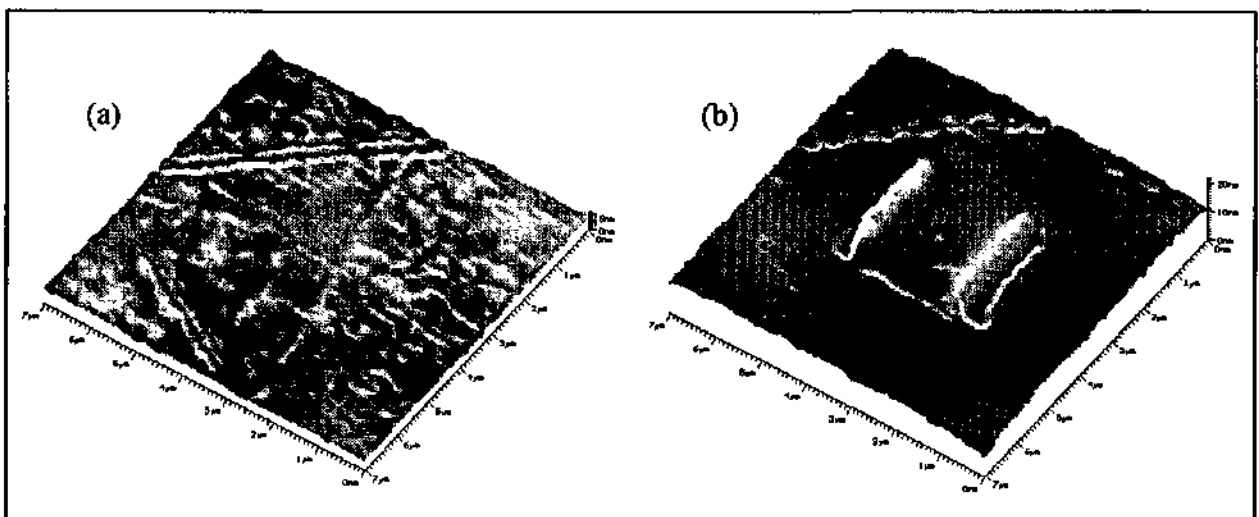


Figure 15 : SFM surface profiles of a DLC hard disk overcoat (a) before and (b) after scratching a central square ($2 \times 2 \mu\text{m}$) using a diamond-coated tip for 20 cycles with applied force $25 \mu\text{N}$. Note the plateau-like upheaval of material and the deep grooves around the perimeter.

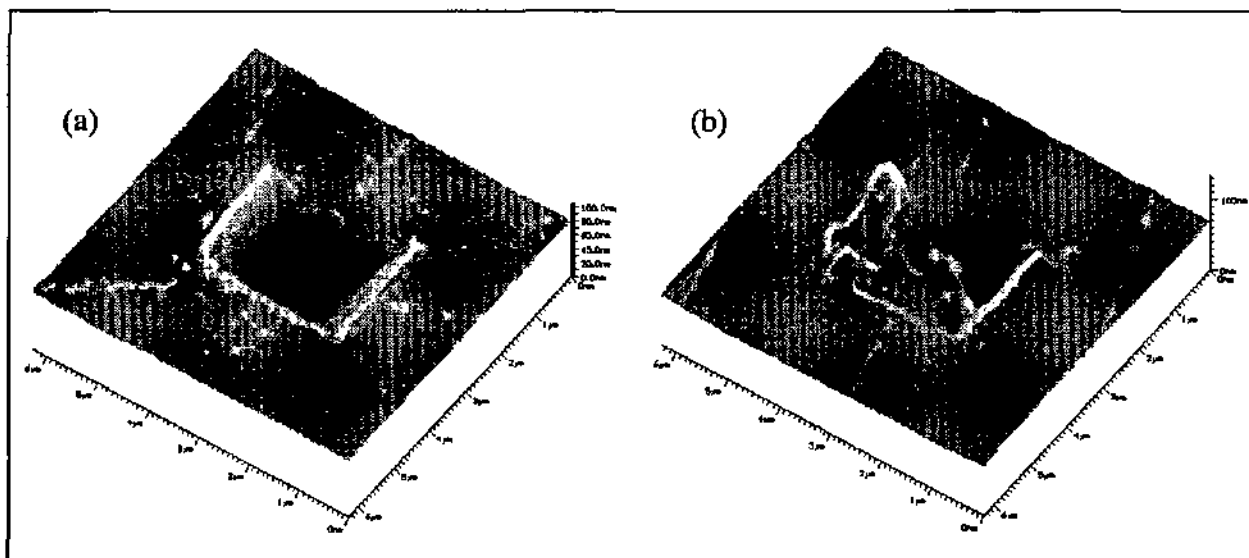


Figure 16: SFM surface profiles of central worn region ($2 \times 2 \mu\text{m}$) after scratching with a diamond-coated tip for 20 cycles with applied force $55 \mu\text{N}$. Both samples are hard disk overcoat materials, but have significantly different wear behaviours; (a) is fluorinated amorphous carbon and (b) is silicon-containing (20%) amorphous carbon.

The SFM surface profiles shown in Fig. 16 represent the effects of identical scanning scratching on two different overcoat materials and the significant variation in wear behaviour between them. The fluorinated amorphous carbon showed no upheaval effects; material was simply scooped out of the $2 \times 2 \mu\text{m}$ region with plastic deformation being characterised by pile-up on either side of the worn area. Wear debris was easily removed by the first imaging scan and little was observed around the damaged zone in subsequent scans. The Si-containing amorphous carbon also exhibited plastic deformation effects but, in contrast, large amounts of wear particles and clusters remained in the worn area even after many imaging scans thus confirming a significant bonding force between such debris and the carbon surface. In addition, the inside walls of the worn area are far less defined than for the fluorinated amorphous carbon. The addition of fluorine to hard disk overcoats serves the purpose of retaining hardness whilst creating a self-lubricating interface with the head slider. Silicon additions can also increase wear resistance but larger proportions are needed (30-40%) and the chemistry of the surface and sub-surface layers can become very complicated, especially when the overcoat is subjected to an oxygenated environment where surface silicon dioxide may significantly alter the wear properties.

2.5 Conclusions

The use of the SFM for nanoscale scratching and wear studies has been demonstrated and shown to be one of the only techniques able to accurately evaluate surface wear properties at ultra shallow depths. A modern magnetic hard disk is expected to survive more than 10 million revolutions without error, which means that the surface must wear at a rate of one atomic layer per hundred thousand to one million sliding cycles. The demand for this almost zero-wear condition is currently stimulating much research into surface modification techniques such as fluorination and ion-implantation, as these have been shown to improve wear resistance. However, adequate methods for characterising surface layers and simulating the expected service conditions are required in order to further research work in this field. The SFM is unique in the sense that it serves a double purpose; to create simulated damage to a surface and then to quantitatively measure the effects of such damage in a fast and efficient way. The development of better SFM cantilevers and tips, especially those that are diamond-coated, will no doubt produce far more reproducible scratching and imaging tools which can be tailored to specific applications, e.g., doped diamond-coated tips will allow wear behaviour to be investigated as a function of electrical potential.

Chapter 3

Nanoindentation

The measurement of the hardness of materials finds its roots in the field of mineralogy where it depends on the ability of one solid to scratch another or to be scratched by another solid. The method was first put on a semi-quantitative basis by Mohs in 1822 who selected ten minerals as standards and developed a hardness scale between them. Since then, several static indentation methods have been used to determine hardness as a function of applied load and size of the permanent impression remaining after an indenter has been withdrawn from the tested surface. With the development of more and more complex materials, the volume to be measured has decreased in size in order to give local property information at specific locations. Nanoindentation is a recent addition to the range of methods available and has found great success in the measurement of material properties at very low loads and shallow depths, allowing very small material volumes to be evaluated in a controlled and quantitative way.

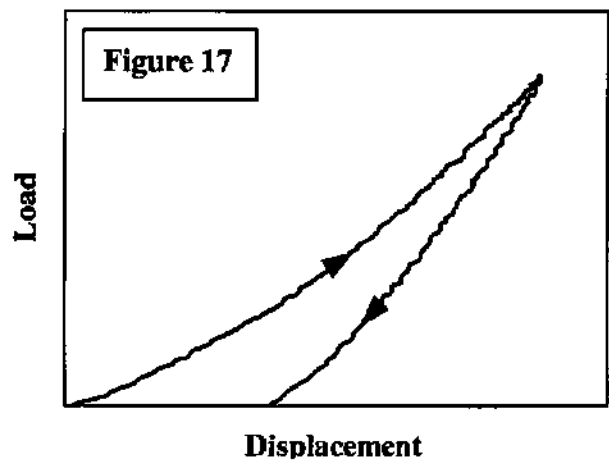
3.1 Historical background

In an introductory paper in 1934, O'Neill⁷³ remarked that hardness 'like the storminess of the seas, is easily appreciated but not readily measured'. The first standardised hardness test, developed by Brinell⁷⁴ in 1900, used a spherical indenter of hard steel or tungsten carbide, after which a pyramidal indenter was developed in 1925 by Vickers⁷⁵. It was soon found that diamond was the most suitable indenter material, its shape being gradually refined over the last 50 years. Microhardness testing, as the logical successor to conventional hardness testing, operates with loads in the range 0.01 – 2 N and the size of the residual indentation can still be measured via optical microscopy, although very small imprints nearing the resolution limit of optical methods cannot be measured accurately. In order to measure hardness with even lower loads, a different method has been developed which does not rely on assessing the size of the imprint, but instead continuously measures the penetration depth and load as an indenter (of known geometry) is

pushed into the sample material. With modern 'depth-sensing' instruments it is possible to measure displacements of a nanometer scale and so the term *nanoindentation* has now become widely accepted for this method.

Apart from simply measuring hardness, nanoindentation instruments are also able to measure other material properties such as modulus of elasticity, residual stress, time-dependent creep and relaxation, fracture toughness and fatigue. For very thin films and coatings, nanoindentation has become popular because it allows a wide variety of mechanical properties to be measured without removing the film from its substrate.

A typical load-displacement curve is shown in Fig. 17. After initial contact of the indenter on the surface (contact load less than a few μN or less), the load is increased at a predefined rate to the desired maximum and then decreased, at the same rate, to zero. The unloading curve follows the partial elastic recovery of the sample material, and it is this phenomenon that allows the derivation of information on elastic modulus, as will be explained later in more detail. With a sharp indenter the contact area is initially small, and there is no distinct elastic region at the beginning of the test, i.e., the deformation has both elastic and plastic displacements from the outset. Furthermore, the contact area continuously changes as the indenter is driven into and withdrawn from the specimen and these factors complicate the analysis of the data.



3.2 Indenter geometry

The main requirements for the indenter are high elastic modulus, no plastic deformation, low friction, smooth surface, and a well-defined geometry that is capable of making a well-defined indentation impression. The first four requirements are satisfied by using diamond material, but a well-defined perfect tip shape is very difficult to achieve. An ideal indenter has a flat-ended

geometry in order to avoid problems due to contact area changes, but in practice such geometries are rarely used because it is difficult to assure that the contact between a flat-ended indenter and the sample surface is uniform, due to surface roughness and misalignment of the indenter. Thus, pointed tips of known geometry are nearly always used. The most common for nanoindentation studies are the Vickers, Berkovich and spherical geometries. The three-sided pyramidal geometry of the Berkovich naturally terminates at a point, thus facilitating the grinding of diamonds which maintain their sharpness to very small scales. Berkovich tip defects, as characterised by the effective tip radius, are frequently less than 50 nm in many of the better diamonds. For the Vickers indenter, on the other hand, it is more difficult to maintain geometric similarity at such small scales because the square-based pyramidal geometry does not terminate at a point but rather at a 'chisel' edge. Conical and spherical indenters are the most difficult to grind accurately and so can have severe tip defects at small scales. In nanoindentation studies, conical indenters having a half-included tip angle of 70.3° are commonly used because they have the same area-to-depth relationship as the Vickers and Berkovich.

Although the Berkovich is the most suitable for very shallow penetration depths, the Vickers may be useful in measuring the properties of single crystals with 4-fold symmetry, or to directly compare hardnesses obtained in nanoindentation experiments with conventional Vickers microhardness results. In addition, the Vickers indenter is the primary indenter used in measuring the fracture toughness of brittle materials by the indentation cracking method⁷⁶. The conical indenter has advantages when one wishes to avoid deformation phenomena caused by the sharp edges of the Berkovich and Vickers indenters, e.g., when cracking is to be avoided in brittle materials or when large strain gradients around the circumference of the contact complicate the understanding of indentation phenomena. The conical indenter is also more amenable to analysis than the Berkovich or Vickers; virtually all modelling of indentation contact by sharp indenters uses the conical geometry⁷⁷, and with very few exceptions⁷⁸, most finite element simulations of indentation by sharp indenters have used the conical geometry to take advantage of the axial symmetry⁷⁹⁻⁸⁰. Spherical indentation overcomes many of the problems associated with pointed indenters. With a spherical indenter, one is able to follow the transition from elastic to plastic behaviour and thereby define the yield stress⁸¹. However, a sharper tip is desirable for extremely thin films requiring shallow indentation.

In order to accurately assess mechanical properties, the geometry of the indenter must be known and any deviations from an ideal symmetry corrected for in subsequent calculations. For the Berkovich, Vickers and 70.3° conical indenters, the ideal area function, $A = 24.5h^2$, this being the ideal area function which all three diamonds would exhibit if they were ground to perfect geometric form. Fig. 18 summarises the area functions of the three indenters over their range of applicability, i.e., contact depth, h_c , from 20 to 7000 nm. These were determined experimentally using a fused silica quartz sample for depths ranging from 20 to 1500 nm and an aluminium single crystal for larger depths, the two data sets being combined using curve fitting procedures.

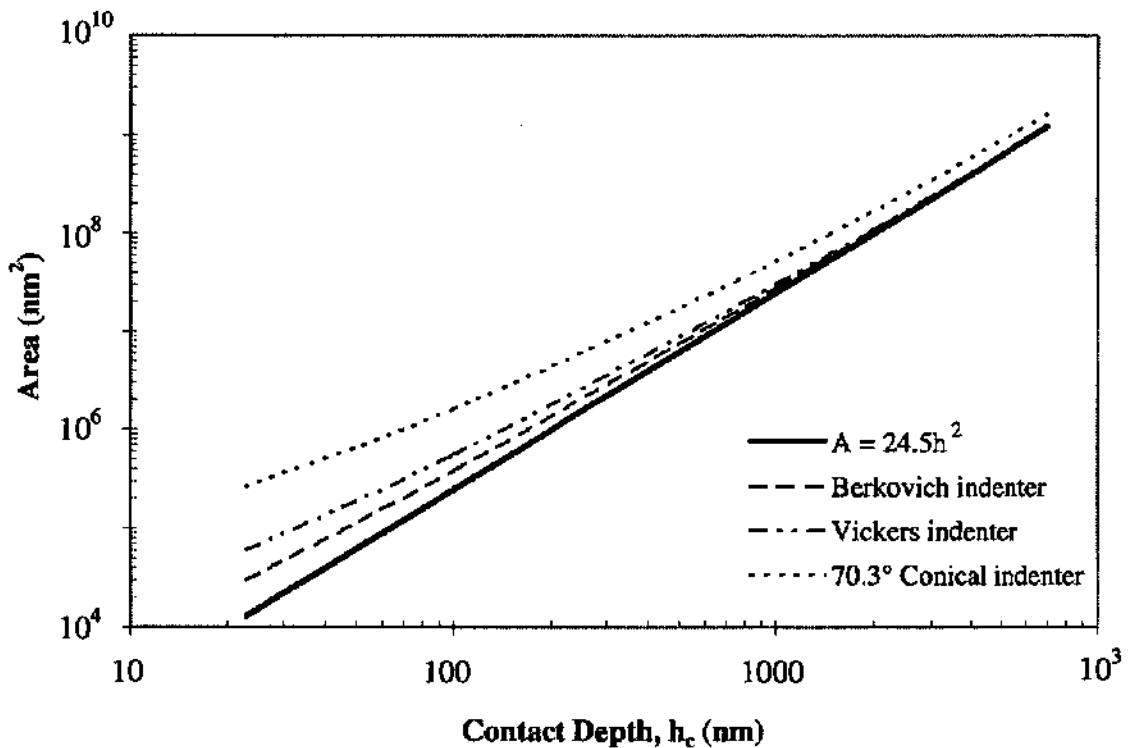


Figure 18 : Experimentally determined area functions for the three commonly used nanoindentation indenters.

The plot shows that while the geometry of the Berkovich indenter is in closest agreement with the ideal case, the 70.3° cone shows significant deviations over most of the applicable contact range. Such deviations are consistent with the notion that the 70.3° cone is very blunt and possibly more sphere-like than sharp at the scales of interest for nanoindentation. The Vickers indenter lies somewhere in between. Recent work⁸² has shown how the tip defect confuses the interpretation

of hardnesses measured by nanoindentation methods, since there is a change in the mode of deformation from purely elastic at low loads to elastic/plastic at high loads. This phenomena is more important in hard materials such as ceramics and glasses than it is in soft metals.

3.3 Analysis of indentation data

The two mechanical properties measured most frequently using load and depth-sensing indentation techniques are the hardness, H , and the elastic modulus, E . Such parameters can be calculated from nanoindentation data by several different methods, although the most common procedure is to analyse the load-displacement curve, which consists of a loading and an unloading portion. The loading data are usually influenced more by the plastic properties of the material and the unloading data by the elastic properties. The loading portion is that from which hardness is usually calculated, but can also provide additional information as will be explained later, especially regarding the properties of thin films. The unloading data are analysed according to a model for the deformation of an elastic half space by an elastic punch which relates the contact area at peak load to the elastic modulus. Methods for independently estimating the contact area from the indenter shape function are then used to provide separate measurements of E and H .

3.3.1 The unloading curve

The elastic contact problem, which plays a key role in the analysis procedure, was originally considered in the late 19th century by Boussinesq⁸³ and Hertz⁸⁴. Boussinesq developed a method based on potential theory for computing the stresses and displacements in an elastic body loaded by a rigid, axisymmetric indenter. His method has subsequently been used to derive solutions for a number of important geometries such as cylindrical and conical indenters⁸⁵. Hertz analysed the problem of the elastic contact between two spherical surfaces with different radii and elastic constants. His now classic solutions form the basis of much experimental and theoretical work in the field of contact mechanics⁷⁷ and provide a framework by which the effects of non-rigid indenters can be included in the analysis. Another major contribution was made by Sneddon, who

derived general relationships between the load, displacement and contact area for any punch that can be described as a solid of revolution of a smooth function⁸⁶⁻⁸⁷. His results, which are used extensively in analysing nanoindentation data, show that the load-displacement relationships for many simple punch geometries can conveniently be written as

$$P = \alpha h^m \quad (1)$$

where P is the indenter load, h is the elastic displacement of the indenter, and α and m are constants. Values of the exponent m for some common punch geometries are $m = 1$ for flat cylinders, $m = 2$ for cones, $m = 1.5$ for spheres in the limit of small displacements, and $m = 1.5$ for paraboloids of revolution.

Modelling indentation contact in a way that includes plasticity is a much more complex problem. Since the constitutive equations are nonlinear and a number of material parameters must be included to describe material behaviour (e.g., yield strength and work hardening coefficient), analytical solutions are not easily obtained⁷⁷. As a result, much of our understanding of the importance of plasticity in indenter contact problems has been derived through experimentation and finite element simulation.

The earliest experiments in which load and displacement sensing indentation methods were used to measure mechanical properties were performed by Tabor⁸⁸, who studied the indentation of a number of metals deformed by hardened spherical indenters. A similar study was subsequently undertaken by Stillwell and Tabor to examine the behaviour of conical indenters²⁴. One particularly important observation resulting from these studies concerns the shape of the hardness impression after the indenter is unloaded and the material elastically recovers. The experiments revealed that, at least in metals, the impression formed by a spherical indenter is still spherical with a slightly larger radius than the indenter, and the impression formed by a conical indenter is still conical with a larger included tip angle. The importance of these studies is that since elastic contact solutions exist for each of these geometries (i.e., a spherical indenter in a spherical hole and a conical indenter in a conical hole), the ways in which plasticity affects the interpretation of elastic unloading data can be dealt with by taking into account the shape of the perturbed surface in the elastic analysis. Tabor used these results to show that the shape of the entire unloading

curve and the total amount of recovered displacement can be accurately related to the elastic modulus and the size of the contact impression for both spherical and conical indenters. In addition, these studies showed that :

- (1) The diameter of the contact impression in the surface formed by conical indenters does not recover during unloading – only the depth recovers.
- (2) The indentation must be loaded and unloaded a few times before the load-displacement behaviour becomes perfectly reversible, i.e., a limited amount of plasticity sometimes occurs in each of the first few loadings and unloadings.
- (3) Effects of non-rigid indenters on the load-displacement behaviour can be effectively accounted for by defining a reduced modulus, E_r , through the equation

$$\frac{1}{E_r} = \frac{(1-\nu^2)}{E} + \frac{(1-\nu_i^2)}{E_i} \quad (2)$$

where E and ν are Young's modulus and Poissons ratio for the sample and E_i and ν_i are the same parameters for the indenter.

Interest in load and displacement sensing indentation testing as an experimental tool for measuring elastic modulus began in the early 1970s with the work of Bulychev, Shorshorov and co-workers⁸⁹⁻⁹⁰. These researchers used instrumented microhardness testing machines to obtain indentation load-displacement data similar to that shown schematically in Fig. 19, which was then analysed according to the equation

$$S = \frac{dP}{dh} = \frac{2}{\sqrt{\pi}} E_r \sqrt{A} \quad (3)$$

where $S = dP/dh$ is the experimentally measured stiffness of the upper portion of the unloading curve, E_r is the reduced modulus and A is the projected area of the elastic contact. By measuring the initial unloading stiffness and assuming that the contact area is equal to the optically measured area of the hardness impression, the modulus can thus be derived. Equation (3) has its origins in elastic contact theory and, although derived for a conical indenter, has been shown to apply to *any* indenter that can be described as a body of revolution of a smooth function⁹¹.

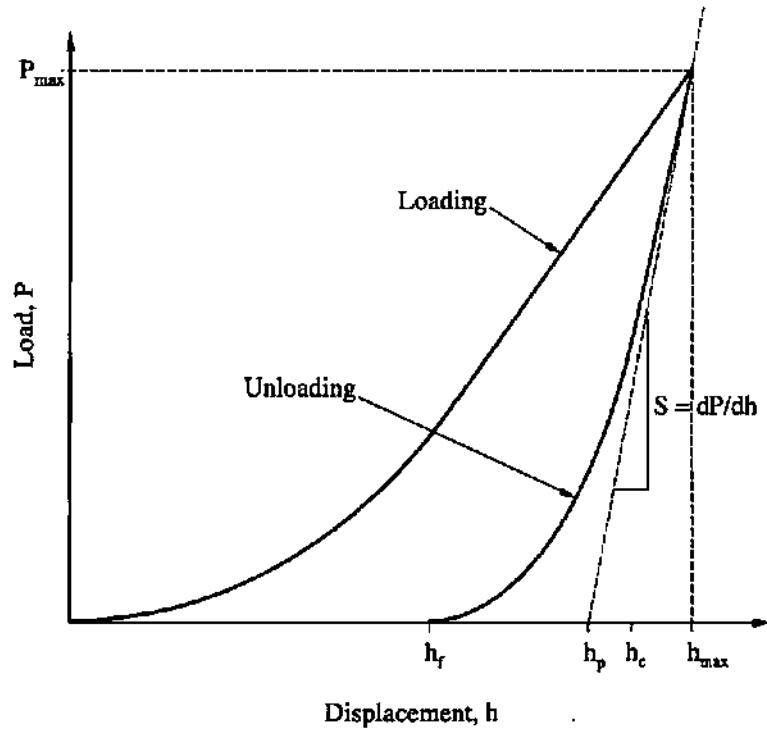


Figure 19: Schematic representation of a typical load-displacement curve, together with the quantities used in the analysis ; peak indentation load, P_{max} ; indenter displacement at peak load, h_{max} ; final depth of the contact impression after unloading, h_f ; plastic indentation depth, h_p ; contact depth, h_c ; and the initial unloading stiffness, S .

Due to the submicron dimensions of impressions produced in nanoindentation, and the obvious difficulties involved in accurately measuring them, other methods are required for determining contact areas. Pethica *et al.* suggested a simple method based on measured indentation load-displacement curves and a knowledge of the indenter area function, that is, the cross-sectional area of the indenter as a function of the distance from its tip¹⁹. Using TEM replication methods to establish the area function, Oliver *et al.* found that the final depth, h_f , gives a better estimate than the depth at peak load²⁵. Doerner and Nix then developed a comprehensive method for determining hardness and modulus from load-displacement data²⁷. Their approach assumed that, during the initial stages of unloading, the area of contact remains constant as the indenter is unloaded. However, for most materials, the initial stages of their unloading curves are very rarely linear. Oliver and Pharr noticed that unloading data are better described by power laws such as that of equation (1), with exponents ranging from about 1.2 to 1.6, and that the indenter contact

area changes continually as it is withdrawn³². Their method, having been generally accepted with slight modification, merits some explanation, especially since it is used for analysing the indentation data presented later in this thesis.

Fig. 20 shows a cross-section through a typical indentation and identifies the parameters used in the analysis. At any time during loading, the total displacement, h , is written as

$$h = h_c + h_s \tag{4}$$

where h_c is the vertical distance along which contact is made (the contact depth) and h_s is the displacement of the surface at the perimeter of the contact. At maximum load, the load and displacement are P_{max} and h_{max} , respectively, and the radius of the contact circle is a . Upon unloading, the elastic displacements are recovered, and when the indenter is fully withdrawn, the final depth of the residual impression is h_f .

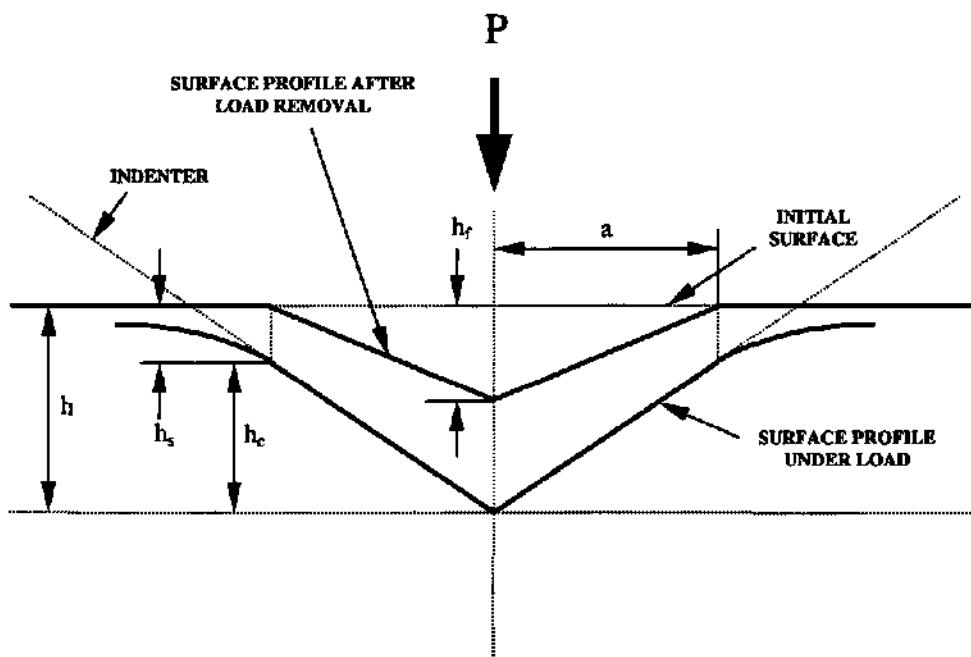


Figure 20 : Schematic representation of the indenting process illustrating the depression of the sample around the indentation and the decrease in indentation depth upon unloading (from Oliver & Pharr³²).

Equation (3) can be rewritten to give an expression which relates the reduced modulus, E_r , to the contact area, A , and the measured stiffness, S :

$$E_r = \frac{\sqrt{\pi}}{2} \frac{S}{\sqrt{A}} \quad (5)$$

Measurement of the initial unloading slope can thus be used to determine the reduced modulus if the contact area at peak load can be measured independently. The area of contact at peak load is determined by the geometry of the indenter and the depth of contact, h_c . The projected contact area at peak load, assuming that the indenter geometry can be described by an area function $F(h)$, can be computed from the relation

$$A = F(h_c) \quad (6)$$

The functional form of F must be established experimentally prior to analysis. To determine the contact depth from the experimental data, equation (4) can be rewritten as

$$h_c = h_{max} - h_s \quad (7)$$

Since h_{max} can be experimentally measured, the key to the analysis then becomes how the displacement of the surface at the contact perimeter, h_s , can be ascertained from the load-displacement data. The deflection of the surface at the contact perimeter depends on the indenter geometry. For a conical indenter, Sneddon's expression for the shape of the surface outside the area of contact⁸⁶ can be used to give

$$h_s = \frac{(\pi - 2)}{\pi} (h - h_f) \quad (8)$$

The quantity $(h - h_f)$ appears in this expression rather than h by itself since Sneddon's solution applies only to the elastic component of the displacement. In addition, Sneddon's force-displacement relationship for the conical indenter yields

$$(h - h_f) = 2 \frac{P}{S} \quad (9)$$

where S is the stiffness. Substituting equation (9) into (8) and noting that the contact area of interest is that at peak load, one obtains

$$h_s = \varepsilon \frac{P_{\max}}{S} \quad (10)$$

where the geometric constant ε for the conical indenter is given by

$$\varepsilon = \frac{2}{\pi}(\pi - 2) \quad (11)$$

or $\varepsilon = 0.72$. By performing the same procedure we can obtain this equation with different geometric constants ; for the flat punch, $\varepsilon = 1$, and for the paraboloid of revolution, $\varepsilon = 0.75$.

In addition to the modulus, the data obtained using this method can be used to determine the hardness, H , defined as the mean pressure the material will support under load :

$$H = \frac{P_{\max}}{A} \quad (12)$$

where A is the projected contact area at peak load evaluated from equation (6). Because unloading data is inherently nonlinear, the stiffness must be assessed from a simple power law relation of the form

$$P = A(h - h_f)^m \quad (13)$$

where the constants A , m and h_f are all determined by a least squares fitting procedure. The initial unloading slope is then found by analytically differentiating this expression and evaluating the derivative at the peak load and displacement.

3.3.2 The loading curve

For most bulk solids, the hardness and modulus are calculated from the unloading portion of the load-displacement curve, as explained in the previous section. However, in some cases, this method is not suitable for estimating the real contact area and thus the mechanical properties of the material. This is particularly the case for highly elastic materials such as many of today's tribological coatings, e.g., carbon nitride, some forms of DLC, silicon nitride, etc. In such materials the loading curve can be analysed; the overall response of the material to the applied load is modelled as the sum of its elastic and plastic components.

Sneddon⁸⁶ gives the relationship between the load, P , and the penetration depth, h , in the case of a rigid conical indenter loaded onto an elastic material, as

$$P = \frac{2Eh^2}{(1-\nu^2)\pi} \tan\theta \quad (14)$$

where E is the modulus, ν is the Poisson ratio and θ is the half-angle of the conical indenter. It is noticed that the normal load is proportional to the square of the penetration depth, the proportionality factor being dependent on both the elastic parameters (E and ν) and the geometrical properties of the contact, θ . In this case, the mean contact pressure, or hardness, H , is independent of the load, the penetration depth and the contact radius, a :

$$H = \frac{P}{\pi a^2} = \frac{E}{2(1-\nu^2)} \cot\theta \quad (15)$$

Loubet *et al.* studied the case of Vickers indentation on elastoplastic materials²⁵ and confirmed the relationship

$$P = K_{exp} h^2 \quad (16)$$

where K_{exp} is the experimentally measured gradient of the resultant straight line plot. Hainsworth and Page⁴², using a Berkovich indenter geometry, furthered the analysis by forming an expression

which accounts for the instantaneous elastic contribution of real materials and the dimensions of practical indenters :

$$P = E \left(\psi \sqrt{\frac{H}{E}} + \phi \sqrt{\frac{E}{H}} \right)^{-2} h^2 = K_m h^2 \quad (17)$$

The constants ψ and ϕ , and thus K_m , can be evaluated from experimental values of K_{exp} observed for a range of samples of well known E and H values. In addition, Hainsworth and Page have applied the model to coated systems (Fig. 21) ; the coating deforms elastically and plastically (I) after which a transition region can be observed where the gradient of the P vs h^2 relationship is more complex as the coating, the interfacial region and the substrate all deform together. In this region (II), the P vs h^2 relationship will not necessarily display either the same slope or even be a straight line. Finally, at large displacements, the highly fractured coating will no longer play any significant role in supporting the applied load and the predicted curve should again be a straight line with a gradient that can be predicted from the modulus and hardness of the substrate alone (III). The extent of each of the three distinct regions will depend on the mechanical properties of the system's components and the thickness of the coating being tested.

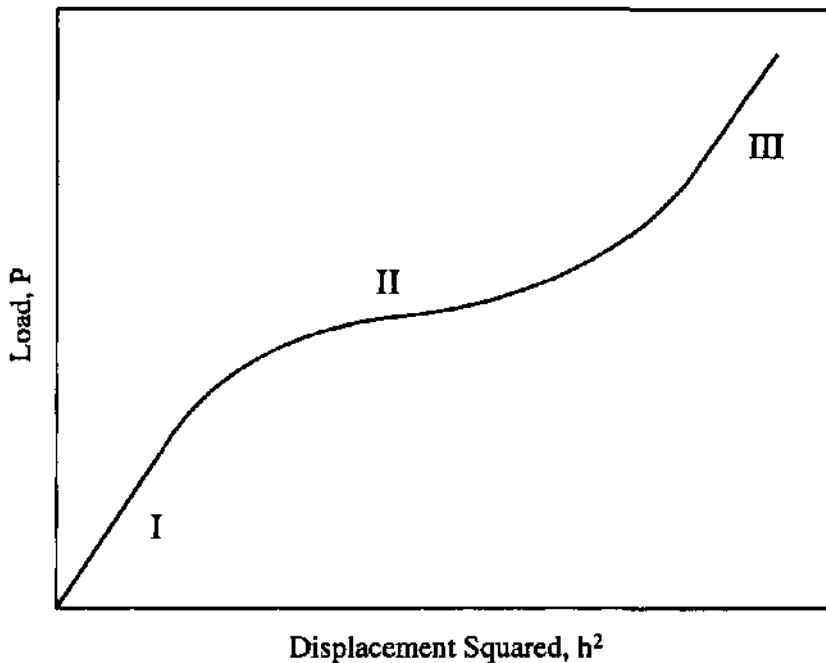


Figure 21 : Predicted P vs h^2 relationship for coated materials (from Hainsworth *et al.*⁴²).

This model not only allows the differing regimes of behaviour of coated systems to be identified, but also allows experimental verification of the load-displacement range over which *coating only* behaviour is being assessed. For many systems this depth is approximately one tenth of the coating thickness. However, a necessary criterion for measuring the plastic properties of a coating is that it yields before the substrate ; the use of soft substrates will always create the situation where the substrate yields before the coating and in this case the hardness of the coating alone cannot be assessed.

3.3.3 The work of indentation

When measuring the hardness of a material, it can be shown that the material offers an average pressure of resistance²⁰ to the indenter which is known as the *dynamic hardness*, and which is numerically equal to the ratio

$$\frac{\text{energy of indenter}}{\text{volume of indentation}} \quad (18)$$

With nanoindentation techniques, the dynamic hardness can be calculated using a *work of indentation* approach^{24, 42} in which the area enclosed by the loading-unloading curve (the plastic work of indentation) is divided by the residual volume of the indentation impression. This residual volume, V , can either be measured directly using a three-dimensional mapping technique such as scanning force microscopy (SFM) or calculated from the load-displacement curve and the indenter geometry using

$$V = \frac{1}{3}(A_p \times h_f) \quad (19)$$

where A_p is the plastic contact area and h_f is the final depth of the residual impression after unloading. However, estimating A_p from the load-displacement curve is subject to the same reservations concerning analysis of the unloading curve as have been explained in previous sections, namely the assumption that the unloading data follows a power-law fit which may not be the case for all materials.

3.3.4 Cyclic indentation

The load-displacement curve, under different loading conditions, can be used to investigate a variety of mechanical phenomena such as transition from elastic to plastic deformation, creep deformation, formation of sub-surface cracks and crystallographic phase transitions. Cyclic (or *multicycle*) indentation can be utilised to investigate the unloading/reloading behaviour of different materials and can highlight the effects of mechanical hysteresis, i.e., energy absorption on each cycle. A typical load-time sequence is shown in Fig. 22 which includes three loading-unloading cycles, hold for 100 seconds at 10% of the peak load, reload, hold for 100 seconds, and unload completely.

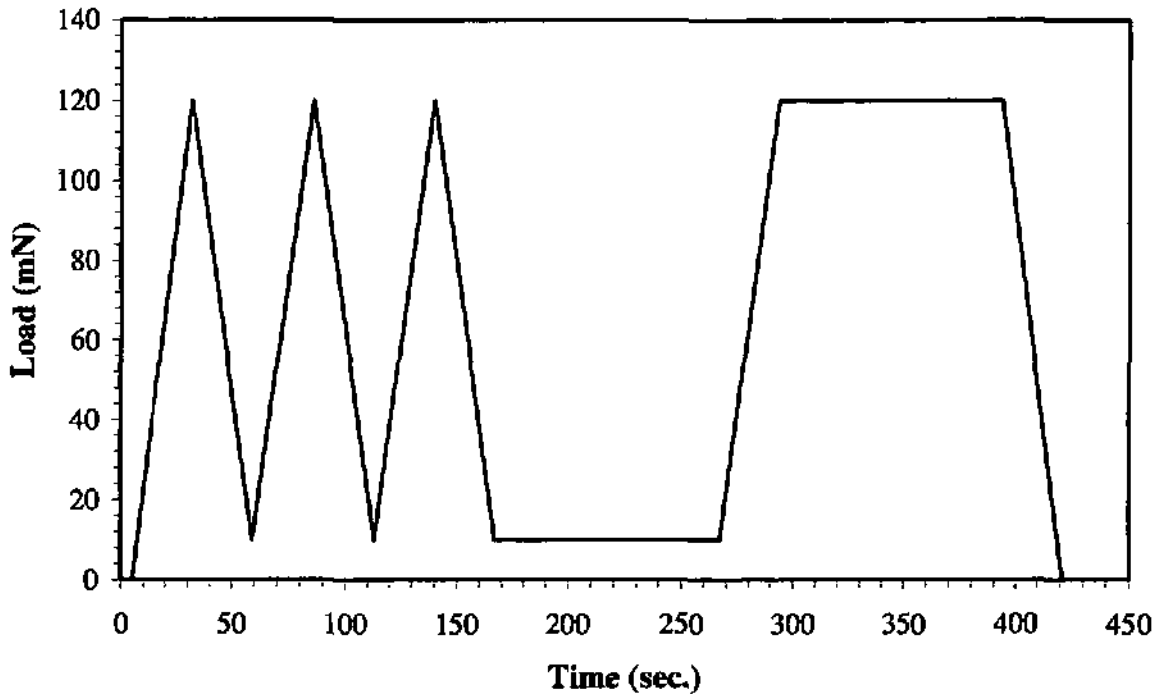


Figure 22 : A typical load-time sequence ; peak load = 120 mN (from Oliver *et al.*³²).

Cyclic indentation can be particularly useful for examining the elastic-plastic response of materials ; for example, if the distance between h_{max} and h_f (see Fig. 19) remains constant after cycling then the elastic-plastic response is very stable and therefore the plastic zone under the indentation, once formed, is able to support the load on each cycle without growing significantly larger.

3.4 The importance of pile-up

In the previous sections explaining the analysis of indentation data from the load-displacement curve, one assumption is always made ; that the maximum penetration depth of the indenter, h_{max} , is correct and can be accurately used to predict the indenter contact area. This assumption holds quite well for hard materials which work harden, but in the case of soft materials, the contact area may be underestimated by as much as 40% due to effects of material pile-up around the indentation imprint. For coated systems, particularly soft films on hard substrates, pile-up is significant because of the constraint the substrate exerts on plastic deformation of the film.

3.4.1 Bulk materials

The schematic profiles in Fig. 23 highlight the two types of material response encountered in nanoindentation tests on bulk materials, commonly termed *pile-up* and *sink-in*, depending on whether the material displaced by the indenter during the test is pushed to the sides of the imprint or is compressed into the bulk, respectively. Although both phenomena are commonly encountered in practice, little research has been done to date to investigate the exact mechanisms responsible for such material flow. However, several hypotheses have been put forward, including dislocation movement⁴³, elastic recovery²⁵, phase transformation⁹², residual stress relaxation⁴³, release of stored strain energy⁹³, etc. Quantitatively measuring the very small material volumes that pile-up around indents is very difficult, the only really effective means being SFM.

An idea of material response can be obtained using the ratio of final depth, h_f , to the depth of the indentation at peak load, h_{max} . This parameter, h_f/h_{max} , can be easily extracted from the unloading curve and has the limits $0 \leq h_f/h_{max} \leq 1$. The lower limit corresponds to the fully elastic case, whereas $h_f/h_{max} = 1$ corresponds to the case of no elastic recovery after unloading. Finite element analysis⁹⁴ has confirmed that pile-up is significant when $h_f/h_{max} > 0.7$ and the material does not appreciably work harden. For such materials, failure to account for the pile-up can lead to an underestimation of the contact area, which in turn results in an overestimation of the hardness and elastic modulus.

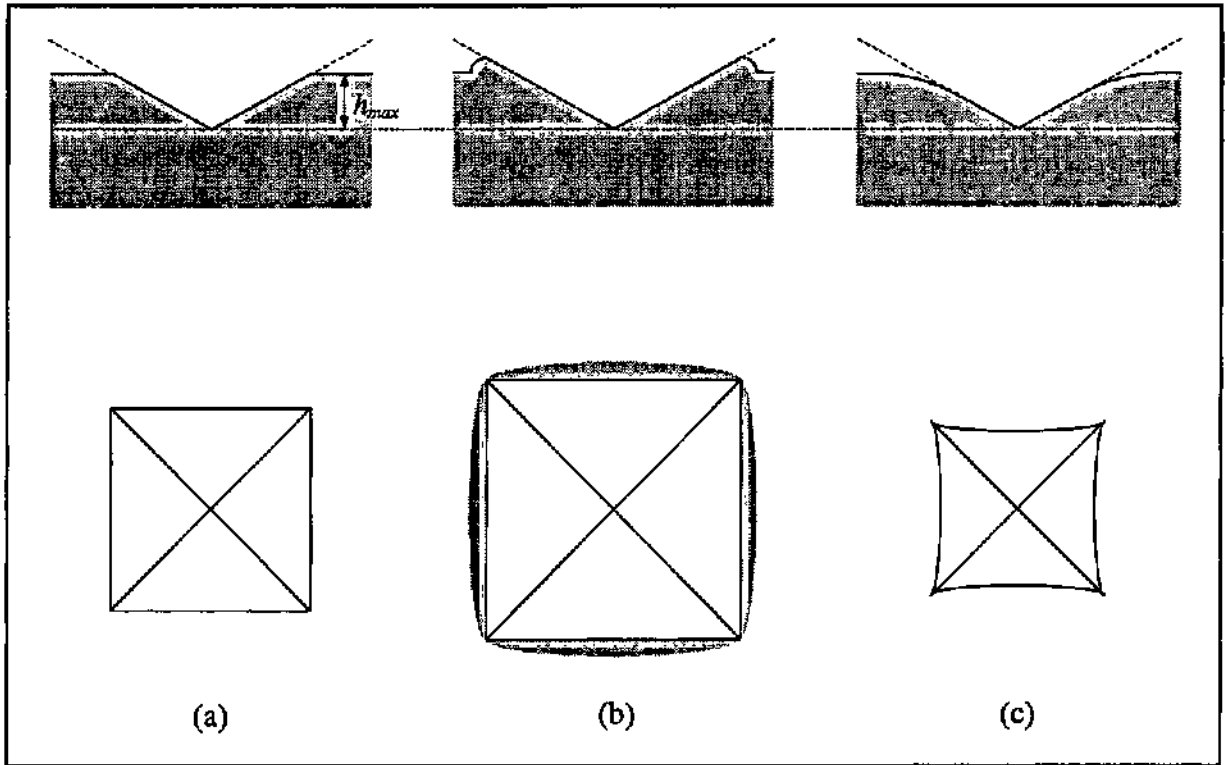


Figure 23 : Schematic profiles through Vickers indentations with different material response (top) and corresponding residual imprints (bottom) for the case of (a) perfectly plastic material, (b) material exhibiting 'pile-up', and (c) material exhibiting 'sink-in'. Note that the maximum penetration depth, h_{max} , is the same for the three cases but that the residual contact area is different.

Patterns of plastic flow caused by indentation can be classified into two categories : those which emphasise flow from under the indenter into the bulk (1), and those which emphasise flow outwards into pile-ups (2). The former category visualises the displacement of matter along lines approximately radially directed from the indentation, the plastic displacement field having a divergence which leads to the local storage of matter in the bulk, causing elastic compressive stress there, and of course compensating tension outside the plastic field. The latter category includes the models based on simple approximation to slip line fields, the plastic displacement field is rotational and divergence free. All the volume under the indenter is transferred to the pile-ups and there is no accompanying elastic dilatation. Both categories can be thought of as alternative patterns available to the material in response to indentation. Because type (1) is accompanied by a build-up of elastic stress, it is the pattern which will be initially dominant in

most materials, although the less hard the material the sooner the pattern will subsequently change to type (2) as plastic deformation favours the outward flow of matter into pile-ups. The elastic energy density will be proportional to the square of the local flow stress, which is in turn proportional to the hardness.

This can be experimentally verified by measuring the ratio of the volume of material above the original surface level, V_a , to that below it, V_b . It can be noted that for pure type (2) flow, the ratio $V_a/V_b = 1$, and the recovery $(h_{max} - h_f)/h_{max} = 0$; whereas for pure type (1) flow, the ratio $V_a/V_b = 0$, and the recovery equals some finite value depending on the elasticity of the material.

3.4.2 Coated systems

Many thin film systems consist of very soft films on very hard substrates. This is particularly common, for instance, in the semiconductor industry where films of aluminium, gold and copper are often deposited on silicon ($H = 12$ GPa), germanium ($H = 10$ GPa) and ceramic ($H = 10 - 40$ GPa) substrates. The film hardness is usually in the range $0.1 - 1$ GPa, making it at least one order of magnitude softer than the material on which it is deposited. One important consequence is that when a hardness impression is made, there is a tendency for material to pile-up around the imprint to a much greater degree than it would in a bulk material⁸². This is due to the severe constraint imposed on plastic deformation in the film by the relatively undeformable substrate. Since current techniques for analysing nanoindentation data do not make provisions for the extra contact area produced by the pile-up, the enhancement of pile-up in soft films on hard substrates has important consequences for the measurement of mechanical properties by such methods. In addition, pile-up effects must be taken into account because it is not always possible to make indentations on thin film systems which are shallow enough to avoid influences from the substrate.

Pile-up behaviour for coated systems can be investigated as a function of the maximum penetration depth, h_{max} , normalised with respect to the film thickness, t_f (see Fig. 24). This ratio, h_{max}/t_f can be plotted against hardness and modulus for normalised depths ranging from well below the film thickness to well above it. In this way, the influence of the substrate can be

directly correlated to any variations in H and E and, with a knowledge of the imprint surface topography at each depth, can be better explained in terms of pile-up effects.

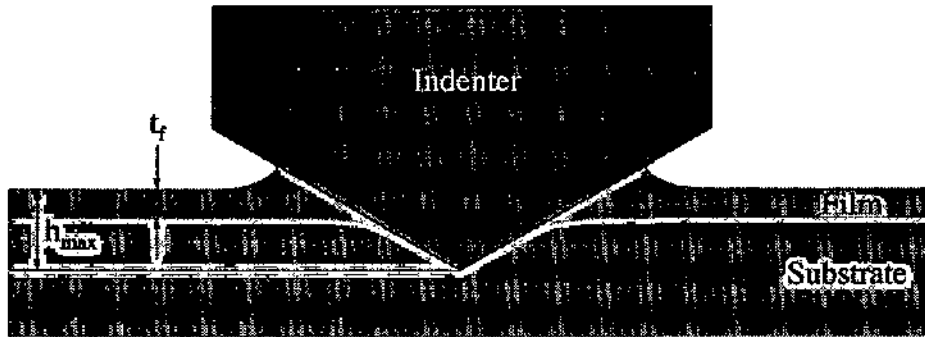


Figure 24 : Schematic illustration of the indentation of a soft film on a hard substrate and definition of the quantities of the ratio h_{max}/t_f .

An example is shown in Fig. 25 for indentations made into a sputtered gold film ($t_f = 200$ nm) on a silicon substrate. At small depths well below the film thickness (Fig. 25 (a)), there is very little pile-up, consistent with the behaviour of sputtered gold. However, at depths close to and greater than the film thickness (Fig. 25 (b)), the amount of pile-up is substantial giving the indentation an almost circular appearance even though it was made with a square (Vickers) pyramid. For depths much greater than the film thickness (not shown), the amount of pile-up is not as large because a greater portion of the deformed volume is in the hard silicon substrate. Thus, it is apparent that the constraint that the hard substrate imposes on the plastic deformation in the film enhances pile-up by an amount which is greatest at indentation depths around the film thickness. The cross-sectional profiles through the indentations are a good way of comparing the material response at different depths and investigating any residual indenter effects at the film-substrate interface. The SFM is again shown to be one of the only methods available for accurately quantifying such phenomena.

For the case of hard coatings, which tend to exhibit much less pile-up effects, the surface usually supports the indenter elastically up to a critical load at which plastic response begins, either in the form of cracking or yielding of the substrate.

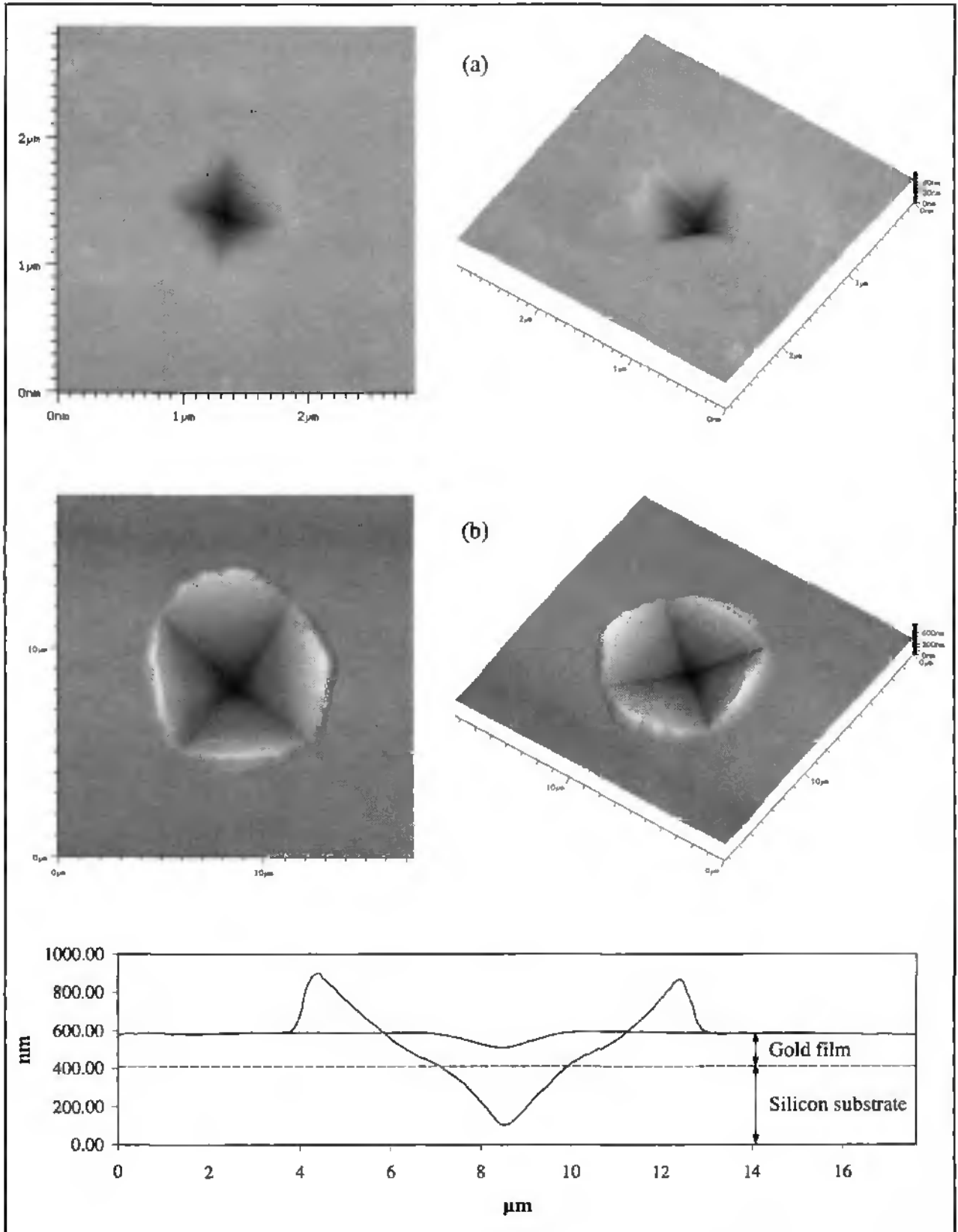


Figure 25 : SFM images of two indentations into a sputtered gold film on a silicon substrate, together with surface profiles showing the effect of pile-up for penetration depths greater than t_f . The ratio h_{max}/t_f is 0.39 for (a) and 2.35 for (b) ($t_f = 200$ nm).

The SFM approach to nanoindentation

Although the scanning force microscope was initially developed primarily as a surface imaging tool, its capability has also been extended to nanoscale scratching (Chapter 2) and indentation studies. The major advantage of a SFM system over conventional depth-sensing indentation techniques is the combination of imaging and indentation capabilities, together with the higher resolution force detection. The main drawback is the asymmetry of the created indentation owing to the cantilever bending under load and non-linearity in the piezo movement.

4.1 Nanoscale mechanics

Before being able to accurately measure surface mechanical properties with the SFM, it is important to understand the force interaction between the tip mounted on a cantilever beam and the sample surface as a function of relative tip-sample separation. The resulting plot, referred to as a *force curve*, contains information about (i) the magnitude and functional dependence of long range attractive and adhesive forces, (ii) the point of tip-sample contact, (iii) the tip-sample contact area, and (iv) the elastic modulus of the sample material⁹⁵. A typical force curve is shown in Fig. 26 and its measurement starts with the sample far away from the tip and the cantilever in its rest position. As the cantilever tip is moved in the direction of the sample, the cantilever bends towards the sample due to attractive surface forces. The maximum forward deflection of the cantilever multiplied by the effective spring constant, k_c , of the cantilever is the pull-on force (point A). As the tip is moved closer to the sample, it is pushed back through its original rest position (point B, i.e., zero applied load) until a predetermined tip position is achieved which corresponds to the maximum applied load (point C). On unloading, the cantilever movement changes direction and passes through the position corresponding to the pull-off force (point D), until the cantilever separates (point E) and returns to its rest position when the sample is once again far away from the tip. In general, the pull-off force (or *adhesion*) is greater than the pull-on

force. Note that the top right hand quadrant of the force curve in Fig. 26 corresponds to a conventional load-displacement curve as described in Chapter 3 for depth-sensing nanoindentation.

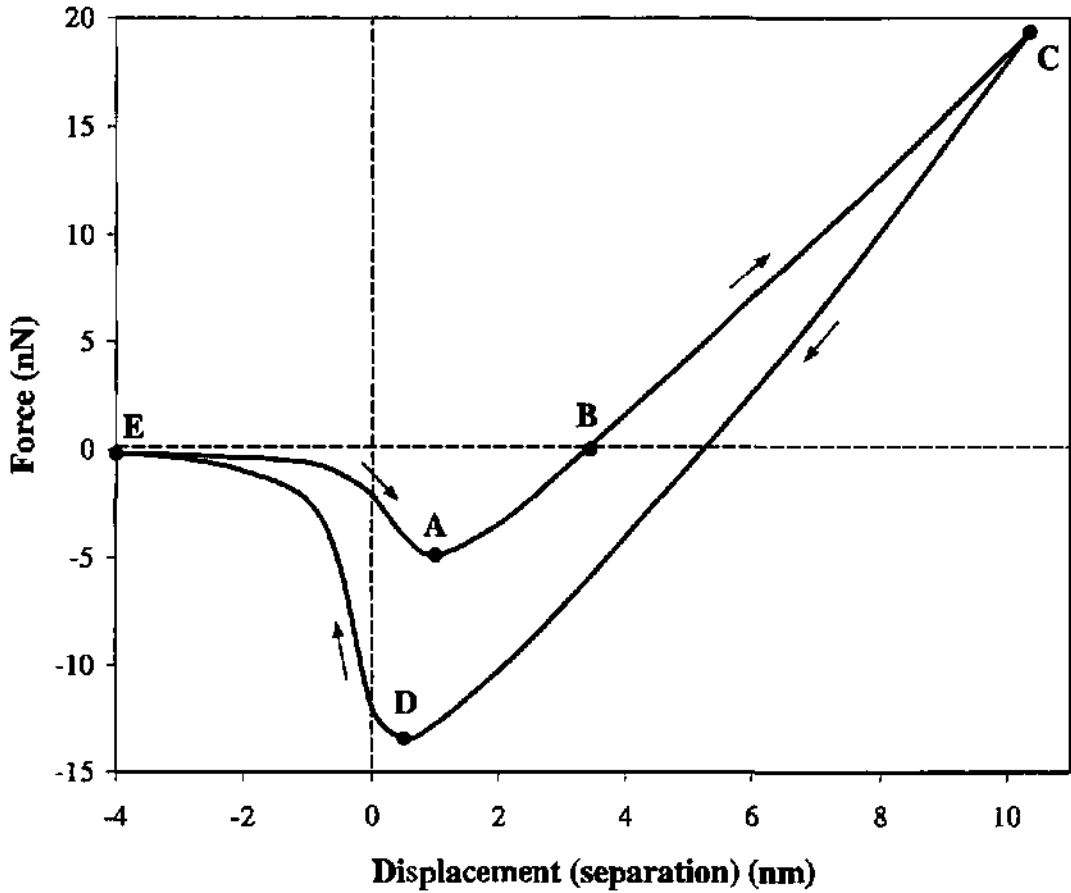


Figure 26 : Typical force-displacement curve for a cantilever tip approaching and contacting a sample surface; (A) maximum pull-on force, (B) zero applied load, (C) largest applied load, (D) maximum pull-off force, and (E) separation. Note the presence of long-range attractive forces.

To extract the nanoscale mechanical response of the material from the contact portion of the force curve, the tip-sample interaction is modelled as two springs in series, as shown in Fig. 27. After contact is made between the tip and the sample surface, piezo displacement results in both tip deflection and sample indentation, the amounts of which depend on the relative stiffnesses of the sample and the cantilever⁹⁶. The relationship between the displacement of the piezoelectric

actuator (Δh_p), the displacement due to tip deflection (Δh_t), and the indentation displacement (Δh_i) is simply

$$\Delta h_i = \Delta h_p - \Delta h_t \cos\theta \quad (20)$$

where the $\cos\theta$ term corrects for the angle of the cantilever to the horizontal. The applied force, P , can be calculated directly from the tip displacement by

$$P = k_c \Delta h_t \quad (21)$$

where k_c is the spring constant of the cantilever. The resolution of the calculated forces is generally of the order 1 to 50 nN, depending on cantilever stiffness, because noise in the tip displacement detector limits depth resolution to 0.1 nm.

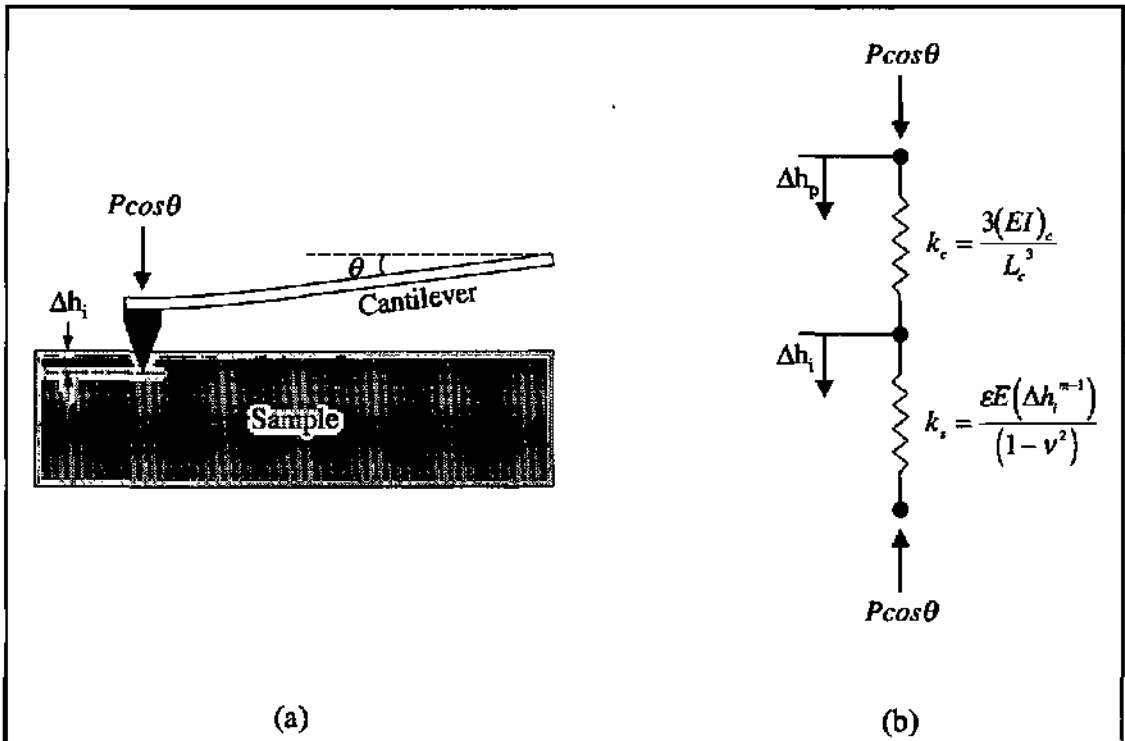


Figure 27 : Schematic (a) and spring model (b) for tip-sample contact during nanoindentation. The term I in the equation defining the spring constant of the cantilever, k_c , denotes the cross-sectional moment of inertia. This equation is only valid for a cantilever with constant cross-section.

To calculate the load applied to the sample, P is multiplied by $\cos\theta$ to again account for the angle of the cantilever. For a sample which is infinitely stiff with respect to the tip, no indentation will occur and $\Delta h_p = \Delta h_t$. From simple beam theory and considering the angle, θ , of the cantilever, the angle change of the cantilever at the tip ($\Delta\theta_t$) and the tip displacement (Δh_t) are related by

$$\Delta\theta_t = \frac{3\Delta h_t}{2L_c \cos\theta} \quad (22)$$

where L_c is the length of the cantilever. This angle change is directly related to the change in photodiode voltage, V_t , by system conversion and calibration factors⁹⁶ which can be summarised by a constant, C_θ , such that

$$\Delta\theta_t = \frac{\Delta V_t}{C_\theta} \quad (23)$$

By combining equations 22 and 23, the slope of the force curve, Σ , is shown to have an upper limit, Σ^* , given by

$$\Sigma^* = \frac{\Delta V_t}{\Delta h_p} = \frac{3C_\theta}{2L_c \cos\theta} \quad (24)$$

For a sample that deforms due to the force applied by the cantilever, Σ will be reduced from Σ^* by a reduction factor, $f = \Sigma/\Sigma^*$, such that larger values of f correspond to stiffer samples. The amount of indentation, Δh_t , at different points along the force curve can be calculated using equation 20. The applied load, P , can also be calculated using equation 21 if k_c is known. The indentation displacement, Δh_t , is then related to the applied load, P , through the relation by Sneddon

$$P = \frac{\varepsilon E h^m}{(1-\nu^2)} \quad (25)$$

where ε is a constant which depends on the geometry of contact, E and ν are the sample elastic modulus and Poisson ratio respectively, and m is a power law exponent determined from a curve

fit of P as a function of h as described in Chapter 3.3.1 for analysis of the unloading curve via the Oliver and Pharr method³². Thus the hardness and modulus of the sample material can be calculated as explained previously.

4.2 Instrumental set-up

The apparatus used for nanoindentation is based on the Atomic Scale Tribometer (AST) (see Chapter 1.3) but with various modifications. The standard piezo tube of the AST head is replaced with a feedback controlled piezo actuator which only allows vertical movement (i.e., z-direction) but has a displacement resolution of 0.25 nm over a 16 μm full range. Owing to the internal feedback system, the laser beam can no longer pass through the centre of the cylindrical piezo tube and so the cantilever is side-mounted and the tube offset such that the laser can focus unimpeded on the cantilever. The approach mechanism consists of a stepper motor controlling the rear leg of the head, giving a step resolution of 20 nm.

Because of the restriction of the piezo to solely vertical displacements, imaging as with conventional SFM operation is not possible. This problem has been solved by building a scanner table on which the head can be placed. The table consists of a standard piezo tube on which the sample is mounted allowing vertical and lateral displacements with range 6 μm and 120 μm respectively. This lower piezo is connected so that it is powered by the same high voltage amplifiers as the upper piezo of the head. Both 5-pole and 9-pole operation is possible with the lower piezo. This means that either piezo can be used independently but not both at the same time. The usual configuration for imaging is to use the lower piezo for scanning the sample, the cantilever being kept stationary by the upper piezo and its displacement being measured by the optical beam deflection system incorporated in the head. This has the advantage of reducing imaging artefacts due to non-linear lateral motion of the cantilever whilst scanning. The upper piezo is kept stationary by holding it at fixed potential in order to reduce errors due to compliance of the lead zirconate titanate (PZT) material. However, other configurations can be used, such as the lower piezo for lateral scanning and the upper piezo for vertical displacement control. The complete set-up is shown in Fig. 30. Coarse lateral positioning is achieved via the micrometer displacement stage on which rests the modified AST head.

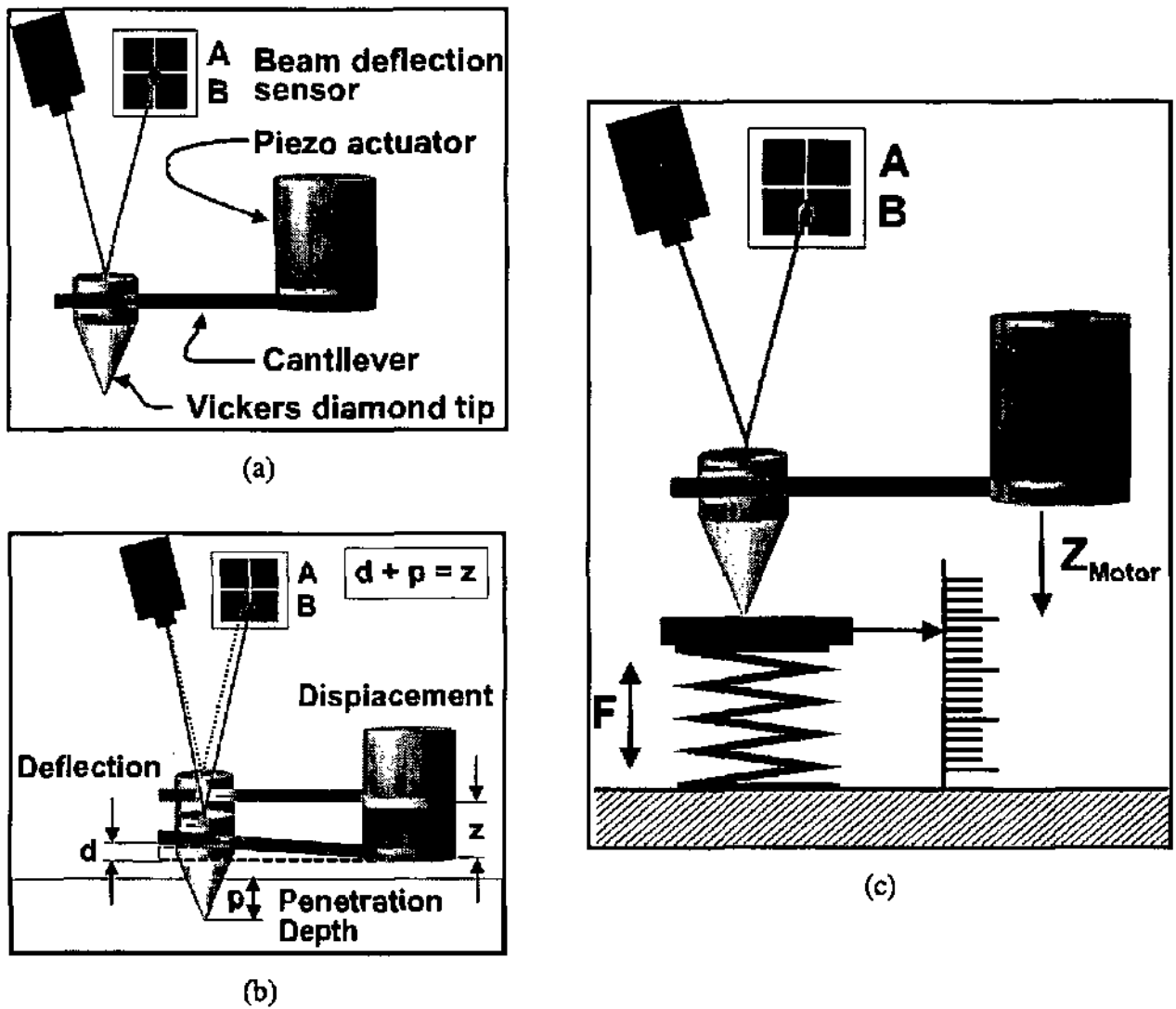


Figure 28 : Principles of SFM nanoindentation showing (a) basic components of the system, (b) the calculation of the penetration depth, p , as a function of cantilever deflection, d , and piezo displacement, z , and (c) force calibration procedure by placing diamond tip on a high precision weight balance.

The cantilever used for nanoindentation consists of a copper-beryllium beam of force constant $\sim 10^4 \text{ Nm}^{-1}$ on which is braised a polished Vickers diamond. When the tip is driven into the sample surface by a distance z , the cantilever deflects by a distance d , measured by the laser deflection system, and thus the penetration depth, p , can be calculated by the equation $p = z - d$ (Fig. 28 (b)). Determination of the calibration constant, C_θ is performed by indenting onto an 'infinitely stiff' material such as sapphire, enabling the cantilever deflection to be calibrated with

respect to the photodiode voltage, V_t . Force calibration is performed by placing the cantilever tip onto a high precision digital microbalance and measuring applied force versus piezo voltage (Fig. 28 (c)). Typical dimensions of the cantilever beam are given in Fig. 29 and it can be seen that a square mirror is glued on the backside of the cantilever onto which is focussed the laser beam from the optical deflection system. This is because the surface roughness of the Cu-Be material gives insufficient reflection intensity back to the photodiode. It is important to remember that the tip is mounted a finite distance from the end of the cantilever and so the *effective* cantilever length is in fact less than the total length and must be compensated for.

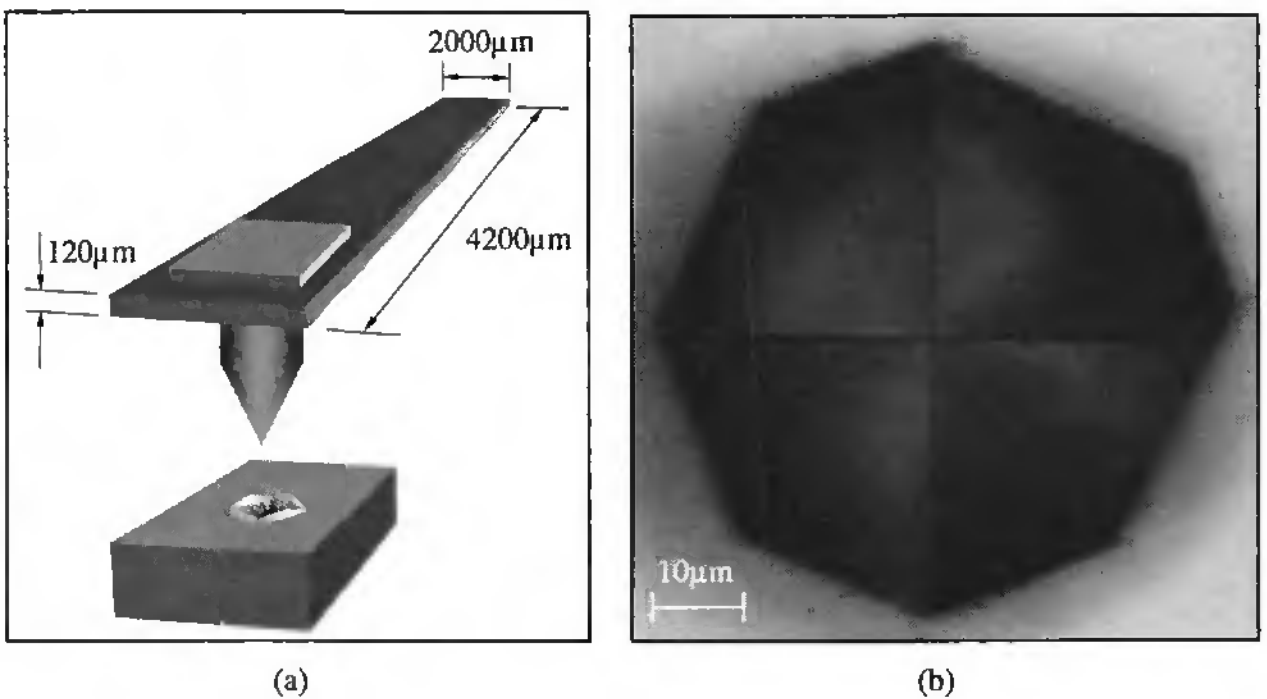


Figure 29 : Schematic illustration (a) of the Cu-Be cantilever beam with its dimensions. The braised Vickers diamond and glued mirror are also shown. The optical micrograph (b) shows the characteristic 4-faced pyramidal geometry of the Vickers indenter.

With the aforementioned set-up the maximum force is 40 mN with a resolution of 10 μ N. Different cantilever dimensions can be used to provide varying stiffnesses for particular applications ; for example, a lower force constant would be required for indentation into soft polymeric materials. However, the deflection of a cantilever with small force constant must not be too large otherwise significant deviation from a vertical indenter position will occur.

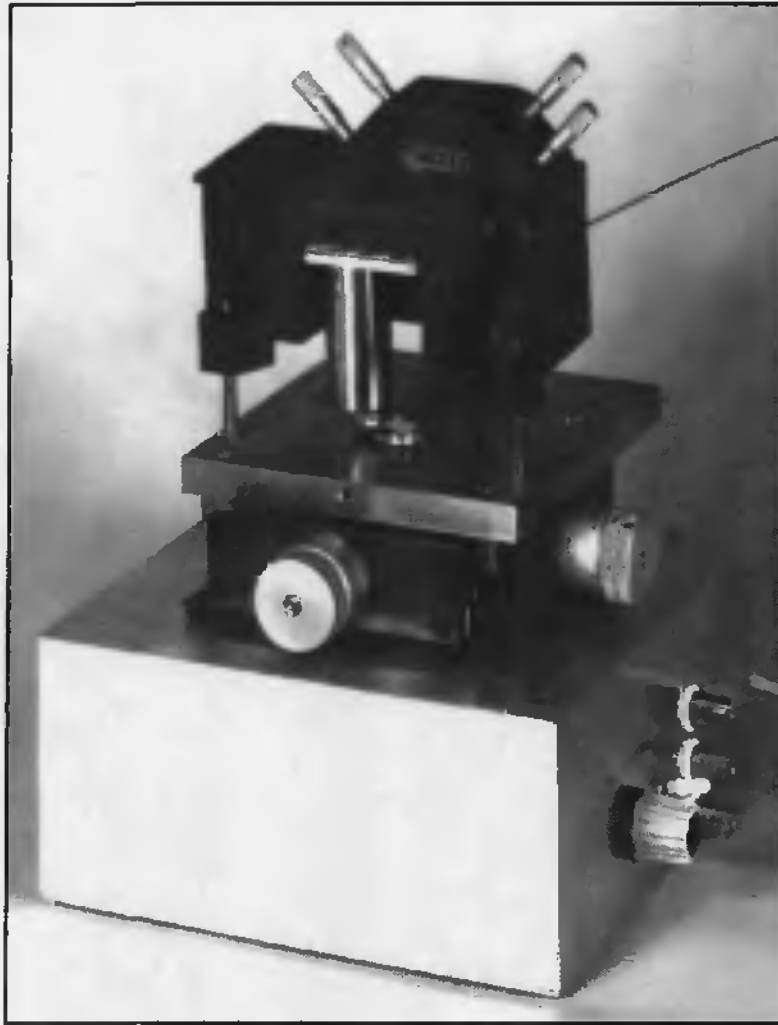


Figure 30 : The AST adapted for nanoindentation and mounted on the scanner table. Note the offset piezo tube of the head, allowing the laser beam to reflect directly off the side-mounted cantilever.

4.3 Modelling of cantilever displacement

The following section describes and models the various types of error which can occur when performing indentation with an indenter mounted on a cantilever beam. Experimental evidence (Fig. 32) suggests that such inaccuracies can be neglected for small penetration depths but that at greater depths ($>2 \mu\text{m}$) the indentation data can be seriously affected. The inherent effects of non-linearity, hysteresis and creep in the piezo also become more significant as the penetration depth is increased, and are explained elsewhere⁹⁷.

4.3.1 Longitudinal displacement of indenter

As the tip comes into contact with the sample surface and begins to penetrate it, the cantilever is deflected from the surface and the tip tends to move away from the cantilever base, as depicted in Fig. 31 (i). This bending produces a force parallel to the cantilever axis, applied at the tip. For every bending angle at the end of the cantilever it is possible to calculate the ratio of tip height, H , to cantilever length, L . Point P , at the centre of the base of the diamond tip undergoes a displacement Δx_1 , defined by

$$\Delta x_1 = -L(1 - \cos \beta) \quad (26)$$

The tip advances by a distance $\Delta x_2 = H \sin \beta$, such that, when both these terms are equal, the tip does not have a horizontal component and thus

$$\frac{H}{L} = \frac{1 - \cos \beta}{\sin \beta} \quad (27)$$

As long as this equation remains unsatisfied, a longitudinal force produces a moment on the cantilever, tending to cause an S configuration as shown in Fig. 31 (ii), or a further deflection in terms of the ratio H/L and angle β . This longitudinal force, N , can be approximated by balancing the sum of the x components and substituting into the corresponding stress equation

$$\Delta x = \Delta x_1 + \Delta x_2 = -L(1 - \cos \beta) + H \sin \beta \approx \frac{\beta L}{2} \left[\frac{2H}{L} - \beta \right] \quad (28)$$

$$\frac{\Delta x}{L} = \frac{\sigma}{E} = \frac{N}{EA}$$

$$N = \frac{EA\beta}{2} \left[\frac{2H}{L} - \beta \right] \quad (29)$$

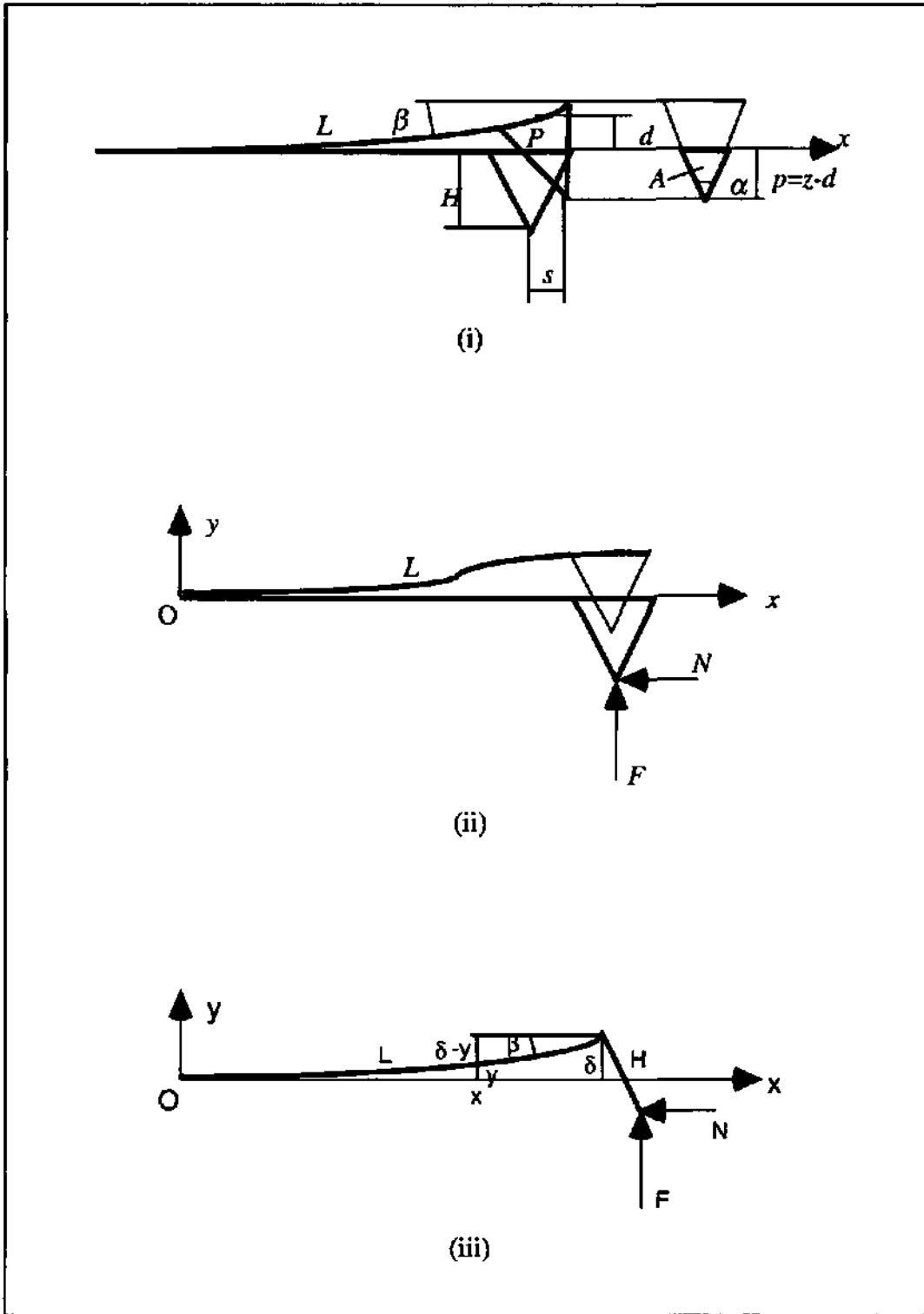


Figure 31 : Cantilever deflection mechanisms for tip/surface contact; (i) bending due to longitudinal force N , (ii) deflection in S configuration, and (iii) model taking into account the cantilever bending in the moment calculation.

The section of the diamond tip over which this force is applied is defined by

$$A = p^2 \tan \frac{\alpha}{2} = (z - d)^2 \tan \frac{\alpha}{2} \approx z^2 \tan \frac{\alpha}{2} \quad (30)$$

Modelisation of the cantilever deflection has been done for three situations, in increasing order of precision, but first the effect of shear must be considered:

4.3.2 Shear force effect

The vertical force, F , produces a shear effect. The angle, β , and the deflection, d , due to this force are given by

$$\beta \approx \tan \beta = \eta \frac{F}{Gbh} \quad \text{and} \quad d = \eta \frac{FL}{Gbh}$$

where G is the shear modulus, this being an order of magnitude smaller than the modulus of elasticity, E . The area section of the tip, $A = bh$ and η is a coefficient smaller than 1. Both β and d are such small components that they can be regarded as being negligible and thus shall be ignored in the following models.

MODEL 1 : Cantilever deflection for constant longitudinal moment of force

This first model assumes that the moment, $M(x)$, due to the longitudinal force on the cantilever is constant and is described by the following equations:

$$M(x) = HN - (L - x)F$$

$$\frac{1}{\rho} \approx y'' = -\frac{M(x)}{EI}$$

$$\beta \approx \tan \beta = y'(L) = \frac{FL^2}{2EI} \left[1 - \frac{2H}{L} \frac{N}{F} \right]$$

$$d = y(L) = \frac{FL^3}{3EI} \left[1 - \frac{3H}{2L} \frac{N}{F} \right]$$

$$I = \frac{bh^3}{12}$$

The angle ρ corresponds to the radius of curvature of the deflected cantilever and I represents its moment of inertia. The sign of the force N depends on the ratio H/L and on the angle. Its magnitude depends on the force F , the material being tested, the angle, the diamond, etc. The influence of the angle should be noted as this is used for determining both the applied force and the penetration depth.

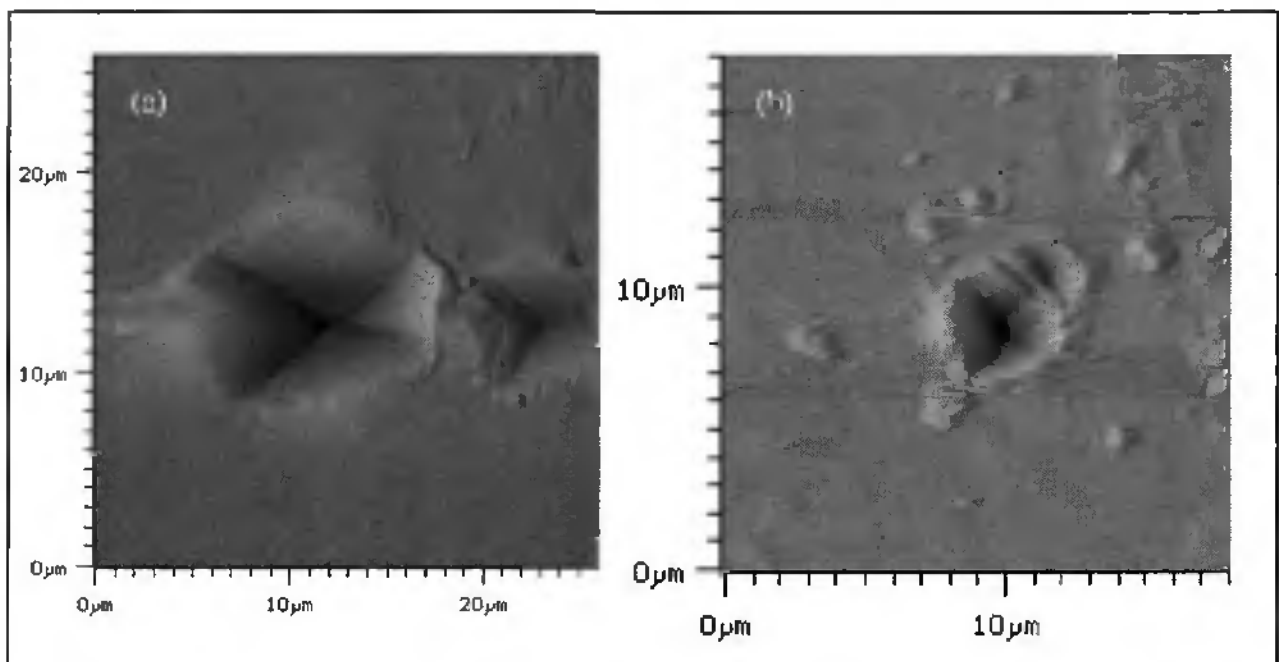


Figure 32 : Indentations on pure aluminium demonstrating errors encountered when using SFM for nanoindentation ; (a) non-symmetrical imprint (due to cantilever bending) and horizontal movement of tip at the base (caused by longitudinal force, N) ; (b) piezo creep causing overlap of two imprints made in the same position.

MODEL 2 : Cantilever deformation taken into account

Contrary to the previous model, this takes into account the deformation of the cantilever in the moment calculation, but it neglects the angle at the cantilever extremity ($\cos\beta = 1$ and $\sin\beta = 0$). The following nomenclature are shown in Fig 31 (iii).

$$M(x) = N(H \cos\beta - \delta + y) - F(L - x + H \sin\beta)$$

$$M(x) \approx N(H - \delta + y) - F(L - x)$$

$$\frac{1}{\rho} \approx y'' = -\frac{M(x)}{EI}$$

$$\beta \approx \tan\beta = y'(L) = \frac{1}{\cos KL} \left[\frac{F}{N} (1 - \cos KL) - KH \sin KL \right]$$

$$d = y(L) = \frac{-H}{\cos KL} (1 - \cos KL) + \frac{1}{K} \frac{F}{N} \tan KL - \frac{F}{N} L$$

$$I = \frac{bh^3}{12} \quad \text{and} \quad K^2 = \frac{N}{EI}$$

If the critical force, $N_c = \frac{\pi^2 EI}{4L^2}$, is exceeded then the cantilever will buckle. Note that this critical value does not depend on the height, H , of the diamond tip.

MODEL 3 : Cantilever deformation taken into account

This model takes into account both the deformation of the cantilever and the angle at the cantilever extremity in the moment calculation. The equations now become:

$$M(x) = N(H \cos \beta - \delta + y) - F(L - x + H \sin \beta)$$

$$\frac{1}{\rho} \approx y'' = -\frac{M(x)}{EI}$$

$$d = y(L) = \frac{1}{K} \frac{F}{N} \tan KL - \frac{H}{\cos KL} (1 - \cos KL) \left(\cos \beta - \frac{F}{N} \sin \beta \right) - \frac{F}{N} L$$

$$\sin \beta = \frac{1}{\cos KL} \frac{1}{1 - HK \frac{F}{N} \tan KL} \left[\frac{F}{N} (1 - \cos KL) - HK \sin KL \cos \beta \right]$$

$$I = \frac{bh^3}{12} \quad \text{and} \quad K^2 = \frac{N}{EI}$$

Contrary to the previous two models, these equations must be solved numerically for the angle and the displacement.

4.4 Results

Although the main results for the SFM-based nanoindentation instrument are presented in section 7.2, certain aspects still need to be shown, such as its ability to image with the same tip as has made the indentation.

Fig. 33 shows a set of results for an indentation made on a bulk aluminium sample. The two images represent the same $4 \times 4 \mu\text{m}$ area of surface before and after indentation with a Vickers indenter to a maximum depth of 257 nm. The surprisingly good resolution obtained with such an indenter allows the effects of pile-up around the imprint to be investigated, as well as the extent to which the surface has been modified as a result of the indentation. However, it should be noted that images smaller than those shown were more affected by the spherical geometry of the indenter at its tip and therefore resolution was reduced. Continued scanning over the same area did show some surface damage due to the high stiffness of the cantilever beam.

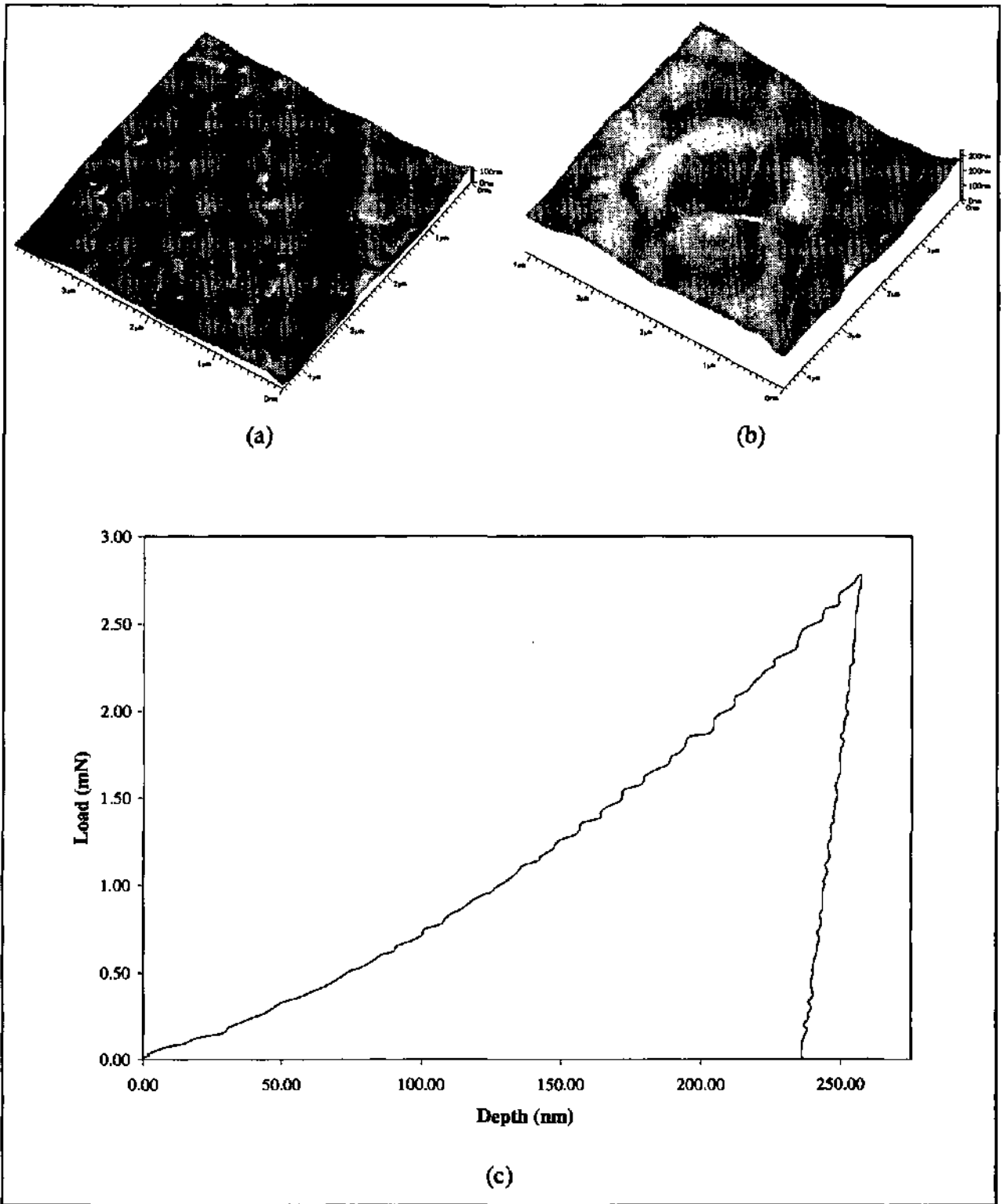


Figure 33 : Typical results from the SFM based nanoindentation instrument on a bulk aluminium sample. Image (a) shows the surface before indentation, image (b) the surface afterwards. Both images were made using the same Vickers indenter which made the imprint. The curve (c) gave values of $H = 850$ MPa and $E = 89.49$ GPa for a loading rate of 6 mN/min.

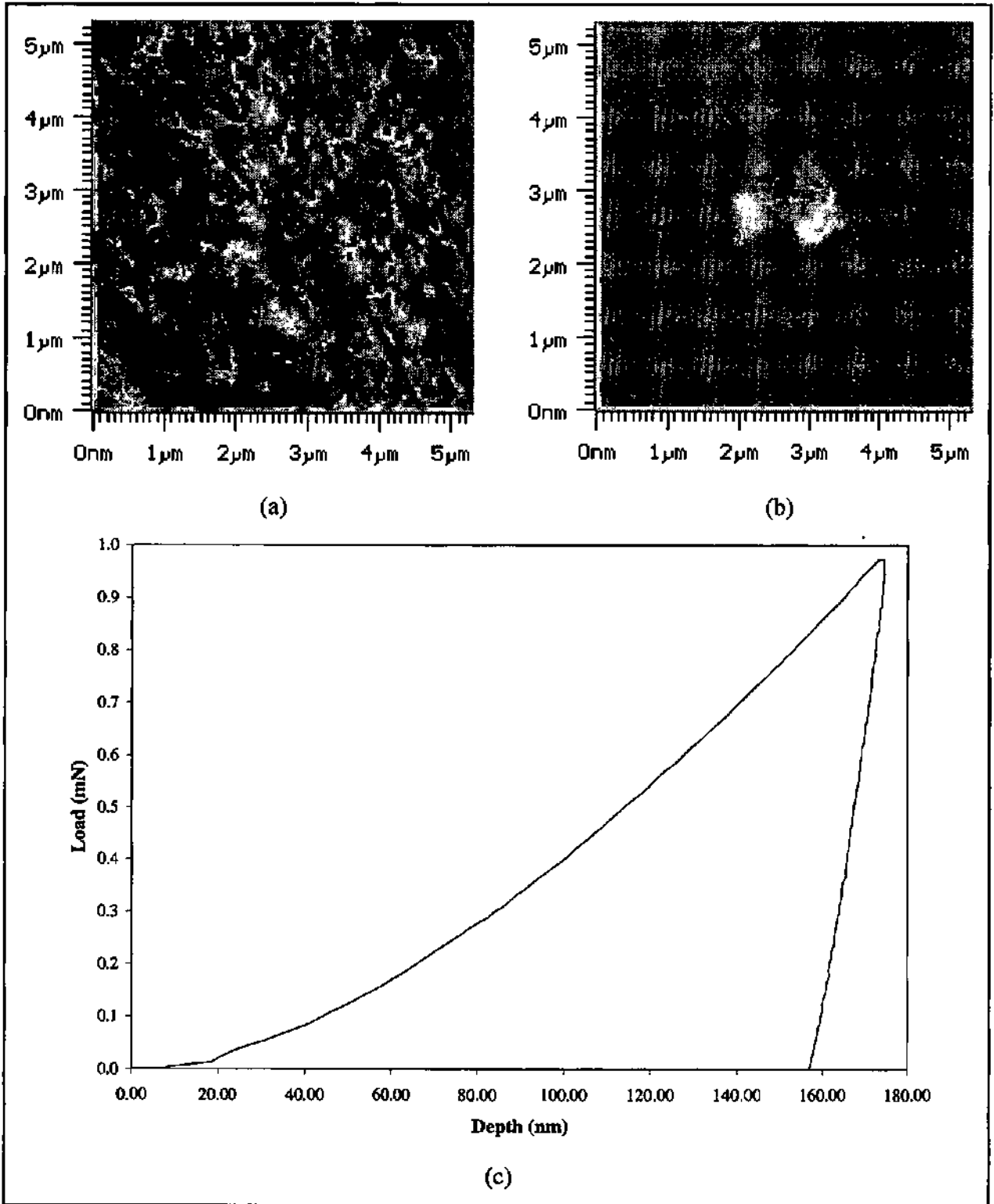


Figure 34 : Typical results from the SFM based nanoindentation instrument on a gold sample. Image (a) shows the surface before indentation, image (b) the surface afterwards. Both images were made using the same Vickers indenter which made the imprint. The curve (c) gave values of $H = 632$ MPa and $E = 40.48$ GPa for a loading rate of 3 mN/min.

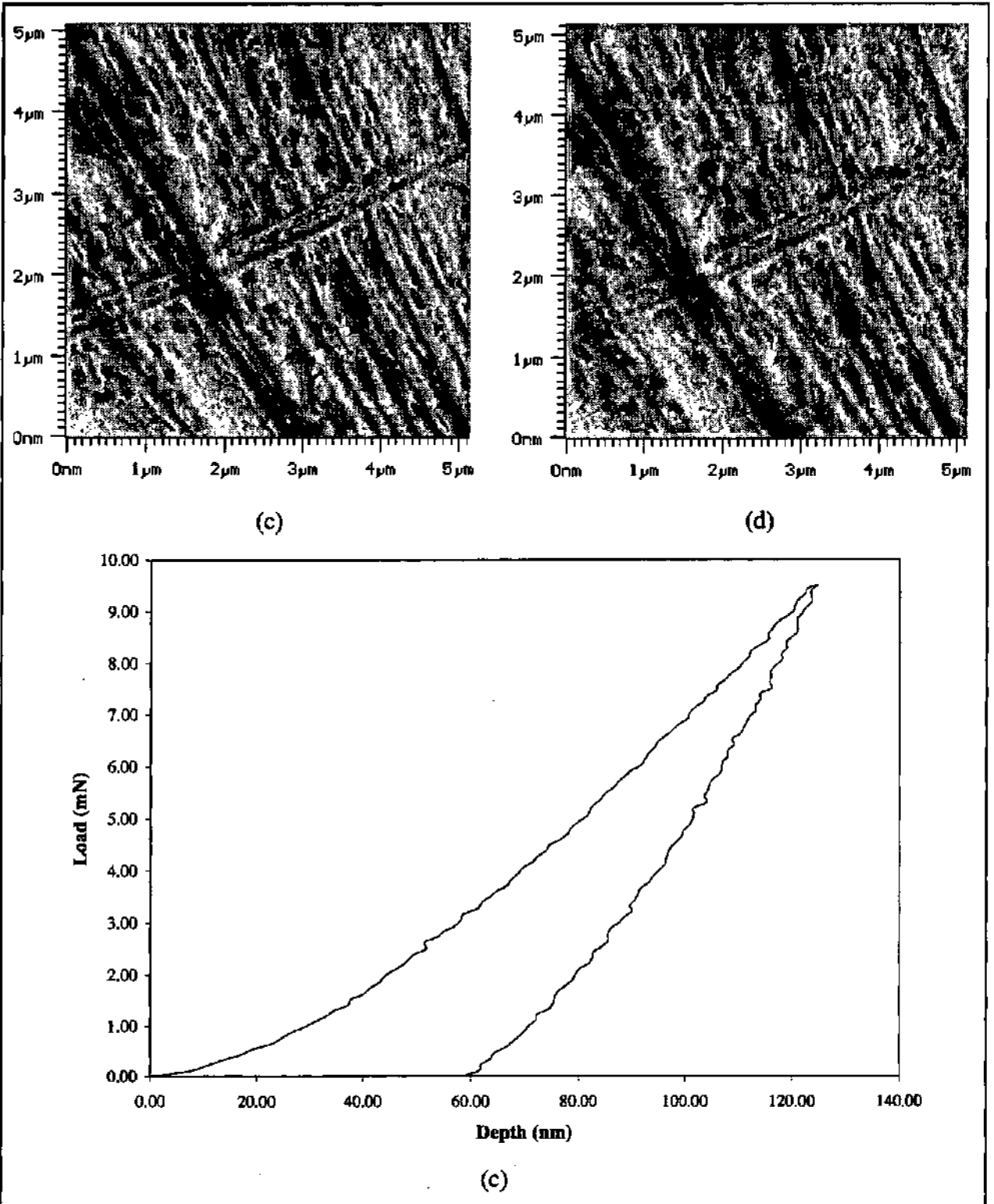


Figure 35 : Typical results on a TiN-coated steel sample. Image (a) shows the surface before indentation, image (b) the surface afterwards. Both images were made using the same Vickers indenter which made the imprint. The curve (c) gave values of $H = 12.98$ GPa and $E = 188.13$ GPa for a loading rate of 20 mN/min. Coating thickness is 1.7 μm.

Figs. 34 and 35 show similar sets of results on a soft gold sample and a hard TiN coating respectively. The images of the gold surface before and after indentation do not have the same level of contrast : this is because the image-processing software divides the colour scale over the full range of vertical data and so there is better contrast for flatter images, i.e. Fig 34 (a). For the TiN sample it can be seen that the residual indentation depth (~60 nm) is of the same order as the surface roughness of the sample, meaning that for smaller depths the Vickers indenter cannot adequately resolve the impression that it has made during the load-unload cycle. Regarding the quality of the indentation curves, Figs 33-35 represent the best obtained with the system in its present state, the maximum penetration depths in each case being relatively large (>100 nm). For small depths (<50 nm) a number of experimental discrepancies were observed which could not be explained, examples of which are shown in Fig. 36. Such artefacts were most noticeable around the point at which maximum load was reached, characterised by instability or 'doubling-back' of the unloading curve. A possible cause of such phenomena was longitudinal displacement of the indenter at max. load, or buckling of the cantilever, although neither could be easily proved.

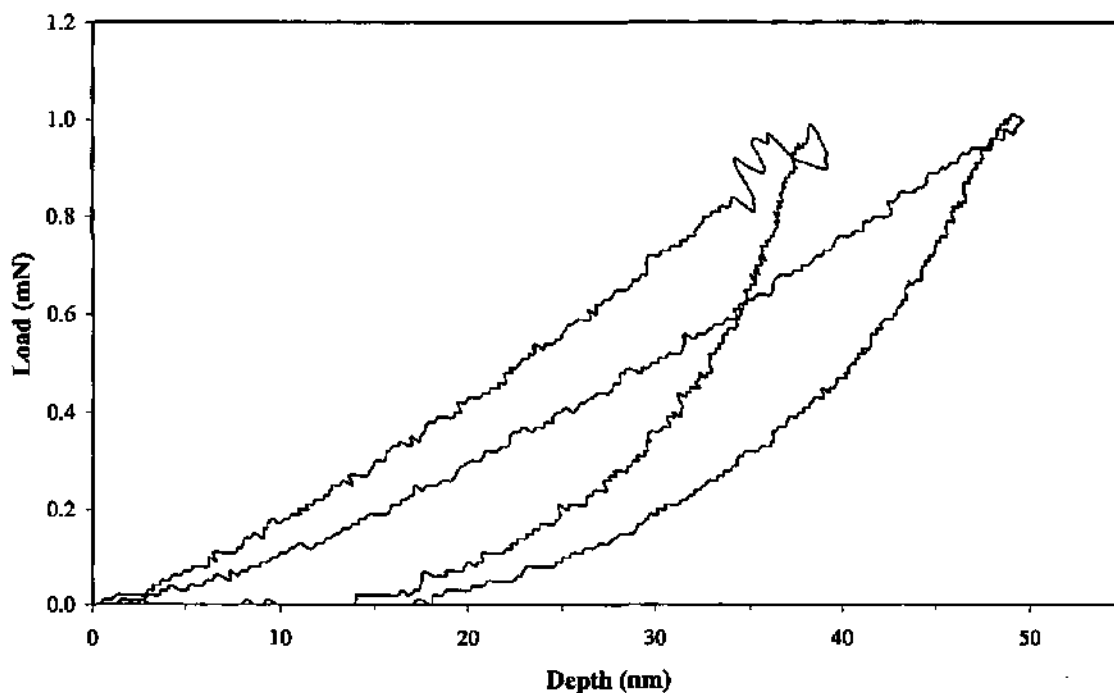


Figure 36 : Typical artefacts characteristic of low load measurements with the SFM-based indentation method. Two curves are shown for different materials, together with the instabilities encountered at the end of the loading cycle.

However, a limited number of adequate low-load curves were realised with the system, an example of which is shown in Fig. 37 for a residual penetration depth of 16 nm. In order to gain an accurate tangent to the unloading curve, a polynomial fitting procedure was used to normalise the data and extract values for the hardness and modulus. In the case of annealed titanium the calculated values corresponded reasonably well with those found in the literature for conventional depth-sensing indentation. Similar low-load measurements on a selection of other materials were successful, although in several cases (mainly soft materials), the deviation and low density of data points meant that no quantitative values could be calculated and dispersion between data sets was large.

The use of the cantilever system, apart from the aforementioned instabilities, was found to be sensitive to background noise, whether acoustic or electronic. The best measurement conditions were obtained by mounting the complete system on a pneumatic vibration-isolation table to reduce low frequency noise and operating it in controlled conditions regarding temperature and humidity, to prevent thermal drift effects and expansion/contraction of the metallic components.

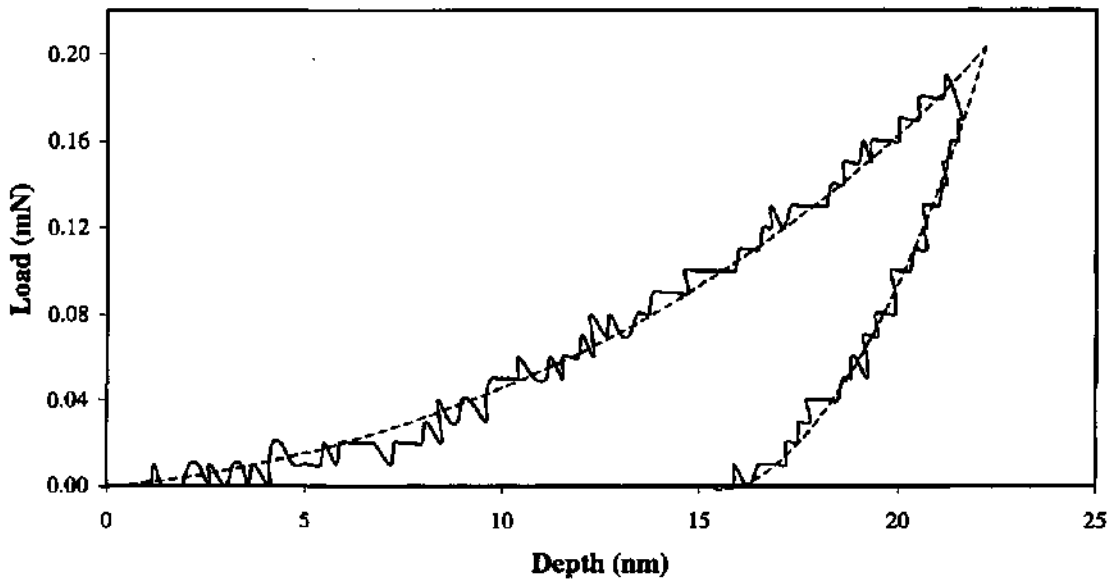


Figure 37 : Typical low load indentation on annealed titanium. A polynomial fit (shown in brackets) to this rather noisy curve enables calculation of H (= 2.014 GPa) and E (= 159.9 GPa).

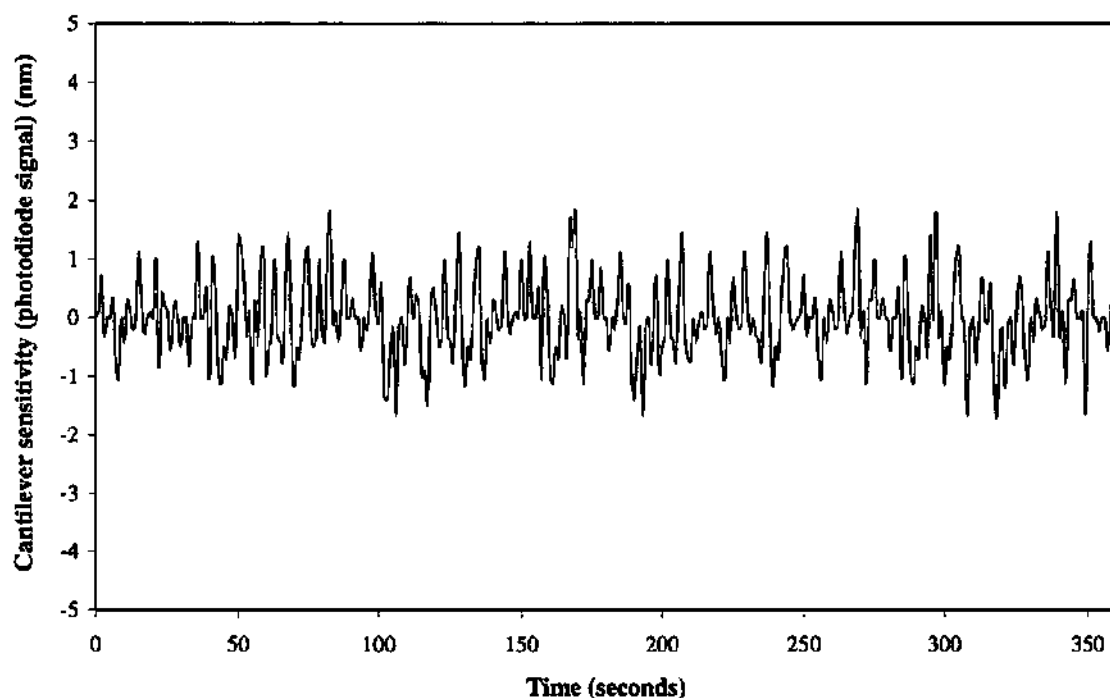


Figure 38 : Sensitivity of the SFM-based system over a 6 minute period when mounted on a pneumatic anti-vibration table. The cantilever tip is in contact with a polished sapphire sample.

The sensitivity of the cantilever was verified for the condition when it is in contact with a sample of high stiffness (e.g., sapphire) over a preset period of time. The oscilloscope plot shown in Fig. 38 represents the amplitude of the cantilever over a period of 360 seconds, measured as a direct signal from the photodiode which records cantilever displacement via a focussed laser beam (i.e., the difference between the upper and lower quadrants, or the *A-B* signal). The signal is stable over an amplitude of approximately ± 2 nm which is satisfactory if it is considered that usual penetration depths are at least a factor of 2 or 3 greater than this, and that measurement time for a load-unload cycle is of the order of 60 seconds.

Regarding the stability of the laser interferometric deflection measurement, small deviations in laboratory temperature were found to cause significant drift in the intensity of the beam reflected off the cantilever into the photodiode. This was due to minute changes in cantilever angle caused by thermal effects.

4.5 Conclusions

The principle of the SFM has been successfully applied to the nanoindentation of a variety of materials, but has proved unsatisfactory in the quantitative and reproducible measurement of surface mechanical properties such as hardness and elastic modulus. However, the ability of a very well polished Vickers diamond tip to image a surface, as well as to indent it, has been demonstrated. The system clearly has applicability to specific investigations where *in-situ* imaging directly after indentation is of interest, as well as where selection of a suitable site for indentation is important. For example, in the field of polymers, the effects of time-dependant relaxation and viscoelasticity could be directly measured owing to the very short delay between a loading cycle and subsequent imaging of the surface. In addition, the soft nature of polymeric materials means that cantilever beams with much lower force constants can be used, thus increasing imaging resolution and reducing damage to the surface as a result of scanning.

With regard to the use of a Vickers indenter, however accurately polished, there will always remain a finite sphericity at its apex, resulting in poor imaging resolution. The obvious alternative would be to use a Berkovich geometry which can be ground to a much finer apex, but the disadvantages here are that the tip-sample contact pressure can be appreciably higher resulting in damage to the sample surface, as well as possible damage to the tip itself.

The combined system prototype

The preceding chapters have shown independently the values of the SFM as well as those of a similar instrument capable of depth-sensing indentation. It has also been shown how a Vickers indenter can be used for imaging a surface. However, another objective of this thesis was to combine the indentation system with a conventional SFM and an optical microscope, in order to be able to easily select a particular sample site for indentation and image it with high resolution. Because the SFM-based indentation method is not able to image a surface with sufficient accuracy, a separate imaging station is required and therefore the development of a precise translation system is required, capable of positioning a specific sample area under either an indenter or an SFM tip with micron lateral precision.

5.1 Design constraints

Although various alternative solutions and configurations have been investigated, the simplest method for combining a nanoindentation unit, a SFM head and an optical microscope is to mount them vertically above a sample translation system which allows positioning under any of the three measuring 'stations'. Assuming this configuration, various constraints dictate the final layout of the system, namely :

- (1) Both the indentation unit and SFM require separate automated approach systems.
- (2) Sample translation must be possible along two perpendicular axes.
- (3) An adequate method of calibrating sample position under any one station is needed.
- (4) The effects of thermal expansion/contraction should be minimised, as these will seriously reduce positioning accuracy.
- (5) Various safety features are required to prevent 'crashing' of components into each other.
- (6) Samples of any size should be measurable.

- (7) A positioning accuracy of 1-2 μm in each axis is required at any one position.
- (8) Manual focussing of the optical microscope must not be impeded.
- (9) Movement of the sample in micron steps must be possible whilst scanning.
- (10) Coarse sample movement is needed as well as automatic movement.
- (11) The SFM head should be free-standing in order to focus the laser correctly and change cantilever tips when required.
- (12) The maximum scan range of the SFM must be increased above 20 μm .
- (13) The complete system should be as compact and user-friendly as possible.

The chosen configuration is shown schematically in Fig. 39. Sample displacement is achieved using two perpendicularly mounted electromechanical tables (X and Y axes), whilst an additional two tables control the vertical movement of the indentation head (Z_{IND} axis) and SFM head (Z_{SFM} axis) respectively. The three stations are mounted on an aluminium bar which can be displaced vertically via its support posts, allowing high samples to be accommodated below them.

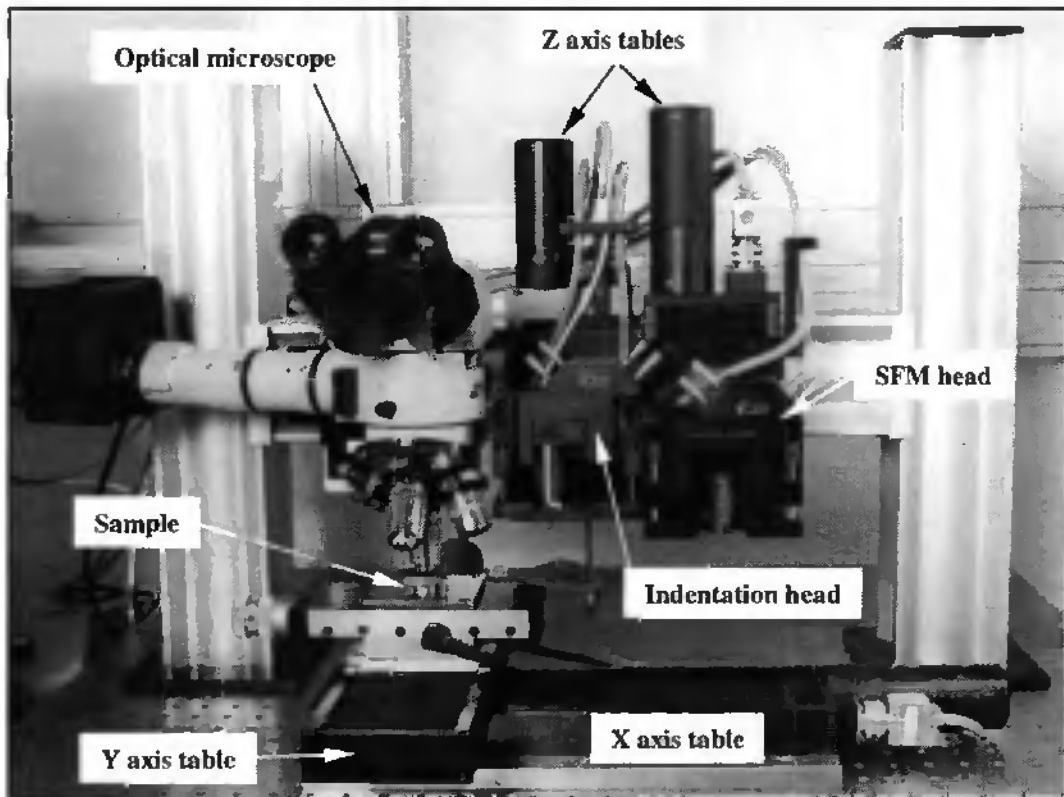


Figure 39 : The combined system prototype in which the three measuring stations are mounted vertically above an electromechanical sample positioning system.

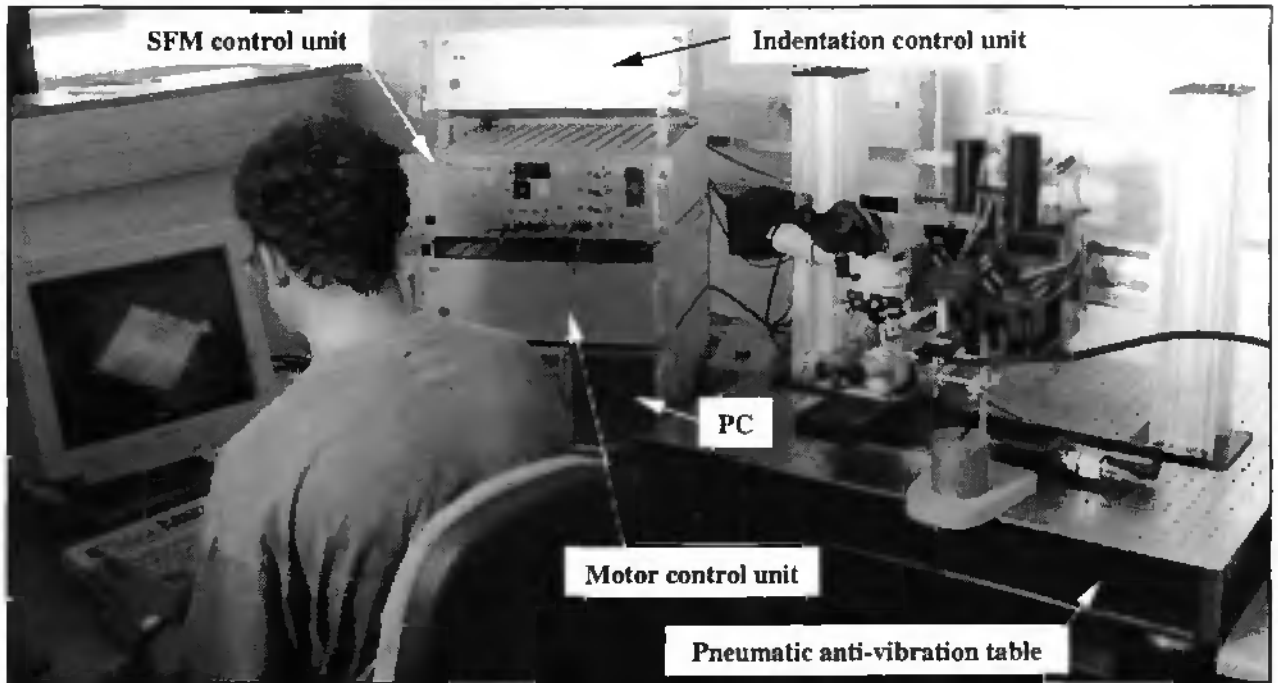


Figure 40: The complete system mounted on a pneumatic anti-vibration table and shown together with control units, external light source and monocular lens (50 \times) for monitoring the approach of either the SFM or indentation heads.

The sample is mounted on a micrometer displacement table which means that a specific site can be moved to manually. This also extends the maximum lateral range of the X axis table by several centimeters, useful for wide samples such as standard 4-inch wafers. Both the indentation and SFM heads are freestanding and mounted with their three legs in positioning grooves for easy access. All cables are suitably routed to prevent interference and the various bulky supporting blocks are machined from aluminium to reduce thermal effects. The *Nikon* optical microscope is focussed manually and is fitted with objectives up to 1000 \times magnification and Normarski contrast, as well as a crosshair reticule for calibrating sample position. The complete system (Fig. 40) is mounted on a pneumatic anti-vibration table and all control electronics are housed on a separate table to prevent vibration and electronic noise. In addition, an external light source is used for illuminating the sample during approach of either head and a low magnification monocular lens is used for monitoring. The SFM head (in this case the Atomic Scale Tribometer™ – see Chapter 1.3) is fitted with a piezo tube of long length, thus providing a total lateral scan range of up to 27 μm (5-pole mode) and 11 μm (9-pole mode).

5.2 The electromechanical positioning system

The four electromechanical translation tables used in this setup are basic mechanised displacement stages as manufactured by *Micro Controle*, but with various modifications. The standard stepper motor driving the screw shaft is replaced with a continuous current motor and a coder wheel with 1000 divisions. This gives each table, considering a lateral movement of 2.5 mm for one revolution, a theoretical 'step' resolution of 0.25 μm . Each motor assembly is connected to a standard data acquisition card allowing software control of positioning, as well as direct monitoring of actual position. The ranges of the X, Y, Z_{IND} and Z_{SFM} axes are 200, 100, 50 and 50 mm respectively. Because of the inherent inaccuracy caused by play in the screw shaft, the tables were verified by measuring the error between programmed position and actual position using a capacitive displacement sensor (accuracy = 0.01 μm). This was repeated for up to 30 cycles and the loss of positioning accuracy was found to increase in an approximately linear fashion as shown graphically for the X axis (table with longest range) in Fig. 41. Temperature changes, although only slight, were also found to influence positioning accuracy.

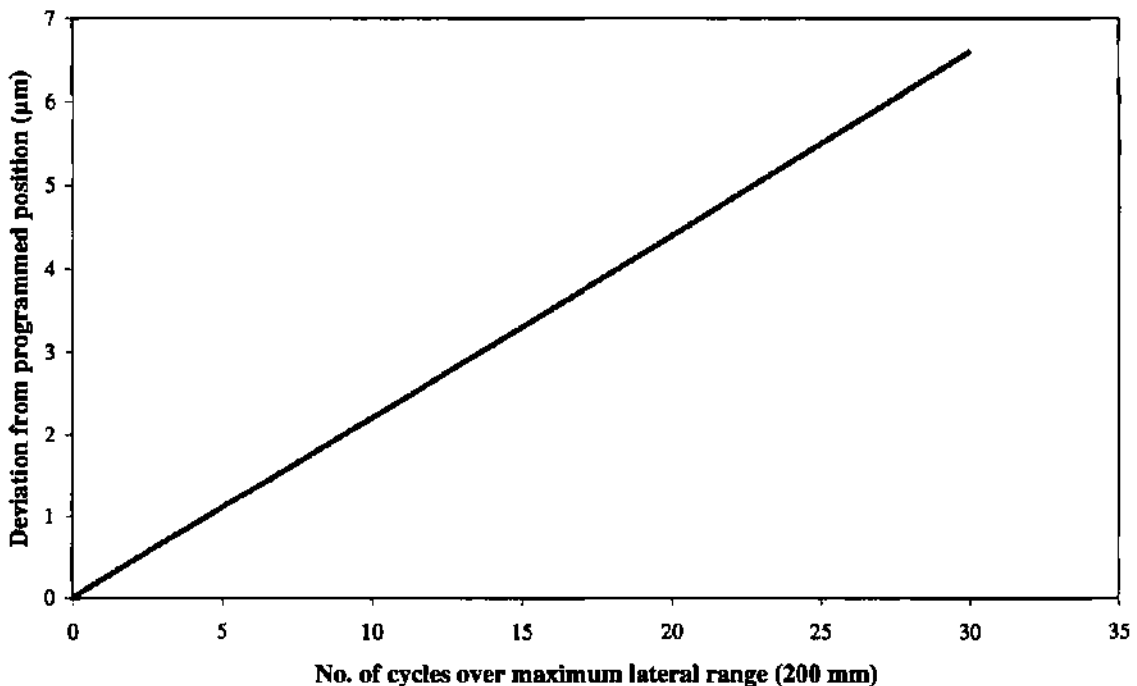


Figure 41 : Deviation from programmed position for the X axis electromechanical translation table, plotted as a function of number of cycles over the maximum lateral range.

5.3 Software

Certain software modifications are required in order to permit simultaneous operations to be performed. The indentation head is operated by a software package, as is the SFM head. Both packages were modified to allow table movement and initialisation of table position. This is particularly important for the SFM software as it was a requirement that the X and Y axes should be displaceable during actual scanning of the tip. However, it was soon found that the tables produced different levels of vibrational noise, due to the control electronics constantly correcting the actual position. Thus an option was added which allowed the power to either table to be switched off once the required position had been located.

In terms of safety factors, various sub-routines are incorporated into both softwares to prevent accidental crashing of either head into the sample. Additionally, an external stop button is incorporated so that the whole system can easily be cut at any given time. Regarding the relative positioning of the sample under any one of the three stations, the optical microscope position is made the reference (or absolute zero), from which the other two positions are calculated as relative vectors and stored in a calibration file which can be read by either software package. When displacing the sample between stations, both the indentation and SFM heads are raised in order to reduce any risk of a tip remaining in contact.

5.4 Calibration of sample position

Sample position is calibrated as two separate procedures ; (i) calibration of distance between indentation head and optical microscope ; (ii) calibration of distance between SFM head and optical microscope. Each position is stored as an XYZZ vector with respect to the optical microscope. For (i) a fairly large indentation is made on a flat sample (usually aluminium for convenience), which can easily be found under the optical microscope. For (ii) a calibration sample is required which can be easily centred under the optical objective, and which can be centred within the $27 \times 27 \mu\text{m}$ maximum scan range of the SFM. To solve such a problem requires the fabrication of a defined surface structure whose centre can be located from any other position. To this end, a grating has been fabricated by circular etching in quartz with period $1 \mu\text{m}$

and depth ~ 100 nm. Therefore, when an SFM image is made on any part of this structure, the curvature indicates in which direction the sample must be moved in order to find the centre. Fig. 42 shows a typical SFM image of the *fresnel*-type grating used. Such a structure can also be easily focussed under the 1000 \times objective of the optical microscope.

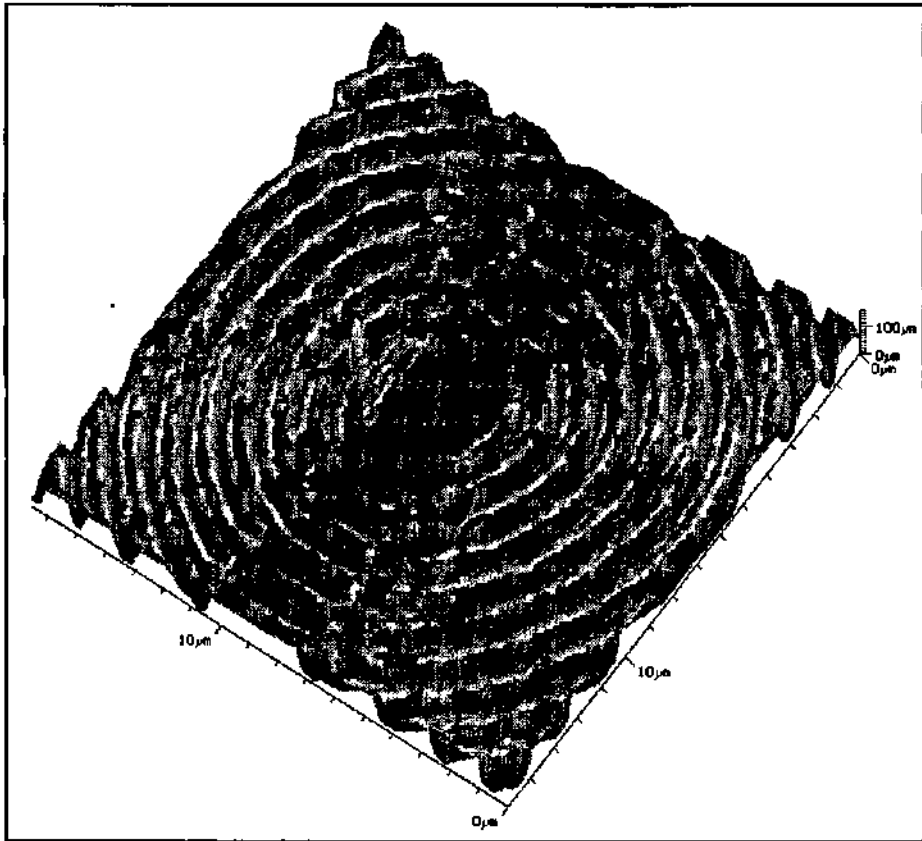


Figure 42 : SFM image of the *Fresnel* lens calibration grating, etched in quartz and having period $1 \mu\text{m}$ and depth ~ 100 nm.

5.5 Results

The positioning accuracy of the system has been demonstrated for an etched high speed steel sample, this being chosen for its distribution of small-sized grains ($5 - 10 \mu\text{m}$) having different mechanical properties. Fig. 43 shows a series of 5 indentations positioned in a cross configuration with only $2 \mu\text{m}$ spacing on an M_6C carbide particle.

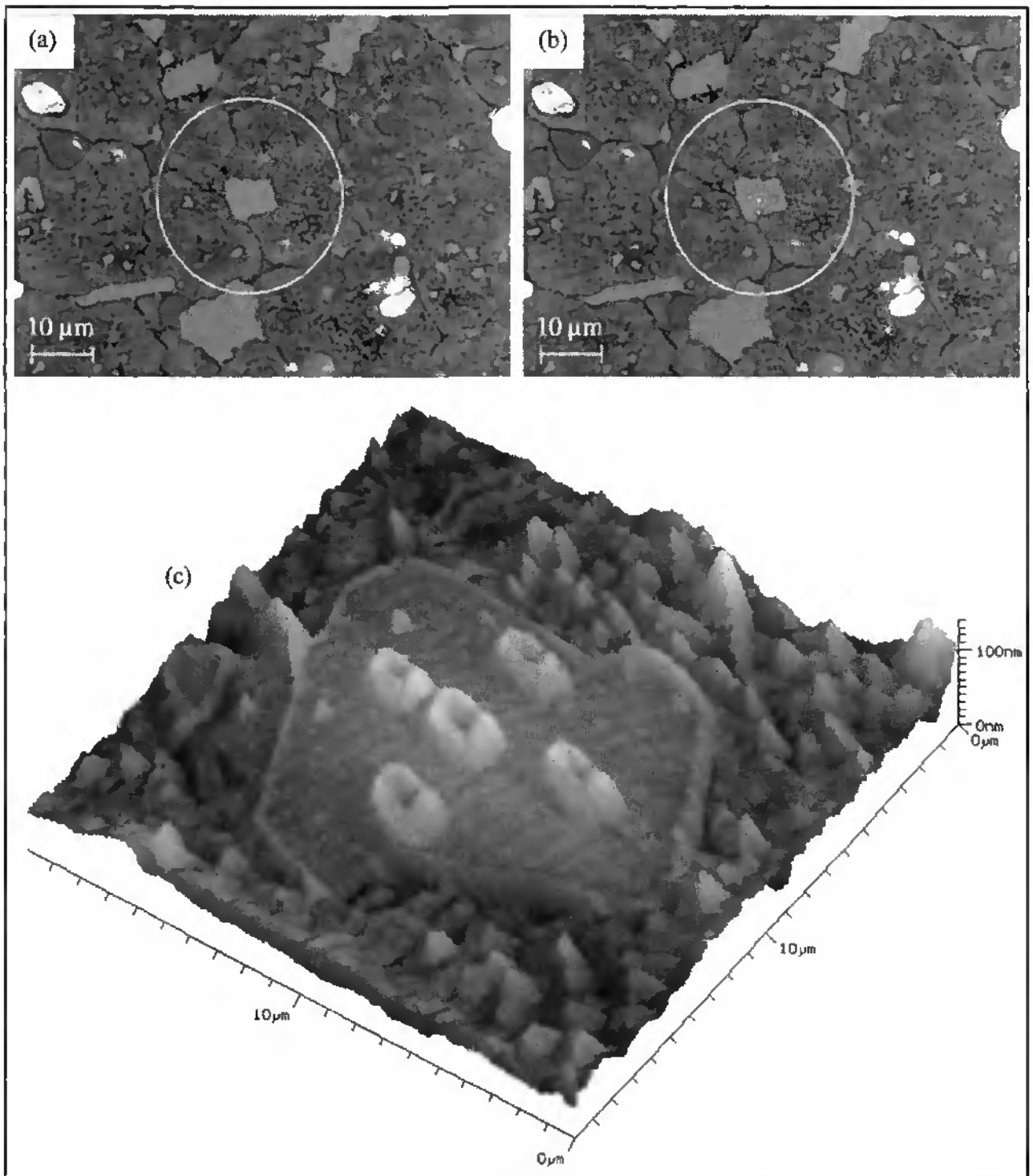


Figure 43 : Micron positioning accuracy of the combined system demonstrated by 5 indents (max. load = 1 mN) placed in a cross configuration with 2 μm spacing on an M₆C carbide particle. Optical micrographs (a) and (b) show the selected area before and after indentation, and (c) is an SFM image of the indented particle. *This 'swiss cross' was measured on 1st August, 1995.....the swiss national festival !*

This example effectively demonstrates the overlap between conventional optical microscopy and the scanning force microscope. For the former, the micrographs are made at 1000× resolution, the limit for an optical microscope operating in air. The SFM, on the other hand, is capable of a vertical resolution in this case exceeding 120 000×. Full results obtained with the combined system are presented in Chapter 7.

5.6 Conclusions

The combined system has been successfully used to study a variety of materials. It has also shown to be useful simply for SFM imaging of selected sample areas in addition to residual indentation impressions. A positioning accuracy of 1 μm has been achieved, which, considering the composite error of three electromechanical displacement tables when at any one position, is highly satisfactory and opens up a whole new range of possibilities for the localised characterisation of materials. The net advantages of combining a SFM with a nanoindentation unit and an optical microscope have been shown, as well as the significant additional information which can be gained with such a setup. The expertise gained during the development of this system has proved the backbone for the subsequent realisation of the Nano Hardness Tester, described in the next chapter.

Realisation of the Nano Hardness Tester

This chapter describes the development and first use of the Nano Hardness Tester™ (NHT), a direct result of the know-how and experience amassed and documented in the preceding chapters of this thesis. This instrument overcomes the limitations of previous prototypes, is far more compact and user-friendly, and is presently commercialised by CSEM Instruments. The NHT in its present form consists of a measuring head for performing indentations and an optical microscope for selecting a specific sample site prior to indentation and for checking the location of the imprint after indentation. Both components are directly linked by an electromechanical positioning system (2 axes) as described in the previous chapter. A compact SFM can also be mounted in place of an objective lens on the optical microscope, and this will be explained later in more detail.

6.1 The differential-capacitive measurement technique

The NHT measuring head is shown schematically in Fig. 44. The load is directly applied by an electromagnet assembly via a vertical rod, the end of which houses the indenter, usually a diamond ground to a Vickers or Berkovich geometry. Displacement of the indenter is measured by a differential capacitive detector, meaning that the rod displacement is measured differentially with the displacement of a sapphire reference ring which remains in contact with the sample surface during each loading-unloading cycle. In this way the indenter motion is always *relative* to any movement of the sample which, with a static system, would cause error due to elasticity of the sample or compliance of the supporting framework. The vertical rod is supported by two guide springs whose stiffness control the compliance of the measuring head. This allows a certain flexibility in head design ; for example, one head can be fitted with springs of low stiffness for measuring soft materials such as polymers, and another fitted with much stiffer springs for measuring hard materials. During the development phase it was noticed that ferromagnetic

materials caused significant perturbations of the system due to interference between the magnetic field generated by the coil/electromagnet assembly and the sample. This problem was solved by adding a magnetic barrier, in the form of a pure ferrite disc (manufactured by *ARMCO*), between the two springs to shield the electromagnet assembly and cancel any magnetism effects around the vertical rod.

When performing a typical measurement, the entire head is lowered onto the sample surface with its weight (approximately 550 g) transferred to the sample via the sapphire reference ring. The indenter is first displaced manually in order to ascertain the exact point at which the tip begins contact with the sample surface. This contact point must be adjusted such that it is within the measurement range of the coil (0 – 50 mA). A fresh sample area can then be selected, the head relowered, and a complete loading-unloading cycle completed in which the control electronics automatically detect the contact point between the indenter and sample.

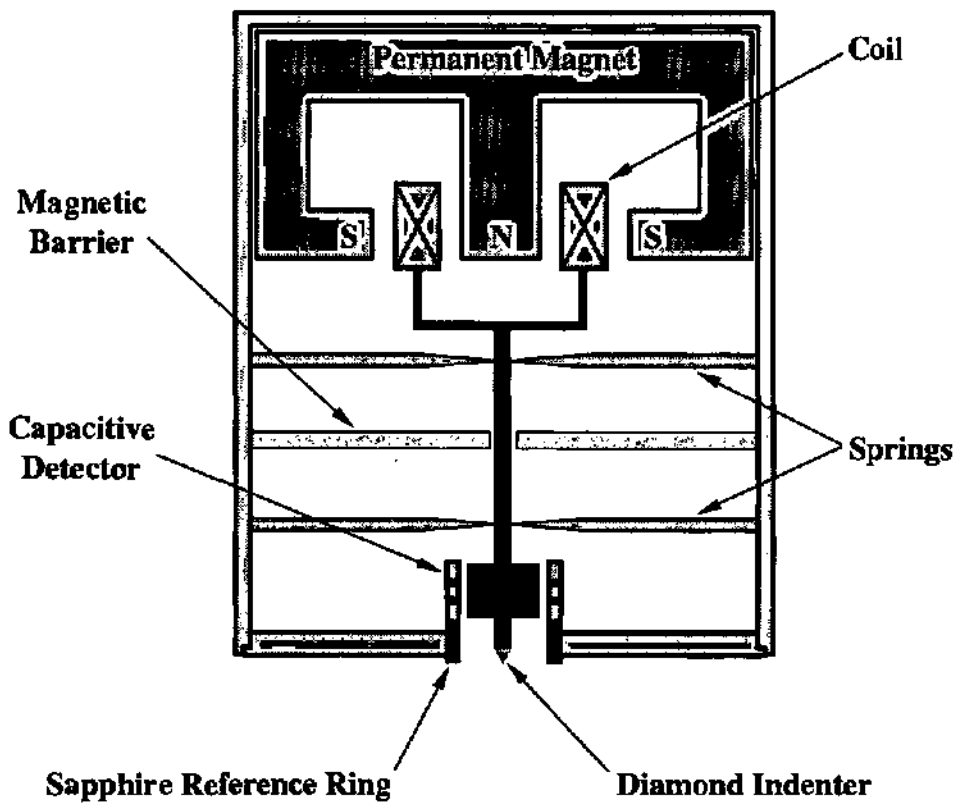


Figure 44 : Schematic representation of the NHT measuring head showing the coil and magnet assembly (applied load) and the differential capacitive detector (displacement).

The entire operation is software controlled with various additional options such as predetermined sample translation between successive measurements, multicycle indentation (either constant or progressive loading) and adjustable loading rate. The outer limits of the loading-unloading cycle can be preprogrammed as either a maximum load or a maximum penetration depth.

After storage, an analysis sub-routine allows any load-displacement curve to be treated as raw data or fitted polynomially. The hardness and modulus are calculated from the unloading portion of the curve using the modified Oliver and Pharr method outlined previously in Chapter 3.

6.2 System calibration

Accurate measurements can only be performed if the applied load, displacement, indenter area function, spring stiffness and system compliance are all adequately calibrated. The applied load (or force) is usually calibrated by placing the measuring head on a high precision digital microbalance having a precision of 0.0001 g ($\approx 1 \mu\text{N}$). Fig. 45 shows a typical force calibration over the full range of coil current, from which a straight line can be fitted and a calibration constant of 7.92 mN/mA calculated. Alternatively, the applied load can be calibrated in a reverse sense ; in this case various fixed masses of 20 mg are suspended from the vertical rod of the measuring head until a total mass of 1 g is reached. For each mass applied, the current required to rezero the capacitive detector is measured and from this the calibration constant can be evaluated.

Displacement calibration is performed using a feedback-controlled piezoelectric actuator (manufactured by *Queensgate Instruments* ; model DPT-C-S). The piezo is mounted beneath the vertical rod of the measuring head and made to displace over its full range (16 μm), whilst the capacitive bridge of the head control unit is adjusted until the piezo displacement equals that measured by the capacitive detector.

The system compliance is calibrated by modelling the frame and sample as two springs in series, and the indenter area function by measuring the contact compliance and plastic penetration depth for a large number of indentations at varying depths in an isotropic material with uniform hardness. Both such procedures are fully explained for this instrument in section 7.3.

The stiffness of the two springs, or *spring constant*, is calibrated by performing an indentation cycle without contact, in order to plot indenter displacement as a function of applied force. A typical example is shown in Fig. 46, for which the spring constant is found to be 889.8 nm/mN. This calibration should be repeated at regular intervals so that any changes can be accounted for, such as due to fatigue in the spring after a large number of cycles. It should be noted that two springs are used in the design of the measuring head in order to assure a high lateral rigidity of the vertical rod which houses the indenter (the lateral rigidity is in fact approximately a factor of ten greater than the axial rigidity of the head). The springs are fabricated from thin copper-beryllium sheet so that the vertical rod is supported in each case by three equiangled flanges, these ensuring total elasticity in the vertical movement of the rod.

After total system calibration, the NHT measuring head is found to have load and displacement resolutions of 10 μN and < 1 nm respectively.

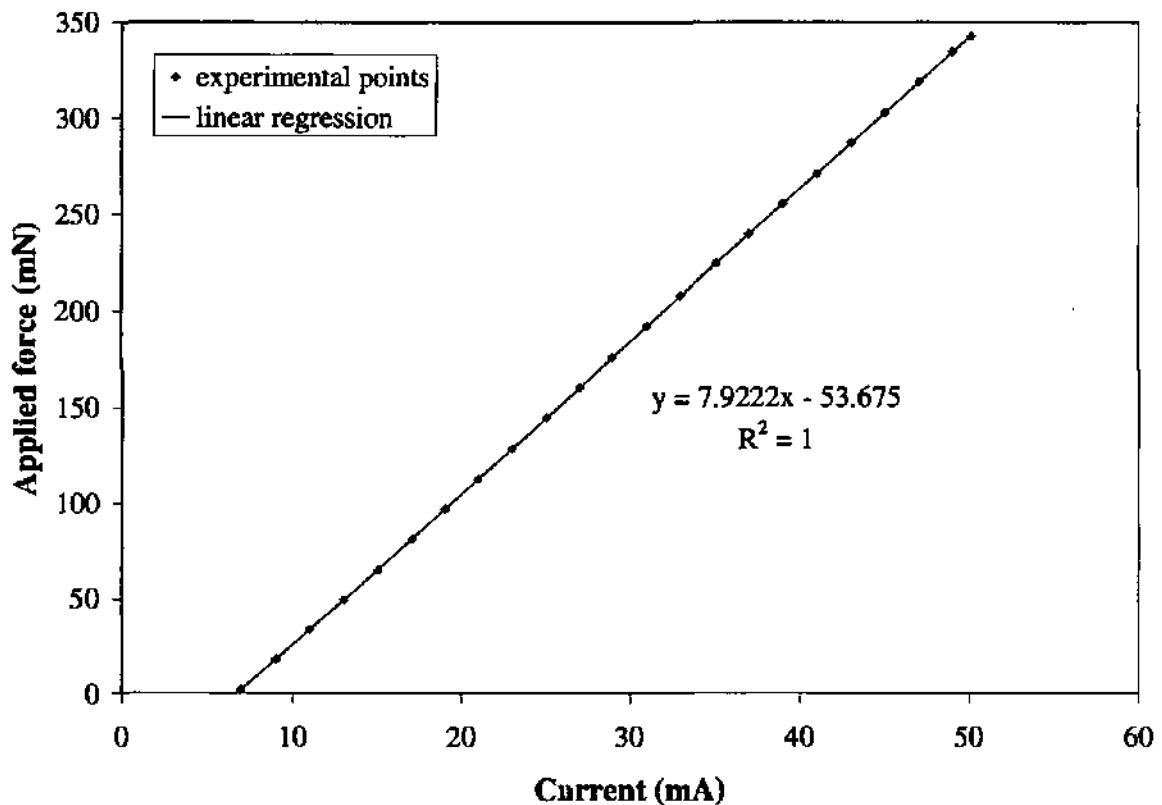


Figure 45: Calibration of applied force as a function of the current in the coil, giving a calibration constant of 7.92 mN/mA.

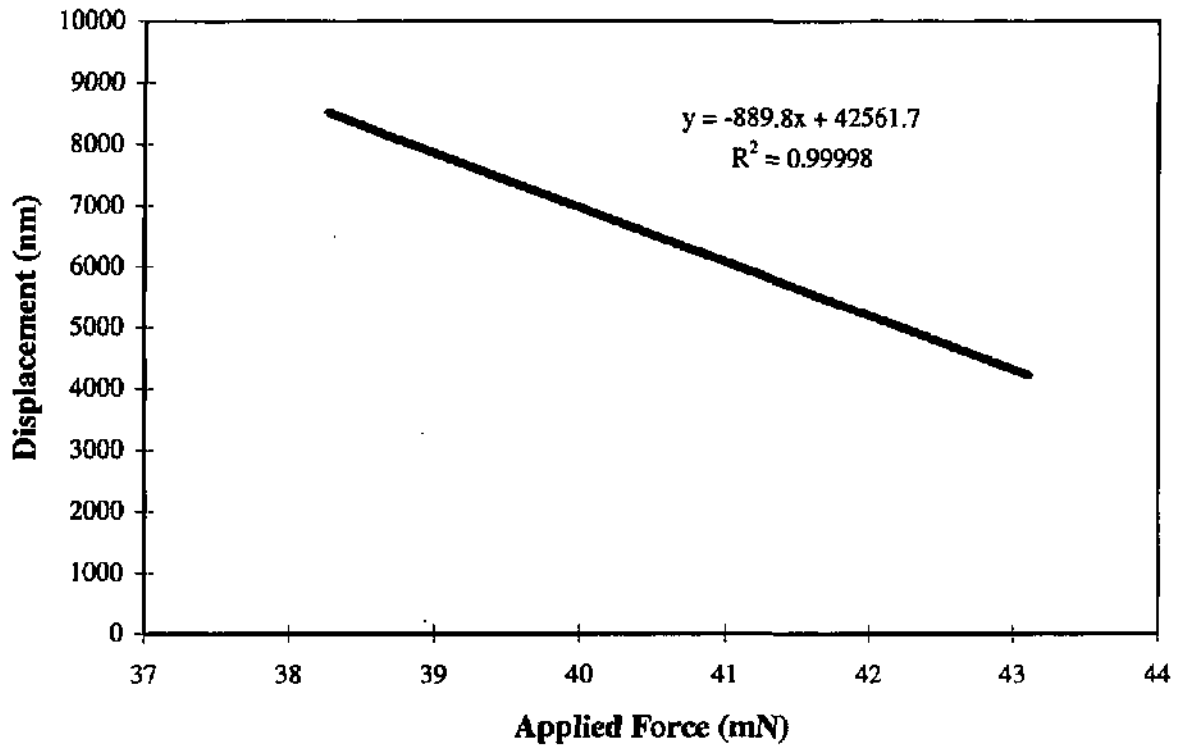


Figure 46 : Typical calibration of spring compliance for the NHT head. The experimental points have been fitted with a linear regression, from which the average gradient gives the spring compliance. In this case, after averaging over 4 measurements, the value is found to be 889.8 nm/mN.

6.3 Integration of a compact scanning force microscope

The complete NHT system (Fig. 47) is housed in a solid die-cast frame to ensure compactness and stability. The measuring head and optical microscope are mounted side-by-side and linked by two electromechanical displacement translation tables (X and Y axes), allowing a specific sample site to be automatically positioned under either head or microscope with a precision of 1 μm . The measuring head is protected from accidental damage by a stiff housing and is lowered and raised automatically via a Linear Variable Differential Transformer (LVDT) housed within the frame. The two perpendicularly mounted tables can be moved vertically over a range of ~ 12 cm and locked in position, thus permitting large samples to be measured easily. The optical microscope

has two objective lenses (50× and 1000× magnification) and is focussed manually using a conventional thumbwheel.

An SFM *objective* can be mounted together with the two standard objectives, this requiring modification of the thumbwheel assembly and integration of an electric motor which permits the SFM head to be approached automatically until its cantilever tip contacts the sample surface. This particularly compact SFM is manufactured by *Surface Imaging Systems (SIS)* and cantilever deflection is detected using an optical interferometer which does not necessitate complicated optics as in other instruments.

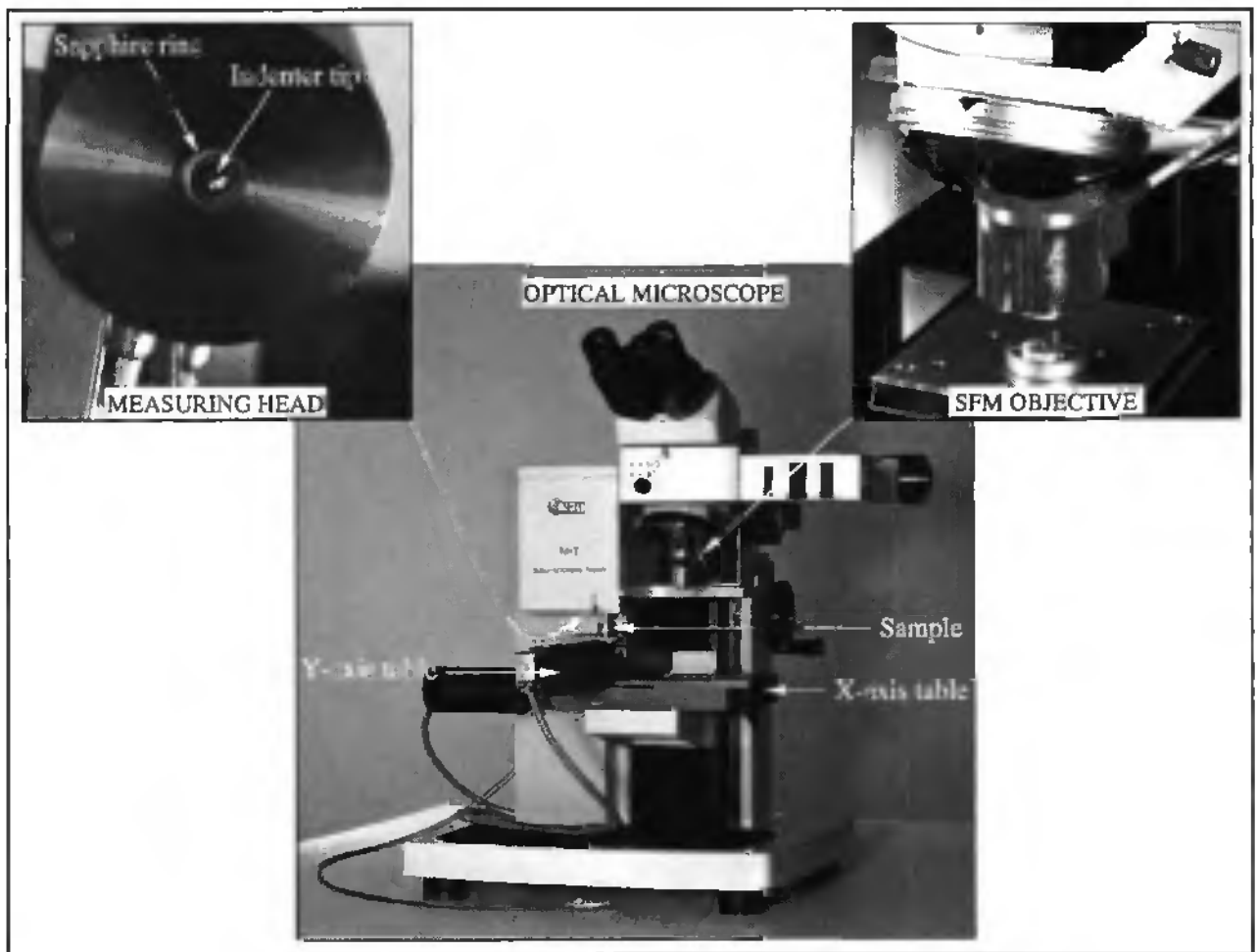


Figure 47 : The complete NHT system with integrated SFM mounted as an objective on the optical microscope. A close-up view from under the measuring head shows the sapphire reference ring around the indenter. The XY displacement tables allow the sample to be automatically positioned under any one of the three stations.

Integration of the SFM objective means that, as with the combined system (Chapter 5), three measuring stations are available under which a specific sample site can be quickly and accurately positioned via the two electromechanical tables. A separate software package for controlling table displacement allows lateral movement of the sample whilst the SFM tip is in contact : this greatly aids the calibration procedure (the same as previously described in section 5.4, using a circular etched grating).

The complete NHT system is mounted on a pneumatic anti-vibration table to dampen external vibrations and minimise noise whose frequencies may perturb the measuring head or SFM. The influences of thermal drift and external noise on the measuring head have been investigated elsewhere⁹⁹ and have shown that, in its present form, the NHT is a very stable instrument.

6.4 The SIS objective SFM

This SFM head simply houses a standard piezo tube which is feedback controlled in all three axes by capacitive strain gauges which practically eliminate the inherent piezo limitations of hysteresis and non-linearity. The total lateral scan range is 20 μm and an optical fibre focusses a beam on the backside of the cantilever, the reflected intensity being measured by a separate control unit. Operation of the unit is fully automatic and user friendly, and standard Si_3N_4 cantilevers can be used.

The deflection of the cantilever is transformed into a measurement signal by a glass-fibre interferometer which serves as a position detector. This signal is sent to the control electronics where the tip position is continuously adjusted during scanning to compensate for height variations. This feedback control loop ensures that cantilever deflection remains constant during a measurement and is recorded as a direct representation of the surface topography of the sample. The glass-fibre interferometric deflection sensing system is shown schematically in Fig. 48 and has been chosen owing to its compactness and insensitivity to interference and noise. Light emitted by the laser diode is coupled into a monomode glass-fibre which transmits the light, of wavelength λ , in one direction only. The beam is directed via a beam-splitter onto the reflective backside of the cantilever, the end surface of the fibre acting as a half-mirror, both of which form

a *Fabry-Perot* interferometer¹⁰⁰. The reflected light is transmitted back to the fibreoptical coupler where it is outcoupled and its intensity measured by a photo diode. This signal takes the form of a sinusoidal wave when plotted as intensity versus distance between the end surface of the fibre and the reflecting backside of the cantilever. Typical intensity variations have a period of $\lambda/2$, the highest sensitivity of this technique being obtained if variations of the measured signal are determined between a minimum and a maximum (or vice versa). If the cantilever is adjusted into a nearly linear range of this signal function then deflections can be detected with a resolution of 0.01 nm. Since the force applied by the cantilever on the surface should remain constant, the Z-piezo is used to compensate as described previously, thus ensuring that the cantilever tip remains in the most sensitive detection range of the interferometer. The objective SFM has been shown in practice to have an effective vertical resolution of 0.05 nm owing to the instability of the microscope on which it is mounted¹⁰¹.

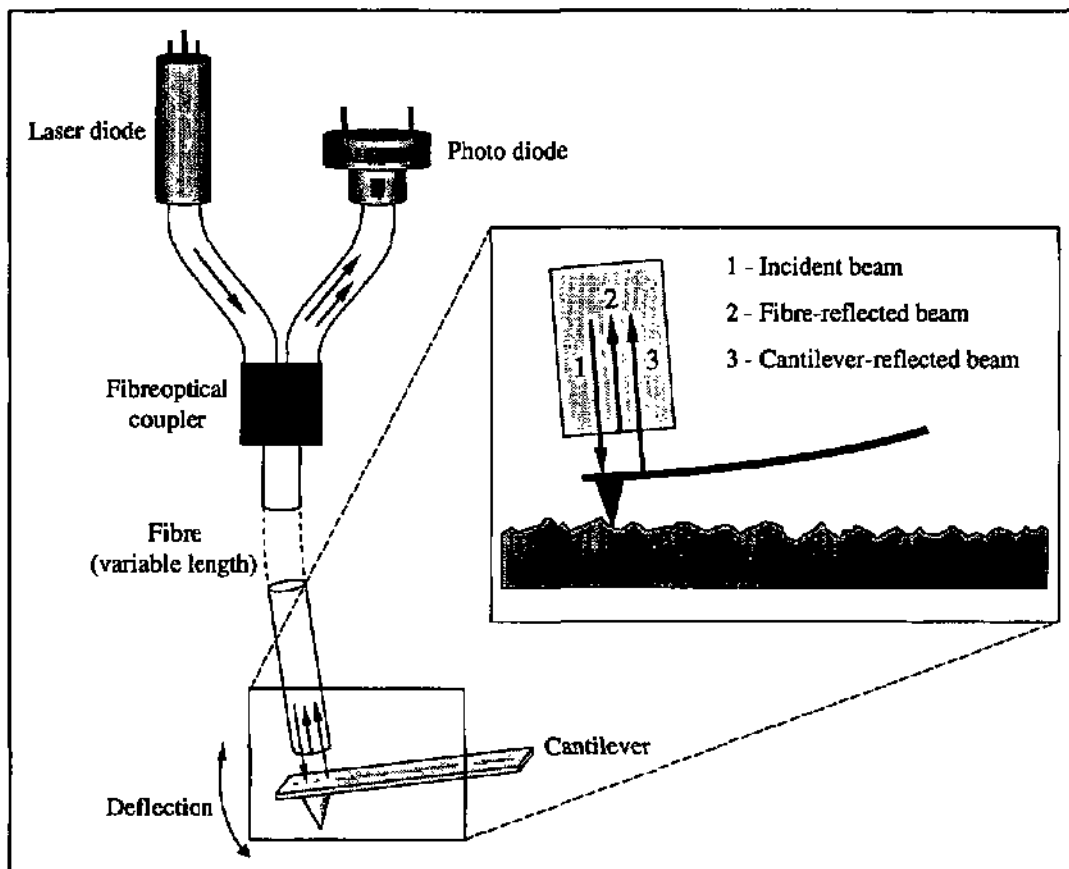


Figure 48 : Schematic representation of the glass-fibre interferometer setup used for measuring cantilever displacement with the SIS objective SFM.

6.5 Results

The main applications of nanoindentation combined with scanning force microscopy are presented in Chapter 7. However, some basic results as well as other interesting applications are described in this section.

Fig. 49 shows indentation data for two similarly work-hardenable but soft metals, in this case pure copper and gold. The SFM images confirm the effects of pile-up around the residual imprint and for the copper it is easily noticed that the edges of the Vickers impression are convex (or barrel-shaped). If a metal has been highly worked, so that no appreciable work-hardening is produced by the indentation process itself, the metal behaves approximately as an ideally plastic material and the displacement of the the metal will follow a classical flow pattern, the displaced material tending to flow up the faces of the indenter, but since it will be less constrained on the faces than on the corners, it will rise more at these regions than at the edges. Thus with a Vickers indenter, the indentation will be wider at the centre of the faces than at the edges. Note that all cross-sectional profiles for Vickers indentations are measured vertically through the centre of two opposite imprint edges.

If a metal has not been highly worked, the displaced material is pushed out at some distance from the indenter ; early displacement of material in the plastic region produces appreciable work-hardening and it becomes easier to displace the adjacent material which lies deeper below the indentation. The imprint is therefore sunk below the original level of the surface and the effect is more marked at the centre of the faces than at the edges. This produces concave (or pincushion-shaped) residual impressions. This phenomenon, although well-documented for metals, is often encountered with other classes of materials. Fig. 50 shows indentation data for sapphire and tantalum, the former being a ceramic material of high hardness (in this case measured as 21 GPa) and one which is susceptible to brittle cracking as a result of indentation. The SFM images confirm that both materials exhibit concave imprint edges. However, the corresponding profiles show that the sapphire imprint is significantly sunk-in below the original surface, whereas the tantalum has a certain amount of pile-up material. In addition, the sapphire SFM image and profile show a 'step' of material (right side of profile) which is above the original surface. This is caused by cracks propogating away from the indenter under the surface during loading.

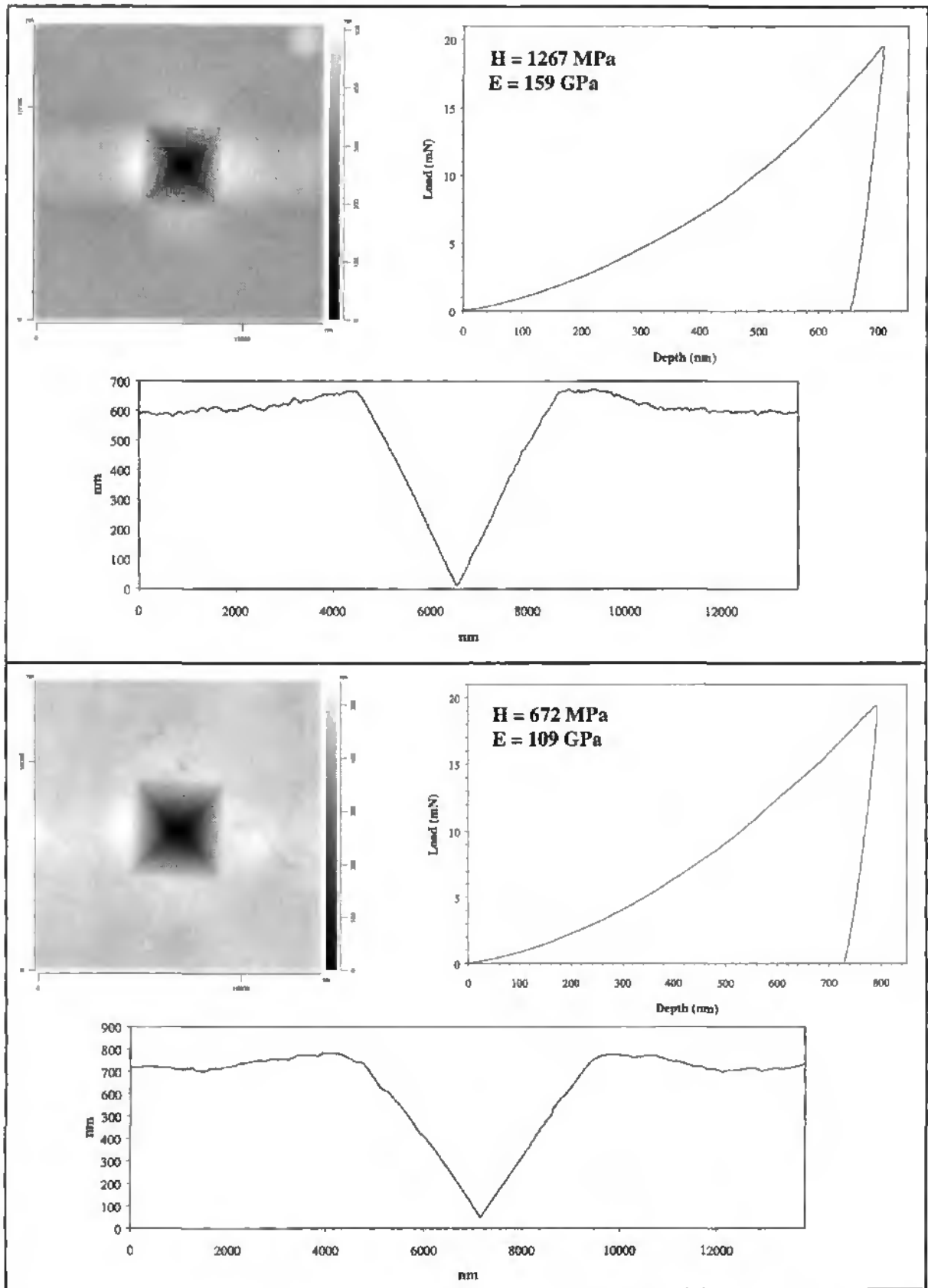


Figure 49 : Vickers indentation data for copper (top) and gold (bottom), including load-displacement curve, SFM image and cross-sectional profile through imprint.

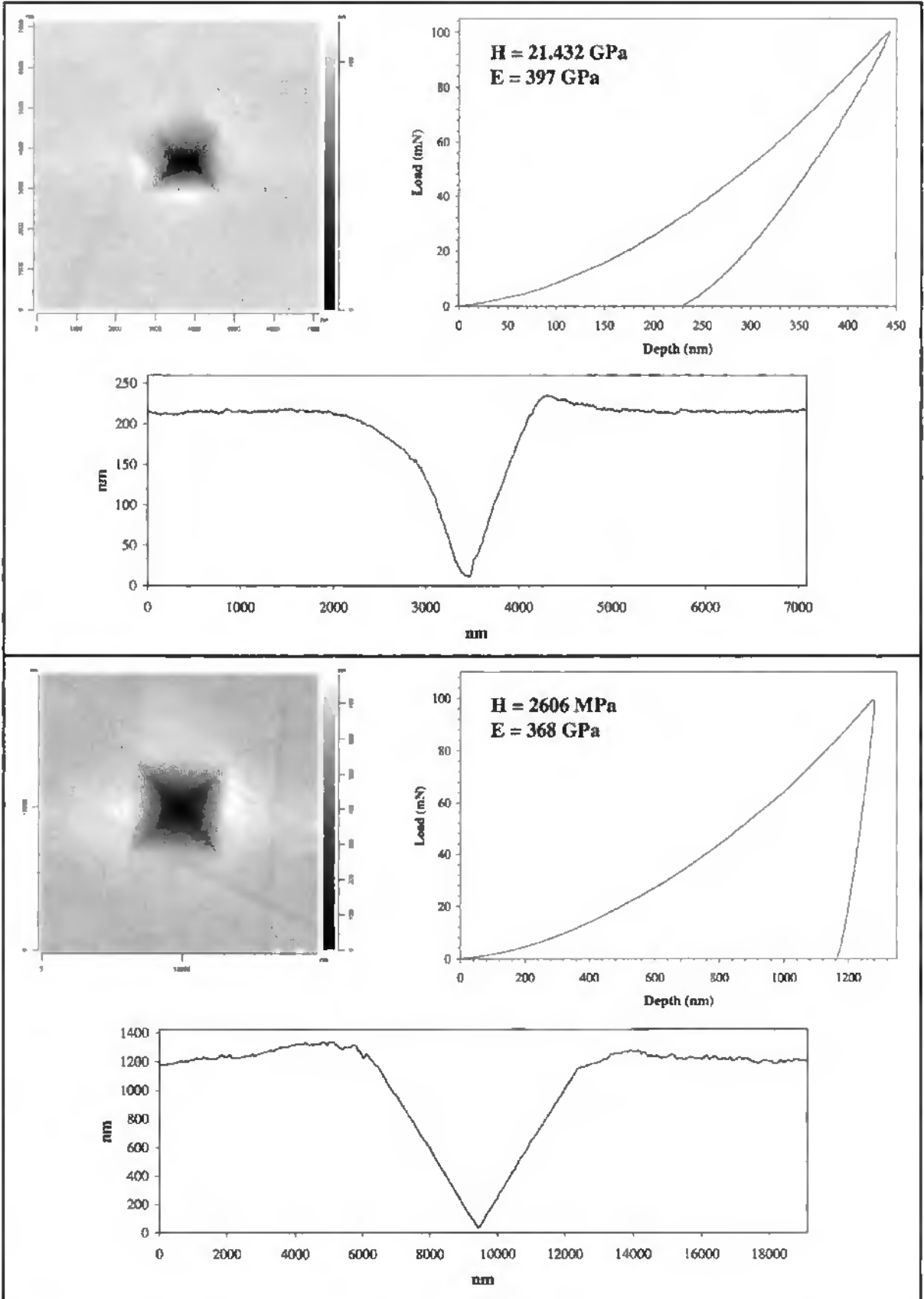


Figure 50 : Vickers indentation data for sapphire (top) and tantalum (bottom), including load-displacement curve, SFM image and cross-sectional profile through imprint.

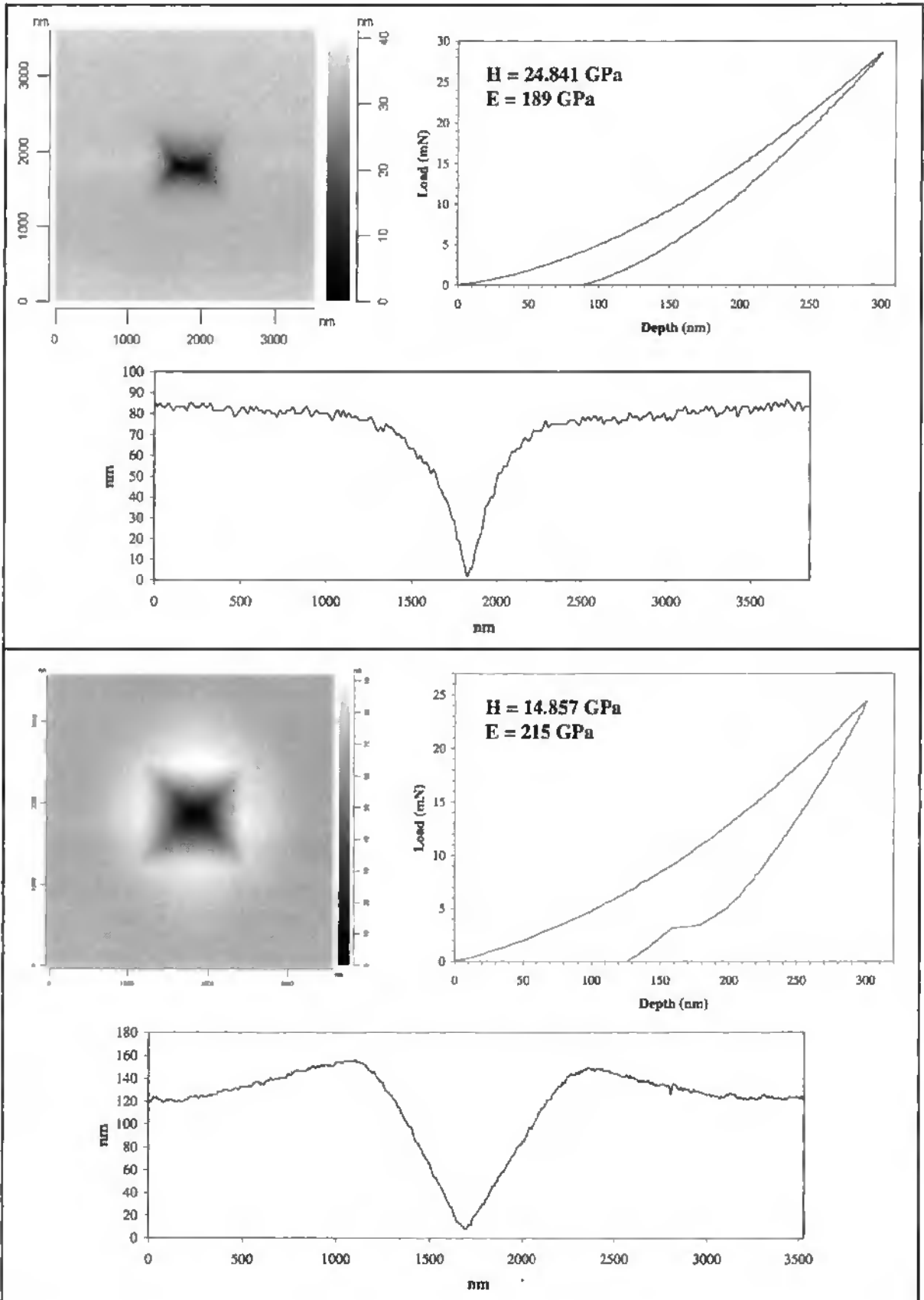


Figure 51 : Vickers indentation data for DLC (top) and TiN (bottom) thin films deposited on a polished Si wafer. The former exhibits a huge depth relaxation upon unloading.

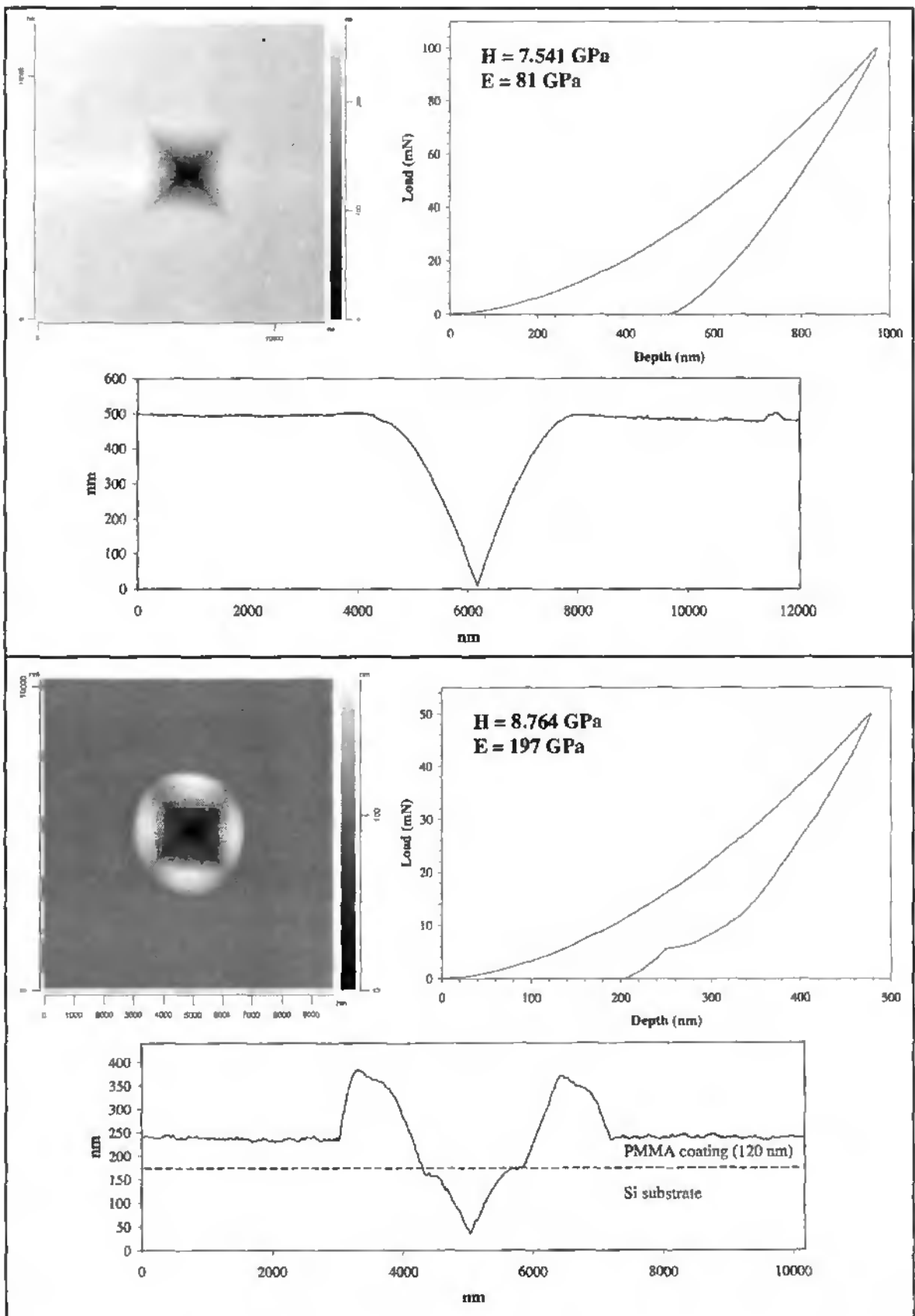


Figure 52: Vickers indentation data for glass (top) and PMMA on Si (bottom). The latter exhibits large pile-up of the photoresist and characteristic pop-in of the Si substrate.

Fig. 51 shows indentation data for two high-tech coating materials which are now commonly used in tribological applications. Diamond-like carbon (DLC) films are already well known for their high hardness (20-30 GPa), high elastic modulus, low friction, chemical inertness and good wear resistance. The load-displacement curve confirms the huge depth relaxation upon unloading, leaving a residual imprint depth less than one third of the maximum penetration depth. The SFM image shows the relatively large tip defect of the particular Vickers indenter used for this indentation. Such a defect is not uncommon in the field of micro- and nanoindentation, owing to the difficulty in polishing a four-faced diamond pyramid to a reasonable tip. For the example shown, it is noticed that the indenter has a flat across its tip of approximate length 500nm, although this only becomes noticeable for residual indentation depths inferior to 100 nm. Such a phenomenon does question the accuracy of hardness and modulus values calculated from such shallow indentations, but because of the iterative calibration procedure used for determining the indenter area function, this effect is taken into account for depths greater than 25 nm.

For the TiN coating in Fig. 51, the measured hardness and modulus are in fact composite values for the coating and Si substrate. Significant pile-up is evident around the imprint, possibly caused by delamination or cracking between the coating (thickness ~100 nm) and the substrate. The apparent irregularity in the unloading curve is characteristic of indentation into silicon and is often referred to as a *pop-in*. This effect is discussed later in more detail, but for the case of coated Si, is a good indication that the substrate is making a substantial contribution to the indentation properties. Another such example is shown in Fig. 52 for a Si substrate coated with a thin film (120 nm) of polymethyl methacrylate (PMMA). In this case the soft polymeric coating has been pushed away from the indenter causing large pile-up, but has made virtually no contribution to the measured hardness value, this being only slightly lower than the literature value for [100] silicon.

The indentation on glass in Fig. 52 shows the characteristic sink-in and concave imprint edges often found in ceramic materials. Fig. 53 shows examples of multicycle indentations on both glass and sapphire materials, where four cycles to 90% unload have been completed after initial loading to a maximum of 100 mN. Both materials show large amounts of elastic recovery during unloading and the multicycle curves confirm that the unloading and reloading cycles are nearly the same. This behaviour is often observed in ceramic materials, such low hysteresis and good reversibility suggesting that deformation in these materials is almost entirely elastic after initial

loading. This is somewhat surprising for brittle materials which are naturally susceptible to cracking under load. However, it is probable that any cracks created during initial loading are not able to propagate during successive unloading and reloading cycles and thus the material withstands these cycles without any sign of energy dissipation via further cracking. The indentation data for monocrystalline titanium carbide (Fig. 59) further confirms such observations.

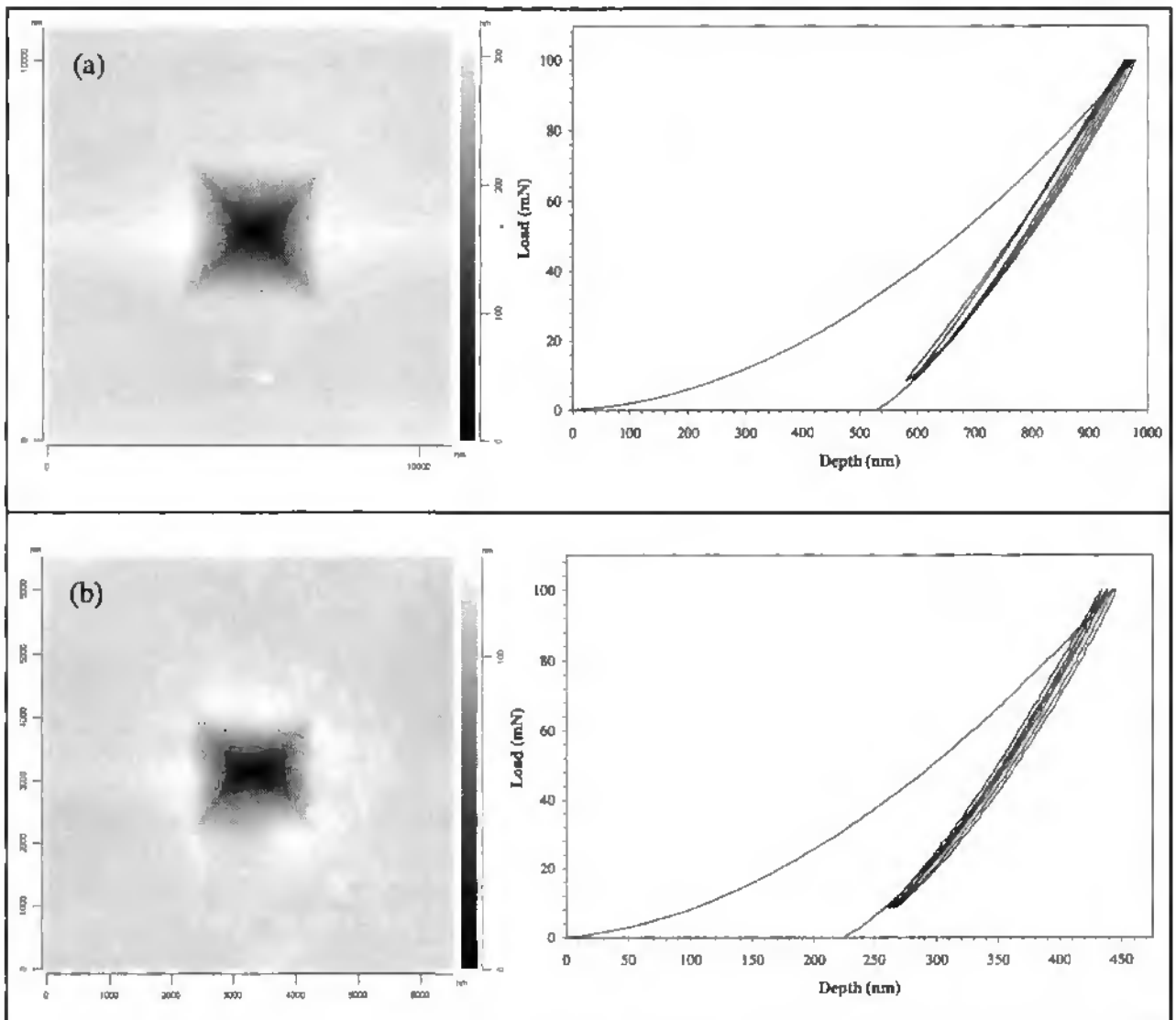


Figure 53 : Multicycle Vickers indentation data for glass (a) and sapphire (b). In both cases a maximum load of 100 mN has been followed by unloading down to 90% and reloading to 100 mN. This cycle is repeated four times before finally unloading completely.

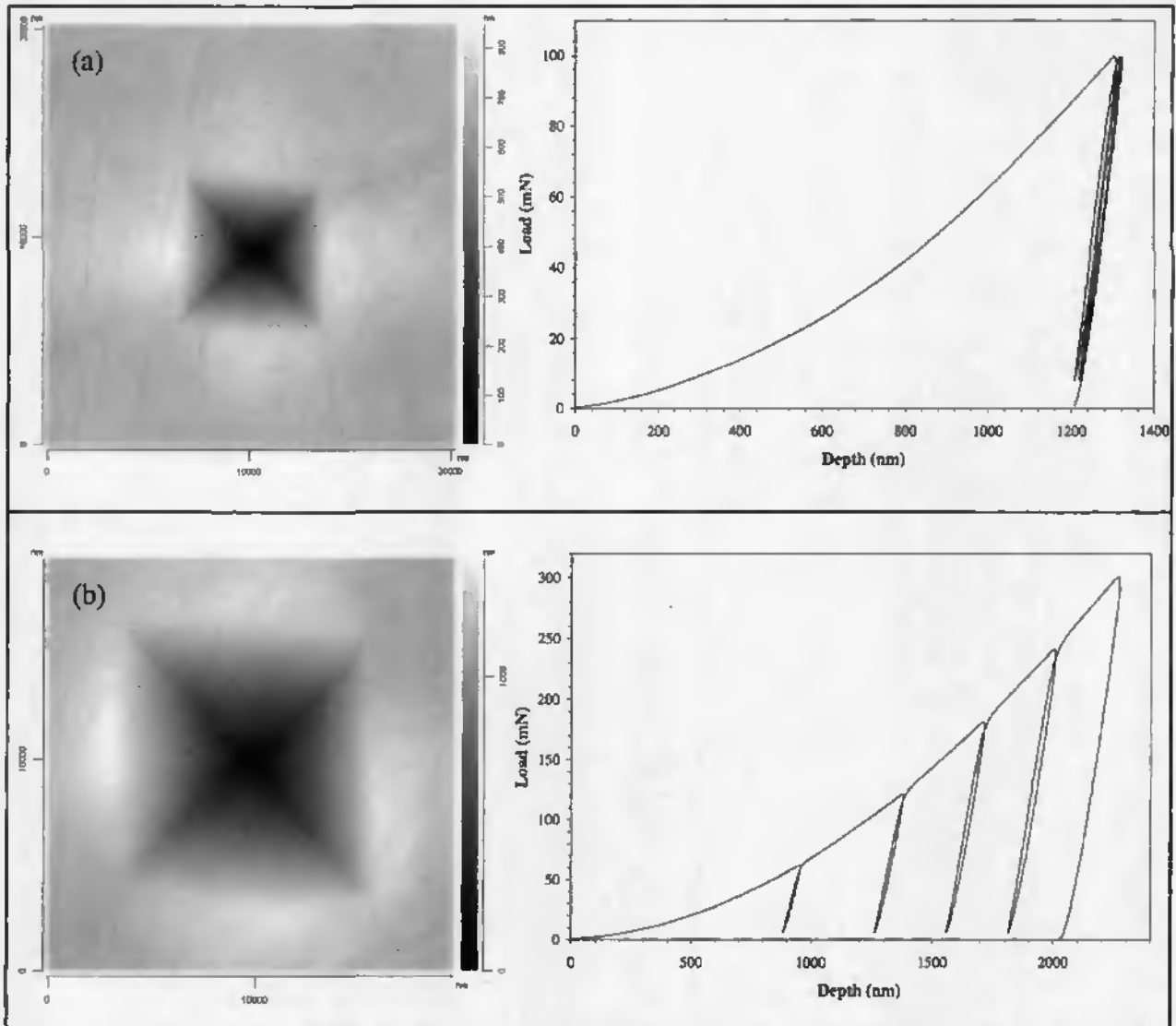


Figure 54 : Multicycle Vickers indentation data for tantalum. A series of four cycles from max. load (100 mN) down to 90% unload are shown in (a), whereas (b) shows four cycles to 90% unload but with a 60 mN load increase after every cycle.

For most metals the measured hardness is relatively small compared to the elastic modulus ; most of the indenter displacement is accommodated plastically, and only a small portion is recovered during unloading. Fig. 54 (a) shows that for such metals (in this case tantalum) the peak load displacements shift to higher values during successive cycles at the same maximum load. If the load is increased after each cycle (Fig. 54 (b)), distinct hysteresis loops are observed whose widths increase with applied load and which suggest a small but increasing amount of reverse plasticity upon each loading cycle.

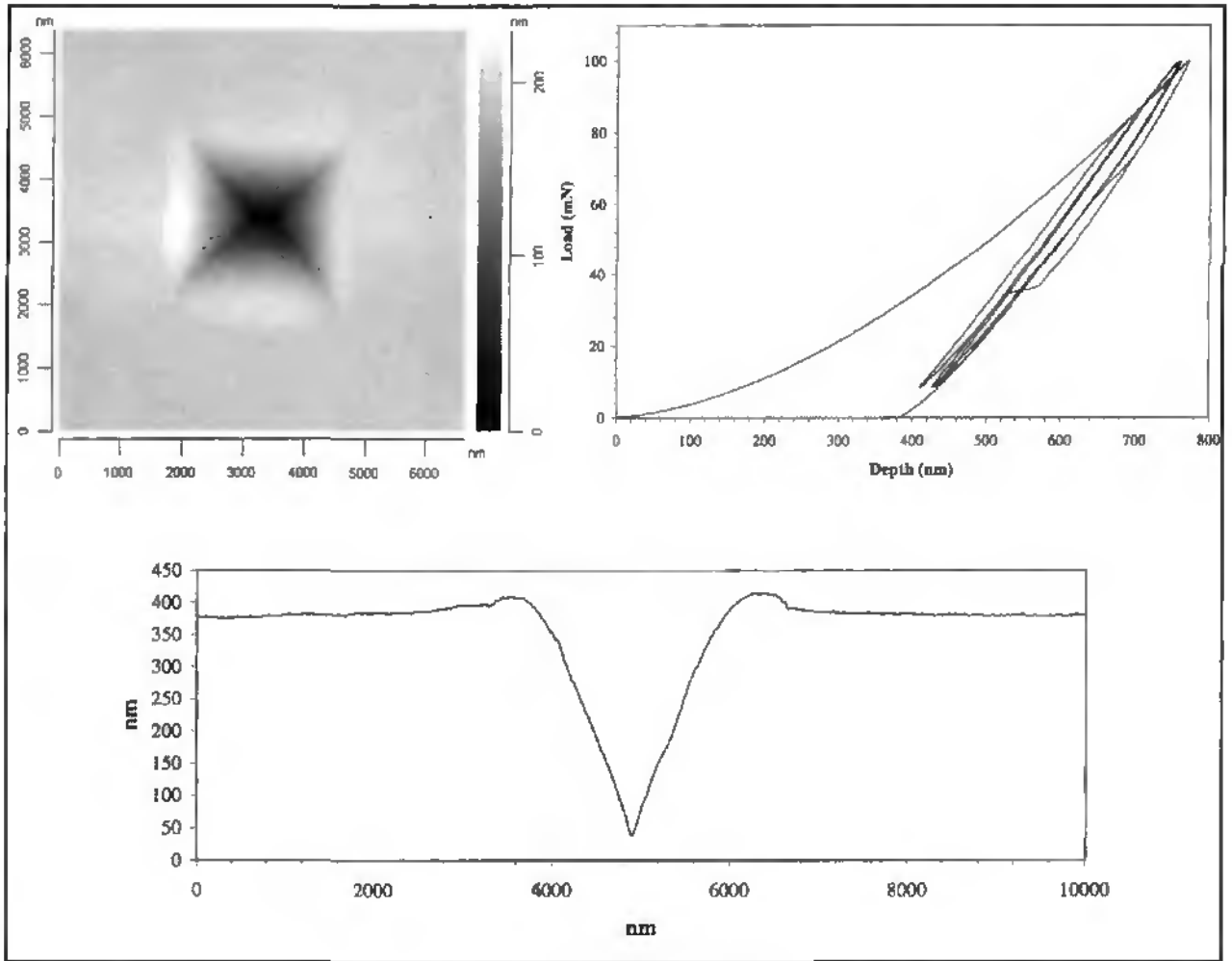


Figure 55 : Multicycle Vickers indentation data for a [100] silicon wafer (p-type) for a series of four cycles from max. load (100 mN) down to 90% unload, together with cross-sectional profile through the imaged residual imprint.

Silicon exhibits a rather unique behaviour when indented with a sharp indenter, this being characterised by a distinct discontinuity or pop-in during unloading as mentioned previously. Fig. 55 shows this effect during the first unloading portion of a fourfold multicycle. Subsequent cycles have a relatively large hysteresis suggesting that deformation is not entirely elastic. Such a phenomenon is observed in each of the [100], [110] and [111] orientations and has been widely published^{2, 32, 92, 102}. The load below which the pop-in disappears is generally in the range 5-20 mN and the hysteresis is thought to be due to a pressure-induced phase transformation from the normal diamond cubic form to a denser β -tin structure. Fig. 56 (a) shows the radial cracking which occurs at high loads (generally > 200 mN), whereas Fig. 56 (b) shows the drastic effects of

increasing the load in 75 mN steps over four load-unload cycles. The cross-sectional profiles (Fig. 56 (c) and (d)) confirm the substantial uplift of material around the residual imprint as a result of lateral cracking below the indenter, in addition to the radial cracks propagating away from the corners of the imprint. In contrast to normal metals, the energy absorbed by silicon is significant on each cycle and obviously contributes actively to the observed cracking; for example, in Fig. 56 the maximum load in (b) is 50 mN less than that attained in (a) but the SFM images show greater cracking in the former than in the latter.

Fused silica is a member of the silicon family which exhibits a very large elastic recovery during unloading, as depicted in the load-displacement curves of Fig. 57. For relatively low loads, in this case 30 mN, the residual imprint has quite an unusual appearance suggesting that the sides of the indentation are elastically recovered during unloading, whilst the corners are not. With a Berkovich indenter, additional plasticity may well be caused by the stress concentration at its edges, meaning that the indenter is able to permanently mark the position of the corners of the indentation at maximum load. If the applied load is increased tenfold to 300 mN, as shown in Fig. 57 (b), the load-displacement curve has the same shape and the calculated hardness and modulus are the same as for a low load indentation. However, the SFM images and their respective cross-sectional profiles show that the residual imprint is quite different at high applied loads; subsurface median and lateral cracking has caused uplift of the sides of the imprint and a large flake of material is also visible at one corner of the indentation. This characteristic material response is highly reproducible and such large flakes of uplifted material are always found over a corner, indicating that lateral crack propagation is obviously higher at zones where stress concentrations are high.

Fig. 58 shows Berkovich indentation data for monocrystalline tungsten where the material response is again different depending on the applied load. It has already been shown that both the hardness and modulus of tungsten increase as the load is decreased⁹⁹ and that at very small loads (< 1 mN) the behaviour is almost perfectly elastic, after which a yield point is observed corresponding to the onset of plasticity, and a permanent residual impression is formed³². It is interesting to note that at a relatively low peak load of 5 mN (Fig. 58 (a)), significant pile-up is visible around the residual imprint, whereas at a much higher peak load of 100 mN, pile-up is negligible (Fig. 58 (b)). This would indeed suggest that tungsten has properties in the near-surface region which are different to those of the bulk, probably due to a surface oxide layer.

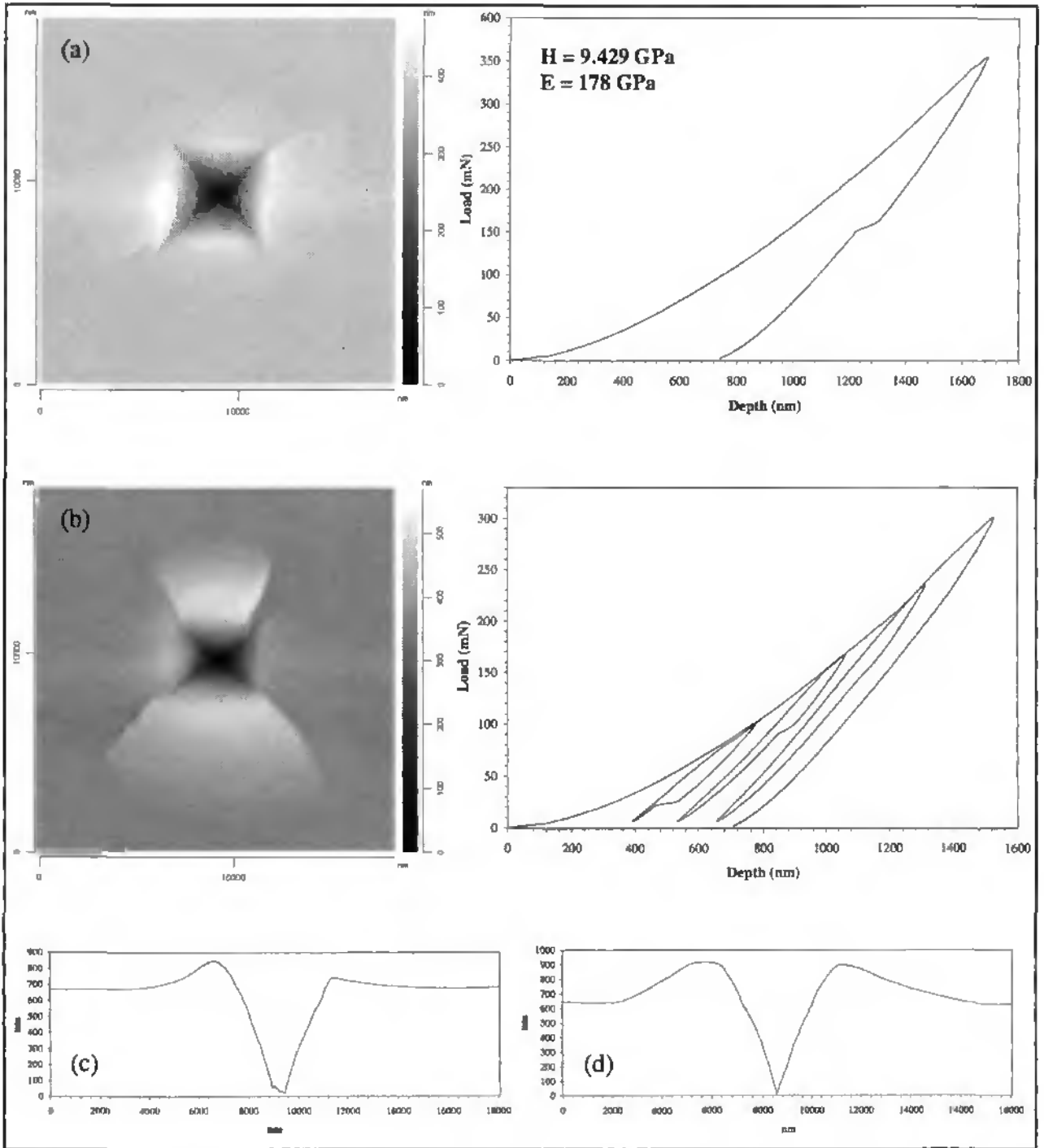


Figure 56 : Vickers indentation data for a [100] silicon wafer (p-type). Example (a) shows the cracking which occurs at opposite edges of the indenter after a monocycle up to 350 mN, whereas (b) shows the drastic effects on the residual imprint after four cycles to 97% unload with a 75 mN load increase after every cycle. The profiles (c) and (d) represent horizontal and vertical cross-sections, respectively, through the SFM image in (b).

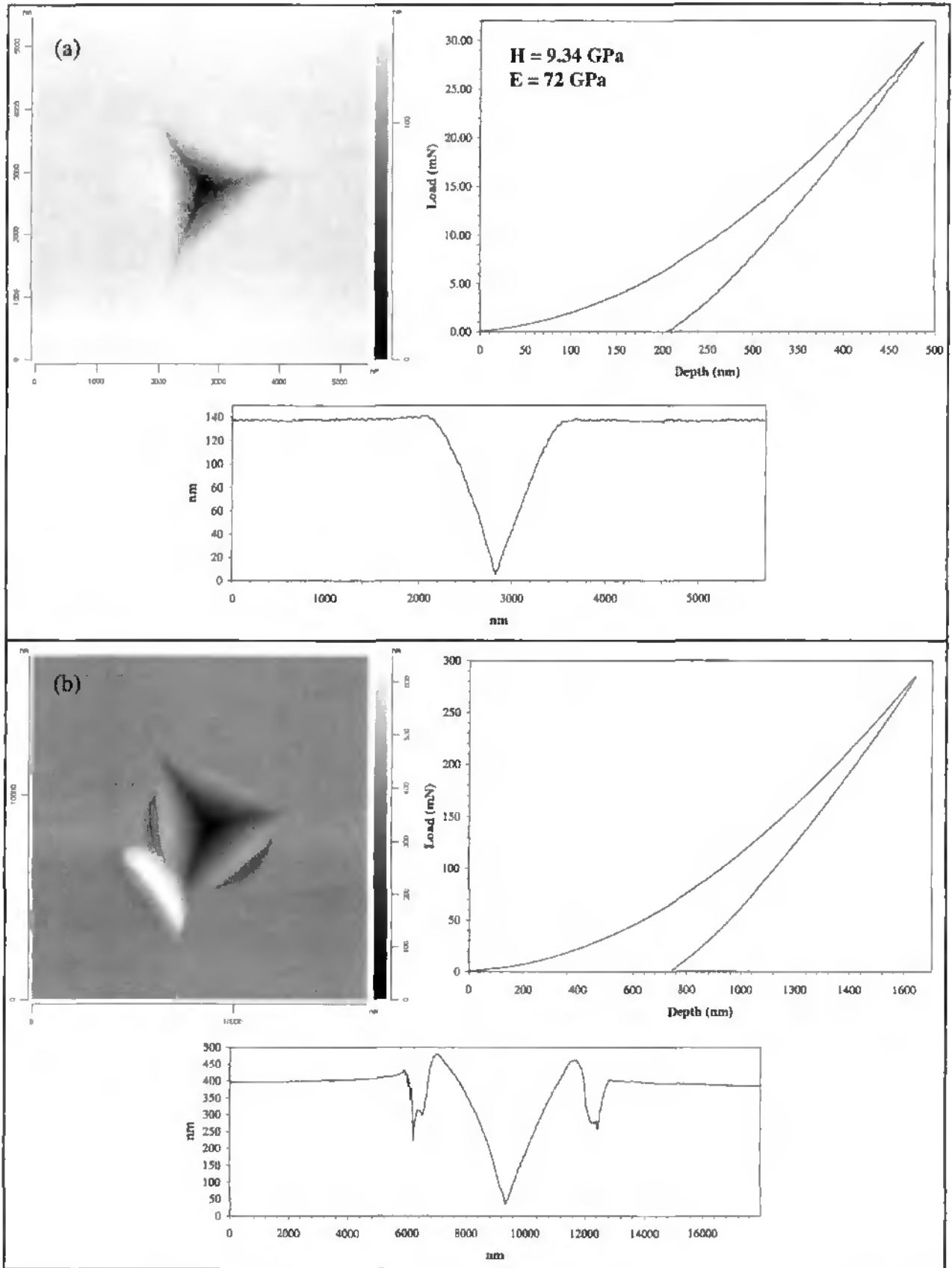


Figure 57 : Berkovich indentation data for fused silica showing the low load regime (max. load 30 mN) (a) and the cracking effect at high loads (max. load 300 mN) (b).

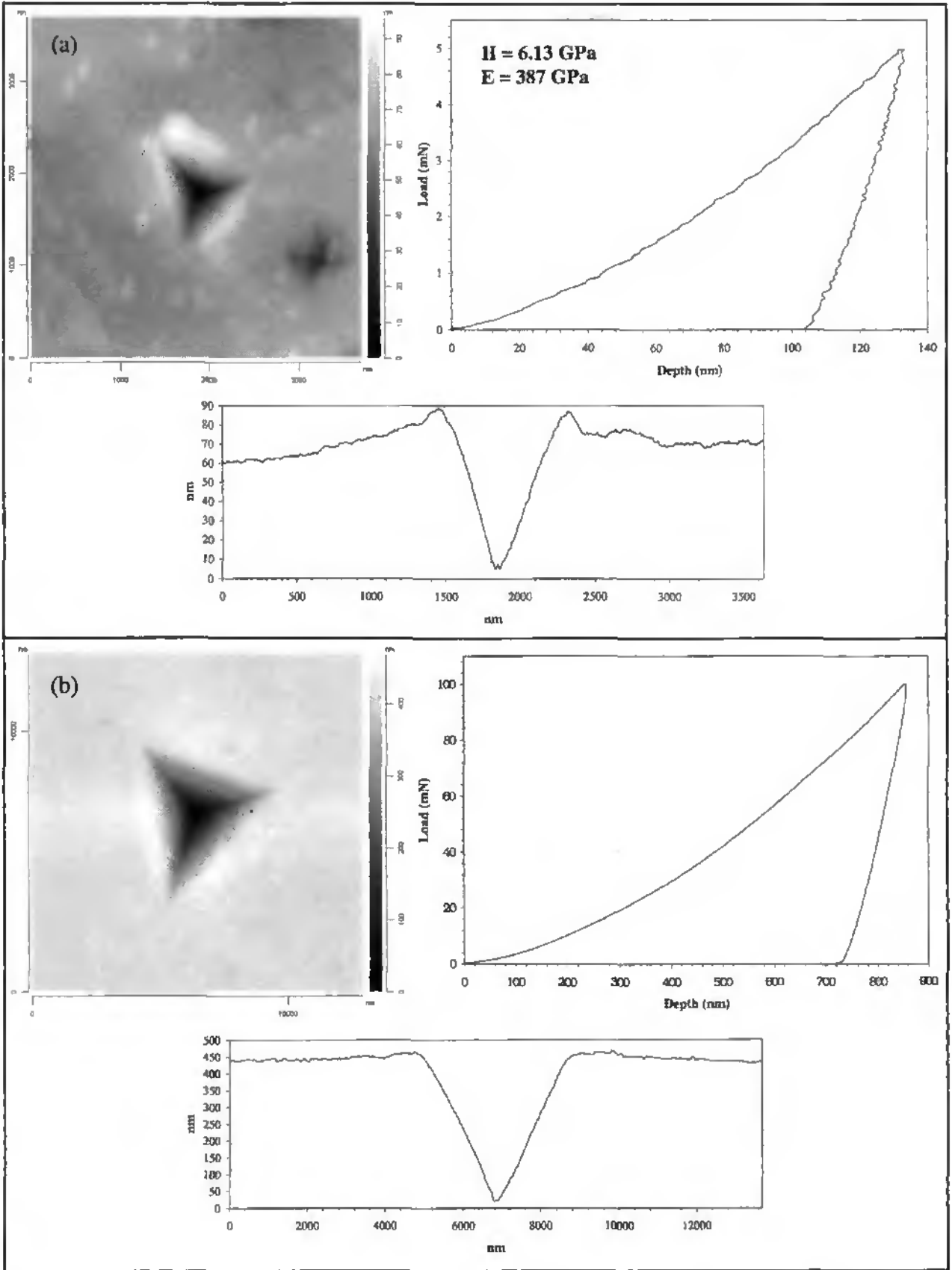


Figure 58 : Berkovich indentation data for tungsten (monocrystalline); pile-up at low loads (max. load 5 mN) (a) is much greater than at high loads (max. load 100 mN) (b).

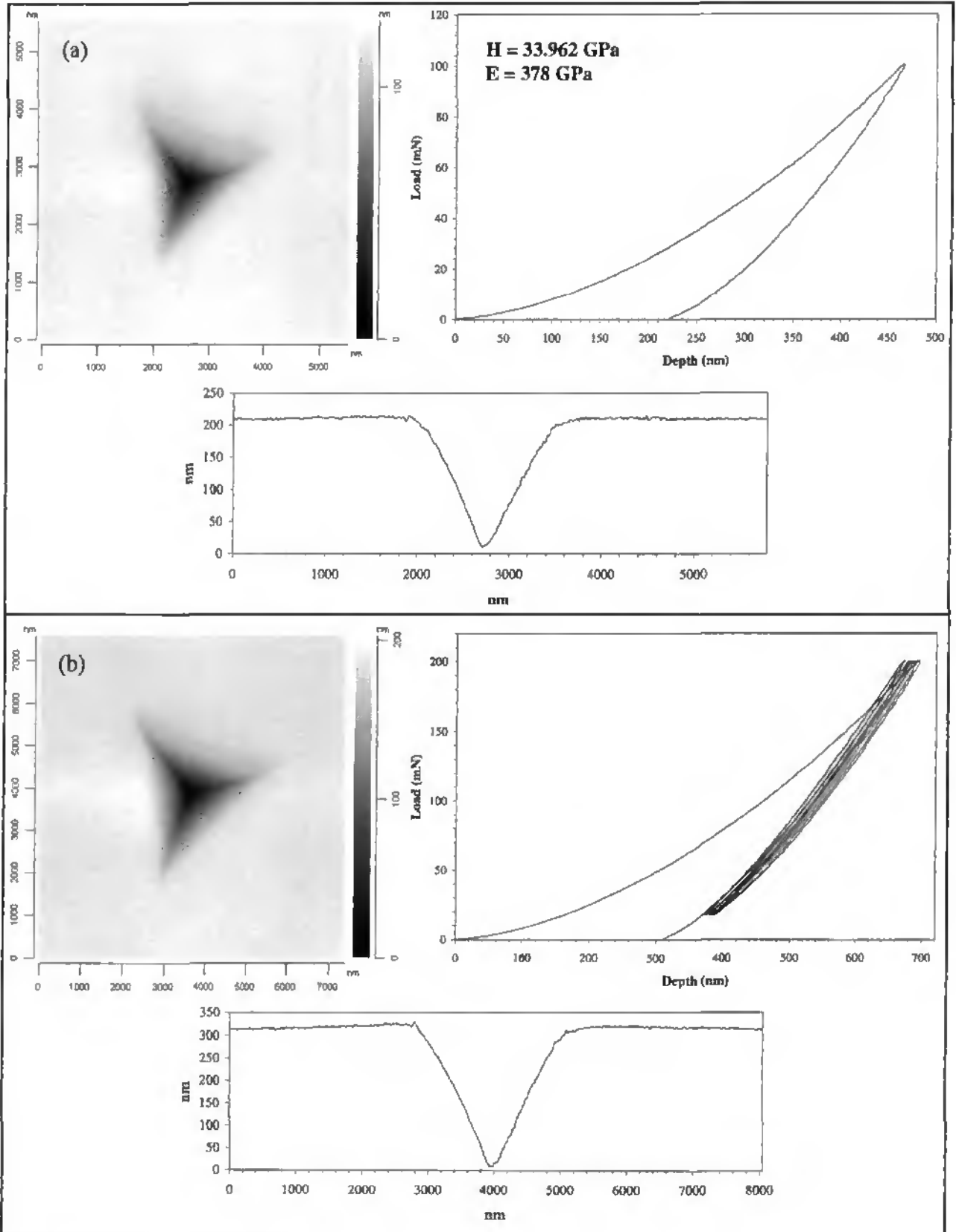


Figure 59 : Berkovich indentation data for titanium carbide (monocrystalline) showing a single cycle (a) and a fivefold multicycle to 90% unload (b).

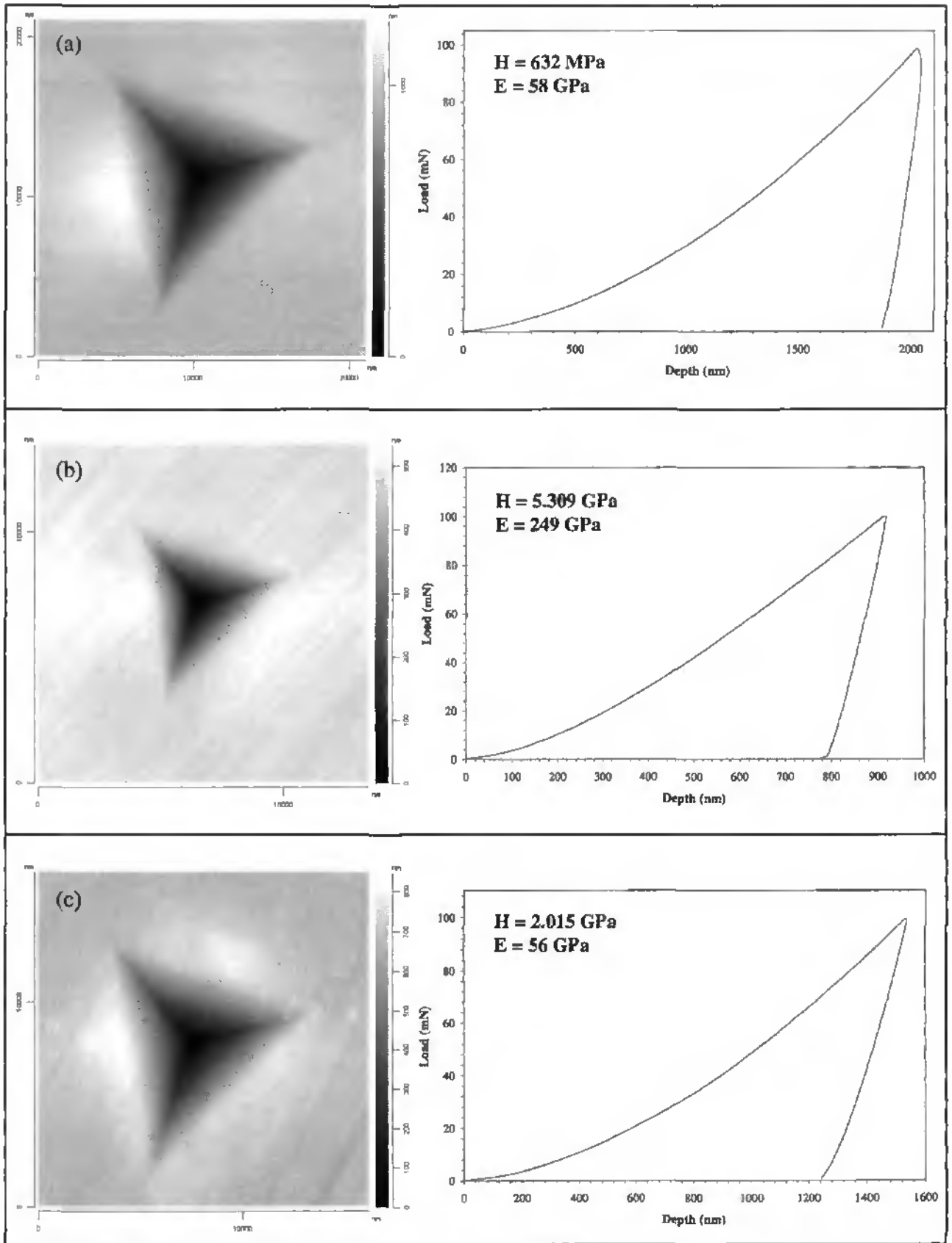


Figure 60 : Berkovich indentation data for antimony (a), rhodium (b) and yttrium (c). The maximum applied load in each case is 100 mN.

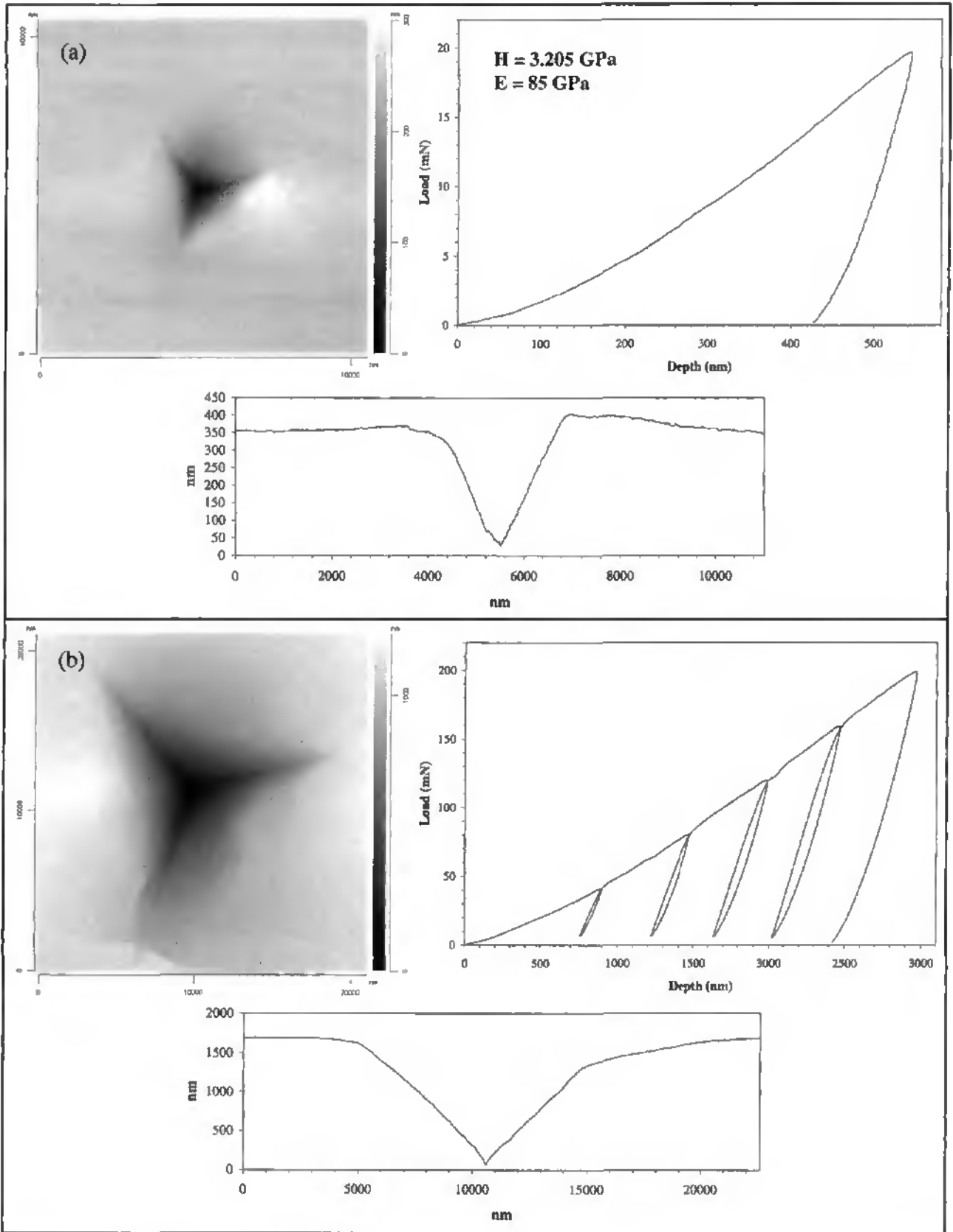


Figure 61 : Berkovich indentation data for cobalt. A monocycle to 20 mN is shown in (a), whereas (b) shows 4 cycles to 95% unload with a 40 mN increase on every cycle.

Indentation data for some less common metals are summarised in Figs. 60, namely antimony, rhodium and yttrium. All three show properties characteristic of work-hardenable metals where pile-up is evident around the residual imprint. Some results for cobalt are presented in Fig. 61, this being a hard and brittle metal which readily cracks when locally compressed. The cross-sectional profiles show the sink-in and uplift of material which occurs around the indenter, and the multicycle force-displacement curve shows significant hysteresis on each unload-reload cycle.

For coated systems, the NHT with integrated SFM is ideal for mapping the material response as a function of indentation depth. The net hardness of a composite coating-substrate system is a complicated function of the coating thickness, coating hardness, substrate hardness and the adhesion between the coating and the substrate. Much of the previous work in this domain, using standard indentation techniques, has failed to accurately differentiate between the effects of all such parameters. In addition, for soft coatings on a hard substrate, there is a tendency for material to pile-up around the residual imprint to a much greater degree than it would in a bulk material. This is due to the severe constraint imposed on plastic deformation in the film by the relatively undeformable substrate. Since present methods of analysing nanoindentation load-displacement curves do not account for the extra contact area produced by the pile-up, the enhancement of pile-up in soft films on hard substrates has important consequences for the measurement of mechanical properties by such methods.

Results are presented for three common coatings sputtered onto a Si [100] substrate, namely gold, aluminium and titanium, having thicknesses of 100 nm, 300 nm and 200 nm respectively. In all three cases, a series of indentations has been made at maximum depths (h_{max}) varying over the range 25 – 1200 nm. This corresponds to the maximum range of depths over which the NHT can measure in its present configuration for the specified samples. The residual imprint at each depth has been directly imaged with the SFM, allowing the cross-sectional profiles at each depth to be plotted and the effects of pile-up investigated. In addition, the evolution of hardness and modulus has been plotted as a function of the maximum penetration depth, h_{max} , normalised with respect to the film thickness, t_f . If it is considered that the substrate begins to affect the indentation behaviour of the coating when $h_{max}/t_f > 0.1$, then clearly all the measurements made are influenced, in varying degrees, by the Si substrate.

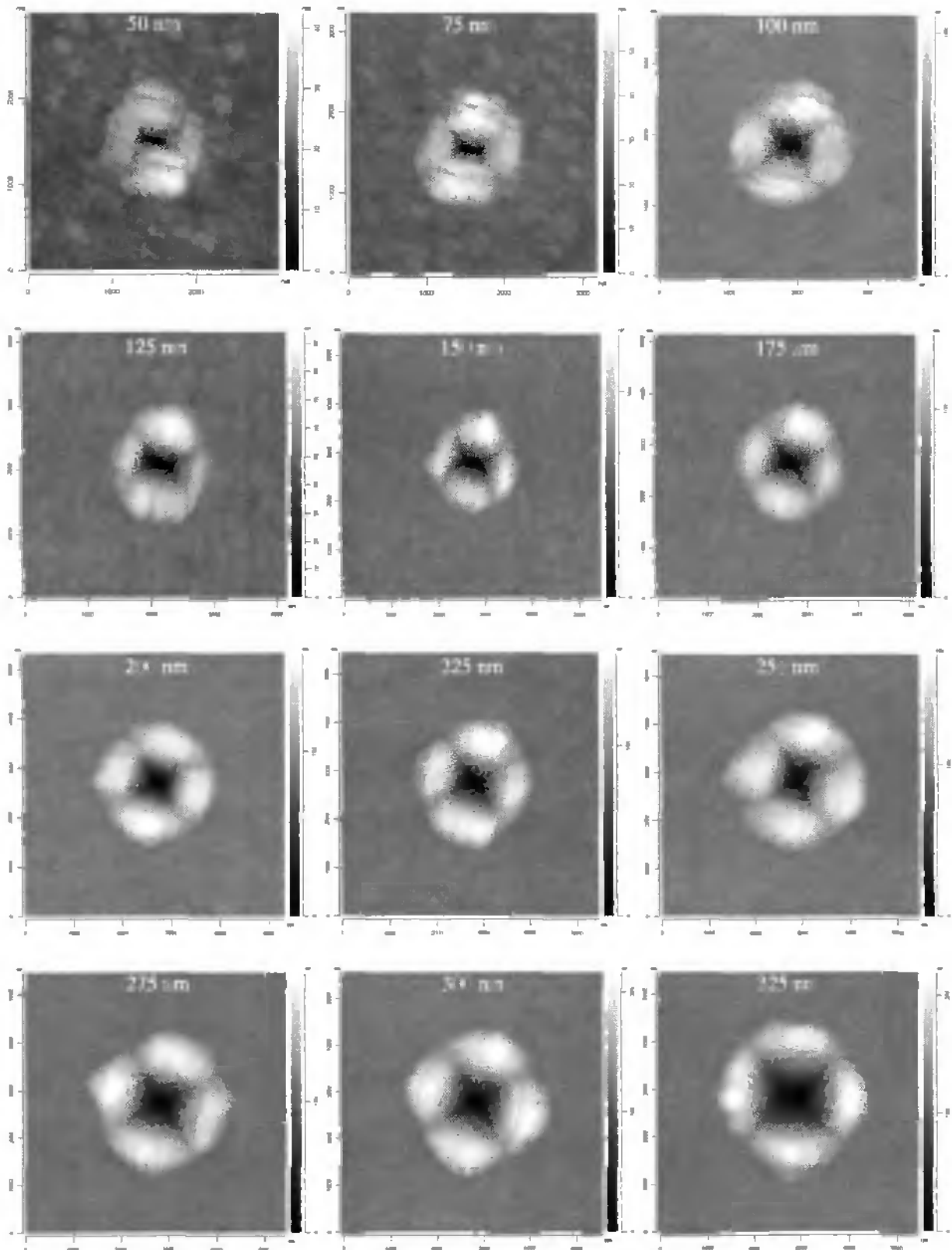


Figure 62 : Series of SFM images of residual imprints for depths (h_{max}) from 50 nm up to 325 nm. The sample is a gold film (thickness = 100 nm) sputtered onto a Si [100] substrate. Note the evolution of pile-up with increasing depth.

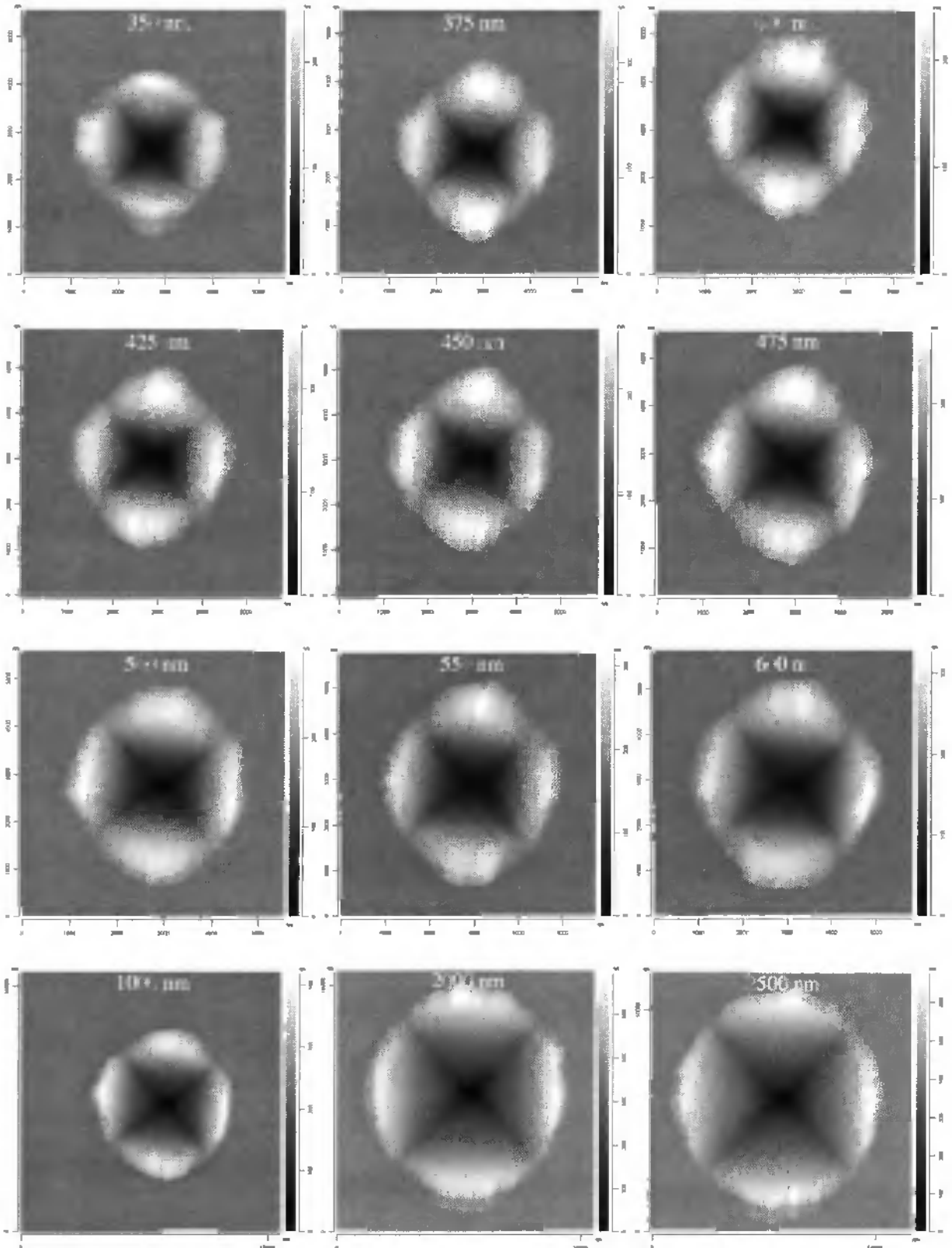


Figure 63 : Series of SFM images of residual imprints for depths (h_{max}) from 350 nm up to 2500 nm. The sample is a gold film (thickness = 100 nm) sputtered onto a Si [100] substrate. Note the evolution of pile-up with increasing depth.

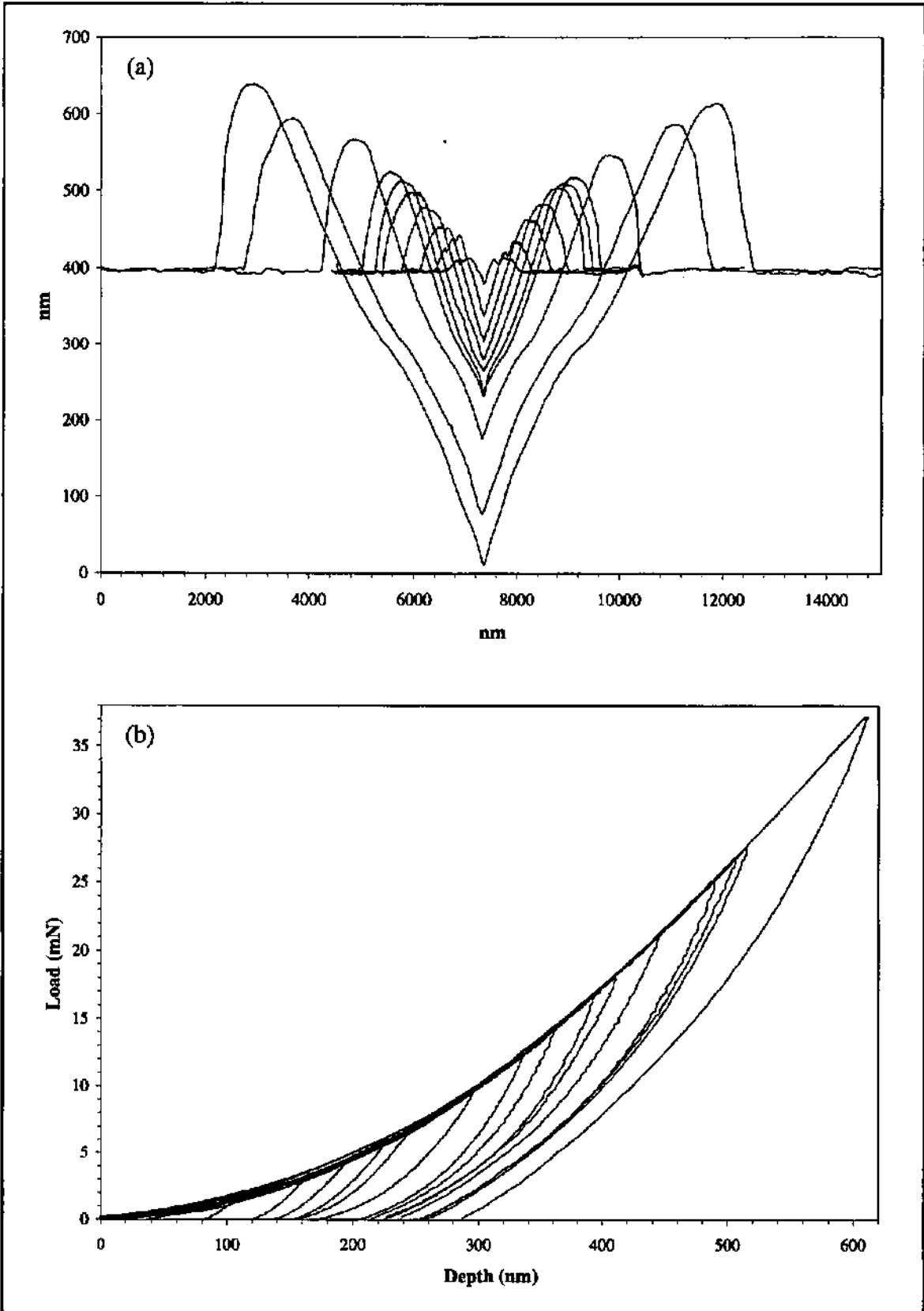


Figure 64 : A selection of cross-sectional profiles corresponding to images in Figs 62-63 are plotted together in (a), whereas (b) shows the evolution of the load-depth curves.

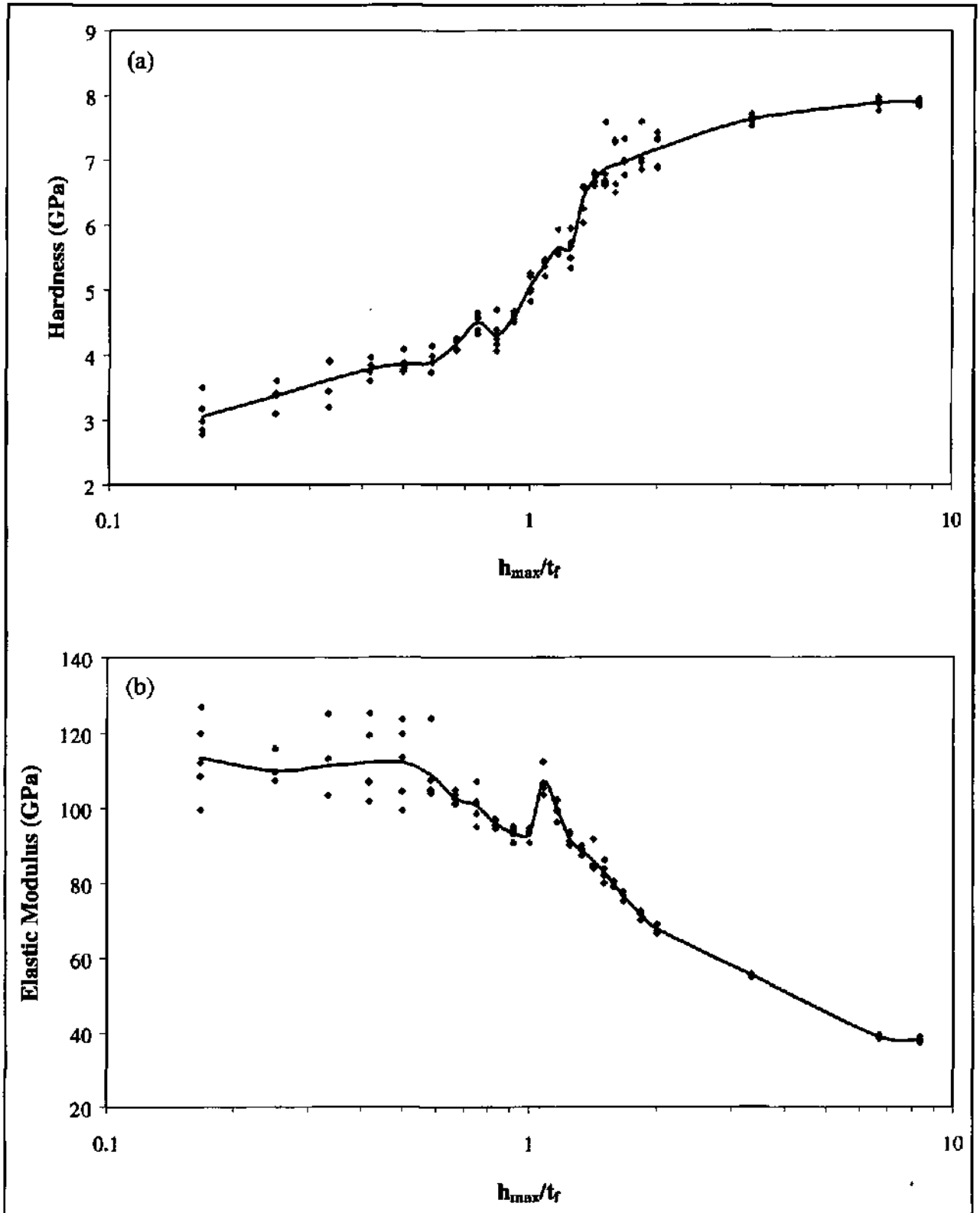


Figure 65 : The variation of hardness (a) and elastic modulus (b) are plotted as a function of the normalised depth (h_{max}/t_f) for a gold film (thickness = 100 nm) sputtered onto a Si [100] substrate.

The results for the gold-on-Si composite system are summarised in Figs. 62-65. This was the only coating-substrate combination measured with a Vickers indenter and at very low depths (50 – 75 nm) the non-symmetrical tip defect is evident in the SFM images (Fig. 62), causing more material to be pushed away from the longer edges of the indenter tip. As h_{max} is increased, the pile-up behaviour is seen to depend on the depth of the indentation relative to the film thickness and the amount of pile-up can be significant at certain depths. At small depths, material is pushed to the sides of the indenter tip giving the residual imprint a rectangular shape owing to the aforementioned tip defect. At higher depths, at and above the film thickness (i.e., $h_{max}/t_f \geq 1$), the amount of pile-up is very large relative to the indented area and gives the residual imprint a circular appearance even though it has been made with a square pyramid. For depths much greater than the film thickness (e.g., indent for $h_{max} = 2500$ nm in Fig. 63), the relative amount of pile-up is significantly smaller because a greater portion of the deformed volume is in the harder Si substrate. This evolution of pile-up with penetration depth is represented in Fig. 64 (a) by plotting a selection of cross-sectional profiles through imaged imprints. At depths greater than the film thickness (in this case 100 nm), the transition between the coating and substrate is clearly visible, as is the elastic relaxation of the Si substrate which gives a bulge in the profile at the interface (this can be compared with the profile in Fig. 55 for uncoated silicon). The increasing influence of the substrate can also be seen in Fig. 64 (b) where the elastic component of the unloading curve becomes greater as the penetration depth increases.

The variation in hardness as a function of normalised depth is plotted in Fig. 65 (a) and correlates well with the expected behaviour of a soft coating on a hard substrate. At small depths, the hardness (although already a composite hardness of the coating-substrate system) tends toward a value < 3 GPa, this value approaching that of the sputtered gold coating (< 1 GPa). At larger depths the hardness increases rapidly and tends toward that of the substrate (~ 9 GPa), the steepest increase being at depths close to the film thickness. The elastic modulus (Fig. 65 (b)) is seen to decrease from approximately 110 GPa to 40 GPa, with a slight increase around the film thickness, after which it falls off rapidly. From previous measurements on bulk gold (e.g. Fig. 49) a value of 110 GPa would seem reasonable for the elastic modulus at small depths where the substrate influence is at its lowest. However, the measured modulus for Si is 170 GPa, indicating that the plotted modulus ought to increase, especially for depths where $h_{max}/t_f > 1$.

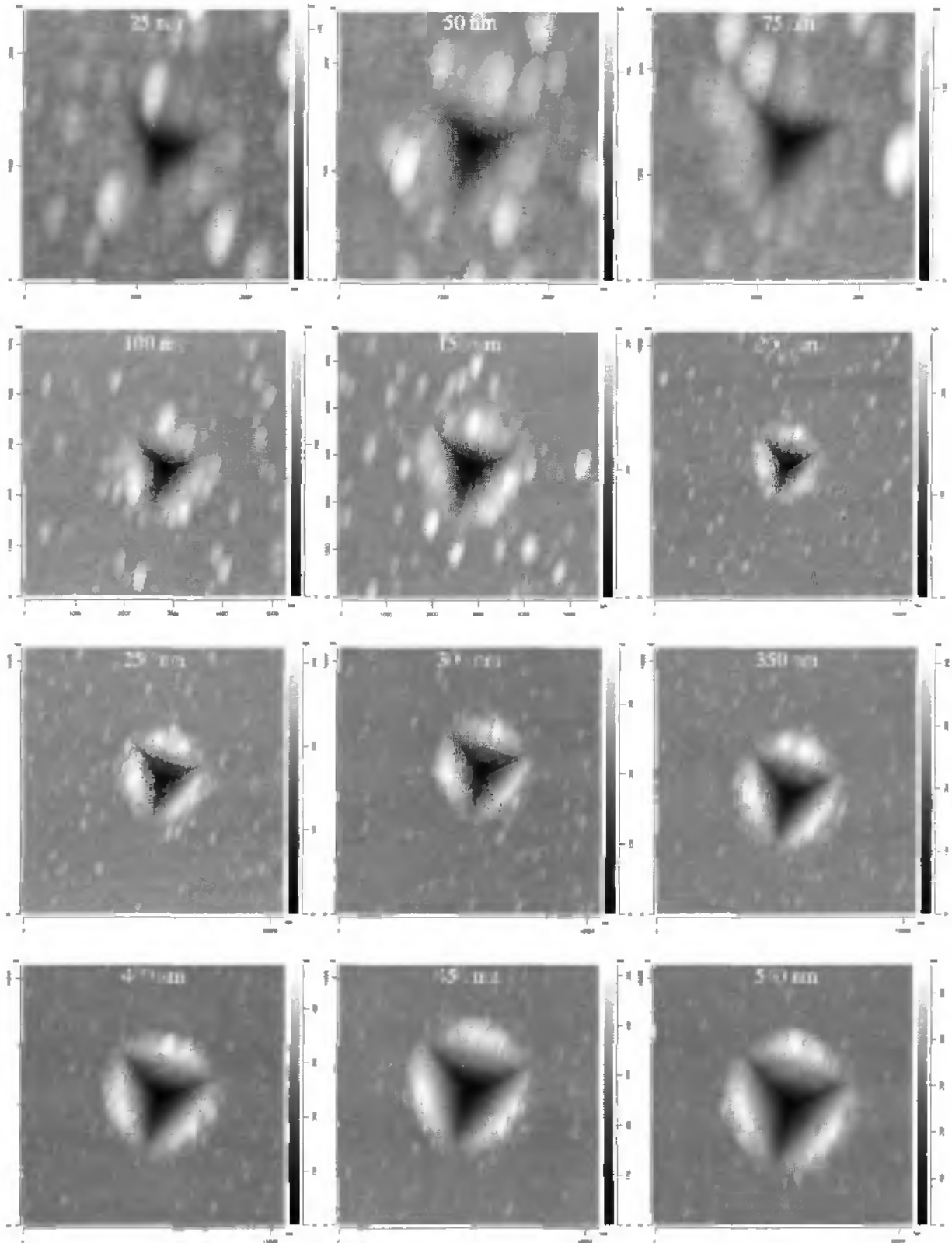


Figure 66 : Series of SFM images of residual imprints for depths (h_{max}) from 25 nm up to 500 nm. The sample is an aluminium film (thickness = 300 nm) sputtered onto a Si {100} substrate. Note the evolution of pile-up with increasing depth.

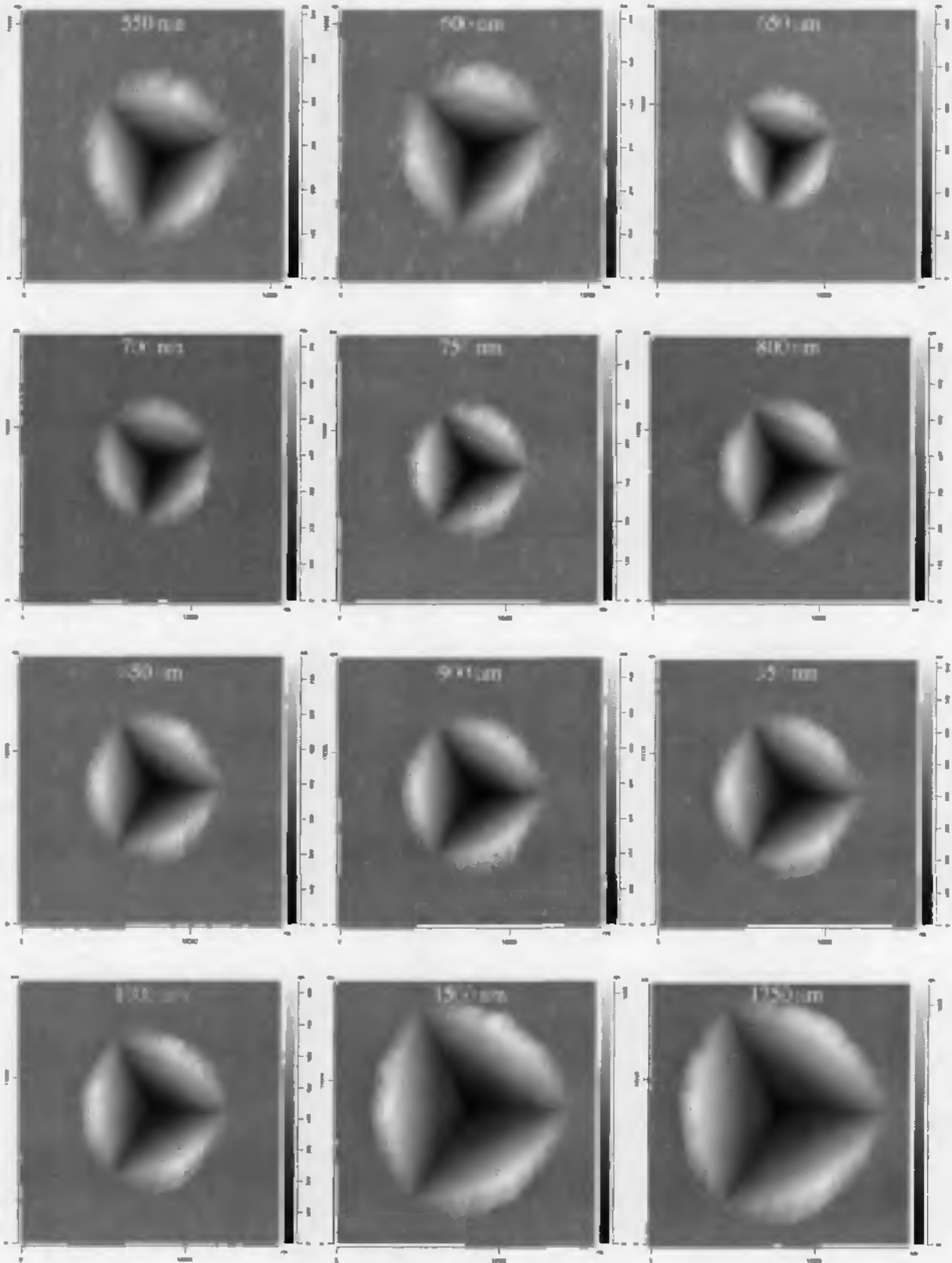


Figure 67 : Series of SFM images of residual imprints for depths (h_{max}) from 550 nm up to 1750 nm. The sample is an aluminium film (thickness = 300 nm) sputtered onto a Si [100] substrate. Note the evolution of pile-up with increasing depth.

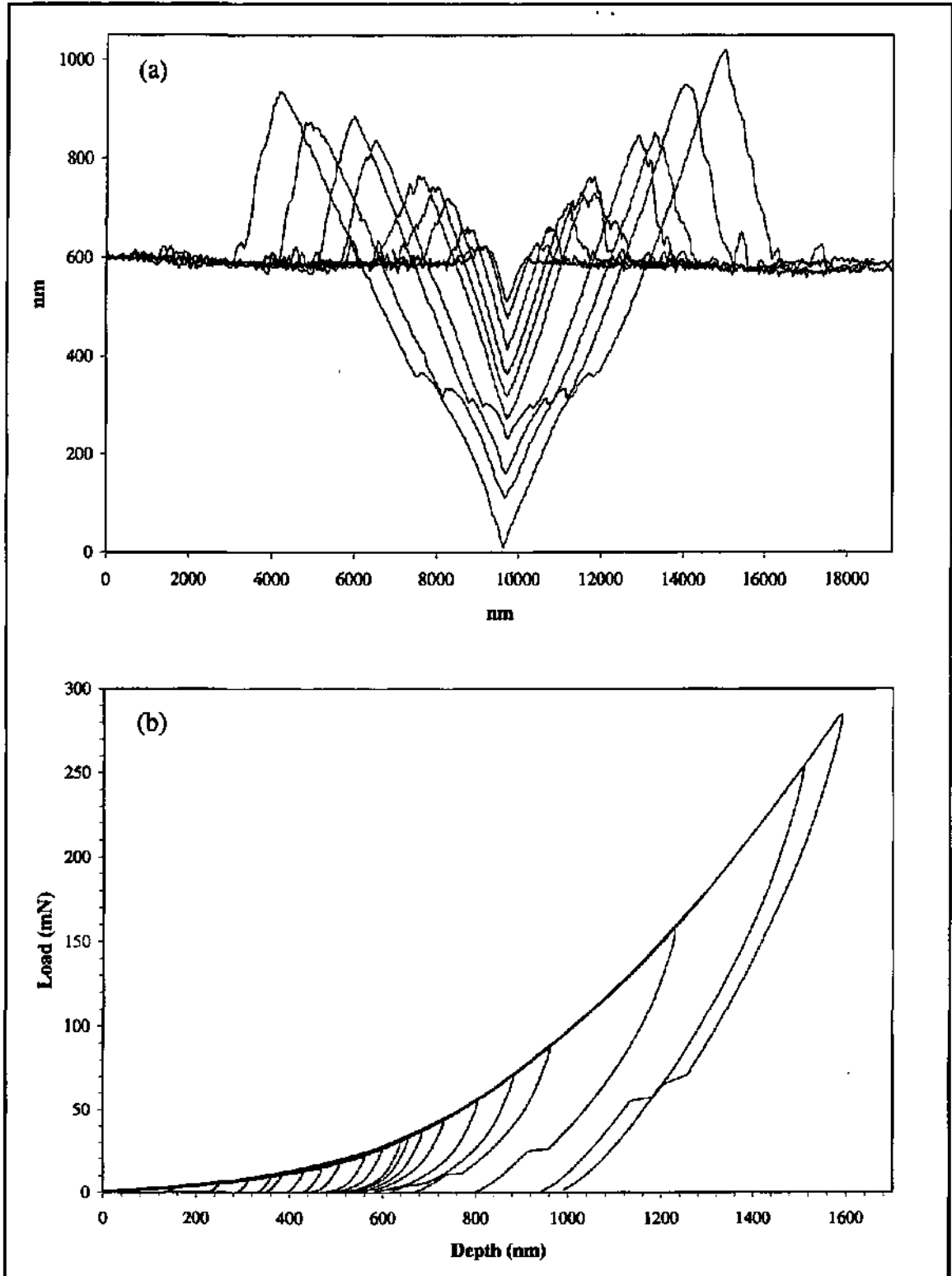


Figure 68 : A selection of cross-sectional profiles corresponding to images in Figs 66-67 are plotted together in (a), whereas (b) shows the evolution of the load-depth curves. The increasing influence of the Si substrate is evident for maximum penetration depths exceeding the aluminium film thickness (300 nm).

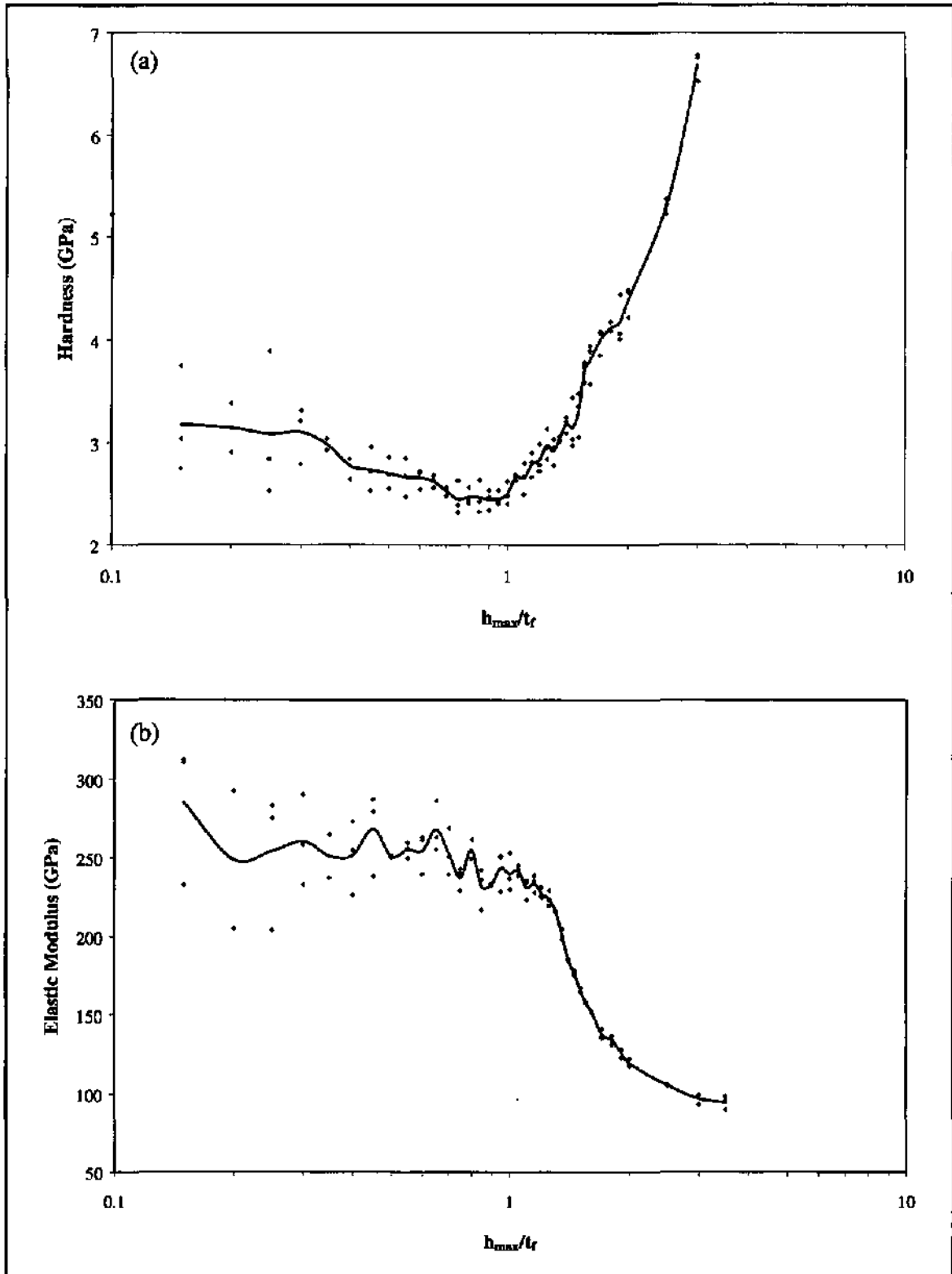


Figure 69 : The variation of hardness (a) and elastic modulus (b) are plotted as a function of normalised depth (h_{max}/t_f) for an aluminium film (thickness = 300 nm) sputtered onto a Si [100] substrate.

Some previous work⁸² has already shown that the elastic modulus is often significantly underestimated for soft coatings on hard substrates; during unloading, the Si substrate experiences a much greater elastic recovery than the gold coating. Thus, during unloading, the recovered displacement is significantly different in the lower portion of the unloading curve, i.e., after contact with the Si is lost. This produces a bend in the curve and changes its shape such that the assumed power-law fitting relation no longer fits correctly. The resultant effect is that the unloading stiffness derived from the power-law fit is underestimated, which translates to an underestimation of the elastic modulus. This is evidently the case for the unloading portions of the curves shown in Fig. 64 (b).

The results for the aluminium-on-Si composite system are summarised in Figs. 66-69, for which a Berkovich indenter was used in preference to a Vickers. The SFM images show that very little pile-up is evident at low depths, this being characteristic of sputtered aluminium. For depths where $h_{max}/t_f > 0.1$, the amount of pile-up around the residual imprint increases gradually, producing a circular shaped imprint. The evolution of cross-sectional profiles is summarised in Fig. 68 (a) and it is interesting to note the variation in residual depth for the Si substrate below the surface, depending on the value of h_{max} . At the greatest depths, the observed transition between the Al film and its substrate is nearer to the surface owing to the increased elastic relaxation of the latter upon unloading. This is an important factor which should always be considered when estimating the thickness of a coating from the profile of a residual indentation, especially for the case of substrate materials which exhibit large elastic recovery. For the case considered, an estimate of the film thickness from the deepest profile would suggest a value of approximately 220 nm when in reality the thickness is accurately known (from the deposition rate) to be 300 nm.

The variation in hardness as a function of normalised depth is plotted in Fig. 69 (a) and shows a very steep increase, tending toward that of Si, as soon as the indenter begins to penetrate the substrate. This would imply that the influence of the soft aluminium coating on the composite hardness value decreases very rapidly once $h_{max}/t_f > 1$. For $h_{max}/t_f < 1$, the hardness is seen to rise gradually as the value of h_{max}/t_f decreases and is significantly greater than the accepted value (< 1 GPa) for aluminium. This can be explained by the certain presence of a harder oxide layer near the surface of the aluminium, as well as the surface roughness being of the same magnitude as the indentation depth for $h_{max}/t_f < 0.4$ (also shown as greater dispersion in the experimental points at

such shallow depths). The variation in elastic modulus, shown in Fig. 69 (b), is, similarly to the previous gold-on-Si example, not as expected. A value of approximately 250 GPa is maintained up until the coating thickness, after which a rapid decrease is observed which tends toward a value of approximately 100 GPa. Considering that aluminium and silicon have respective moduli of 75 GPa and 170 GPa, the results would seem very confusing. The underestimate of modulus for $h_{max}/t_f > 1$ can, however, be accounted for by the unloading curves having a shape which does not fit accurately to the usual power law fit (as explained previously). This is evident from the curves in Fig. 68 (b), particularly for maximum penetration depths between 300 and 1000 nm. The overestimate of modulus for $h_{max}/t_f < 1$ is directly related to the pile-up behaviour, and at very shallow depths, to the certain presence of a surface oxide layer. Tsui *et al*⁸² have recently shown, for the aluminium-on-glass system, that an increase in contact area due to pile-up can underestimate the true contact area by as much as 80%, resulting in significant overestimation of the measured hardness and modulus. This theory would seem to hold well for the Al-on-Si system, judging by the substantial pile-up observed in the SFM images of residual imprints.

The results for the titanium-on-Si composite system are summarised in Figs. 70-73. As opposed to the aforementioned Au-on-Si and Al-on-Si systems, the plasma deposited titanium is in fact harder than the Si substrate, due to the high internal stresses produced as a result of deposition and the oxide film (usually TiO₂) which forms immediately on removal of the sample from the reactor. The SFM images (Figs. 70-71) clearly show the surface morphology and grain structure of the deposited coating. For the imaged indentation made with $h_{max} = 25$ nm, the residual imprint is barely visible and is of a similar magnitude as the surface roughness (~20 nm). As h_{max} is increased, no apparent pile-up effects are noticeable until the substrate is reached, suggesting that plastic flow is far more restricted than that of softer coatings. For depths where $h_{max} > 200$ nm (the film thickness), the amount of pile-up increases gradually but it can be observed that the surface morphology of the piled-up material remains the same as that surrounding it. This would suggest that, contrary to soft coatings where material is obviously pushed to the sides of the indenter, the material has undergone uplift due to substrate relaxation on unloading. This is further confirmed by the concave edges of the imprint.

The variation in hardness as a function of normalised depth is plotted in Fig. 73 (a) and shows a steep decrease from a value approaching 16 GPa at shallow depths, to approximately 11 GPa at the coating-substrate interface. For values of $h_{max}/t_f > 1$, the hardness decreases more gradually

down to a value of 9 GPa, this being the hardness of the substrate. The greater dispersion of experimental points at shallow depths can be attributed to surface roughness effects and the varying influence of the surface oxide layer, which, for such a thin film, may well extend a significant distance into the coating. The variation in elastic modulus, shown in Fig. 73 (b), descends from 270 GPa to 140 GPa, with no apparent discontinuity as a result of the coating-substrate interface. A slight underestimate of modulus is observed for $h_{max}/t_f > 1$ and this can be attributed, as before, to an artefact caused by the unloading curves not following a power law relationship all along their length. The evolution of cross-sectional profiles in Fig. 72 (a) shows the sudden increase in pile-up at depths close to the coating-substrate interface.

Having discussed three common coating-substrate systems, it is clear that their properties as measured by nanoindentation are a complex mixture of many factors. For hard-coated systems, the indentation response is characterised by the coating being bent and stretched as the substrate has yielded to accommodate the indenter displacements. The applied load is supported by a combination of elastic flexure of the coating, plastic yielding of the substrate and any internal stresses generated in the coating as it is deformed. The measured hardness value is therefore not an accurate measure of either of the phases present, and so should not be compared with the hardness of bulk solids, except when the properties are obviously those of one component of the system. For soft-coated systems, the indenter cuts through the softer surface layer and pushes it away from the indented area. For this process to occur, the coating must flow extensively and plastically under the shear component of the contact stress caused by the loaded indenter before any significant yielding of the substrate occurs. It is therefore of the utmost importance to establish the dominant deformation mechanism by directly imaging the indented area, as demonstrated here with a high resolution SFM.

Depending on the dominant deformation mechanisms, the substrate will always play some part in determining the contact response of a coated system, since it will react to any displacement of the coating lower surface (i.e., it will react as an elastic foundation of a particular stiffness, or a foundation which is flowing plastically and creating stresses in the coating by material movement, or, in the case of polymers, one which behaves viscoelastically). The precise isolation of properties which relate to the coating alone can only be realised if all of the discussed factors are considered and taken into account¹⁰³.

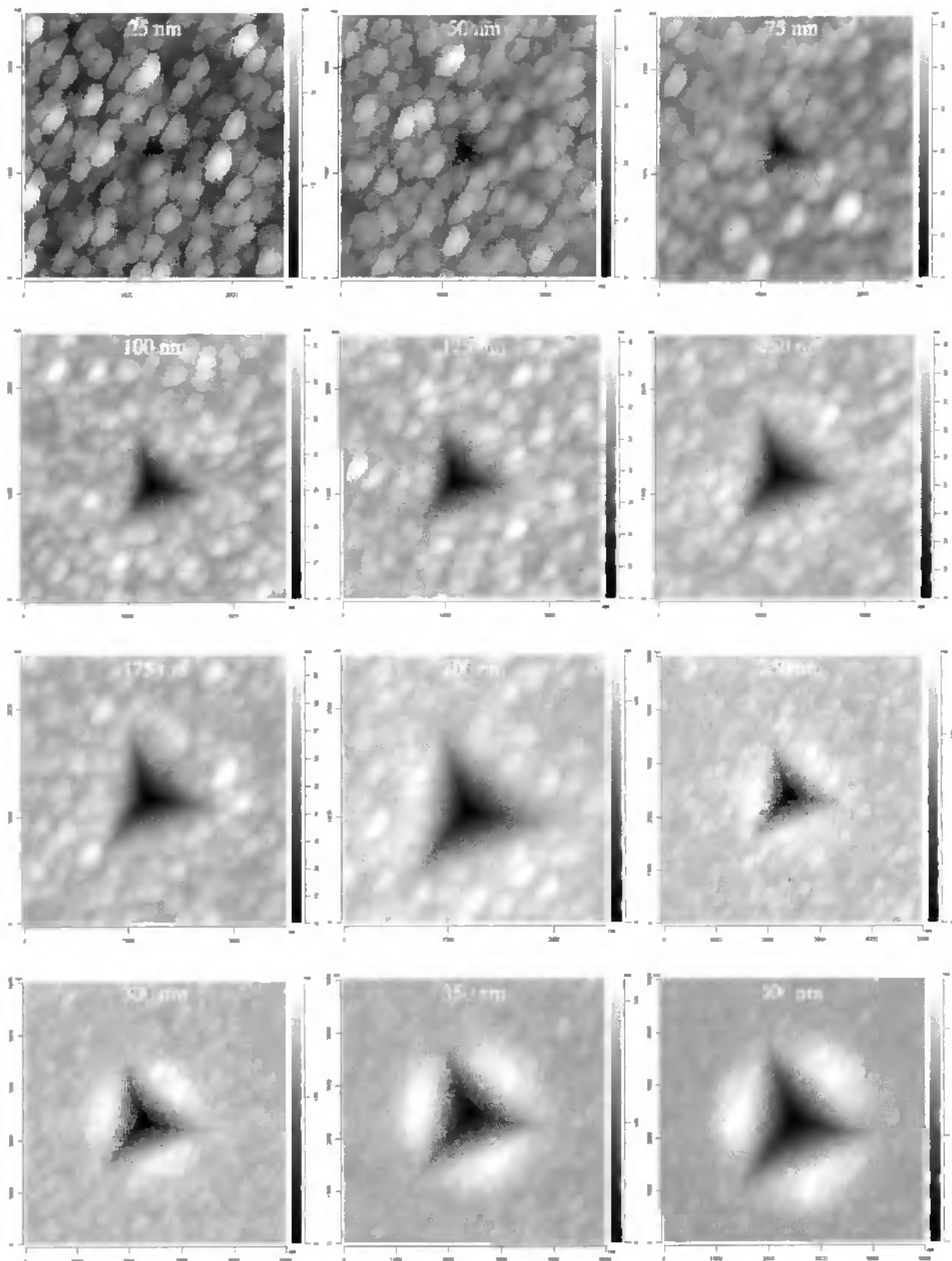


Figure 70 : Series of SFM images of residual imprints for depths (h_{max}) from 25 nm up to 400 nm. The sample is a titanium film (thickness = 200 nm) sputtered onto a Si [100] substrate. Note the evolution of pile-up with increasing depth.

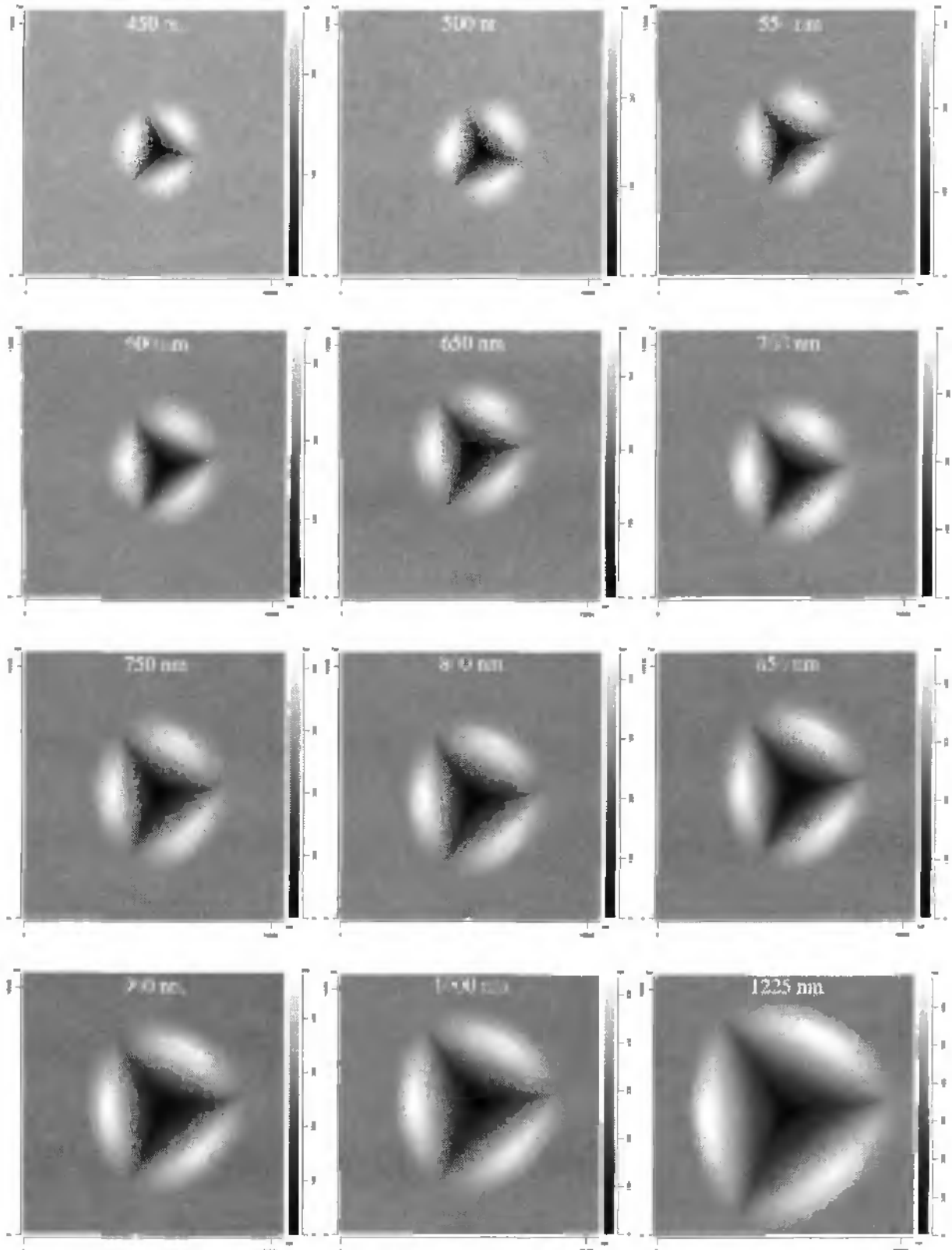


Figure 71 : Series of SFM images of residual imprints for depths (h_{max}) from 450 nm up to 1225 nm. The sample is a titanium film (thickness = 200 nm) sputtered onto a Si [100] substrate. Note the evolution of pile-up with increasing depth.

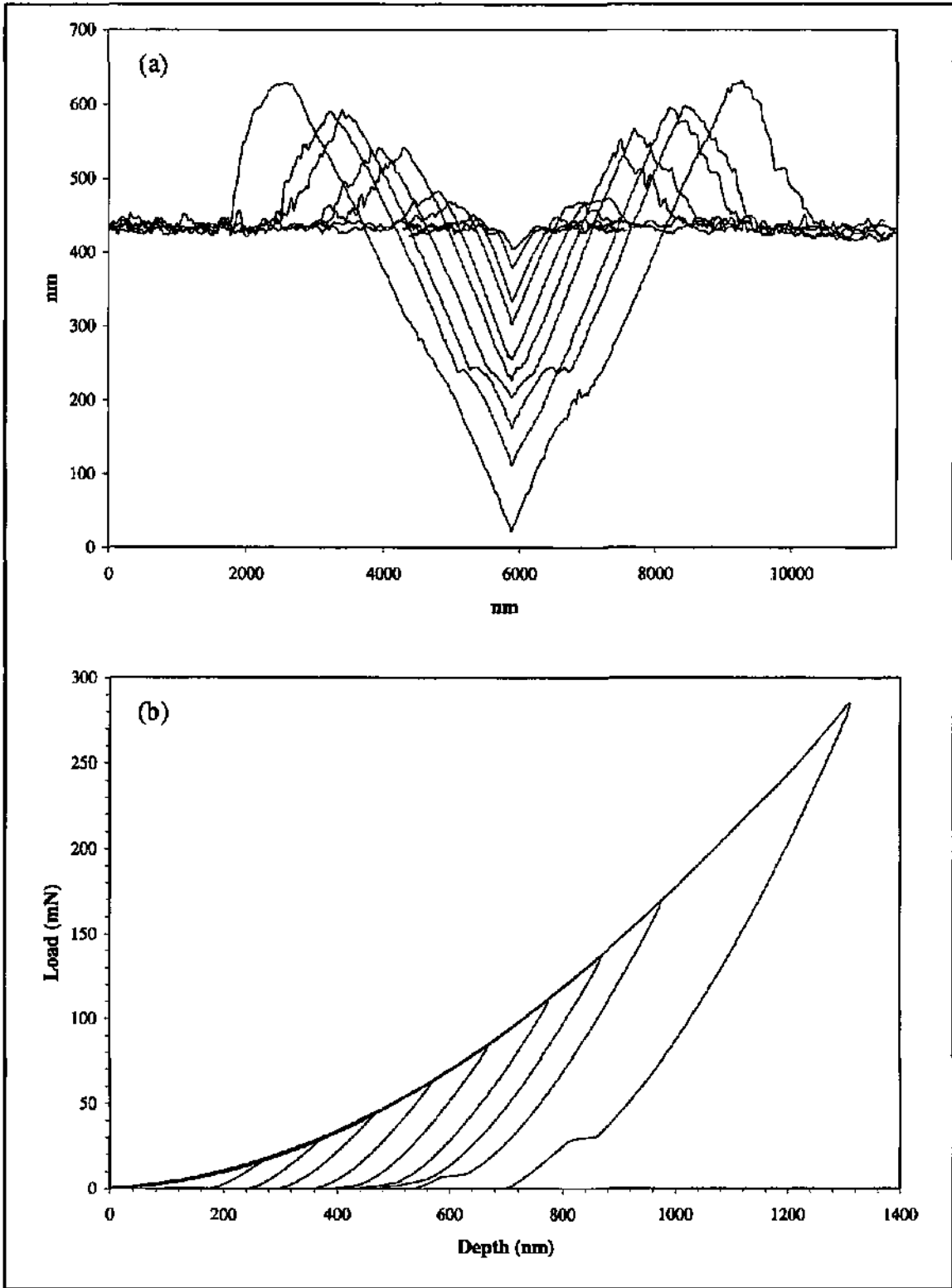


Figure 72 : A selection of cross-sectional profiles corresponding to images in Figs 70-71 are plotted together in (a), whereas (b) shows the evolution of the load-depth curves. The increasing influence of the Si substrate is evident for maximum penetration depths exceeding the titanium film thickness (200 nm).

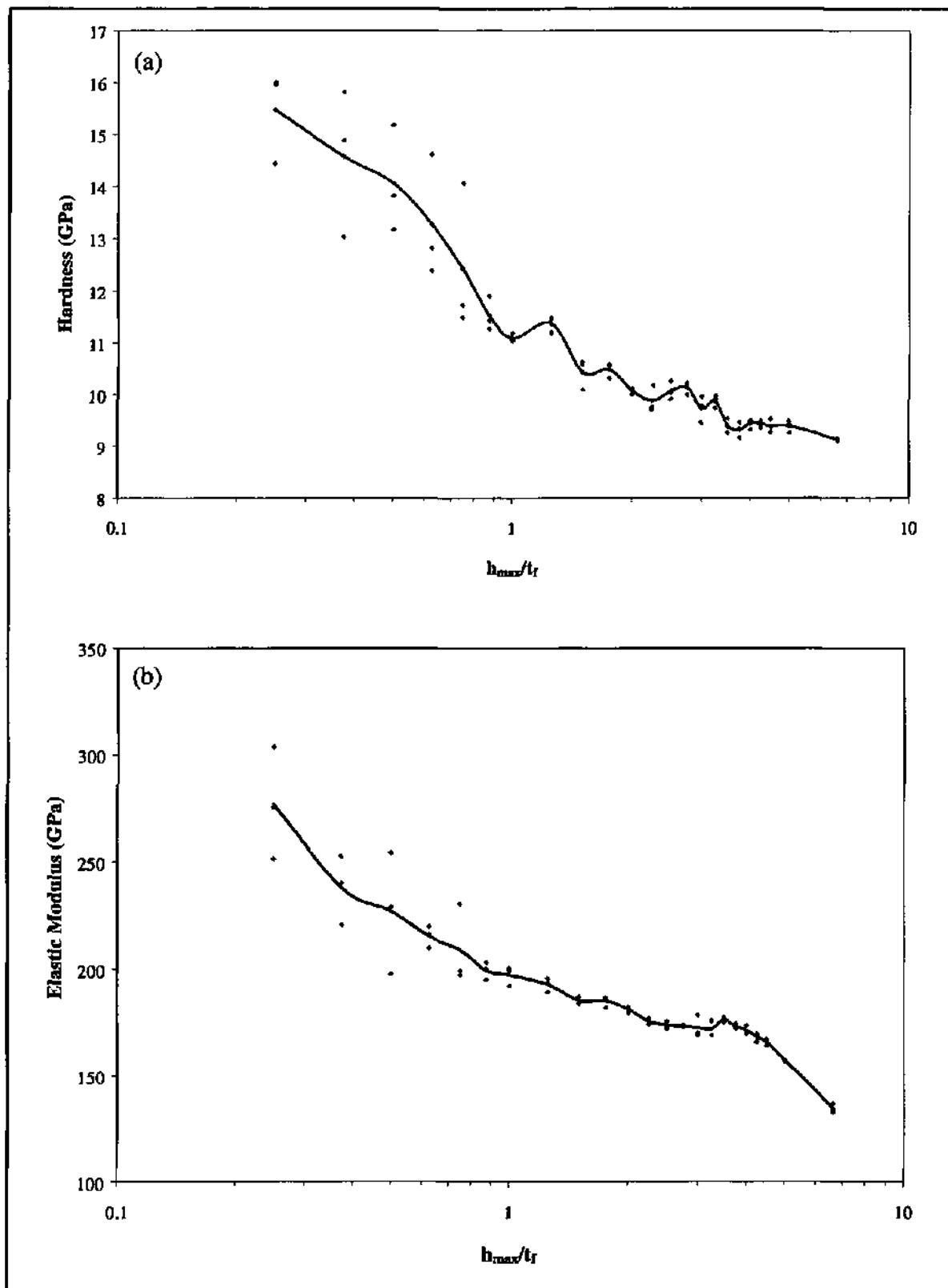


Figure 73 : The variation of hardness (a) and elastic modulus (b) are plotted as a function of normalised depth (h_{max}/t_f) for a titanium film (thickness = 200 nm) sputtered onto a Si [100] substrate.

Apart from imaging the residual imprint of an indentation, the integrated SFM can also be used to check and quantify the tip defect and symmetry of the indenter used. The actual indenter tip, being fused to a vertical rod, can easily be removed from the NHT measuring head and positioned accurately under the SFM objective. Fig. 74 shows a series of SFM images of the Vickers and Berkovich indenters used for the indentations presented in this chapter. As explained previously, the images made of Vickers imprints at shallow depths showed a significant tip defect for this indenter, in the form of a flat across its tip of approximately 500 nm in length. A large scan of the indenter tip shows good symmetry between the four faces (Fig. 74 (a)), whereas a close-up of the actual tip apex shows the bluntness at this scale, as well as the flat whose length can again be measured as approximately 500 nm (Fig. 74 (b)). In contrast, the scan of the Berkovich indenter confirms that the tip geometry remains more well defined near its apex and that it does not suffer from the inherent bluntness of Vickers indenters (Fig. 74 (c)). Thus, it would seem that a Berkovich geometry is far better suited to indentation depths less than 100 nm.

Although the SFM has a limited vertical range, most nanoindentations are less than 5 μm in depth, so the instrument is well suited to the measurement of the *active* portion of the indenter. In addition, the high resolution of the SFM allows shape information to be extracted directly from the images, as well as any deviation from a perfectly sharp pyramidal geometry. Previous work in this domain¹⁰⁴ has shown that the area function of a pyramidal indenter can be directly calculated from information gained from an SFM image, after correcting for the effects of pixellation and SFM probe shape. Pixellation occurs due to the fact that SFM data are acquired in digital form and so have a finite number of data points. For example, for a lateral scan size of 20 μm , and using the maximum number of points per line (512), the separation between each data point will be $20\,000/512 = 39$ nm. This means that an image of a typical pyramidal indenter will in fact be made up of steps of lateral separation 39 nm. If the contact area is to be calculated from such data then this may produce significant error, and so various correction routines must be used. Obviously, this effect is also present in SFM images of residual imprints and should be taken into account if pile-up volumes or contact areas are to be calculated.

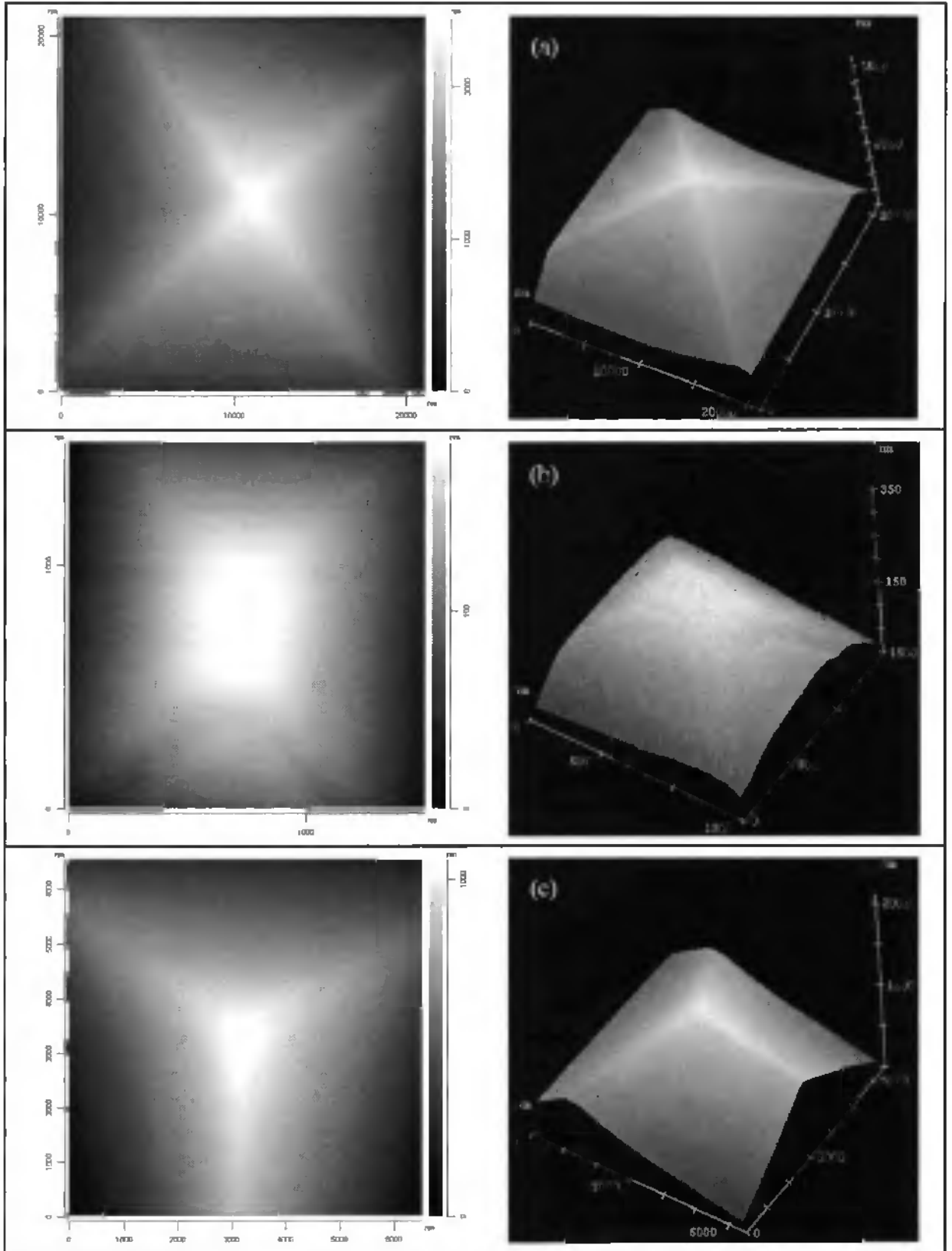


Figure 74 : SFM images of diamond indenters; (a) $21 \times 21 \mu\text{m}$ overview and (b) $1.5 \times 1.5 \mu\text{m}$ close-up of Vickers indenter, and (c) $6.5 \times 6.5 \mu\text{m}$ image of Berkovich indenter. Each pair of images consists of a top view (left) and a 3-D (right).

6.6 Conclusions

The NHT instrument, in its present configuration with integrated SFM, has been shown to provide highly precise hardness and modulus data for a wide range of materials, as well as significant additional information concerning the true response of a material to indentation at a nanometric scale (e.g., elastic/plastic deformation, cracking, creep, phase transformation, etc.). Regarding common coated systems, the NHT has proved that load-displacement information alone is not always able to determine the true deformation mechanisms occurring at the tip-sample interface, and that SFM imaging of the residual imprints at various depths is an invaluable means of characterising coating-substrate deformation behaviour. In addition, the NHT/SFM is capable of providing load-displacement data together with topographical information (i.e., surface roughness, extent of pile-up/sink-in effects, true area of contact, volume of material displaced, indenter tip shape, etc.) in a fast and efficient manner. The differential indentation method has been shown to have enhanced precision, a low effective frame compliance and low drift.

Chapter 7

Published results and applications

7.1 Surface characterisation of bearing components

Paper presented at the 10th International Colloquium on Tribology – Solving Friction and Wear Problems, Technisches Akademie Esslingen, Germany, January 1996 and published in the proceedings

Surface Characterisation of Bearing Components

N. RANDALL

CSEM, Neuchâtel, Switzerland

Summary

With the advent of new manufacturing techniques and better materials for contacting surfaces, modern bearing balls and races have benefited from harder surface coatings and much improved surface finish quality. Conventional methods of characterising surface topographical features, such as stylus profilometry, have gradually become incapable of evaluating a bearing surface with sufficient precision, and thus other alternatives have been required. One of these, the Atomic Force Microscope (AFM) has already established itself as a very powerful tool for surface characterisation with nanometric precision. AFM analysis has been developed so that important parameters, namely surface roughness, can be easily extracted from a measured area. A selection of three bearing balls, of different materials and all polished to *grade 3* quality, and a corresponding bearing inner race, were analysed using three of the most common techniques presently available, namely stylus profilometry, optical profilometry and AFM. The resulting roughness values were compared and showed that substantial variations exist between techniques.

1. INTRODUCTION

The interplay between different bearing components in dynamic contact is very much dependent on the topography of the interacting surfaces, and to this end their roughness has an important role to play in minimising friction, wear, scuffing and other mechanisms leading to failure of the system. The surface roughness, and related parameters, are thus crucial in gaining a better understanding of the tribological processes which occur on a sub-micron scale between two contacting bodies.

Owing to the limitations of traditional characterisation methods, such as stylus, optical, electron-beam and others [1, 7], alternatives have been developed to cope with the ever increasing surface finish quality required in today's bearing components. One of these, the Atomic Force Microscope (AFM) [2, 8], has proved revolutionary in recent years for the analysis of surface topography down to a nanometer scale [6]. Previous work [1, 3-5] has already shown the potential of such an instrument for controlling surface roughness in a wide variety of industrial applications, and for investigating nanotribological interactions with previously unmatched resolution. In addition, the AFM technique is able to provide quantitative information regarding microstructural variations across surfaces which, when combined with roughness data, gives a much better picture of the processes occurring between sliding contacts and how they can be optimised.

In this paper, the AFM is compared with two standard analytical techniques currently used in industry for routine roughness measurements, namely a stylus profilometer and an optical profilometer. Measurements performed on three different bearing balls of diameter 3.175mm and their corresponding bearing inner race showed that variations exist between techniques, with the AFM proving in some ways superior for the routine characterisation of bearing components.

2. EXPERIMENTAL

2.1. Outline of instruments used

All three instruments are presently available commercially for the local characterisation, in 2- or 3- dimensions, of surface topographical features and for industrial quality control in bearing systems. The first, a standard stylus profilometer [9] uses a diamond stylus of tip radius 1.5-2.5 μm with a vertical resolution of 3nm and a lateral resolution of 1 μm . This method, probably the most widely used for measuring roughness, moves the stylus over a surface and records vertical displacements providing a line profile from which the roughness can be calculated. It is limited by its lack of lateral resolution and so has limited use for measuring modern sub-micron features, such as low-period gratings, thin-film coatings and other common micro-fabricated structures. Having reached the resolution limit of this method, others have been developed in recent years in an

attempt to improve the accuracy of surface roughness measurements.

One such method, and the second of the instruments used for this work, is the optical profilometer [10] which focuses light from a laser diode on the sample surface. The light reflected back from the surface is focused through a lens system onto two halves of a differential photodiode, such that both halves are equally illuminated when the focal length of the objective lens is identical to the lens-surface separation. A feedback loop ensures that this separation is maintained as the lens moves over the sample surface and thus the lens position follows the variation in surface profile. The laser spot has a diameter of $1\mu\text{m}$, the instrument having a vertical resolution of 10nm and a lateral resolution of $1\mu\text{m}$. To this end, the optical method is not really an improvement of the stylus, only an alternative.

The atomic force microscope, however, has vertical and lateral resolutions far superior to the aforementioned profilometers, namely 0.1nm and 0.2nm respectively. With a doped silicon tip of radius $<150\text{\AA}$, this instrument easily provides accurate imaging in 3 dimensions down to a sub-nanometer scale. The tip, integrated into a cantilever, is moved across the sample surface by a piezoelectric scanning element which is controlled in the x , y and z directions. The subsequent cantilever deflections are detected by a laser system and recorded via a four-quadrant photodetector. An electronic feedback loop ensures that the piezo scanner follows the z movement of the cantilever as the tip moves over the surface. The data is recorded in the form of a 3 dimensional image, from which the relevant roughness parameters can be obtained, either as a cross-sectional line or as a surface profile.

The AFM used for this work, commonly known as the Atomic Scale Tribometer (AST) [11, 12], has already proved itself in the field of surface characterisation and nanoscale tribology [13]. The stand-alone measuring head (shown in Fig. 1) allows samples of unlimited size to be imaged and measures both the vertical and lateral deflection of the cantilever, although for this work only the vertical signal (topography) was recorded for roughness analysis.

2.2. Sample description and measurement procedure

The following types of bearing component were subjected to roughness measurements using stylus profilometry, optical profilometry and atomic force microscopy;

- (1) AISI 440C steel bearing ball.
- (2) AISI 440C steel bearing ball coated with TiC ($3\mu\text{m}$ thick).
- (3) Si_3N_4 ceramic bearing ball.
- (4) ABEC 7 bearing inner race.

The three bearing balls were all of diameter 3.175mm and polished to the *grade 3* AFBMA standard [14] which specifies for this grade an allowable bearing diameter variation of $0.08\mu\text{m}$ and a maximum surface roughness arithmetic average (R_a) of 12nm . The bearing inner race was carefully sectioned prior to analysis in order to allow measurements to be made in two perpendicular directions, namely the *transverse* direction (across the machining grooves) and the *longitudinal* direction (along the machining grooves). It should be noted that during use the bearing balls run along the race in the longitudinal direction.

With the stylus and optical profilometers, three surface profiles were taken on each sample, in different areas, and an average calculated for the roughness. With the AFM, five $10\mu\text{m} \times 10\mu\text{m}$ images were made on each sample in a similar manner.

The only surface roughness parameter common to all three analytical methods is the root mean square (rms) value, so this was used for easier comparison between different samples and methods. However, the standard roughness parameter used in industry is the R_a or centre-line-average value so it is important to explain the relationship between these two values. The arithmetic mean roughness, R_a , is simply the average deviation of the profile from the reference mean line, and is defined by equation (1), where L is the assessment length, y the peak height and x the peak spacing.

$$R_a = \frac{1}{L} \int_0^L |y(x)| dx \quad (1)$$

$$R_{rms} = \sqrt{\frac{1}{L} \int_0^L y^2(x) dx} \quad (2)$$

The root mean square roughness, R_{rms} , is the standard deviation of the distribution of surface heights, and is defined by equation (2) which also describes its relationship to R_a . The R_{rms} value is actually the only roughness parameter with basic significance and is fundamental in describing surface roughness by statistical methods. With all three measuring techniques the reference mean line was calculated as a polynomial function, thus allowing smooth background curvature to be subtracted from the data set before subsequent roughness calculation.

3. RESULTS AND DISCUSSION

The average rms roughness values measured by each method are summarised in Table 1 and are shown graphically in Fig. 2. It can be seen that the results obtained by stylus profilometry are directly comparable to those by optical profilometry for all samples, whereas a discrepancy exists between these two methods and AFM for the bearing inner race. This is perhaps best explained by looking at the AFM topographical images displayed in Fig. 3 in which the different surface morphologies are clearly identifiable. The bearing inner race surface (Fig. 3 (iv)) has directional machining grooves along the longitudinal direction and so it would be expected that the roughness in such a direction should be different to that in a transverse direction. However, as both the stylus and optical methods take surface profiles of length 1.5mm and 1mm respectively, with a lateral resolution no better than $1\mu\text{m}$, they should not be expected to accurately detect machining grooves spaced on average $<0.5\mu\text{m}$ apart. Furthermore, when comparing such millimetre-scale profile lengths with AFM profile lengths of $10\mu\text{m}$, it is obvious that a factor of 10^2 exists between them and that both profilometers are taking more into account surface deviations due to non-sphericity and macroscopic imperfections than the far more localised AFM measurements. Previous work [5] explains such phenomena in greater detail.

In order to further investigate the dependence of surface roughness on machining directionality, it was possible via the AFM image processing software to measure the roughness of a

line profile as a function of its angle with the direction of the inner race machining grooves. Such data was very useful in explaining the 10 \times variation between transverse (90°) and longitudinal (0°, 180°) rms roughness values and is displayed graphically in Fig. 4 together with the corresponding AFM image. This reinforces the superiority of the AFM technique in imaging features that are below the resolution limit of conventional profilometers. An interesting point is that for 3.175mm diameter bearing balls loaded to half their load-bearing capacity and seated correctly in the inner race, the contact ellipse (the area of contact between ball and race) has a major diameter of 0.1-0.7mm and a minor diameter of 0.02-0.2mm. This means that the AFM data is of the correct order of magnitude for investigation of the ball/race contact zone and further work may well prove beneficial in optimising this important tribological aspect of bearing technology.

The images shown in Fig. 3 provide direct comparison of three different bearing ball material surfaces with the steel inner race with which they are in rolling contact. It can be seen that the steel surface is the roughest, consisting of sharp features and an R_{rms} value only just within the AFBMA standard for a *grade 3* ball. This is due to the martensitic stainless steel microstructure (AISI 440C) which, due to 1% C and 17% Cr additions, contains two main phases of differing hardness. Thus during grinding and polishing these two phases wear at different rates and thus provide a greater roughness than a single phased material such as TiC. The TiC coating, deposited by Chemical Vapour Deposition (CVD) has a grain size 100 times smaller than that of a steel ball (in the order of 0.1 μ m) and so exhibits less roughness variation due to the superior polish that can be obtained on such a surface. The silicon nitride (Si₃N₄) surface is made up of coarse grains (1-5 μ m) and small pores at grain boundaries resulting from its powder deposition fabrication route. Polishing scratches and microscopic pores are clearly visible in the AFM image which are far below the resolution of a stylus or optical profilometer, but which need to be measured as they have a significant contribution to friction and lubrication at the ball/race interface. Again, only the AFM is able to image such sub-micron features with a high degree of precision.

The outcome of such AFM data, combined with that from the two profilometers, is that, although very useful, roughness data is very subjective in terms of the instrument used, the distance over which it is measured and the way in which it is calculated. The polynomial function used in each method was, in each case, only an approximation of the true background that should be removed and did not take into account surface variations due to waviness effects, holes and other inhomogeneities. Thus, the combination of roughness data with 3 dimensional imaging is definitely a step forward in characterising bearing surfaces. Two areas with a similar roughness value may well exhibit substantially different topographies (as seen with the ceramic and TiC-coated balls) and AFM analysis permits a better appraisal of irregularities which may influence the mechanical and tribological properties of mating surfaces. However, it should be noted that the relatively small scan range of such a technique does limit its ability to provide an accurate roughness value representative of the entire ball surface. Errors may well occur when measuring rough surfaces that have greater variations than the 10 μ m x 10 μ m square recorded. In such cases, the optical and stylus methods are sure to provide a more

accurate global value of the surface roughness, despite their resolution limitations.

4. CONCLUSIONS

A successful, and very interesting, comparison could be made between traditional stylus/optical profilometry and atomic force microscopy for the measurement of bearing balls and their corresponding inner race. Quantitative data obtained with each technique enabled the resolution limits of each instrument to be investigated with respect to the characterisation of common bearing surfaces. It was shown that AFM provides significant additional information, undetected by other means, but that it is still useful to combine such data with that from profilometry measurements in order to gain a more global picture of the sample surface.

Following such an investigation, there is clearly much scope for further work in this field concerning the use of an AFM, in particular:

- (i) Utilisation of the lateral signal of the AST for measurement of the frictional properties of bearing surfaces.
- (ii) In-situ studies of bearing interfaces by simulating a single asperity contact of a real surface with an AFM tip, in a rigidly controlled environment.
- (iii) Analysis of bearing surfaces before, during and after long periods of usage, in order to monitor changes on a sub-micron scale. Localised hardness testing of the outer atomic layers might also be incorporated in such a study.
- (iv) Accurate positioning techniques that allow profilometer measurements to be made on exactly the same surface area as AFM measurements. This is the only practical method of really comparing such instruments.
- (v) Use of an AFM for better characterisation and quality control of finished bearing components. This particularly applies to races owing to controversy between manufacturers concerning their finishing process.

These are only a few suggestions, but they show the wide range of applications that have become possible with the atomic force microscope. Furthermore, the Atomic Scale Tribometer used in this study, with its stand-alone construction enabling it to measure samples of any size and in almost any environment, has been shown to be a most useful tool in further investigating the surfaces of bearing components. It is expected that such instruments will pave the way for routine quality inspection in manufacturing and other industrial fields.

5. ACKNOWLEDGEMENTS

The author would like to thank Nicolas Blanc, Pierre Voumard and Denise Buri for competent technical assistance, and Hans Boving for providing the samples and for many helpful discussions.

REFERENCES

1. Constantin, R.; Christoph, R.; Beguin, J.; Boving, H. and Hintermann, H.: Use of atomic force microscopy for surface roughness determination of ball bearings: *Surface and Coatings Technology* 62 (1993) 517-522
2. Binnig, G.; Quate, C. F. and Gerber, C.: *Phys. Rev. Lett.* 56 (1986) 930
3. Burger, J.; Dietler, G.; Binggeli, M.; Christoph, R. and Marti, O.: Aspects of the surface roughness of ceramic bonding tools on a nanometer scale investigated with atomic force microscopy: *Thin Solid Films* 253 (1994) 308-310
4. Burger, J.; Randall, N.; Christoph, R.; Yan, L. and Parriaux, O.: Characterisation of microoptical elements by a stand-alone Atomic Force Microscope: *Proceedings of the International Symposium on Nanofabrication Technologies and Device Integration*, Lindau S64 April 11-14, 1994
5. Boving, H.; Burger, J.; Leijala, A.; Fluehmann, F. and Hintermann, H.: Aspects on the surface roughness of bearing balls: *Proceedings of the International Rolling Element Bearing Symposium 94*, San Diego, April 1994
6. Sarid, D.: *Scanning Force Microscopy*, Oxford University Press, New York, 1991.
7. Whitefield, R. J.: Non-contact optical profilometer: *Applied Optics* 10 (1985) 2480-2485
8. Rugar, D. and Hansma, P.: Atomic Force Microscopy: *Physics Today* 10 (1990) 23-30
9. Form Talysurf Series 2 Stylus Profilometer with 50mm traverse unit
10. UBM *Microfocus* Optical Profilometer in dynamic focussing mode
11. Atomic Scale Tribometer (AST) manufactured by Centre Suisse d'Electronique et de Microtechnique (CSEM)
12. Niedermann, P.; Burger, J.; Binggeli, M.; Christoph, R.; Hintermann, H. and Marti, O.: A scanning force and friction microscope: *Proceedings of the NATO ARW on "The Ultimate Limits of Fabrication and Measurements"*, Cambridge, April 1994
13. Binggeli, M.; Christoph, R.; Hintermann, H. and Marti, O.: Atomic Scale Tribometer for friction studies in a controlled atmosphere: *Surface and Coatings Technology* 62 (1993) 523-528
14. The Anti-Friction Bearing Manufacturers Association (AFBMA) standard for metal balls No. 10 (1989)

BEARING COMPONENT	AVERAGE ROUGHNESS (R_{rms}) VALUE (nm)		
	STYLUS	OPTICAL	AFM
AISI 440C Steel ball	11.7	12.2	12.6
AISI 440C Steel + TiC ball	7.2	10.9	9.1
Si ₃ N ₄ Ceramic ball	9.1	11.5	10.5
ABEC 7 Inner race (transverse)	17.8	15.7	6.8
ABEC 7 Inner race (longitudinal)	16.6	13.4	1.9

TABLE 1 : Comparison of root mean square (rms) roughness values for the bearing balls and inner race, measured by three analytical techniques.

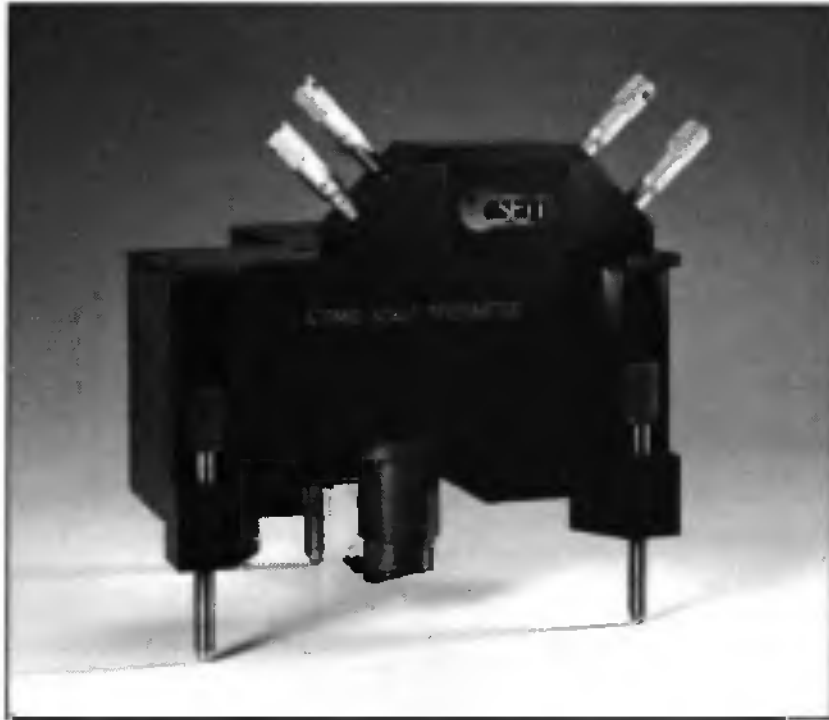


FIGURE 1 : Front view of the Atomic Scale Tribometer (AST) stand-alone measuring head with 10 μm scanner.

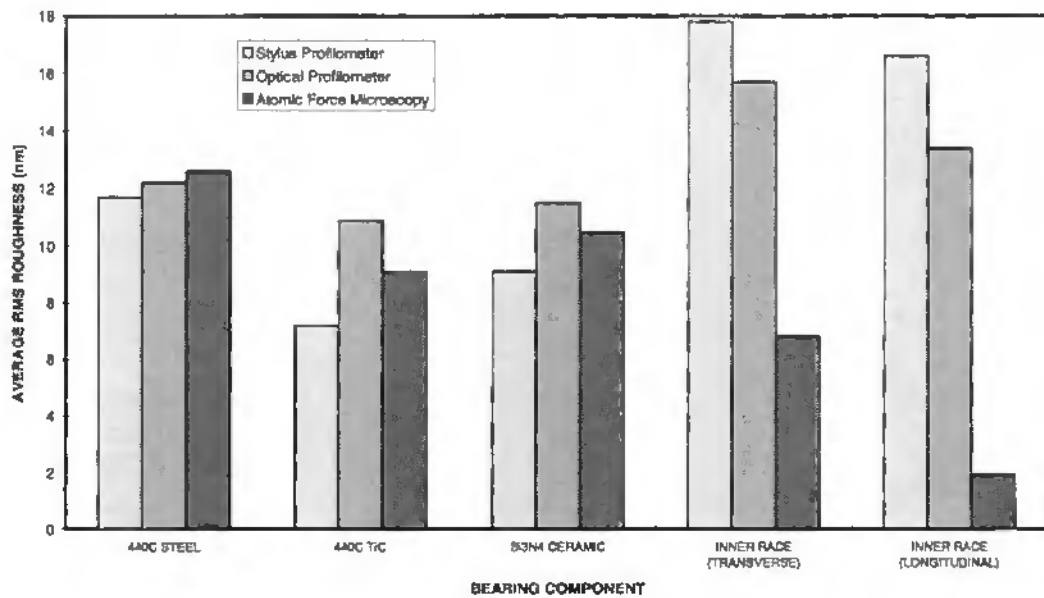


FIGURE 2 : Average RMS roughness data for the four bearing surfaces, plotted to show the variations between each type of analytical technique.

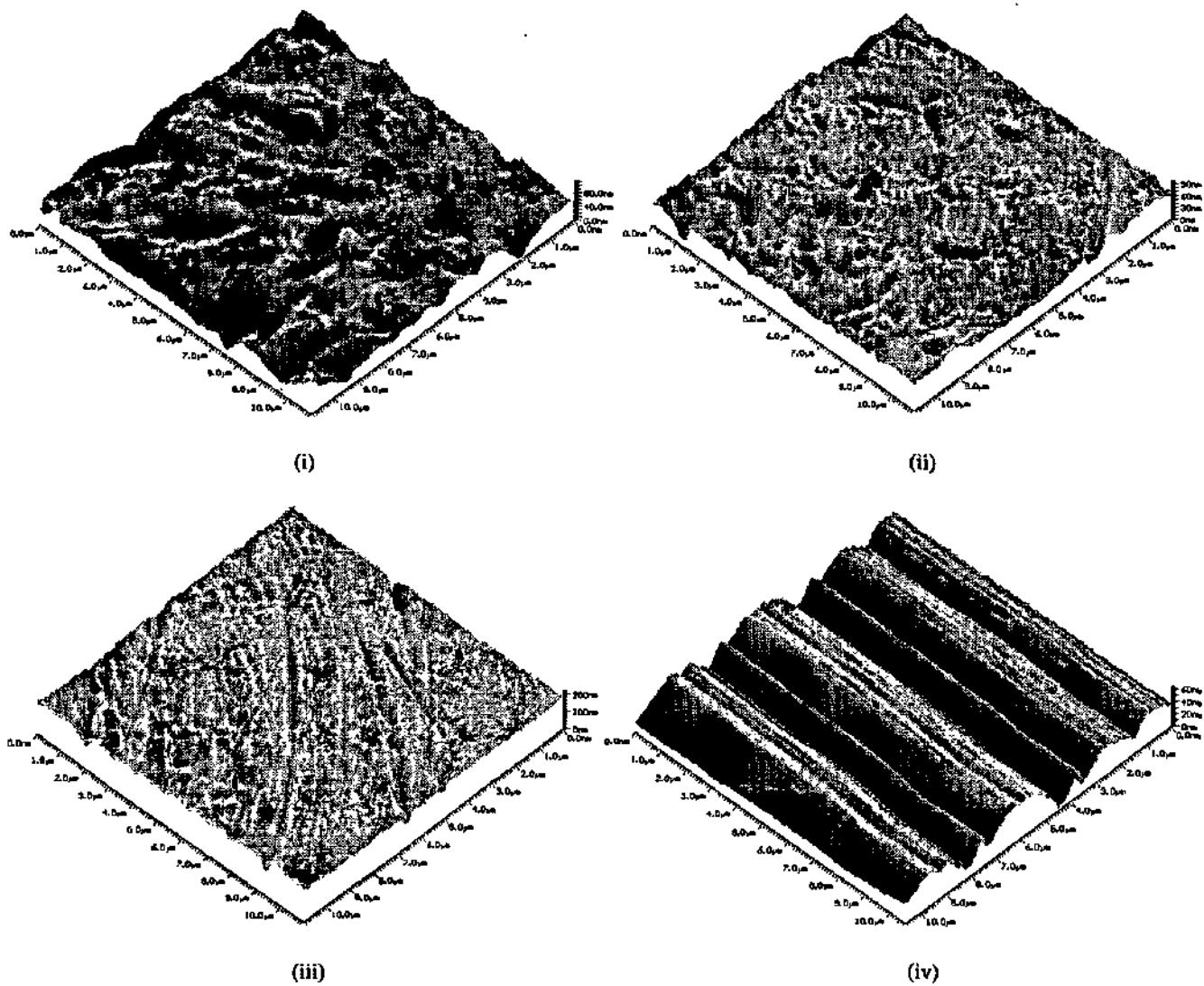


FIGURE 3 : AFM analysis of bearing components; (i) 440C Steel ball, (ii) 440C TiC ball, (iii) Si_3N_4 Ceramic ball, and (iv) ABEC 7 bearing inner race.

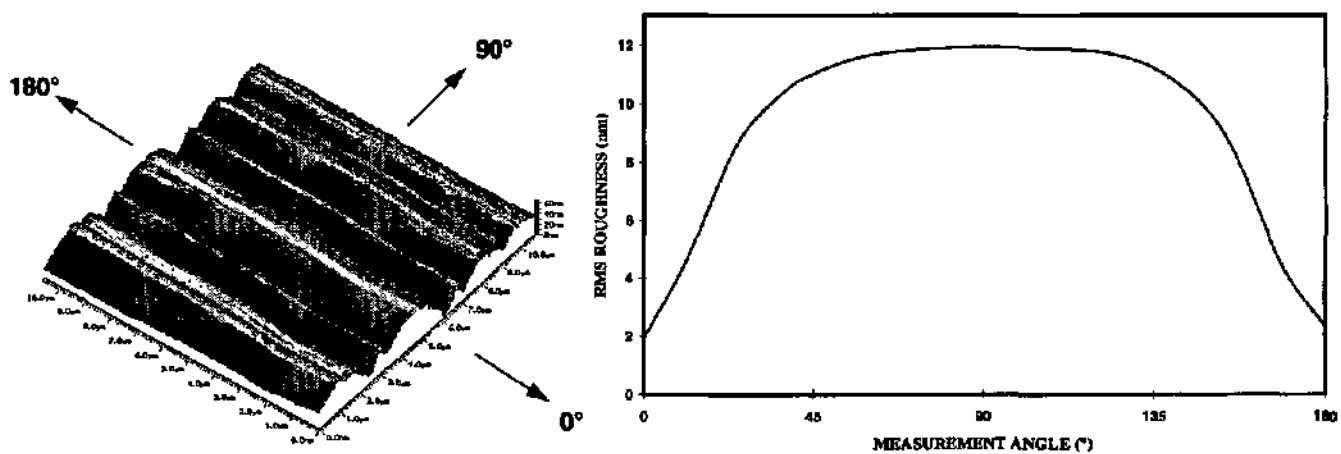


FIGURE 4 : Variation of RMS roughness with angle of measurement for an AFM image of an ABEC 7 bearing inner race.

7.2 Localised micro-hardness measurements with a combined scanning force microscope/nanoindentation system

Paper presented at the International Conference on Metallurgical Coatings and Thin Films (ICMCTF 96), San Diego, USA, April 1996 and published in Thin Solid Films 290-291 (1996) 348-354

Localised micro-hardness measurements with a combined scanning force microscope/nanoindentation system

N. X. Randall *, R. Christoph, S. Droz, C. Julia-Schmutz

Centre Suisse d'Electronique et de Microtechnique S.A., Jaquet-Droz 1, 2007 Neuchâtel, Switzerland

Abstract

Thin-film coatings, modified surface layers and multiple phases are increasingly being used to improve the properties and functionality of engineering materials. Nanoindentation effectively meets the industrial need to measure hardness on a micro- and even nanometer scale and has proved its worth in characterising the mechanical properties of surfaces, subsurface regions, interfaces, phases and grain boundaries in a quasi non-destructive way. The depth-sensing indentation method provides a means of evaluating the elastic and plastic deformations of the tested material, from which the hardness and the elastic modulus can be calculated. The combination of such an instrument with high resolution scanning force microscopy (SFM) and a conventional optical microscope provides a system capable of a more complete analysis of important surface parameters such as surface micro-roughness, topography and grain structure. In addition to the precise measurement of the indentation depth, the displaced material volume can also be measured together with other important information concerning the processes taking place on a microscale whilst performing such an indentation, e.g., plastic flow, micro-fracture, material compression and other interfacial effects. First results obtained on a multiphase high speed steel are presented, showing the net advantages of such a system in carrying out highly localised indentation studies together with precise measurement of imprints via SFM.

Keywords : Nanoindentation ; Scanning force microscopy ; Vickers hardness ; Micron positioning

1. Introduction

Over the last few years great advances have been made in the development of both destructive and non-destructive techniques for the accurate characterisation of materials on a sub-micron (or nanometric) scale. Classical indentation methods, where hardness data is solely available by measuring the size of the impression after removal of the indentation load, have always ignored property variations as a function of elastic recovery. Furthermore, such methods limit the minimum depth of the indentation, meaning that depths of less than 1-2 μ m make the indentation too small for size measurement by conventional light microscopy [1].

More recently, various nanoindentation techniques have been developed which employ much lower loads and which continuously measure force and displacement as an indentation is made [2-6]. Most such techniques apply the load either via a magnetic coil, in which case the load is evaluated from the current in the coil, or via a piezoelectric system which produces the indentation and a capacitive sensor which measures the resultant displacement. With force and displacement resolutions in the ranges 10 nN and

0.1 nm respectively, such instruments are able to produce load-displacement curves that give an accurate representation of the material response, but a true understanding of the elastic/plastic interactions occurring at the interface is not possible solely from such data.

Additional topographical information has, in recent years, become increasingly important for characterising surface deformation in and around the indentation area. Various methods have been proposed, including SEM [7], TEM [8] and STM/SFM [9], with scanning probe techniques being one of the few able to quantitatively measure interfacial effects, such as material pile-up around indentations, with nanometric precision and three-dimensional imaging capability. Such techniques, in particular Scanning Force Microscopy (SFM), are now being used, together with load-displacement data, in order to obtain a more overall picture of the nanoindentation process and a means of quantifying the true elastic/plastic components of the process. In addition, the exact dimensions of the imprint can be obtained, enabling a correlation between hardness and imprint size to be established as with conventional hardness-testing instruments. However, such a correlation does not solve the interpretation problems due to the continuously changing contact area between the tip and the sample during indentation. As has been reported previously [12], these

* Corresponding author.

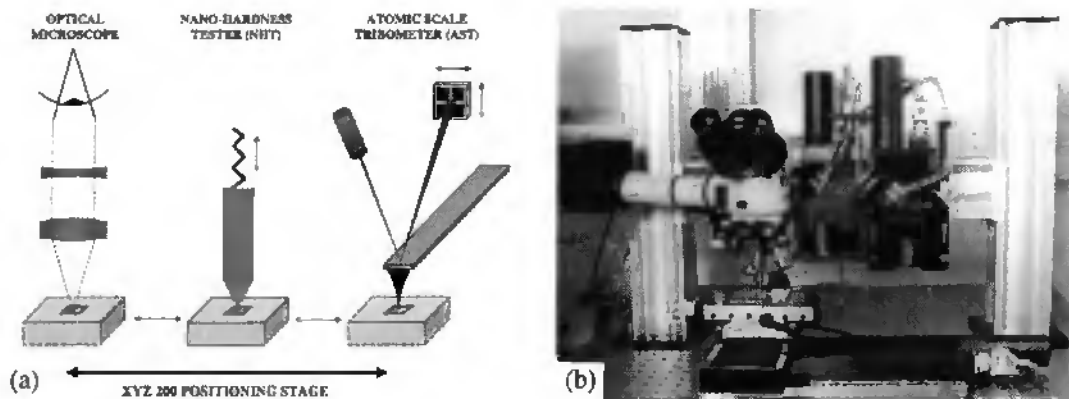


Fig. 1. System set-up for combined optical, SFM and nanoindentation measurements on a sample which can be positioned at any specified site via an electro-mechanical positioning stage. The apparatus is displayed schematically in (a) and the practical set-up is shown in (b).

problems could be avoided by using an indenter tip with a flat-ended geometry, but in practice this is not an acceptable solution because it is difficult to assure uniform contact between such an indenter and the sample (due to surface roughness and misalignment of the tip). Thus, nanoindentation studies are usually performed with either a Berkovich three-sided pyramidal indenter or a four-sided Vickers indenter, the former having the advantage of a superior apex, the latter being more resistant to damage under load. Some work is also being carried out in this field using spherical indenters, where the stress distribution is more uniform and the elastic/plastic transition may be more readily defined [13].

The main drawback of combining indentation techniques with suitable imaging methods is the positioning of the sample. With conventional hardness testing, the indentation can be seen through an optical microscope and so location of a given site is relatively simple. However, with nanometer-sized indentations, very accurate positioning systems are required in order to locate a specific site quickly and efficiently and for imaging an area prior to and after indentation. Such systems are becoming increasingly important in industrial applications, for example in quantifying the wear of hard disc surfaces [10], or for investigating thin-film coatings [11]. Present techniques are often inefficient and time-consuming, the most common being that of making multiple arrays of indentations, with some large enough to be later located under a suitable imaging microscope [7].

The present work stems from the obvious need for a system capable of combining nanoindentation experiments with high resolution microscopy in a logical and user-friendly way. This paper introduces a novel instrumental set-up designed specifically for such use, in which a sample can be transferred between three measuring stages via an electro-mechanical positioning table with a resolution of 1 μm . The first results obtained with the combined system clearly show the advantages possible by imaging an area before and after indentation with both high resolution scanning force microscopy and lower resolution optical microscopy. Some interesting observations concerning the behaviour of different materials are made, showing the potential for more in-depth future studies.

2. Experimental

2.1. Instrumental set-up

The apparatus itself consists of three measuring components, namely a Nikon optical microscope (with objectives up to 1000 \times magnification and Normarski contrast), a Nano-Hardness Tester (NHT) and an Atomic Scale Tribometer (AST) [14]. These components are mounted, side-by-side, above an electro-mechanical positioning system which allows four axes of movement, two for the sample (x and y displacements between any of the measuring instruments) and two for vertical displacement of the NHT and AST. A schematic representation of the basic principle and a view of the system are shown in Fig. 1. The two horizontally mounted tables have a maximum displacement range of 200 mm, the vertically mounted tables 50 mm, all with a theoretical resolution of 0.25 μm .

The distance between the optical microscope and the scanning force microscope (AST) was calibrated using a *fresnel* lens grating made specially for that purpose. Such a grating was of concentric nature and etched in glass with period 1 μm and depth \sim 100 nm, enabling it to be easily seen through the optical microscope and easily measured by SFM. For calibrating the NHT relative position, the sample was changed from the grating to a soft and flat metal (usually polished aluminium). A large indentation was performed such that it could subsequently be found under the optical microscope.

The entire apparatus was mounted on a pneumatic vibration isolation table to keep unwanted noise to a minimum.

2.2 Principles of nanoindentation

The Nano Hardness Tester (NHT) is based upon SFM technology and incorporates a piezoelectric actuator which allows vertical displacement of a Vickers diamond tip into the surface to be measured. The tip is mounted on a stiff cantilever of copper-beryllium (force constant 10^4 N m^{-1})

¹ NHT and AST manufactured by CSEM Instruments, Neuchâtel, Switzerland

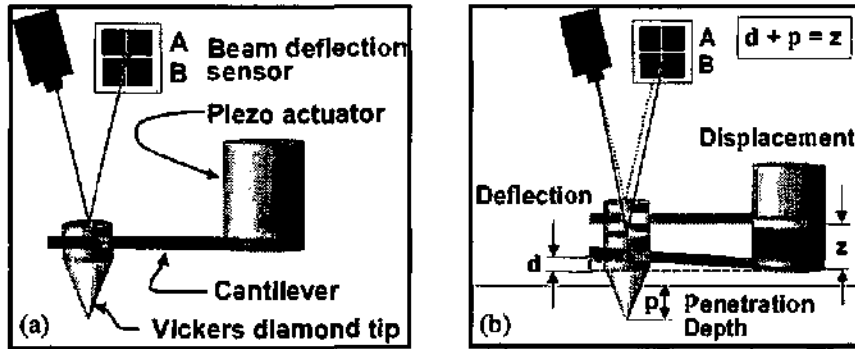


Fig. 2. Principles of nanoindentation showing (a) basic components of the system and (b) the calculation of the penetration depth p as a function of cantilever deflection d and piezo displacement z .

and the corresponding force is measured, via movement of the cantilever, using a standard laser beam deflection system (Fig. 2(a)). When the Vickers tip is driven into the sample surface by a distance z , the cantilever deflects by a distance, d , measured by the laser deflection system, and thus the penetration depth, p , can be calculated by the equation:

$$p = z - d \quad (1)$$

The schematic diagram in Fig. 2(b) shows the principle in more detail. Calibration of the indentation force is carried out by using a high precision weight balance.

The NHT has a maximum piezo displacement of 16 μm with resolution 0.25 nm and the maximum force is 40 mN with 10 μN resolution.

This instrument was initially conceived for indentation experiments where the load and displacement data are simultaneously recorded during indentation to produce a classical force-distance curve. However, the system was still under development when used for this work and was not yet capable of such on-line measurements. The quantitative data that could be measured was the maximum indentation force, the maximum penetration depth and, of course, the dimensions of the imprint via subsequent SFM analysis. An estimate for the classical Vickers hardness, H_v , of a measured material can now be evaluated by considering the Vickers relationship:

$$D = \left[1.854 \frac{P}{H_v} \right]^{1/2} \quad (2)$$

where D is the diagonal of the indentation and P is the load required to produce it. The diagonal of the indentation can be measured using SFM. However, although calibrated, the SFM produces distortion due to piezo non-linearities and hysteresis and thus a factor is introduced into the equation to compensate for this as well as for tip imperfections:

$$kD_e = \left[1.854 \frac{P}{H_v} \right]^{1/2} \quad (3)$$

This correction factor, k , represents the difference between the experimentally measured diagonal, D_e , and the theoretical diagonal, D . It can be found by making a series

of indentations, of known force, on a homogeneous sample whose Vickers hardness is known. The theoretical diagonal can be calculated and compared to the experimental value which is measured using SFM. This factor is then valid for subsequent SFM measurements at the same scan size, made on indentations where the Vickers hardness of the material is not known.

2.3. Sample materials

Indentations were carried out on two different types of material; the first was a pure Fe test sample, used in order to evaluate the correction factor, k , as outlined in the previous section. This material had a known Vickers hardness, H_v , of 597 kg mm^{-2} and a Young's Modulus, E_y , of 37.28 GPa at a force of 150 mN.

The second was an M3 Class 2 high speed steel [15] which had been etched for 15 seconds in a *Nital* solution (4% Nitric acid + ethanol) followed by a deposition of Fe oxide on the surface by cathodic pulverisation. Such a steel, having been vacuum sintered from powder precursors, showed a wide range of separate phases of small size which were ideal for testing the positioning accuracy of the system, and which after etching could easily be distinguished by optical microscopy. This sample, supplied by the Engineering Materials Research Unit, Bradford University, UK, was polished down to 0.25 μm with diamond paste prior to *Nital* etching and deposition of only a few nanometers of Fe_2O_3 .

The microstructure consisted of primary carbides distributed in a martensitic matrix and a quantitative analysis by wavelength dispersive spectroscopy [16] showed that two types of carbide were present, namely MC (where M is V or Cr) and M_6C (where M is Fe, W, Mo, Cr or V). The former have H_v of $\sim 3000 \text{ kgmm}^{-2}$, whereas the latter have H_v in the range 1000-1500 kgmm^{-2} . Grains of MnS are also present in the Fe matrix, having been included as a means of solid lubrication. The MC carbides are globular and dark coloured, the M_6C carbides are angular and lighter coloured and the MnS grains are globular but smaller and pale coloured.

Such a material was also chosen for its practical relevance, namely for use in valve-guides and camshafts in the automobile industry, where its enhanced wear resistance, self-lubricating nature and reliability are of the utmost importance [17-18].

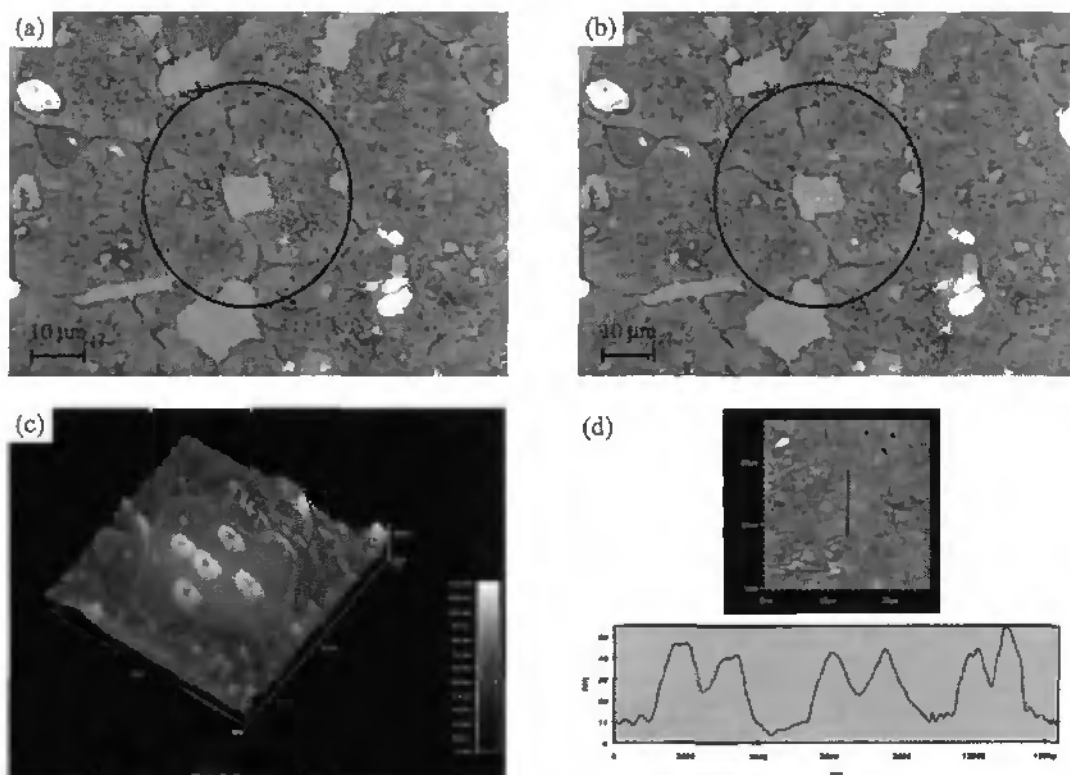


Fig. 3. Multiple nanoindentations on an M_6C carbide particle : (a) and (b) are optical micrographs (at magnification 1000 \times) showing the particle before and after indentation ; (c) shows the corresponding SFM image of the five indents (maximum force 1 mN, spacing 2 μ m) ; (d) represents a cross-sectional profile through three indentations.

2.4. Experimental procedure

Two separate sets of measurements were made, the first being used in order to calculate the factor, k , needed for correcting the second set.

1. A series of indentations were performed on the Vickers test sample with force values varying from 0.1 to 3.4 mN in increments of 0.1 mN.
2. For the high speed steel samples, certain interesting sites were chosen via the optical microscope and indentations subsequently performed. Maximum force values in the order of 1-2 mN were used, and SFM analysis of the areas in question was then carried out. The system was recalibrated before each set of measurements in order to reduce position losses due to laboratory temperature variations.

All indentations were performed using the NHT with a Vickers diamond tip (apex angle 136 $^\circ$) displaced with speed 0.1 μ m s^{-1} . Subsequent SFM analysis was carried out using the AST with sub-nanometer lateral and vertical displacement resolution and a maximum lateral scan range of 25 μ m.

3. Results and discussion

The series of indentations performed on the Vickers test sample with varying force values were used in order to calculate the correction factor, k , as outlined previously,

giving a value of ~ 1.6 for a scan range of 15 μ m. It was possible to obtain reasonable values for the Vickers Hardness, H_V , of the MnS grains by measuring the indent diagonals using the SFM images and multiplying by the same correction factor valid for that scan range. Values in the range 200-300 H_V were obtained, these being in accordance with literature. However, for the indents on the MC and M_6C carbide particles it was impossible to get reasonable measurements of the diagonals due to pile-up, uplift and consequent distortion of the residual imprints. What also needs to be mentioned at this stage is that the reference values of Vickers hardness for the test sample were for an applied force of 150 mN. Thus, at indentation forces of 1-2 mN it is clear that the hardness values cannot be directly correlated, due to the increased effect of surface oxide films and indenter geometry.

Fig. 3 shows the first example of nanoindentations performed on an M_6C carbide particle. The five indentations (all produced at a maximum force of 1 mN) were arranged in a cross configuration on the carbide particle with a spacing of 2 μ m thus demonstrating the micron positioning accuracy of the system. The optical micrographs show the preselected particle before and after indentation, and in addition reveal the complexity of the sintered high speed steel sample material.

The corresponding SFM image shows directly the additional information that is obtained compared to that solely from the optical micrograph. In three dimensions the extent of pile-up around each indent is evident and can be investigated further by taking a suitable cross-sectional profile through three of the indents (Fig. 3(d)). It can clearly

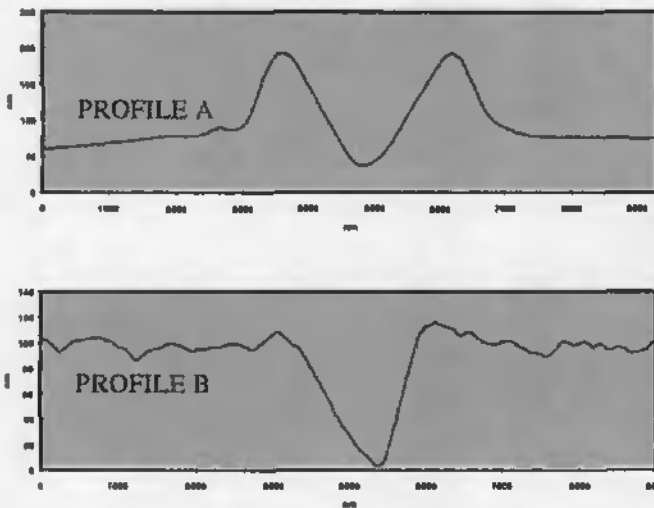
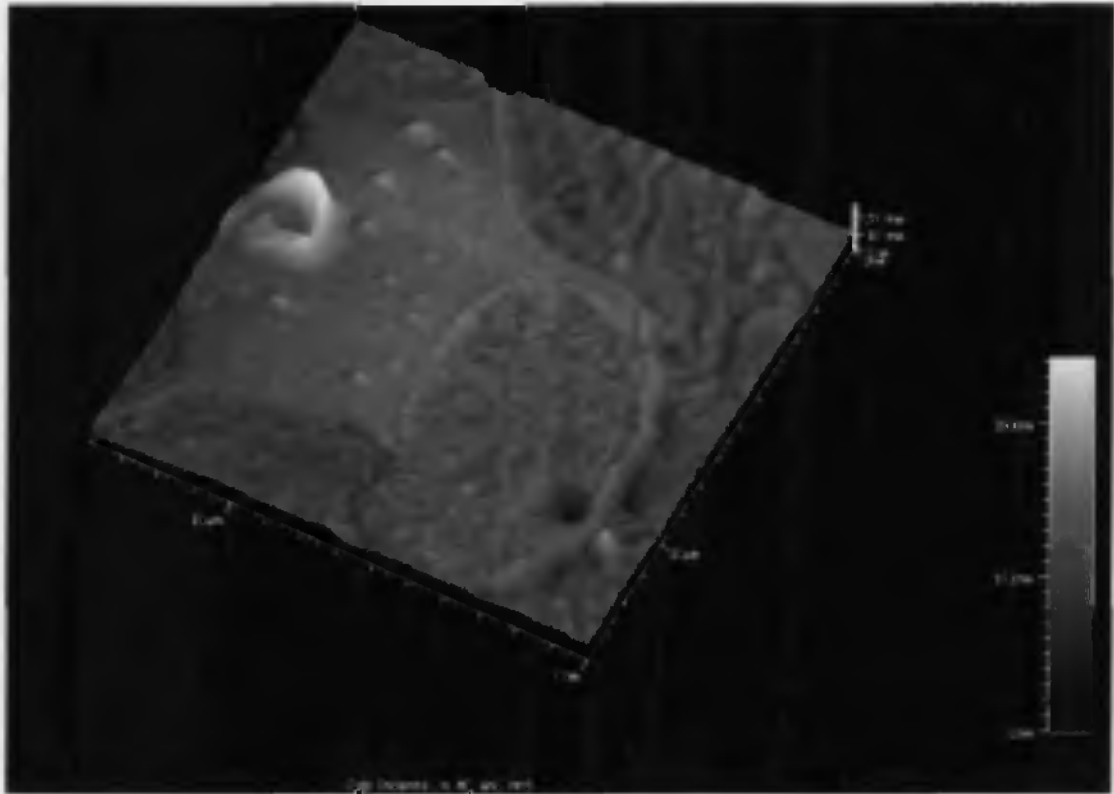


Fig. 4. Nanoindentations on two different phases of a high speed steel. The 3-D SFM image (top) shows the different material response to the 2 mN indentations as do the corresponding cross-sectional profiles (bottom) through an MC carbide particle (profile A) and an MnS grain (profile B).

be seen that substantial uplift has occurred during unloading as well as elastic recovery of the material, the latter possibly being time-dependant although this was not investigated. The shape of the Vickers diamond imprint has become severely distorted due to elastic relaxation of material around the imprint and possibly by adhesion of matter between the indented region and the diamond tip during unloading.

These observations place doubt on the accuracy of calculating the hardness and elastic modulus of a material solely from load-displacement curves. They also emphasise the importance of true three-dimensional imaging in trying

to understand what has occurred during the indentation process and aid in drawing suitable conclusions.

Fig. 4 shows the second example of nanoindentations, this time performed on two different phases (MC and MnS) of the high speed steel. Both were produced with a maximum force of 2 mN and under the high resolution optical microscope, very little difference could be discerned between them. However, the subsequent SFM analysis revealed substantial variations in the material response of the MC carbide particle and the MnS grain. The corresponding cross-sectional profiles show this very clearly. It would seem that the MnS indent is nearly entirely

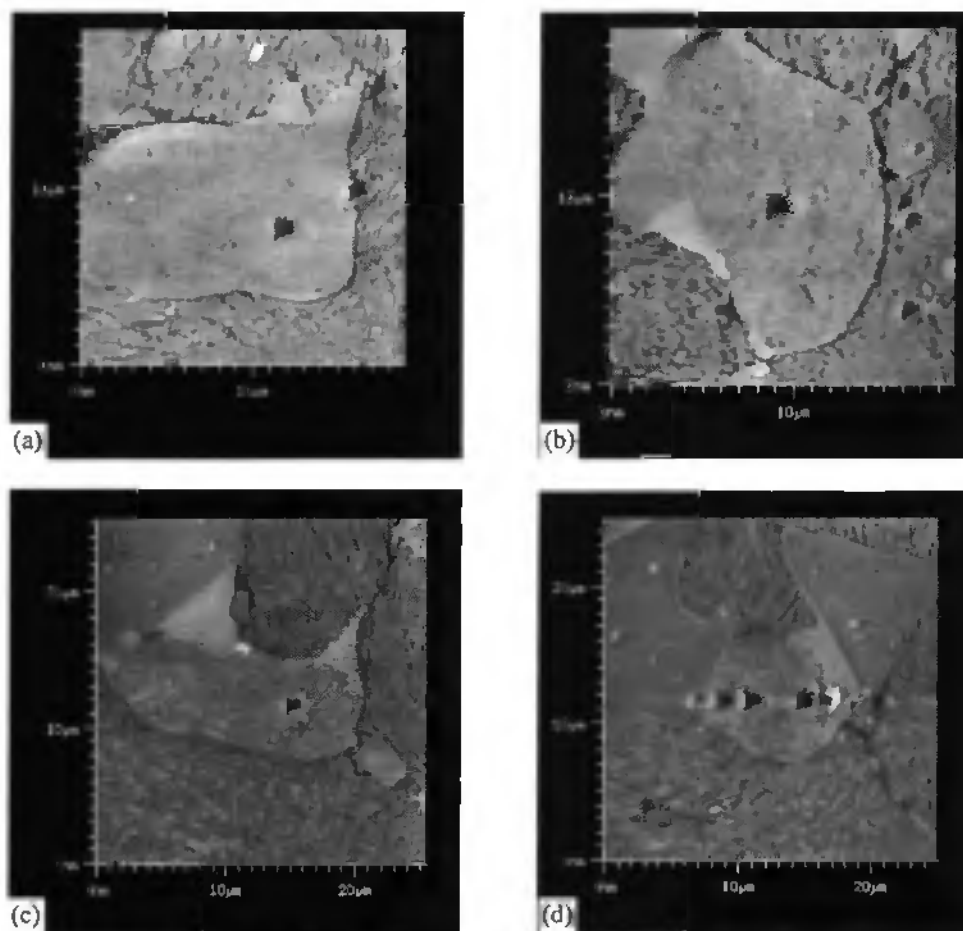


Fig. 5. SFM images of nanoindentations performed on specific sites on a high speed steel, namely: (a) 1 mN indents, one within an MnS grain and one at the MnS/Fe interface (grain boundary); (b) 1 mN indents on (i) MnS grain, (ii) M_6C carbide particle, (iii) and (iv) Fe matrix; (c) 2 mN indent on MnS grain; (d) 7 indents (1 mN) with $2\ \mu\text{m}$ separation across four different grain types (in this case $M_6C/MnS/MC/M_6C$).

plastic and very little pile-up or uplift was in evidence. The MC indent, on the contrary, behaved in a similar way to those performed on the M_6C carbide particle, showing the similar phenomena of uplift and pile-up. In addition, a closer examination of this indent revealed the spiral-like nature of the piled-up material around it. Without further analyses, perhaps using TEM methods, it is not possible to ascertain whether such a spiral phenomena is due to dislocation movement or other dislocation aspects of plastic flow. Such an analysis may well be undertaken in future studies on less complex sample materials, where the positions of dislocations and the way in which they interact can be more easily correlated to the material properties. Some previous studies on single crystals [19] and other materials [9, 20] have already shown that the dislocation mechanism of plastic flow is responsible for pile-up around indentations, and that phase transformations can also influence indentation size, morphology and thus hardness.

However, the fact that the imprint has its apex above the original sample surface in some of the experimentally measured cases on carbide particles would suggest that factors far more significant than simple dislocation movement or residual stress relaxation are responsible for such a marked displacement of material. Without having the corresponding force-displacement curves for the indentations in question, it was not possible to ascertain how

much of this flow may have been due to adhesion between indenter and sample material. Adhesion of this type, measured using the described cantilever deflection method, would be characterised by a negative force component in the unloading curve. Perhaps we need to look at the actual processing history of the high speed steel sample material. Having been sintered from powder precursors and heat treated, it might be correct to assume that the thermal expansion coefficient of the surrounding Fe matrix is greater than that of the carbide particle. Thus, following solidification, the carbide particles are under compression with respect to the matrix. Some of the resulting stored strain energy might be released as a result of the indentation, with matter around the indented area being forced upwards, this giving the observed 'gain' in material after indentation.

The SFM images depicted in Fig. 5 have been included to demonstrate the versatility of the experimental set-up in performing indentations at highly specific locations, ranging from grain boundaries to multiple arrays across different grain types. It is also interesting to note the differences in surface texture between the various grains and the matrix, details inaccessible via optical microscopy. The SFM also has the capability to measure the surface roughness of an area prior to an indentation being made, so as to be able to judge whether such an area is suitable. Variations in the surface topography of a sample material, if small compared

with the size of the indentation, should not have an adverse effect because the sample surface is simply forced downwards. However, when indenting down to nanometric scales, surface roughness may play an increasingly important role, and thus its prior measurement becomes extremely important.

The SFM also permits an accurate measurement of the sample surface inclination with respect to the axis of the diamond indenter. As shown previously by Mulhearn and Samuels [21], a tilt of only a few degrees can cause a significant error due to the indenter tending to slide down the inclined surface, producing a non-symmetric and enlarged residual imprint. This leads to one of the limitations of the present NHT system, in which the diamond indenter tip is applied to the surface via a stiff cantilever. For larger indentations performed on aluminium it was found that all indents with a penetration depth exceeding about 500nm were not perfectly symmetrical and that at greater depths the apex of the diamond tip had moved horizontally during the course of the indentation, producing a longitudinal deformation of the imprint. However, for the far smaller indents presented in this work, such an effect was not encountered.

Regarding the use of scanning force microscopy in imaging indentations, it should be added that several factors must be taken into account when interpreting the results. Firstly, hysteresis and thermal drift of the piezoelectric scanning element lead to distortion of the image, although this can be corrected by software. Secondly, SFM data are acquired in limited numbers of data points and so the sub-nanometer resolution of the instrument is not maintained within the data set for large images. With very shallow indentations this factor becomes increasingly significant. Finally, the SFM tip is of finite size and its point of contact with the surface varies as it moves across the surface, thus producing an error that can only be removed if the tip shape geometry is accurately known.

4. Conclusions

It has been shown that, using the combined nanoindentation/SFM system, it is possible to carry out highly localised indentation studies with micron positioning accuracy and to precisely measure the corresponding areas with SFM. The limitations of the present experimental set-up for obtaining quantitative indentation data have been discussed and the need for further development established. Future work will be performed with a redesigned instrument, capable of measuring an accurate force-displacement curve without the limitations of the present cantilever deflection system, thus allowing direct comparisons to be made between the curve and the corresponding SFM image of the indentation. This work has confirmed the ability of the scanning force microscope to provide significant additional information

concerning the mechanisms occurring in and around the indentation site, and to give quantitative data of imprint dimensions, contact area and volume of displaced material. Further in-depth studies of a wide variety of materials will allow closer standardisation of the nanoindentation method and develop it as a very interesting and valid analytical technique for the characterisation of, amongst others, multiphase alloys, thin films and coatings, micro-welds, hard disk surfaces and microelectronic devices.

Acknowledgements

The authors would like to thank Jean-Marc Durand from the Ecole des Mines in Paris for helpful discussions and for providing the samples, and Jean-Pierre Jeanneret from the CSEM for technical assistance. This work was supported by the Schweizerische Gesellschaft für Reinraumtechnik (SRRT) and the Kommission für Technologie und Innovation (KTI).

References

- [1] T. F. Page, W. C. Oliver and C. J. McHargue; *J. Mater. Res.*, **7** (3) (March 1992).
- [2] P. Grodzinski; *Plastics*, **18** (1953) 312-314.
- [3] M. Nishibori and K. Kinoshita; *Thin Solid Films*, **48** (1978) 325-331.
- [4] J. Loubet, J. M. Georges, D. Marchesini and G. Meille; *J. Tribology*, **106** (1984) 43-48.
- [5] W. D. Nix; *Metall. Trans.*, **20** (1989) 2217-2245.
- [6] J. B. Pethica, R. Hutchings and W. C. Oliver; *Philos. Mag. A*, **48** (1983) 593-606.
- [7] W. C. Oliver; *MRS Bulletin* (October 1986) 15-19.
- [8] M. F. Doerner and W. D. Nix; *J. Mater. Res.*, **1** (4) (1986) 601-609.
- [9] E. T. Lilleodden, W. Bonin, J. Nelson, J. T. Wyrobek and W. W. Gerberich; *J. Mater. Res.*, **10** (9) (September 1995) 2162-2165.
- [10] A. R. Machcha, M. H. Azarian and F. E. Talke; *An investigation of Nano-wear during contact recording*, to be published, 1996.
- [11] T. F. Page and S. V. Hainsworth; *Surface and Coatings Tech.*, **61** (1993) 201-208.
- [12] G. M. Pharr and W. C. Oliver; *MRS Bulletin* (July 1992) 28-33.
- [13] E. R. Weppelmann, J. S. Field and M. V. Swain; *J. Mater. Res.*, **8** (4) (April 1993) 830-840.
- [14] M. Binggeli, R. Christoph, H. Hintermann and O. Marti; *Surface and Coatings Tech.*, **62** (1993) 523-528.
- [15] G. Hoyle; *High Speed Steel*, Butterworth, 1988, p. 93.
- [16] Brite Euram Optistra project report, No. BRE2-CT93-0622.
- [17] C. S. Wright and B. Ogel; *Powder Metallurgy*, **36** (3) (1993) 213-219.
- [18] J. D. Bolton and A. J. Gant; *Powder Metallurgy*, **36** (4) (1993) 267-274.
- [19] N. A. Stelmashenko, M. G. Walls, L. M. Brown and Yu. V. Milman; *Acta Metall. et Mater.*, **41** (10) (1993) 2855-2865.
- [20] D. L. Callahan and J. C. Morris; *J. Mater. Res.*, **7**, (7) (July 1992) 1614-1617.
- [21] T. O. Mulhearn and L. E. Samuels; *Journal of the Iron and Steel Institute*, **180** (1955) 245-254.

7.3 Novel nanoindentation method for characterising multiphase materials

Paper presented at the International Conference on Metallurgical Coatings and Thin Films (ICMCTF 97), San Diego, USA, April 1997 and published in Thin Solid Films 308-309 (1997) 297-303

Novel nanoindentation method for characterising multiphase materials

N. X. Randall ^{a,*}, C. Julia-Schmutz ^a, J. M. Soro ^b, J. von Stebut ^b and G. Zacharie ^c

^a Centre Suisse d'Electronique et de Microtechnique S.A., Jaquet-Droz 1, 2007 Neuchâtel, Switzerland

^b L. S. G. S., URA CNRS 1402, INPL, Ecole des Mines, 54042 Nancy, France

^c Electricité de France, D. E. R., E. M. A., Les Renardières, 77250 Morêt-sur-Loing, France

Abstract

We present the Nano-Hardness Tester (NHT), a new depth-sensing instrument with a differential capacitive sensor providing nanometer depth resolution and allowing partial elimination of the frame compliance. With micron lateral positioning of the sample and topographical measurement of the residual indent, using scanning force microscopy, it is possible to gain a better understanding of the indentation method and its effects on the material being tested. Furthermore, parallel imaging allows the material response to be directly investigated. Experimental results are presented for a selection of aged austeno-ferritic stainless steels, these confirming the ability of the NHT to become a common test instrument in quality assurance and process development of multiphase materials. © 1997 Elsevier Science S. A.

Keywords: Nano-hardness tester; Scanning force microscopy; Multiphase materials

1. Introduction

In recent years the term *nanoindentation* has been applied to depth-sensing indentation testing methods where the size of the residual imprint is of a nanometer scale and where it is too small to be accurately resolved by optical microscopy. Such size limitation has led to a number of techniques for continuously measuring force and displacement as an indenter, of known geometry, is pressed into a sample material [1-5]. The applied force is usually generated via an electromagnet, in which case the current in the coil determines the load, or by a piezoelectric actuator (displacement control) where the inherent inaccuracies in such a system are corrected by interferometry. In most cases, the displacement is measured by a capacitive sensor. With instruments now having microNewton force and nanometer depth resolutions it is possible to produce load-displacement curves representative of the material response in terms of hardness and modulus [6], although a true understanding of the elastic/plastic interactions occurring at the indenter/surface interface is still incomplete from indentation data alone.

Surface imaging techniques have become increasingly important for characterising surface deformation in and

around the indentation area, and for making precise measurements of residual depth and pile-up material. One such technique is the scanning electron microscope (SEM) [7,8] but this has the disadvantage of having to coat non-conducting samples with conducting films whose thickness is of the same order as the indentation depth, and the contrast limitations in obtaining quantitative depth measurements. Scanning probe techniques, especially scanning force microscopy (SFM), are one of the few types of imaging instrument capable of making quantitative measurements at such small scales with nanometric precision and three-dimensional imaging capability [9-12]. In addition, the SFM principle has been used for indenting and imaging with the same tip, made possible by the partial elastic recovery of the imprint [13-15].

Having established the need for combining indentation techniques with suitable imaging methods, there remains the difficulty of accurately positioning the sample so that a specific site can be quickly and efficiently located prior to and after indentation. In this paper a novel nanoindentation technique is presented together with a combined optical/scanning force microscopy set-up capable of accurately imaging residual indentations with nanometer resolution. The samples have been chosen owing to their dual-phase nature, to the fact that their separate phases exhibit a different response to indentation, and because of their industrial importance in nuclear reactors.

* Corresponding author.

2. Experimental

2.1. Instrumental set-up

The apparatus consists of two separate instruments, a Nano Hardness Tester (NHT) and a combined optical/scanning force microscope (SFM) system [16], both developed by CSEM Instruments. The NHT comprises two distinct components, a measuring head for performing indentations and an optical microscope for selecting a specific sample site prior to indentation and for checking the location of the imprint after indentation. Both components are directly linked by an electro-mechanical positioning system which allows movement along two perpendicular horizontal axes with a lateral displacement resolution of $1\mu\text{m}$. This instrument is a development of an earlier ultramicrohardness tester [17] which is based on existing technology [18] and its principle is depicted in Fig. 1. The load is directly applied by an electromagnet assembly to a vertical rod, the end of which houses a standard Vickers diamond indenter. Displacement of the rod is measured by a capacitive detector and the rod is supported by two guide springs. The system has load and displacement resolutions of $10\mu\text{N}$ and $< 1\text{nm}$ respectively.

The NHT (see Fig. 2) has several advantageous features, in particular its differential measurement of the indentation depth, made possible by a sapphire reference ring which remains in contact with the sample during the loading/unloading cycle, giving exact positioning of the indenter tip relative to the sample surface. Thus the overall elastic recoil of the sample and partial frame compliance are compensated, as is most of the associated thermal drift during measurement.

Having performed an indentation at a specific site, the sample is switched to the optical/scanning force microscope

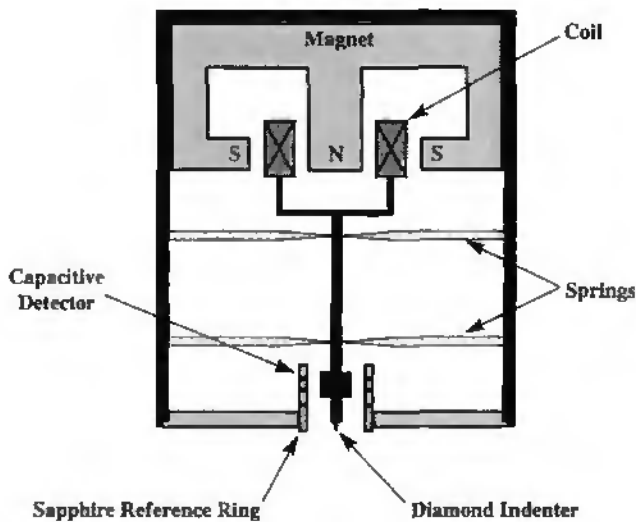


Fig. 1. The basic principle of the NHT's measuring head showing the coil and magnet assembly (applied load) and the differential capacitive detector (displacement).

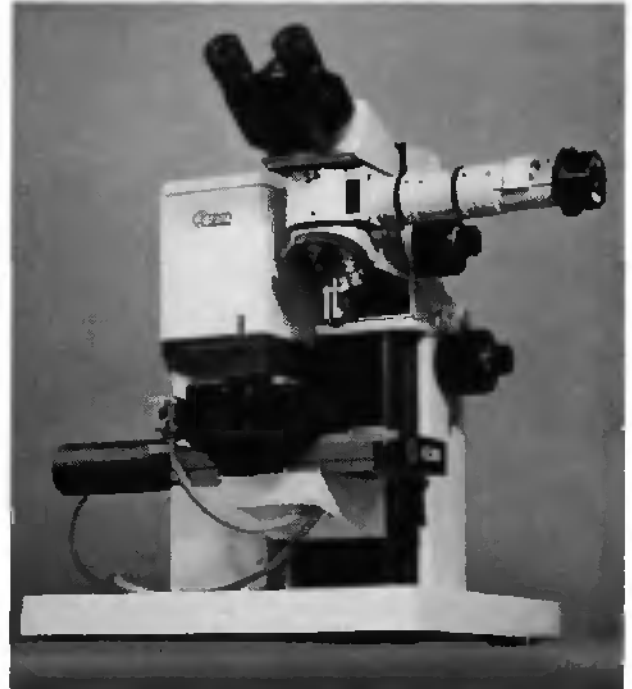


Fig. 2. The complete NHT instrument showing the displacement table for locating the sample either under the measuring head or the integrated optical microscope.

system which permits the residual imprint to be located within the $30\mu\text{m}$ scan range of the SFM via an electro-mechanical positioning system similar to that of the NHT. The particular SFM used was an Atomic Scale Tribometer [19], a stand-alone instrument having sub-nanometer lateral and vertical displacement resolution.

2.2. Sample materials

The samples studied consisted of duplex stainless steels which are widely used in primary cooling circuits of Pressure Water Reactor (PWR) nuclear plants. Such steels are known to be susceptible to long term ageing at intermediate temperatures ($300\text{--}400^\circ\text{C}$). It is now well established that this ageing is due to microstructural evolution of the ferritic phase.

Experimental methods such as TEM, atom probe analysis and neutron scattering have revealed two major phenomena in the ferritic phase [20,21]:

1. Spinodal decomposition of the ferritic Fe-Cr solid solution which leads to the formation of α' Cr enriched domains.
2. Precipitation of an intermetallic compound (G phase) which essentially grows at the α/α' interface.

The chemical composition of the studied duplex stainless steel is shown in Table 1 and the different ageing and heat treatments are shown in Table 2. Water quenching was used to avoid formation of a brittle σ phase. The unaged sample is referred to as C0 whereas the two aged samples are

Table 1

Chemical composition of duplex stainless steel (wt %)

C	P	Si	Mn	Ni	Cr	Mo	N	Nb
0.038	0.027	1.20	0.71	10.43	22.11	2.75	0.042	0.21

referred to as C6 and C7. The microstructure, consisting of austenite in a ferritic matrix, was revealed by mechanical polishing with alumina particles (0.3 μm) followed by etching in electrolytic oxalic acid. The volume fraction of ferrite, determined by surface image analysis, was found to be about 30%. The mean size of the ferrite and austenite grains were 20 and 40 μm respectively [22]. Precise positioning of indentations in the centre of a selected grain and indent sizes at least five times smaller than the grain diameter were important considerations in gaining specific information about mechanical properties.

2.3. Experimental procedure

2.3.1. Calibration of instrument compliance

In order to take into account the frame compliance, both the frame and the sample are simply modelled as two springs in series [18]. The total measured compliance (after correction of the spring compliance), C_{total} , is the sum of the contact compliance, $C_{contact}$, and the frame compliance, C_{frame} :

$$C_{total} = C_{contact} + C_{frame} \quad (1)$$

The total compliance is given by :

$$\frac{1}{C_{total}} = \left(\frac{dP}{dh} \right)_{max} \quad (2)$$

where $(dP/dh)_{max}$ denotes the initial slope of the unloading curve. The reduced Young's modulus, E_r , is given by Sneddon's equation [23] :

$$E_r = \frac{1}{2\beta} \sqrt{\frac{\pi}{A_c}} \cdot \frac{1}{C_{contact}} \quad (3)$$

where A_c represents the projected contact area at maximum load, and β a constant which depends on indenter geometry [24] :

- for a spherical indenter, $\beta = 1$
- for a Berkovich indenter, $\beta = 1.034$
- and in our case, for a Vickers indenter, $\beta = 1.011$

E_r , the reduced Young's modulus, can be expressed as :

$$\frac{1}{E_r} = \frac{(1-\nu_s^2)}{E_s} + \frac{(1-\nu_0^2)}{E_0} \quad (4)$$

where ν_0 and E_0 are respectively the Poisson ratio and the elastic modulus of diamond ($\nu_0 = 0.07$, $E_0 = 1141$ GPa) and ν_s and E_s , the Poisson ratio and the elastic modulus of steel ($\nu_s = 0.3$).

The instrument compliance was determined by performing indentations at different loads on an elastically isotropic material. Such a material is fused silica ($\nu = 0.17$, $E = 72$ GPa) for which the total compliance is of the form:

$$C_{total} = C_{frame} + \frac{12575}{\sqrt{A_c}} \quad (5)$$

For this relationship, C_{total} is obtained directly from the indentation curve, whereas A_c depends on C_{frame} . A simple iterative procedure is therefore used to determine the instrument compliance by estimating C_{frame} and correcting it until convergence is achieved using the equation:

$$A_c = \frac{(12575)^2}{(C_{total} - C_{frame})^2} = \frac{(12575)^2}{(C_{contact})^2} \quad (6)$$

Such a procedure allows us to determine a value of C_{frame} of about 0.16 nm mN^{-1} which is ten times less than the frame compliance values of Nanoindenter II [18] or obtained more recently with a new instrument from Poitiers [25].

2.3.2. Calibration of tip defect for the Vickers indenter

At very shallow indentation depths and low loads it is particularly important to correct for deviations from an ideally perfect indenter geometry. This was first performed by Pethica *et al.* [1] whose method consisted of replicating an indentation with a soft material and measuring the contact area with a scanning electron microscope. The method used by Loubet *et al* [24] and Carpentier [27] consists of plotting the plastic penetration depth, h_c , determined from indentation curves, as a function of the imprint diagonal which is measured by optical microscopy. This procedure is carried out for different materials and at different loads. Carpentier noticed that the tip factor depends not only on the tip shape, but also on the ratio (E/H) which characterises the resistance to plastic deformation of the indented material.

For the present study, the Vickers indenter was calibrated via an *indirect* method which does not necessitate direct

Table 2

Heat treatment and ageing of duplex stainless steel samples

Sample	Heat Treatment ($^{\circ}\text{C-h}$)	Ageing time (h)	Ageing temperature ($^{\circ}\text{C}$)
C0	1120-9 followed by water quenching	None	None
C6		8000	350
C7		1000	400

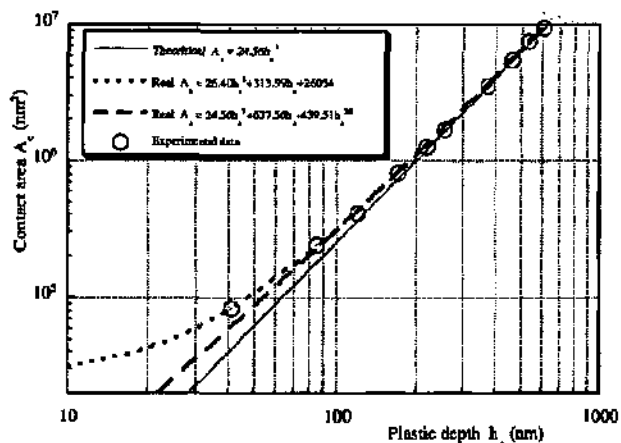


Fig. 3. Tip defect for the Vickers indenter; the bold line represents the theoretical projected contact area ($24.56 h_c^2$), the dotted line the real projected contact area.

measurement of imprint dimensions. Instead, the contact compliance, $C_{contact}$, and the plastic penetration depth, h_c , must be determined for a large number of indentations at varying depths made in an isotropic material with uniform hardness. Such a procedure was carried out using a calibrated fused silica sample and defining A_c in terms of $C_{contact}$ (eqn (6)). The corresponding h_c value was obtained by extrapolating the initial slope of the unloading curve. The tip defect for the Vickers indenter is shown in Fig. 3. By interpolating the experimental points as a polynomial function, the real contact area of the indenter can be defined:

$$A_c = 24.56h_c^2 + 637.90h_c - 439.51h_c^{1/2}$$

It can be seen that the tip defect begins to be noticeable at depths less than ~ 400 nm, and that the real contact area is better described, for small depths, by a 2nd order polynomial:

$$A_c = 26.41h_c^2 + 313.99h_c + 26054$$

The effect of the indenter calibration can be shown by measuring the hardness of fused silica with and without such correction (Fig. 4). Implementing a tip defect correction

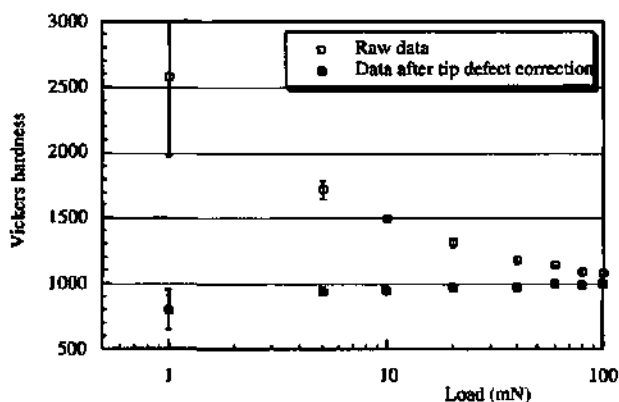


Fig. 4. Influence of tip defect correction on the Vickers hardness at low loads on fused silica.

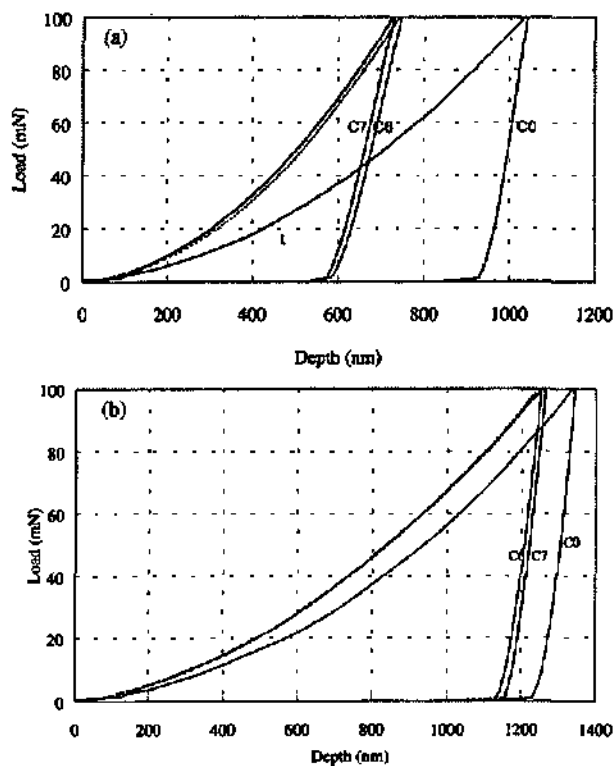


Fig. 5. Indentation curves for the three ageing conditions with a maximum load of 100 mN for (a) the ferrite phase and (b) the austenite phase.

allows the assumption that subsequent measurements will be free from artefacts related to indentation depth.

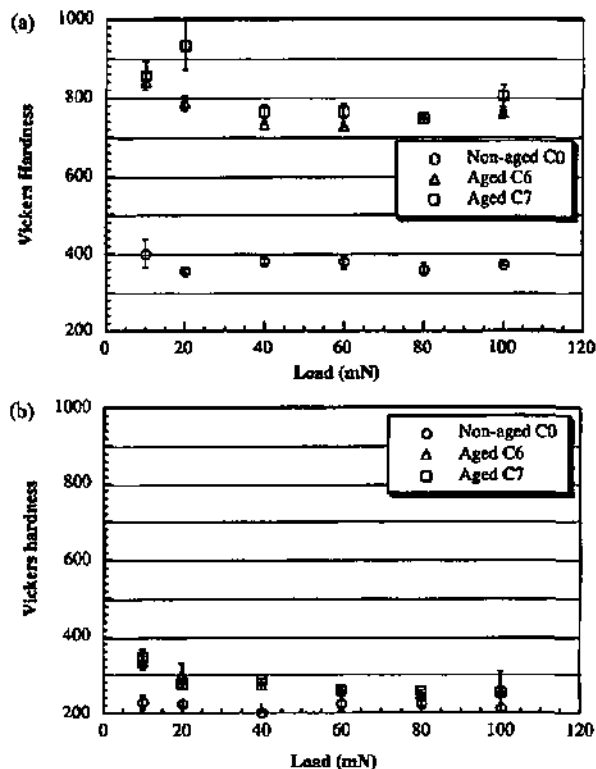


Fig. 6. Influence of ageing on the Vickers hardness of (a) ferrite and (b) austenite phases for different loads.

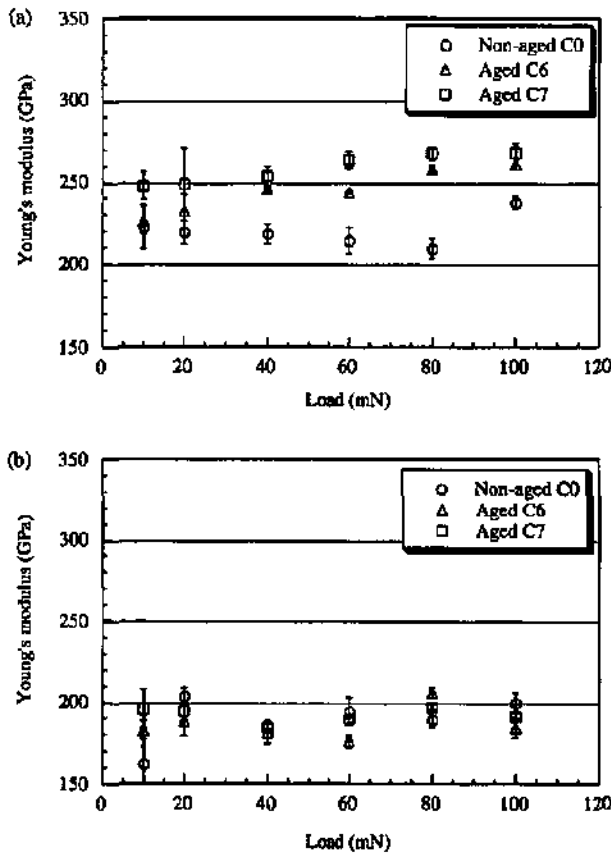


Fig. 7. Influence of ageing on the Young's modulus of (a) ferrite and (b) austenite phases for different loads.

3. Results and discussion

Fig. 5a shows that for an applied load of 100 mN a hardening of the ferrite phase is observed as a result of ageing. Fig. 5b and 6b show the same measurements performed on the austenite phase and a similar hardening effect upon ageing is evident, but to a lesser extent than for the ferrite. In the case of the austenite, such a phenomenon has not previously been noticed due to limitations in conventional microhardness-testing instruments.

Fig. 6a confirms the different levels of hardness of the ferrite as well as the stronger influence of ageing. It can be seen that the hardness increases as the applied load decreases, but this effect cannot be attributed to error in the indenter calibration. This phenomenon, well known as the indentation size effect, has already been described in the literature but different explanations have been given, such as the increase of elastic contribution in indentation due to anisotropic dislocation patterns [28] or friction between indenter and surface [29, 30]. In addition, hardening effects very close to the surface may exist owing to the polishing procedure and the presence of surface oxide films.

Fig. 7 shows that ageing of the ferritic phase leads also to a slight increase in the Young's modulus (approximately 10%). In order to find out how the dislocation mechanism is involved, internal friction measurements would be useful.

On the other hand, considering experimental errors, the Young's modulus of the austenite phase remains constant after ageing.

The SFM images of indentations on both the austenite and ferrite phases are shown on Fig. 8 together with their corresponding cross-sections and load/displacement curves. It is particularly interesting to note the difference between the shape of the residual imprint on each type of phase. For the austenite, the edges of the imprint are convex which would suggest an elastoplastic deformation mode with radial relaxation of material around the indentation during withdrawal of the indenter. On the contrary, the imprint on the ferrite phase exhibits concave imprint edges together with bulging and pile-up of material around the imprint. This phenomenon confirms the rigid/plastic deformation mode of the ferritic phase. It has already been shown [31] that distortion at the edges of a Vickers indent is directly linked to the elastic properties of the material. The SFM also proved an ideal tool for measuring the residual imprint depth (Fig. 8b, c), this correlating well with that obtained with the NHT (Fig. 8a). The aforementioned concave nature of the imprints was greater for the aged samples than for the unaged samples, possibly due to the immiscibility of the solid solution which takes place with ageing and subsequent hardening.

4. Conclusions

The NHT has been introduced as a valid and practical method for investigating and controlling the ageing of austeno-ferritic stainless steels and has clear advantages over conventional methods, especially in terms of resolution, positioning accuracy and its quasi non-destructive measuring ability. The differential indentation method has been shown to have enhanced precision, a low effective frame compliance and low drift. A satisfactory tip defect correction has been demonstrated, as has the application of the NHT to selective indents in individual grains. It has been possible to show the effects of ageing both in the ferrite and austenite phases, the latter having not been previously possible with microhardness testing. The SFM, when combined with a nanoindentation instrument, has been shown to provide substantial additional information, namely:

- Confirmation that the NHT is accurately calibrated by being able to double check the residual imprint depth.
- High resolution imaging of the residual imprints and the surrounding surface morphology.
- Quantitative information relating to piling-up and sinking-in of imprints.

Future work will include similar measurements using a Berkovich indenter as the tip error is less pronounced and a spherical indenter in order to extract stress/strain curves for each phase. The results obtained in this work confirm the ability of the NHT to test the mechanical properties of thin films with a thickness less than 5 μm .

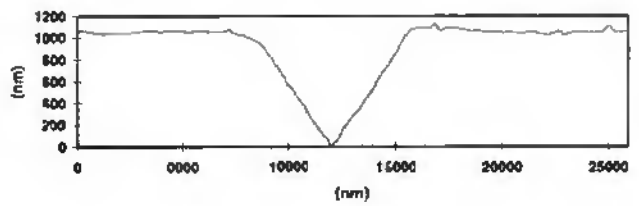
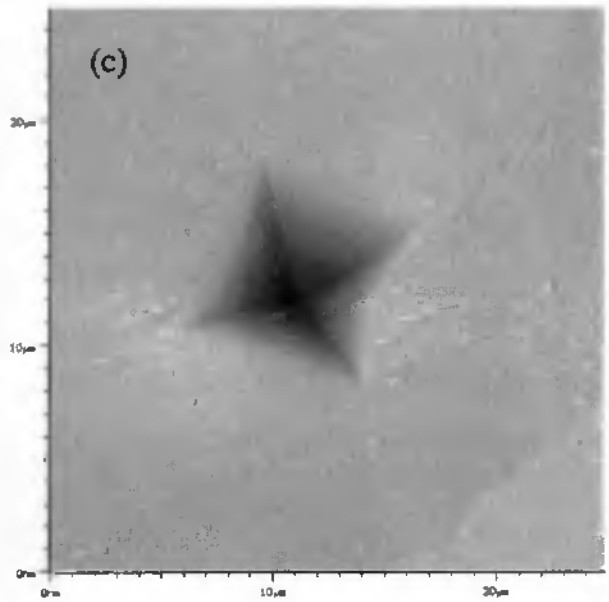
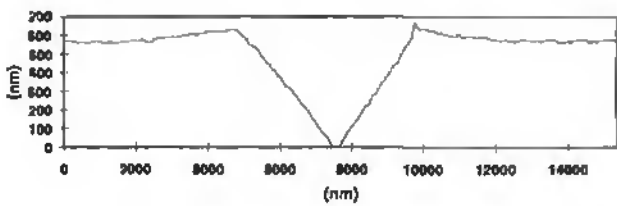
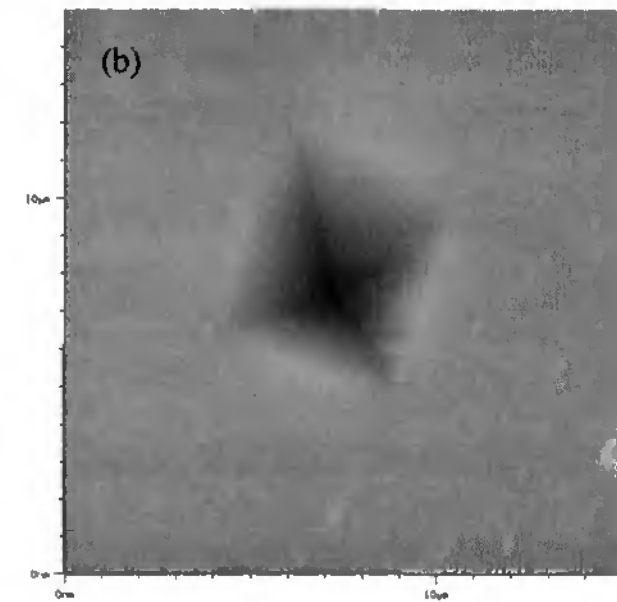
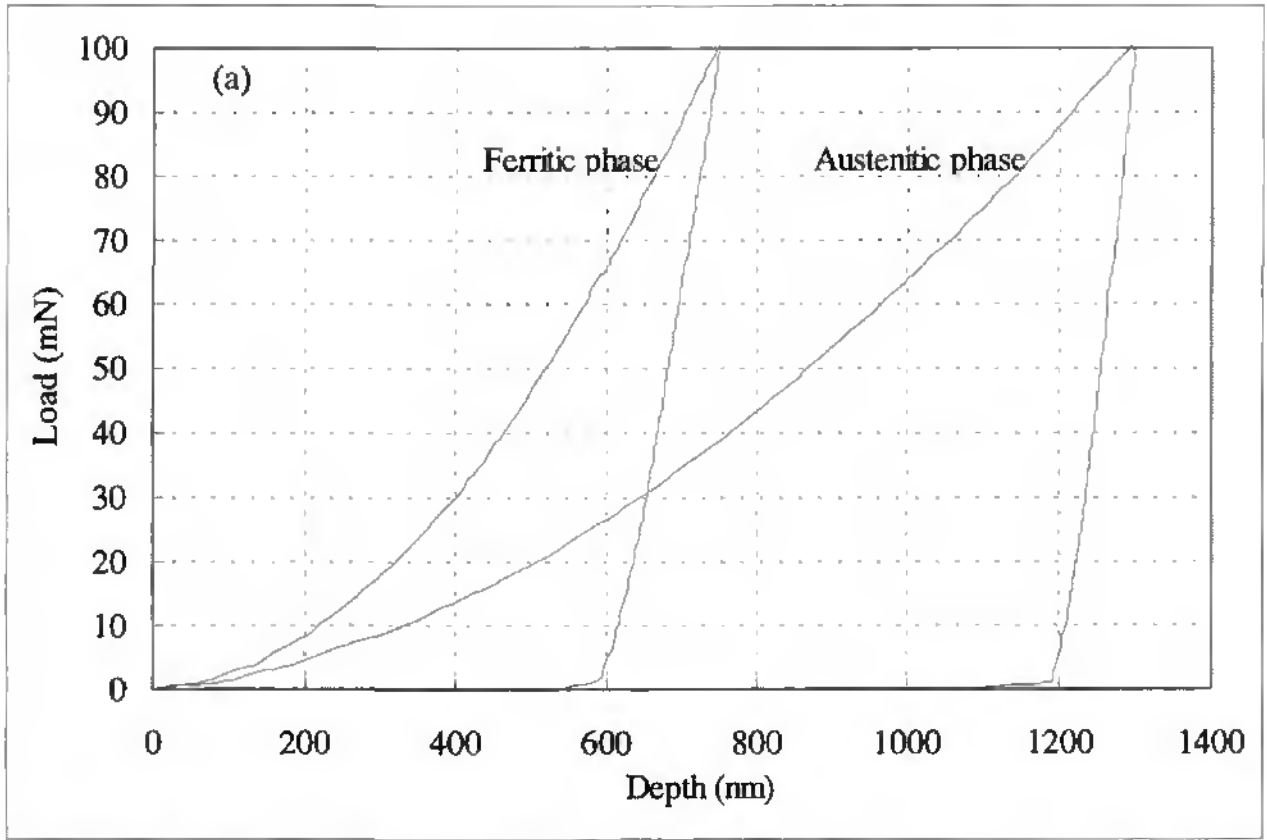


Fig. 8. Indentation curves (max. load = 100 mN) for ferrite and austenite phase (a), together with the corresponding SFM images of the residual imprints for (b) ferrite and (c) austenite and their respective cross-sections. Note the convex and concave nature of the imprints.

References

- [1] J.B. Pethica, R. Hutchings and W.C. Oliver, *Philos. Mag. A*, **48** (1983) 593-606.
- [2] J. Loubet, J.M. Georges, D. Marchesini and G. Meille, *J. Tribology*, **106** (1984) 43-48.
- [3] T.F. Page, W.C. Oliver and C.J. McHargue, *J. Mater. Res.*, **7** (1992) 450-473.
- [4] B. Bhushan, V.S. Williams and R. V. Shack, *Trans. ASME J. Tribology*, **110** (1988) 563-571.
- [5] M. Nishibori and K. Kinoshita, *Thin Solid Films*, **48** (1978) 325-331.
- [6] H.M. Pollock, ASM Handbook, Vol. 18, ASM International, Ohio (1992) 419-429.
- [7] W.C. Oliver, *MRS Bulletin*, **11** (1986) 15-19.
- [8] H. Bangert and A. Wagendristel, *Rev. Sci. Instrum.*, **56** (1985) 1568-1572.
- [9] E.T. Lilleodden, W. Bonin, J. Nelson, J.T. Wyrobek and W.W. Gerberich, *J. Mater. Res.*, **10** (1995) 2162-2165.
- [10] N.A. Stelmashenko, M.G. Walls, L.M. Brown and Y.V. Milman, *Acta Metall. et Mater.*, **41** (1993) 2855-2865.
- [11] S.V. Hainsworth, H. Sjöström, T.F. Page and J.E. Sundgren, in *Thin Films: Stresses and Mechanical Properties VI* (edited by W. W. Gerberich et al), MRS Symposium Proceedings, 1996.
- [12] M.G. Walls, M. Munawar Chaudhri and T.B. Tang, *J. Appl. Phys. D*, **25** (1992) 500-507.
- [13] S. Bec, A. Tonck, J.M. Georges, E. Georges and J.L. Loubet, *Phil. Mag. A*, **74** (1996) 1061-1072.
- [14] B. Bhushan, I.N. Israelachvili and U. Landman, *Nature*, **374**, N^o.6523 (1995) 607-616.
- [15] B. Wei and K. Komvopoulos, *J. Tribology*, **117** (1995) 594-601.
- [16] N.X. Randall, R. Christoph, S. Droz and C. Julia-Schmutz, *Thin Solid Films*, **290-291** (1996) 348-354.
- [17] H.E. Hintermann, *Fresenius J. Anal. Chem.*, **346** (1993) 42-52.
- [18] W.C. Oliver and G.M. Pharr, *J. Mater. Res.*, **7** (1992) 1564-1583.
- [19] M. Binggeli, R. Christoph, H. Hintermann and O. Marti, *Surface and Coatings Technol.*, **62** (1993) 523-528.
- [20] P. Auger, F. Danoix, A. Menand, S. Bonnet, J. Bourgoin and M. Guttmann, *Mat. Sci. Tech.*, **6** (1990) 301-313.
- [21] P. Auger, F. Danoix, O. Grisot, J.P. Massoud and J.C. van Duysen, *Annales de Physique, Colloque C3*, supplement to No. 3, **20** (1995).
- [22] B. Verhaeghe, 'Microstructural study of deformation and rupture modes in an aged austeno-ferritic steel', E. D. F. Report HT-41/96/010/A (1996).
- [23] I.N. Sneddon, *Int. J. Engng. Sci.*, **3** (1965) 47-57.
- [24] R.B. King, *Int. J. Solids Struct.*, **23** (1987) 1657-1664.
- [25] J.C. Dargenton, PhD Thesis, Université de Poitiers (France), Laboratoire de Métallurgie Physique (1996).
- [26] J. L. Loubet, J. M. Georges and G. Meille in *Microindentation Techniques in Materials Science and Engineering*, ASTM STP 889 (Edited by P. J. Blau and B. R. Lawn) ASTM (1986) 72-89.
- [27] L. Carpentier, PhD Thesis, Ecole Centrale de Lyon (France), Laboratoire de Tribologie et Dynamique des Systèmes (1994).
- [28] K. Yasuda, K. Shinohara, C. Kinoshita, M. Arai in *Strength of materials* (Edited by Oikawa et al.) The Japan Institute of Metals (1994) 865-868.
- [29] H. Shi, M. Atkinson, *J. Mater. Sci.*, **25** (1990) 2111-2114.
- [30] H. Li, A. Ghosh, Y.H. Han, R.C. Bradt, *J. Mater. Res.*, **8** (1993) 1028-1032.
- [31] D. Chicot, I. Hage and J. Lesage, *La Revue de Metallurgie-CIT, Science et Genie des Materiaux*, **5** (1995) 636-643.

7.4 Characterisation of DLC multilayers by nanoindentation and scanning force and friction microscopy

Paper presented at the Journées Internationales Francophones de Tribologie (JIFT 97), Neuchâtel, Switzerland, March 1997 and published in Tribologie et Précision, Actes des Journées Internationales Francophones de Tribologie 1997 (editor M. Maillat)

(Translated from the French original)

CHARACTERISATION OF DLC MULTILAYERS BY NANOINDENTATION AND SCANNING FORCE AND FRICTION MICROSCOPY

Nick X. Randall

CSEM Instruments, Jaquet-Droz 1, CH-2007 Neuchâtel, Switzerland

Abstract:

Diamond-like carbon (DLC) has recently become a very important material in applications where the hardness and wear are critical parameters. A new method is presented where the hardness of a multilayer can be measured, and such data combined with that of a microscope capable of simultaneously measuring topographical and frictional properties. This is achieved by coupling a nanoindentation instrument to a scanning force and friction microscope (FFM) via a highly precise mechanical positioning stage which allows an indentation to be located quickly and efficiently under the FFM. Results are presented for an amorphous DLC multilayer having a bilayer thickness of approximately 40nm, for which the friction coefficients of separate layers can be determined by making an indentation and subsequently imaging the imprint with a FFM.

INTRODUCTION

In recent years, the term nanoindentation has been applied to depth-sensing indentation testing methods where the size of the residual imprint is of a nanometer scale and where it is too small to be accurately resolved by optical microscopy. Several techniques have been developed [1-3] for which the applied force is usually applied via an electromagnet and the displacement measured by a capacitive sensor. With force and displacement resolutions in the ranges 10nN and 0.1nm respectively, such instruments are able to produce load-displacement curves that give an accurate representation of the material response, and from which the hardness and modulus can be calculated.

Additional topographical information has become increasingly important for characterising the morphology of an indented area but has been limited by the high resolution needed to accurately image such small imprints and by the difficulties in locating an indented area.

The introduction of scanning force microscopy (SFM) and its related techniques has provided one of the few types of imaging instrument capable of making quantitative measurements at such small scales with nanometric precision and three-dimensional imaging capability [4-6]. Friction force microscopy (FFM), first developed by *Mate et al* [7], has allowed material contrast to be measured due to local variations in friction coefficient. Wearless friction, a common phenomenon in SFM, has been identified as a key goal for the microtribology of very lightweight sliding parts [8].

FFM has already been used to characterise a wide variety of surfaces [9-10] by combining its surface topographical and frictional imaging capabilities. Frictional contrast is achieved experimentally by allowing the normal force F_N to vary during scanning, after which a two-dimensional histogram can be plotted

of lateral force F_L versus F_N . Regions of the surface with different friction coefficients are found to lie along different straight lines in the histogram and can thus be attributed to different materials depending on their location on the histogram. Such a method eliminates the need to calibrate the zero point of the true normal force of the point contact which is difficult because of the presence of van der Waals and capillary attractive forces.

In this paper, the applicability of FFM is demonstrated with regard to gaining additional information from a nanoindentation experiment. By combining both techniques, the hardness/modulus data can be added to the frictional data in order to better interpret the nanotribological properties of the tested material. Results are presented for an amorphous DLC multilayered coating and for a gold-coated mica sample.

EXPERIMENTAL

The apparatus consists of a combined system comprising a CSEM Nano Hardness Tester (NHT) and a SFM, both being directly linked by an electro-mechanical positioning system which allows movement in two perpendicular horizontal axes with a lateral displacement resolution of 1 μ m [11]. The NHT is a depth-sensing instrument having a vertical displacement resolution of 1nm and its principle is described elsewhere [12]. The NHT has several advantageous features, in particular its differential measurement of the indentation depth, made possible by a sapphire reference ring which remains in contact with the sample during the loading/unloading cycle, giving exact positioning of the indenter tip relative to the sample surface. Thus the elasticity of the sample and frame compliance are compensated, as is thermal drift during measurement.

The SFM was a CSEM Atomic Scale Tribometer (AST), a stand-alone instrument capable of simultaneous measurement of normal and lateral (friction) forces using a four-quadrant position-sensitive detector [13].

Two types of samples were used to demonstrate the effectiveness of the experimental set-up. The first consisted of an amorphous DLC multilayer deposited onto a 440C steel substrate by plasma-activated chemical vapour deposition (PACVD). The main gas used was acetylene for the deposition itself after a 2 minute argon pre-etching stage. The temperature on the surface of the sample did not exceed 150°C. The multilayer was built up by alternating the substrate potential between -76V and -288V such that two layers were produced having a nominal thickness of approximately 20nm. The total multilayer thickness was of approximately 4µm. In addition to the multilayer sample, two identical substrates were deposited, one at -76V and one at -288V, in order to compare their properties with those of the mixed sample.

The second type of sample consisted of a gold thin-film coating deposited onto a mica substrate by sputtering and having a thickness of 200nm. This sample was used to show the applicability of FFM to standard coated systems.

The experimental procedure on both sample types was as follows:

- (i.) The sample was located under the NHT measuring head and a series of indentations carried out with a Vickers indenter. For the multilayer sample, the maximum depth was controlled such that it did not exceed one tenth of the total coating thickness (to prevent any contribution from the substrate). For the gold coating, the indentation depth was increased so that the substrate was reached.
- (ii.) The sample was subsequently positioned under the SFM and the indented area imaged by simultaneously recording both the normal and lateral forces. A silicon cantilever of tip radius <150Å was used and the force calibration was performed as described elsewhere [14].
- (iii.) A 2D histogram was built up by plotting F_L versus F_N , from which the separate friction coefficients could be calculated from the slopes of the lines attributed to different materials.

RESULTS AND DISCUSSION

The values of Vickers hardness and Young's modulus for both sample types are summarised in Table 1, as are the coefficients of friction between the silicon cantilever and each material type.

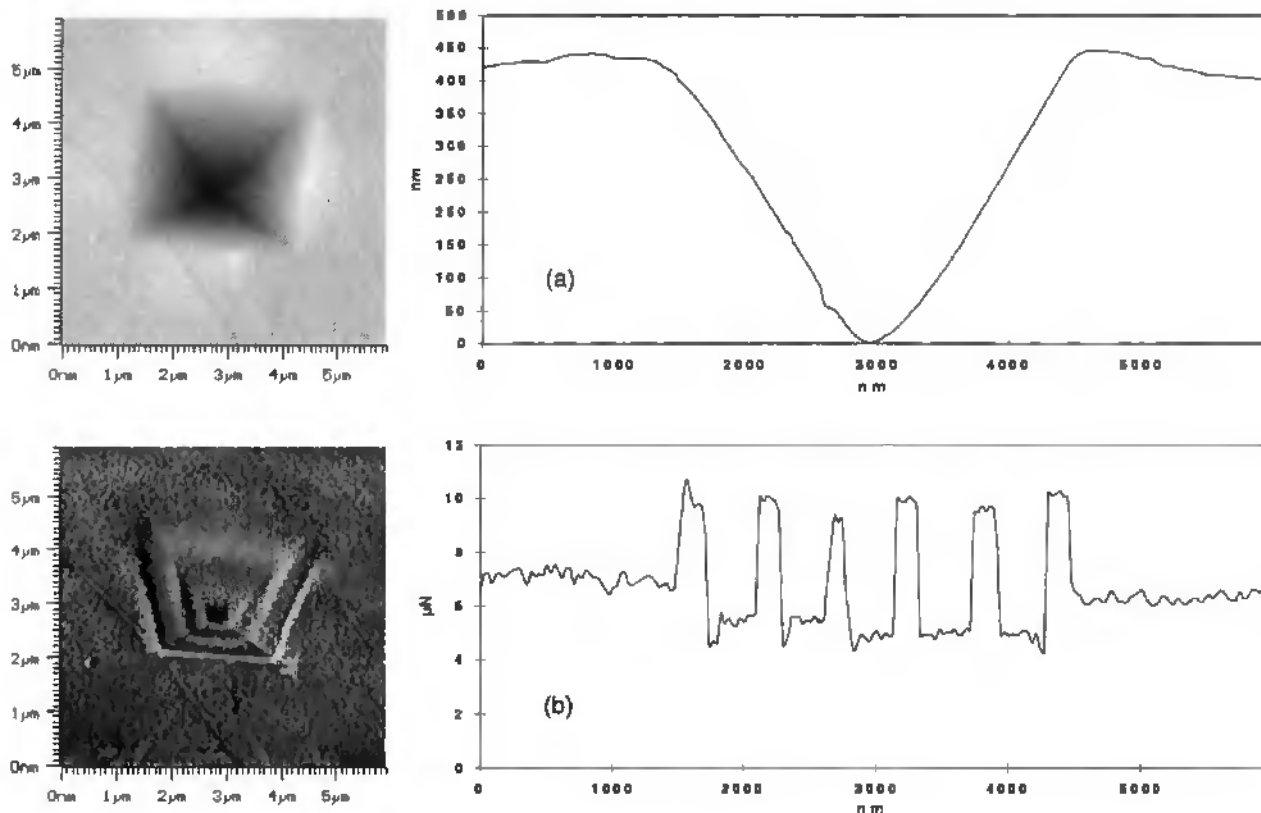


Figure 1 : SFM images of an indentation into an amorphous DLC multilayer with corresponding cross-sections; (a) represents the topographical image where no evidence of the multilayer structure is visible, whereas (b) shows the lateral force image in which layers having different frictional properties can be discerned. The non-symmetrical nature of the imprint is an imaging artefact due to non-linearity of the piezoelectric scanner.

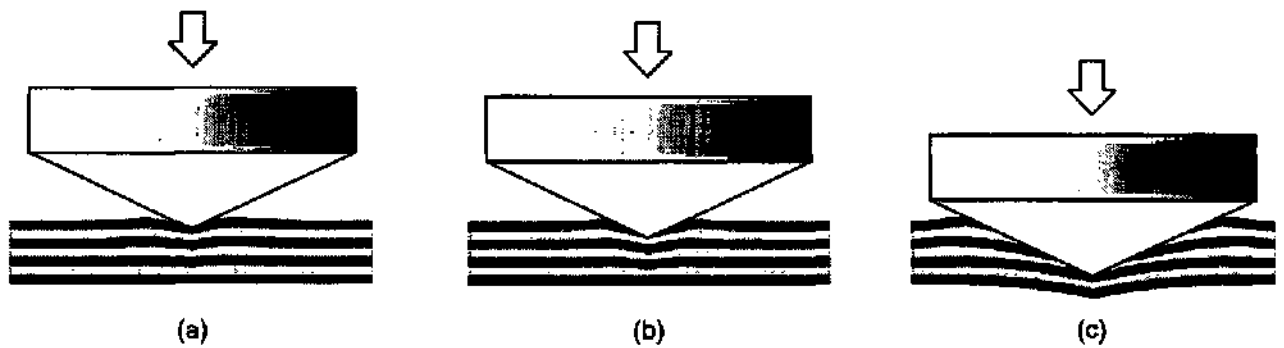


Figure 2 : Schematic representation of a Vickers indenter penetrating a multilayer. After initial contact, the uppermost layer deforms without fracture (a) after which, at a certain critical force, this top layer yields and fractures (b). Smearing of the layers occurs at the maximum penetration depth (c).

Fig. 1 shows the SFM results for the DLC multilayer sample, including the topography and friction images and their respective cross-sections. It is interesting to note that no evidence of the multilayer is visible from the topography but becomes clear from the friction image. The hardness measurements showed that the layer produced at a potential of -76V had a hardness of 28.2GPa whereas that produced at -288V had a higher hardness of 37.3GPa, the combined multilayer having an intermediate hardness value of 31.7GPa. It was hoped that slope differences might be apparent on the loading/unloading curve but for such thin layers no significant variation could be observed with the NHT instrument. By building-up a 2D histogram it was found that the softer layer (-76V) had a friction coefficient of 0.19 and the harder layer (-288V) a coefficient of 0.08, against the silicon cantilever.

By superimposing the friction image cross-section onto that of topography, the layer thickness after indentation could be estimated and was found to be of the order 50-80nm. This was clearly much higher than the 20nm deposition thickness and can be explained as follows: After initial contact of the indenter with the multilayer, and with increasing normal force, the uppermost layers deform without fracture (Fig. 2(a)). At a certain critical force the top layer yields and fractures and material from this layer is smeared by the indenter as it subsequently penetrates the next layer (Fig. 2(b)). This continues until the maximum penetration depth is reached, at which the number of fractured layers is significantly less than the amount of layers present down to that depth, due to the elasticity of each layer combined with the smearing of material by the indenter (Fig. 2(c)). This simple model might help to explain the

above-mentioned 'thickness increase' observed after indentation.

The non-symmetrical nature of the imprints in Fig. 1 was due to a combination of non-linearity of the piezoelectric scanner and slight error in the horizontal alignment of the sample surface relative to the indenter.

Fig. 3(a) shows an SFM topographical image of an indentation into the gold-on-mica sample and it is immediately apparent that the pile-up can be quantitatively measured with this method, as can the secondary pile-up occurring within the imprint due to the indenter penetrating the mica substrate. The corresponding friction image (not shown) was used to calculate the 2D histogram represented in Fig. 3(b) from which the friction coefficients of the two different materials could be calculated (see Table 1).

Regarding the histogram method for evaluating friction coefficients it should be noted that the straight line plot of lateral force versus normal force is an average through a finite number of data points which have a certain dispersion. This may be due to variations in topography which, if the normal force is not controlled correctly, may affect the frictional data. In practice this effect was minimised by slowing down the feedback loop of the SFM system, which also allowed the effects of gradient changes (such as the faces of the indentation imprint) not to influence the frictional data too greatly. However, some filtering of the data was necessary in order to minimise plane defects.

	DLC (-76V)	DLC (-288V)	DLC Multilayer	Gold	Mica
Vickers hardness (GPa)	26.20	37.30	31.70	0.88	6.75
Young's modulus (GPa)	182.4	289.8	218.2	84.6	93.9
Friction coefficient	0.19	0.08	-	0.03	0.43

Table 1 : Summary of hardness, modulus and friction parameters for the measured samples.

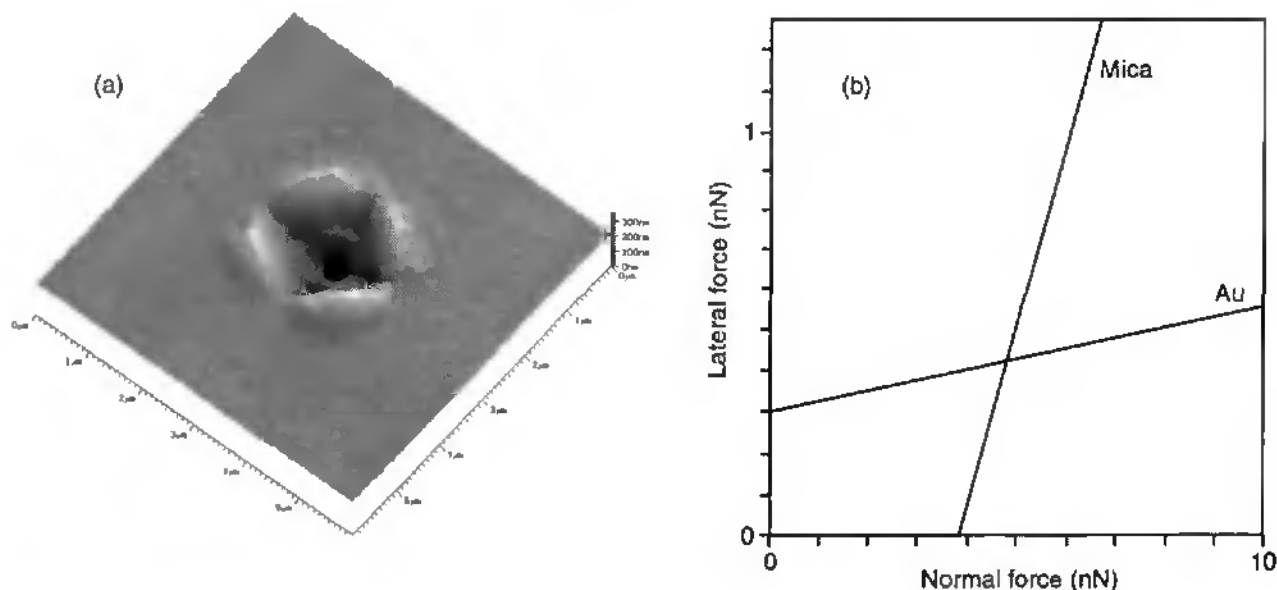


Figure 3 : Topographical 3D representation (a) of an indentation made through a 200nm gold film sputtered onto a mica substrate. Note the pile-up of material around the imprint and the effect of the substrate. The 2D histogram (b) was constructed from the corresponding friction force image and shows friction coefficients of 0.03 for the Au/Si pair and 0.43 for the mica/Si pair.

CONCLUSIONS

The SFM has been demonstrated as an important addition to a nanoindentation apparatus, allowing hardness and modulus data to be combined with high-resolution topographical information as well as frictional properties. With the objective of having a complete tribological testing system, the presented combined instrument has already proved itself for a more complete characterisation of surface coatings, namely thin films and multilayers. Future work will include the use of different tip materials so that microscale friction coefficients between other material pairs may be investigated and compared to existing data from macroscale wear studies.

REFERENCES

- [1.] J. B. Pethica, R. Hutchings and W. C. Oliver, *Philos. Mag. A*, 48 (1983) 593-606
- [2.] J. Loubet, J. M. Georges, D. Marchesini and G. Meille, *J. Tribology*, 106 (1984) 43-48
- [3.] T. F. Page, W. C. Oliver and C. J. McHargue, *J. Mater. Res.*, 7, No. 3 (1992)
- [4.] G. Binnig, C. F. Quate and C. Gerber, *Phys. Rev. Lett.*, 56 (1986) 930
- [5.] D. Sarid in *Scanning force microscopy*, Oxford University Press, New York (1991)
- [6.] D. Rugar and P. K. Hansma, *Physics Today* (Oct. 1990)
- [7.] C. M. Mate, G. M. McClelland, R. Erlandsson and S. Chiang, *Phys. Rev. Lett.*, 59 (1987) 1942-1945
- [8.] R. Kaneko, *Wear*, 168 (1993) 1-5
- [9.] O. Marti, *Physica Scripta*, T49, (1993) 599
- [10.] O. Marti, J. Colchero, H. Bielefeld, M. Hipp and A. Linder, *Microsc. Microanal. Microstruct.*, 4 (1993) 429
- [11.] N. X. Randall, R. Christoph, S. Droz and C. Julia-Schmutz, *Thin Solid Films*, 290-291 (1996) 348-354
- [12.] N. X. Randall, C. Julia-Schmutz, J. M. Soro, J. Von Stebut and G. Zacharie, to be published (1997)
- [13.] M. Binggeli, R. Christoph, H. E. Hintermann and O. Marti, *Surf. Coat. Tech.*, 62 (1993) 523-528
- [14.] P. Niedermann, J. Burger, M. Binggeli, R. Christoph, H. E. Hintermann and O. Marti, in *A scanning force and friction microscope*, NATO-ASI on Ultimate Limits of Scanning Probe Microscopy, Cambridge, England (April 1994)

7.5 Correlation between processing parameters and mechanical properties as a function of substrate polarisation and depth in a nitrated 316L stainless steel using nanoindentation and scanning force microscopy

Paper published in Vacuum 48 (10) (1997) 849-855



Correlation between processing parameters and mechanical properties as a function of substrate polarisation and depth in a nitrided 316L stainless steel using nanoindentation and scanning force microscopy

N X Randall^a, N Renevier^b, H Michel^c and P Collignon^d, ^aCSEM Instruments, Jaquet-Droz 1, CH-2007 Neuchâtel, Switzerland; ^bBalzars S. A., Z. A., Rue J. Monnet, 68390 Sausheim, France; ^cLaboratoire de Science et Génie des Surfaces (URA CNRS 1402), Ecole des Mines, Parc de Saurupt, 54042 Nancy, France; ^dBalzars S. A., Parc d'activités de l'Esplanade, 77462 St Thibault des Vignes, France

received 7 April 1997

The effects of substrate polarisation in a nitrided 316L stainless steel have been investigated in an attempt to accurately correlate processing parameters with surface mechanical properties. Nanoindentation allows the Vickers hardness to be measured at precise depths, meaning that the variation in properties with nitriding depth can be evaluated and correlated with the process parameters. By combining such measurements with surface imaging techniques (scanning force microscopy and scanning electron microscopy) and electron probe micro-analysis, it is possible to explain both the mechanical property and microstructural variations of such layers, having been produced in a low pressure arc plasma discharge at 680K with a mixed Ar-N₂ gas.

In this study the nanoindentation technique is presented as a new and valid method for the characterisation of nitrided layers, shown by hardness measurements on four nitrided layers produced with different substrate polarisation potentials. The net advantages of such an approach over conventional methods (e. g. microhardness testing) and the possibility of detecting microstructural phases previously not well detected by X-ray diffraction, make nanoindentation an attractive tool for a more complete understanding of the nitriding process. © 1997 Elsevier Science Ltd

Introduction

Low pressure thermionic arc nitriding^{1,2} has shown that nitrogen reactivity can be very high in such a process, making it interesting to evaluate its efficiency on austenitic stainless steels. It is known that a nitriding treatment improves the tribological properties of stainless steels without affecting their corrosion behaviour, provided that it is performed below 720-770K^{3,4}. Below such temperatures there is no CrN precipitation within the diffusion layers; only a metastable f.c.c. phase (γ_N) containing a high concentration of nitrogen in solid solution is formed. This supersaturated f.c.c. structure, sometimes described as expanded austenite, can be obtained by different processes^{5,7}, but of greater interest is an MN-like CrN phase which recent PVD studies have shown to exist in the near surface region of the diffusion layer, depending on the process parameters⁸. It is supposed that such a phase is a complex mixture of Cr, Fe and Ni, although the kinetics of the precipitation of this phase are still not well known.

Therefore, an additional characterisation method is required in order to distinguish such a phase from the more common γ_N f.c.c. phase. In assuming that this phase may be present as a function of depth in a nitrided layer leads to the possibility of using a depth-sensitive indentation method which is capable of measuring hardness at very small depths and with high accuracy.

In recent years, nanoindentation has become widely accepted as the logical successor to microindentation, the latter being limited by the resolution of an optical microscope as this is used to determine the imprint diagonal and thus the hardness of the tested material. The nanoindentation principle relies on the continuous measurement of force and displacement as an indenter, of known geometry, is pressed into a sample material⁹⁻¹⁴. The force is usually applied via an electromagnet, in which case the current in the coil determines the load, or by a piezoelectric load cell where the inherent inaccuracies in such a system are corrected by interferometry. The displacement is measured, in most cases, by a capacitive sensor. With instruments now having microNewton force and nanometer depth resolutions it is

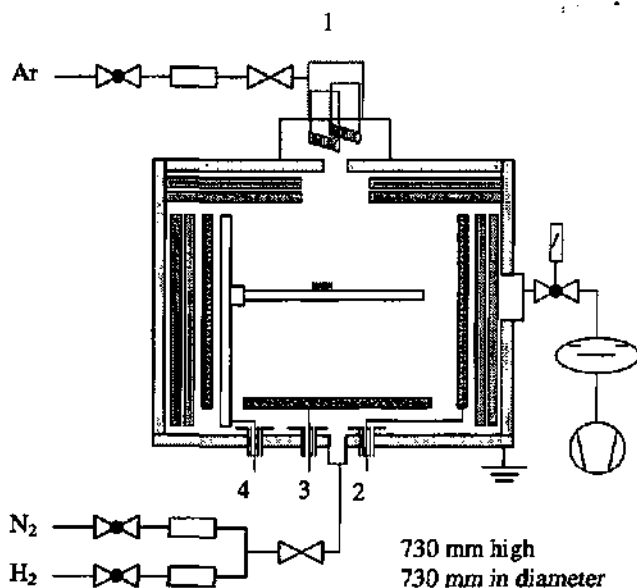


Figure 1. Schematic representation of the main components of the low pressure arc discharge nitriding chamber, comprising: plasma beam source (1); cylindrical (2) and flat (3) anodes; and heating substrate holder (4).

possible to produce load-displacement curves representative of the material response in terms of hardness, modulus and elastic recovery¹³.

Having established the motivation for the present work, a selection of nitrided layers produced with different substrate polarisation potentials are characterised using the aforementioned nanoindentation technique, and the results explained using high resolution scanning force microscopy (SFM), scanning electron microscopy (SEM), electron probe micro-analysis (EPMA), secondary neutral mass spectroscopy (SNMS) and X-ray diffraction.

A clear correlation was found between the nanohardness of the nitrided layers and their polarisation potentials, and in addition, the presence of the MN-like CrN phase at the outer surface was confirmed.

Experimental set-up

Nitriding device. The experimental apparatus used for all nitriding treatments, a Balzers BAI730N, is shown in Figure 1. A high current, low voltage thermionic arc is generated in argon in an ionisation chamber (1 in Figure 1) mounted on the top of the nitriding reactor.

Segmented anodes (2-3 in Figure 1) which are distributed within the reactor spread the plasma throughout the whole processing chamber, thus creating a uniform low pressure plasma (0.4-0.8 Pa). With an appropriate aperture between the ionisation chamber and the reactor, an intense glow discharge supported by a low voltage (25-40 V), high current (120 A on each anode) thermionic arc is created.

A heating resistance (4 in Figure 1) is used to provide a uniform temperature (680 K). Prior to nitriding, a 90 min cleaning treatment is performed in an Ar-25%H₂ gas mixture (corresponding to 0.5 Pa total pressure) in order to remove the surface oxide layer. The four AISI 316L samples to be compared in this study were nitrided for 6 h at 680 K in an Ar-66%N₂ gas mixture with different polarisation potentials as listed in Table 1.

Nanoindentation. The instrument used for nanoindentation was a CSEM Nano Hardness Tester (NHT), comprising two distinct components, a measuring head for performing indentations and an optical microscope for selecting a specific sample site prior to indentation and for checking the location of the imprint after indentation. Both components are directly linked by an electro-mechanical positioning system which allows movement in two perpendicular horizontal axes with a lateral displacement resolution of 1 μm. This instrument is a development of an earlier ultramicrohardness tester¹⁶ which is based on existing technology¹⁷ and its principle is described elsewhere¹⁸. The main advantage of this instrument is its differential measurement of the sample surface, made possible by a sapphire reference ring which remains in contact with the sample during the loading/unloading cycle, giving exact positioning of the Vickers indenter tip relative to the sample surface. Thus the elasticity of the sample and holder is compensated, as is thermal drift during measurement.

Indentations were performed at depths of 100, 200, 300, 400, 500, 750, 1000, 1250, 1500 and 1750 nm on all samples in order to evaluate the evolution of hardness with depth into the nitrided layer. Deeper penetration depths were not used so as to prevent inaccuracies due to substrate effects. The loading rate was kept constant for all measurements and 5 indentations were made at each depth.

Surface characterisation. SFM was carried out using a CSEM Atomic Scale Tribometer^{19,21}, a stand-alone instrument having sub-nanometer lateral and vertical displacement resolution. Topographical images were made at scan sizes of 20 μm and 5 μm, the former to compare height variations between different grains, the latter in order to look at the grain morphology with high resolution and to investigate any correlation between polarisation potential and surface grain structure.

Table 1. Experimental conditions for the four chosen samples

	Experiment 1	Experiment 2	Experiment 3	Experiment 4
Precleaning				
Time (h)	1.5	1.5	1.5	1.5
Polarisation (V)	-50	-20	0	+20
Gas composition	Ar-25%H ₂	Ar-25%H ₂	Ar-25%H ₂	Ar-25%H ₂
Nitriding				
Time (h)	6	6	6	6
Temperature (K)	680	680	680	680
Polarisation (V)	-50	-20	0	+20
Gas composition	Ar-66%N ₂ (at 0.8 Pa total pressure)	Ar-66%N ₂ (at 0.8 Pa total pressure)	Ar-66%N ₂ (at 0.8 Pa total pressure)	Ar-66%N ₂ (at 0.8 Pa total pressure)
N concentration at the surface (at%)	26.9	30.8	26.9	34.5
Layer thickness (μm)	7 ± 1	8 ± 2	7 ± 1	8 ± 2

Optical microscopy was used to evaluate the thickness of each nitrated layer by cutting and polishing a representative section. SEM was used to gain an overview of the grain structure and the dispersion of differing grain types. EPMA and SNMS allowed the surface nitrogen concentration to be quantified and XRD was used to determine the phases present and their orientation.

Results and Discussion

The nitrated layers obtained, having all been subjected to crystallographic compression and spatially anisotropic constraints near the surface, are discussed in terms of their chemical composition. Figure 2 shows a typical glancing angle XRD pattern obtained with an incidence angle of 4° for different nitrating substrate polarisations (-50 V, -20 V, floating potential, +20 V) and the following are observed:

- The f.c.c. base matrix, γ , having a lattice parameter equal to 0.359 nm, was not visible with an incidence angle of 4° and the diffusion layers had thickness 7-10 μm .
- An expanded austenite phase, consisting of an f.c.c. solid solution, γ_N , of lattice parameter between 0.377 and 0.379 nm is observed on all samples and measured along the (111) γ_N plane. A supersaturated austenite phase is also observed, consisting of an f.c.c. solid solution, γ_N^S , which has a higher nitrogen concentration than the expanded austenite phase. This supersaturated phase is only evident for samples 2 and 4, the lattice parameter being measured between 0.387 and 0.389 nm along the (111) γ_N^S plane. In addition, it can be seen that the expanded austenite peaks are broad, this being due to the presence of stacking faults and other defects, high internal stresses and the concentration gradient between each layer. Such phenomena have already been observed by Saker *et al* after PVD treatment²².
- A phase of partially crystallised MN-like CrN is seen, this having a lattice parameter between 0.416 and 0.412 nm as measured along the (111) MN plane. This confirms that precipitation of the MN-like phase has occurred by partial decomposition of the γ_N^S or γ_N phases.

Figure 3 shows a cross-sectional SEM micrograph of the diffusion layers of the nitrated AISI 316L steel sample biased at -20 V. A similar surface structure was observed for all four sample types, this suggesting that regardless of sample polarisation, a partial transformation of γ_N^S or γ_N occurs after 6 h treatment at 680 K. Secondary electron analysis confirmed the presence of a surface layer having a composition different to that of the saturated austenite phase (γ_N) beneath it. This MN-like CrN phase showed a certain fragility near the interface, with ripping of material occurring as a result of polishing. The layer thickness measured between 300 and 600 nm. The γ_N phase had a thickness of approximately 6 μm with stacking faults and twinning planes being clearly visible. The substrate matrix (γ) can be seen below the γ_N phase.

Such a modified surface layer had a nitrogen concentration, as measured by EPMA, of between 27 at.% (samples 1 and 3) and 35 at.%(samples 2 and 4) (Table 1). A correlation could be found between the X-ray diffraction and the EPMA measurements.

The SEM micrograph in Figure 4 shows the different types of grain present and their size variation. The grain boundaries seemed to have height differences which were particularly apparent but difficult to quantify using this method. Hence, a series of SFM images were made in order to investigate such differences, as can be seen in Figure 5a which shows the boundaries between three grains and the cliff-like nature of one such interface. The diffusion layer is subjected to intense compressive strains and the dislocation densities created (in particular stacking faults and twinning planes) are much higher than in the substrate material. Previous work²³ has shown that surface height

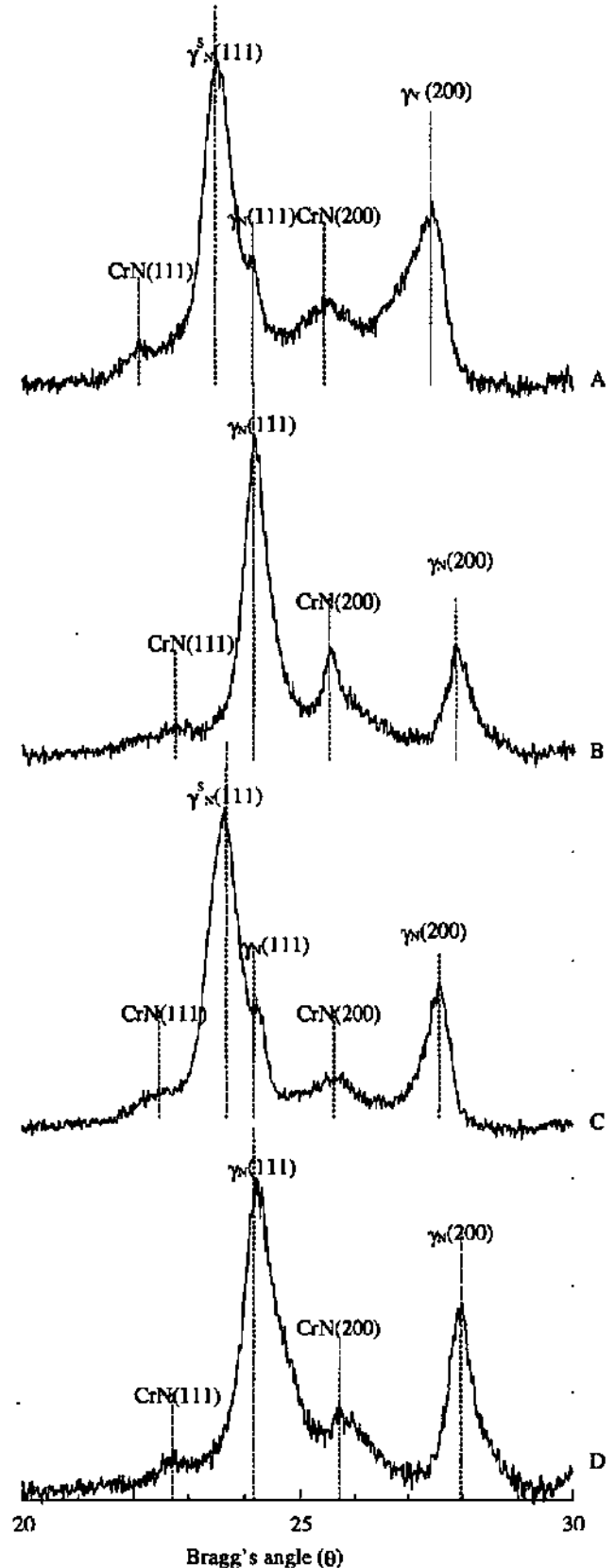


Figure 2. AISI 316L steel sample nitrated in Ar-66%N₂ at 683 K during 6 h at 0.8 Pa and 120 A on each anode, with sample polarisation +20 V (A), floating potential (B), -20 V (C), -50 V (D). The XRD pattern was taken at the outer surface of the sample (λK_{α} Co = 0.17889 nm).

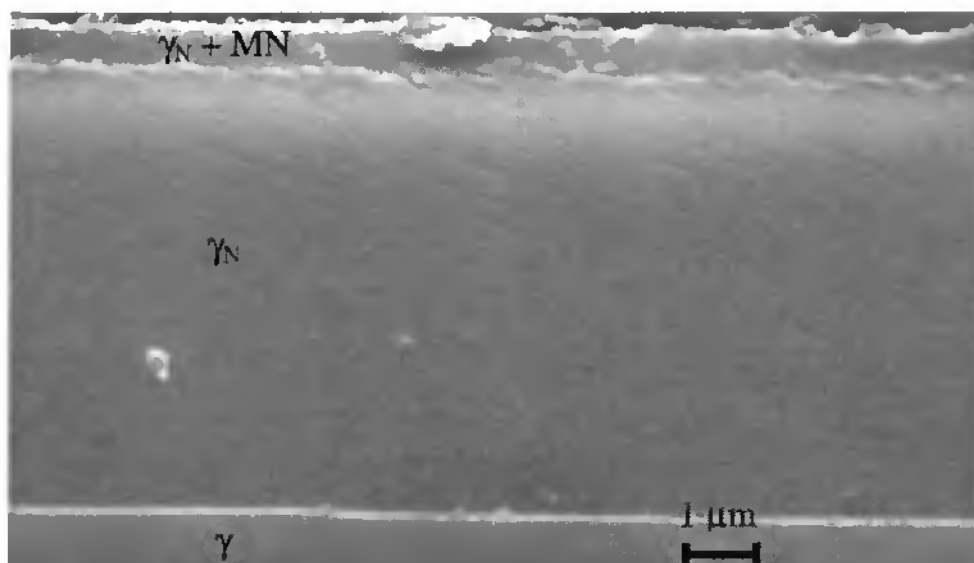


Figure 3. Cross-sectional SEM micrograph of diffusion layers for an AISI 316L steel sample nitrided in Ar-60%N₂ during 6 h at 680 K and at 0.8 Pa and 120 A on each anode at a polarisation of -20 V. The structure is revealed by Parmitter's etching reagent.

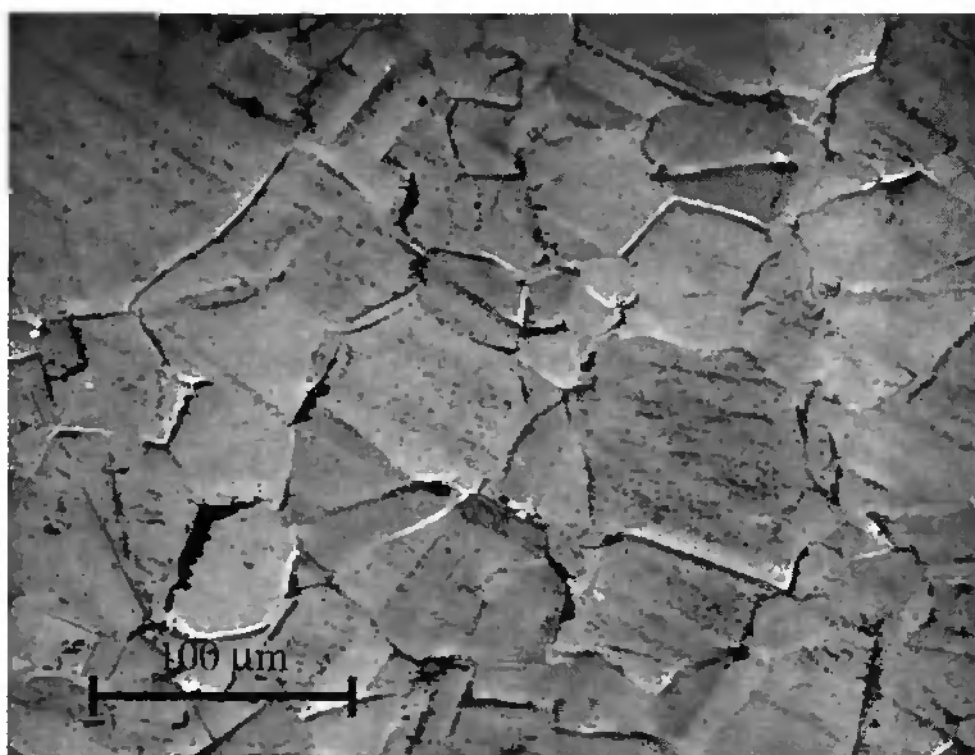


Figure 4. SEM micrograph of surface grain structure (nitriding conditions as in Figure 3).

variation is a good indicator of the degree of modification occurring on the surface of such stainless steels. The height of the cliff shown is in the order of 200 nm, this being due to the high surface nitrogen concentration together with the negative polarisation potential used. The SFM images on all samples confirmed that the height variation becomes more pronounced with greater negative polarisation potentials.

Figure 6 shows the variation of Vickers hardness with penetration depth. Such nanoindentation profiles confirmed a net variation in hardness across the first 1750 nm of the 8-10 μm thick nitrided layers.

Such a variation corresponds with results obtained in a study of nitriding growth rates²⁴ in which different diffusion regimes evolve with time. During the first hour the diffusion layer grows in the form of a γ_N solid solution followed by apparition of the aforementioned cliff-like interfaces. Therefore the change of slope associated with a diffusion transition can explain the formation of new phases within the nitrided layer.

Two separate regions can be distinguished as a function of penetration depth, d_i : In the first region ($d_i < 300$ nm), the presence of a different phase (MN-like CrN) is confirmed by a sharp transition

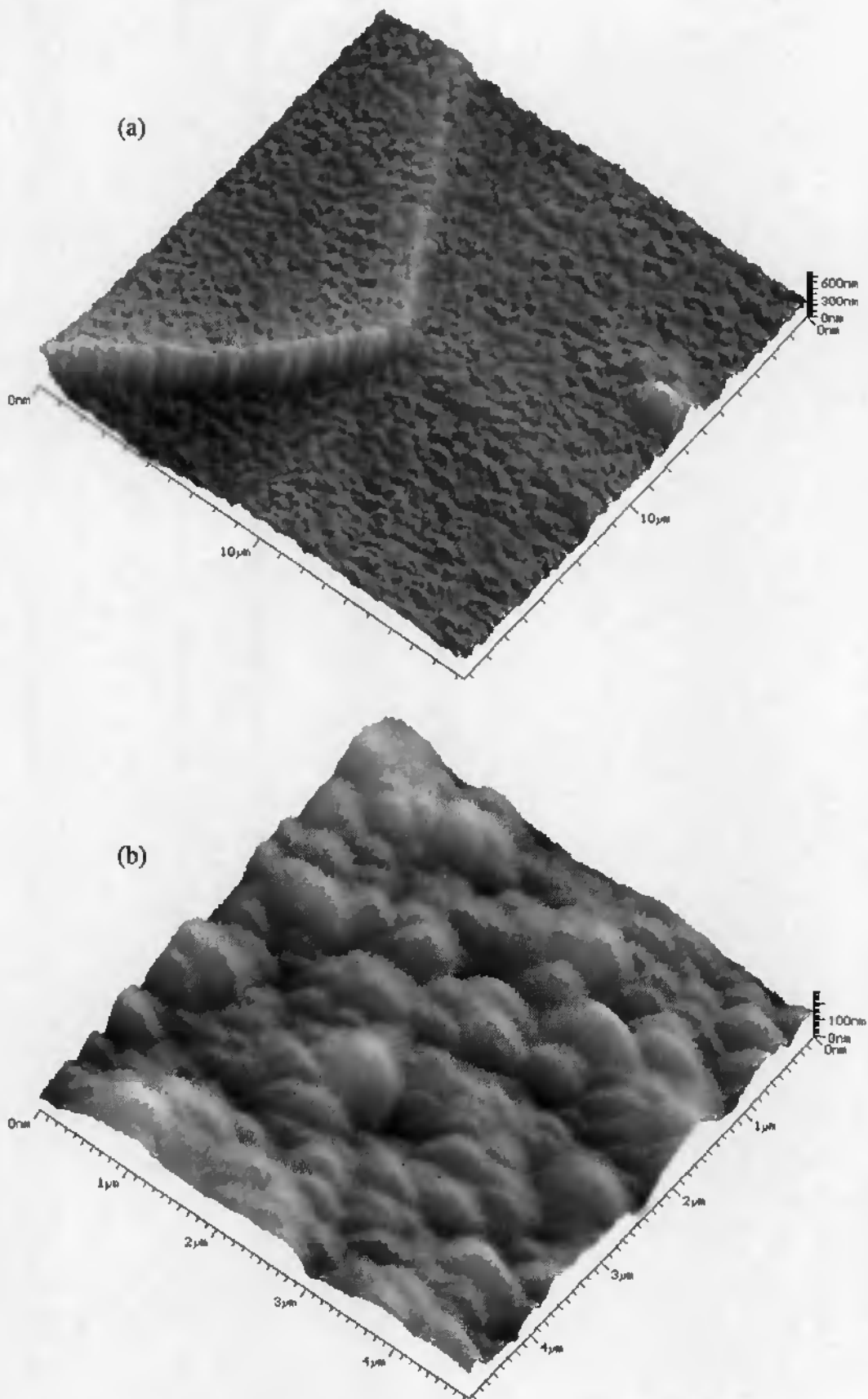


Figure 5. Three-dimensional SFM images of nitrided surface topography (sample polarisation = -20 V): (a) grain boundaries between three grains; and (b) high resolution image of typical grain structure.

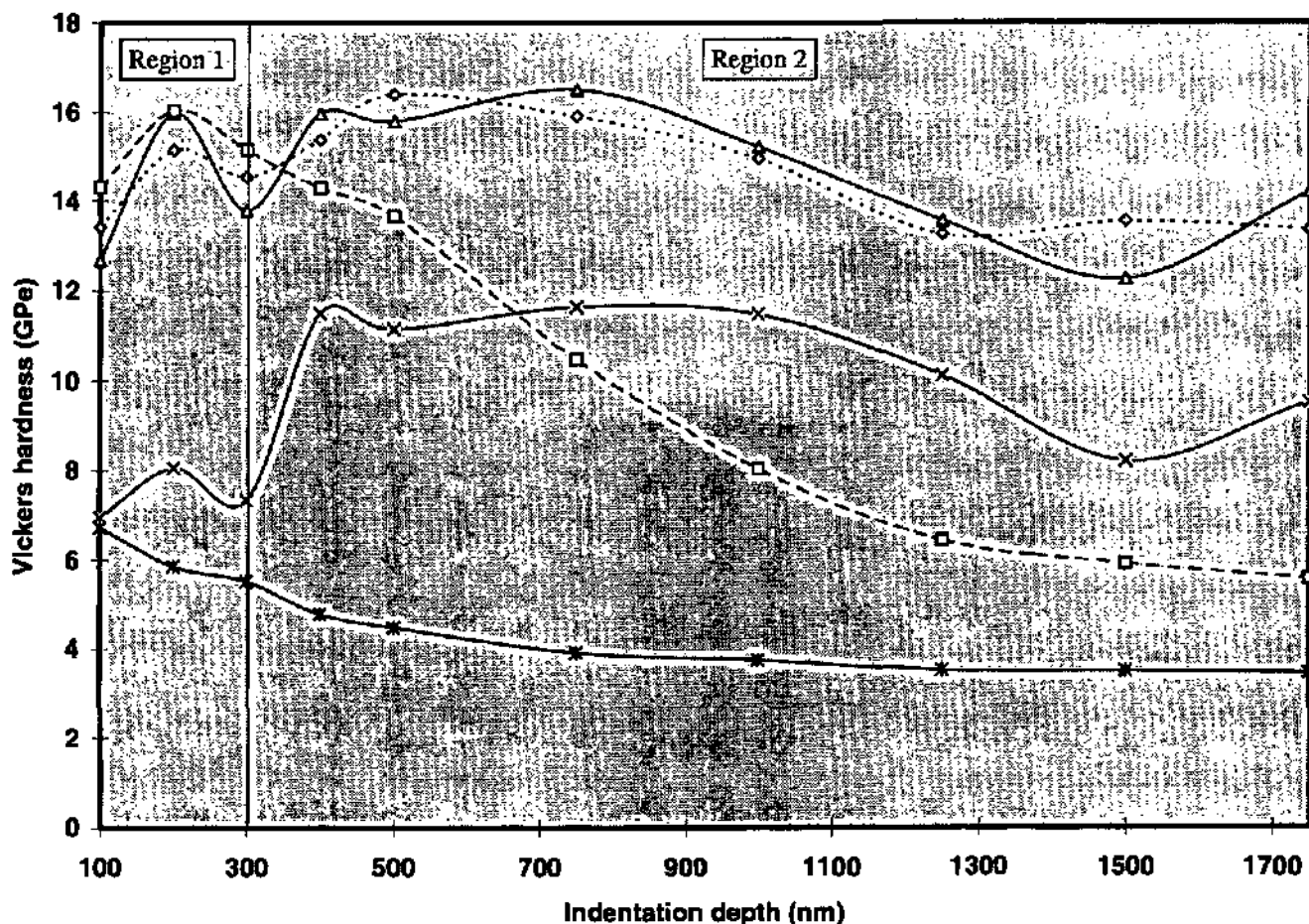


Figure 6. Variation of nanoindentation hardness with depth below surface for the four samples nitrided at different polarisation potentials and the virgin AISI 316L substrate: (\diamond) +20 V; (\times) 0 V; (Δ) -20 V; (\square) -50 V; and ($*$) 316L substrate.

in hardness. This phase, created during the nitriding process and previously observed by Saker *et al* after a 60 h treatment at 620 K²², can be attributed to the decomposition of the γ_N phase during treatment. In the second region ($d_i > 300$ nm), the hardness gradually decreases as reported previously²⁵ with sample 1 (-50 V) decreasing more strongly than the others due to its lower nitrogen concentration at the surface caused by more efficient electron bombardment during nitriding. Samples 2 and 4 (-20 and +20 V respectively) seem to have almost identical hardness profiles, this corresponding to their similar nitrogen concentrations. Sample 3 (0 V) has a profile of the same form as that of sample 2 except that its measured hardness is approximately 30% less. This can be explained by weaker electronic bombardment of the surface which in turn makes the development of internal strains less favourable leading to a reduced hardness of the nitrided layer. This is confirmed by this samples' lower surface nitrogen concentration.

It is now widely accepted that hardness measurements are sensitive to the properties of layers underneath the indenter lying within 10 times the indentation depth. For the measured layers having thicknesses of ~ 10 μm this means that any indentation depth exceeding ~ 1 μm will be subject to substrate effects owing to the elastic/plastic deformation field around the indentation being deeper than the nitrided layer. Evidence of such a phenomenon is visible for

samples 2, 3 and 4, whose hardness profiles decrease gradually but then increase at depths greater than 1.5 μm . Therefore, hardness values truly representative of the nitrided layer are only possible if the indentation depth remains less than this value.

Regarding the nanoindentation profile of the AISI 316L substrate, it was apparent that the measured Vickers hardness increases as the indentation depth decreases. At depths greater than about 700 nm the hardness value stabilised to around 3.8 GPa, this correlating well with values obtained by conventional microindentation. The relatively sharp increase in hardness over the first 500 nm was attributed to a mixture of mechanical and chemical surface artefacts. The former relates to the mechanical polishing of the surface prior to nanoindentation (in this case down to a finish of 0.25 μm using alumina paste) which is known to induce a plastically deformed layer on the surface which is significantly harder than the base material. The latter refers to the oxide and other chemical films that inevitably form on normal experimental surfaces, even if only as a result of atmospheric oxidation. Previous work²⁶ has shown that the presence of an oxide film only 5 nm thick can drastically increase the hardness value obtained when the indentation depth is small enough. The roughness of an indented surface can also contribute to error in the measurement of hardness when such a roughness is of the same order as the indentation depth. However, the SFM imaging of all measured

surfaces prior to indentation determined the surface roughness as being in the range 10-20 nm, which, for penetration depths exceeding 100 nm, could be considered as negligible.

Conclusions

This study has shown that significant variation in mechanical properties is possible in nitrided austenitic stainless steels as a function of substrate biasing. Nanoindentation has been demonstrated as a valid analytical technique for the accurate characterisation of surface nitrided layers and in this case for the confirmation of a distinct MN-like CrN phase, present only within the first 300 nm of the layer, which was not easily detectable by XRD. A correlation has been established between the hardness profiles and the surface nitrogen concentration. SFM has revealed the variation in surface grain structure depending on substrate polarisation and an increase in grain boundary height has been correlated to greater negative polarisation potentials. This study has allowed a more complete characterisation of phenomena occurring in the surface and near-surface regions of nitrided stainless steel.

References

1. N. Renevier, H. Michel, P. Collignon and T. Czerwiec, *Surf. Coat. Tech.*, 86-87 (1996) 285.
2. N. Renevier, H. Michel, P. Collignon and T. Czerwiec, *Surf. Coat. Tech.* 95 (1997) in press
3. E. Menthe, K. T. Rie, J. W. Schultze and S. Simson, *Surf. Coat. Tech.*, 74-75 (1995) 131
4. Z. L. Zhang and T. Bell, *Surf. Eng.*, 1 (1995) 131
5. M. K. Lei and Z. L. Zhang, *J. Vac. Sci. Tech. A*, 13 (1995) 2986
6. C. Cordier-Robert, L. Bourdeau, T. Magnin and L. Foct, *Mat. Lett.*, 20 (1994) 113
7. G. A. Collins, R. Hutchings, K. T. Short, J. Tendys, X. Li and M. Samandi, *Surf. Coat. Tech.*, 74-75 (1995) 417
8. A. Bourjot, M. Focs and C. Frantz, *Plasma Surface Engineering*, 2 (1989) 777-784
9. J. B. Pethica, R. Hutchings and W. C. Oliver, *Philos. Mag. A*, 48 (1983) 593-606
10. J. Loubet, J. M. Georges, D. Marchesini and G. Meille, *J. Tribology*, 106 (1984) 43-48
11. T. F. Page, W. C. Oliver and C. J. McHargue, *J. Mater. Res.*, 7, No. 3, Mar 1992
12. Bhushan, V. S. Williams and R. V. Shack, *Trans. ASME J. Tribol.*, 110 (1988) 563-571
13. M. Nishibori and K. Kinoshita, *Thin Solid Films*, 48 (1978) 325-331
14. H. M. Pollock, *ASM Handbook*, Vol. 18, ASM International, Ohio (1992) 419-429
15. W. C. Oliver, *MRS Bulletin*, Oct. 1986, 15-19
16. H. E. Hintermann, *Fresenius J. Anal. Chem.*, 346 (1993) 45-52
17. W. C. Oliver and G. M. Pharr, *J. Mater. Res.*, 7, No. 6 (1992) 1564-1583
18. N. X. Randall, C. Julia-Schmutz, J. M. Soro and J. Vou Stebut and G. Zacharie, *Thin Solid Films* (1997) in press
19. M. Binggeli, R. Christoph, H. Hintermann and O. Marti, *Surface and Coatings Tech.*, 62 (1993) 523-528
20. N. X. Randall, in *Tribology - Solving Friction and Wear Problems* (edited by Wilfried J. Bartz), Proceedings of the 10th International Colloquium on Tribology, Vol. 3 (1996) 1885-1890
21. N. X. Randall, R Christoph, S. Droz and C. Julia-Schmutz, *Thin Solid Films*, 290-291 (1996) 348-354
22. Saker, C. Leroy, H. Michel and C. Frantz, *Mat. Sci. Eng. A*, 140 (1991) 702
23. M. Samandi, B. A. Shedden, D. I. Smith, G. A. Collins, R. Hutchings and J. Tendys, *Surf. Coat. Tech.*, 59 (1993) 261
24. N. Renevier, H. Michel, P. Collignon and T. Czerwiec, *Surf. Coat. Tech.*, (1997) in press
25. S. P. Hannula, P. Nenonen and J. P. Hirvonen, *Thin Solid Films*, 181 (1989) 343-350
26. J. B. Pethica and D. Tabor, *Surface Science*, 89 (1979) 182-190

7.6 Characterisation of IC aluminium bonding pads by nanoindentation and scanning force microscopy

Paper published in Surface and Coatings Technology 99 (1997) 111-117

Characterisation of integrated circuit aluminium bonding pads by nanoindentation and scanning force microscopy

N. X. Randall ^{a,*}, Egon Holländer ^b, C. Julia-Schmutz ^a

^a Centre Suisse d'Electronique et de Microtechnique S. A., Jaquet-Droz 1, 2007 Neuchâtel, Switzerland

^b Philips Semiconductors, Binzstrasse 44, 8045 Zürich, Switzerland

Received 21 February 1997 ; accepted 6 July 1997

Abstract

The mechanical properties of thin films and surface modified layers can be measured by a variety of different techniques, with nanoindentation being one of the most recent developments in this growing field. It is particularly suited to the characterisation of bonding pads used to connect individual micro-circuits and chips. Such pads are commonly made of aluminium and have a thickness of approximately 1 µm. By using a depth-sensing indentation method it is possible to obtain quantitative values for the hardness and modulus, and thus gain better insight into the response of a bonding pad material to controlled deformation at such small scales. The Nano Hardness Tester (NHT) is a recently developed instrument using an already established method where an indenter tip with a known geometry is driven into a specific site of the material to be tested, by applying an increasing normal load. When reaching a preset maximum value, the normal load is reduced until partial or complete relaxation occurs. At each stage of the experiment the position of the indenter relative to the sample surface is precisely monitored with a differential capacitive sensor, giving a load/displacement curve characteristic of the sample material. By consequently measuring the topography of the residual indent using a surface imaging technique (e.g., scanning force microscopy) and combining this information with the indentation data, it is possible to gain a fuller understanding of the material response, as well as additional information on surface roughness and frictional properties, the latter being of particular importance in bonding applications. Experimental results are presented for a variety of integrated circuit bonding pads, these confirming the ability of the NHT to becoming a common test in quality assurance and process development of thin films and coatings for the microelectronics industry. © 1997 Elsevier Science S. A.

Keywords: nanoindentation, scanning force microscopy, Vickers hardness, IC bonding pads

1. Introduction

In today's integrated circuit (IC) industry, the two major cost considerations during manufacture and testing are money and time. The time-to-market is fast becoming an increasingly important issue, especially for manufacturers of application specific integrated circuits (ASICs) who need to provide new designs at a quicker rate than their competitors. Adequate quality control of a new IC is fundamental during the development phase, allowing design and process engineers to evaluate the functionality of a new device before it reaches the final package test, where the late realisation of design flaws can be extremely costly in terms of time-to-market issues.

IC bonding pads are of paramount importance in serving two functions, the first of which is to provide a defined contact with a test probe in order to test the continuity and basic functionality of a device, the second to provide a platform onto which connecting wires can be attached by thermosonic bonding. The latter is used to establish electrical contacts from a chip to the outer leads via very fine gold wires having a diameter down to 20 µm. Both functions of the bonding pad need to be examined in further detail in order to understand the important role of the pad's mechanical properties.

2. Probe testing process

The most common probes used for testing are tungsten needles which are mounted on cards and arranged so that each probe is positioned above a bonding pad. The complete card is then brought down onto the wafer to be

* Corresponding author.

tested such that each probe is in contact with each bonding pad (Fig. 1). The following problems may occur during this process:

- (1) Probe tips which protrude lower than their neighbouring tips can create deep and damaging scrub marks on the pad making subsequent bonding of connecting wires almost impossible.
- (2) Non-planar probe tips increase the contact resistance between tip and pad, resulting in inaccurate voltage level measurement and false failures during device testing.
- (3) Contamination of the porous tungsten needle (due to stray particles or oxide build-up) and of the bonding pad (Al_2O_3 barrier layer) can increase contact resistance.
- (4) If the pad is of a too soft material then substantial debris may be produced when the needle comes into contact with it. This is a very important consideration for such a particle sensitive environment.

3. Thermosonic bonding process

The gold wire to be bonded is threaded through a ceramic bonding capillary and beated locally with an electron beam such that a ball is formed at its end. This ball is then pressed against the bonding pad and by means of ultrasonic vibration, the gold wire is heated locally to 1060°C , the contact being formed by diffusion of the ball material into the pad material (Fig. 2). The wire is then looped away from the pad via a well-defined motion of the bonding capillary and the second bond is finally made by so-called *stitch-bonding*, where the capillary deforms the wire against the material of the outer leads, producing a wedge-shaped impression on the wire.

The bonding energy is transferred from the capillary to the gold wire, and from the gold wire to the pad by the

ultrasonic motion of the capillary. The surface roughness of the capillary and of the pad at their interface needs to be well-defined for an optimum transfer of energy. Should the pad surface be too smooth then there will be little energy transfer and a bad bond will be produced. However, if the pad or capillary surfaces are too rough then damage will occur to the capillary and the bond itself may well prove to be substandard. Therefore the roughness of the capillary and pad are important in optimizing the thermosonic bonding process. The former has already been investigated by scanning force microscopy (SFM) [1], thus allowing the surface structure of the capillary to be adequately controlled.

Having established the need for adequate quality control of the mechanical properties of aluminium bonding pads, this paper describes the use of a novel nanoindentation system combined with high resolution SFM for the determination of the hardness and surface roughness of such pads.

4. Experimental

4.1. Instrumental set-up

The apparatus consists of two separate instruments, a Nano Hardness Tester (NHT) [2] and a combined optical/SFM system [3], both developed by CSEM Instruments. The NHT comprises two distinct components, a measuring head for performing indentations and an optical microscope for selecting a specific sample site prior to indentation and for checking the location of the imprint after indentation. Both components are directly linked by an electro-mechanical positioning system which allows movement in two perpendicular horizontal axes with a lateral displacement resolution of $1\ \mu\text{m}$.

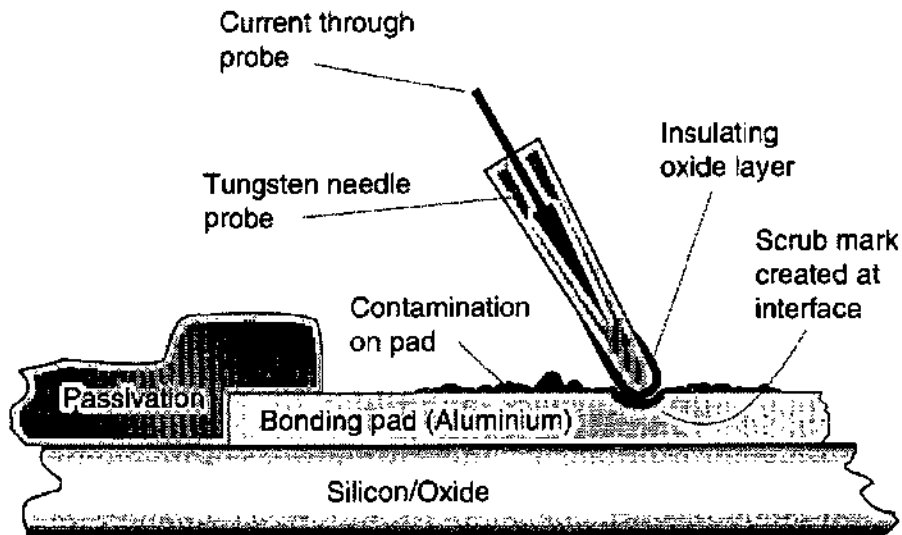


Fig. 1. Schematic representation of the probe testing process in which a tungsten needle probe is brought into contact with the bonding pad.

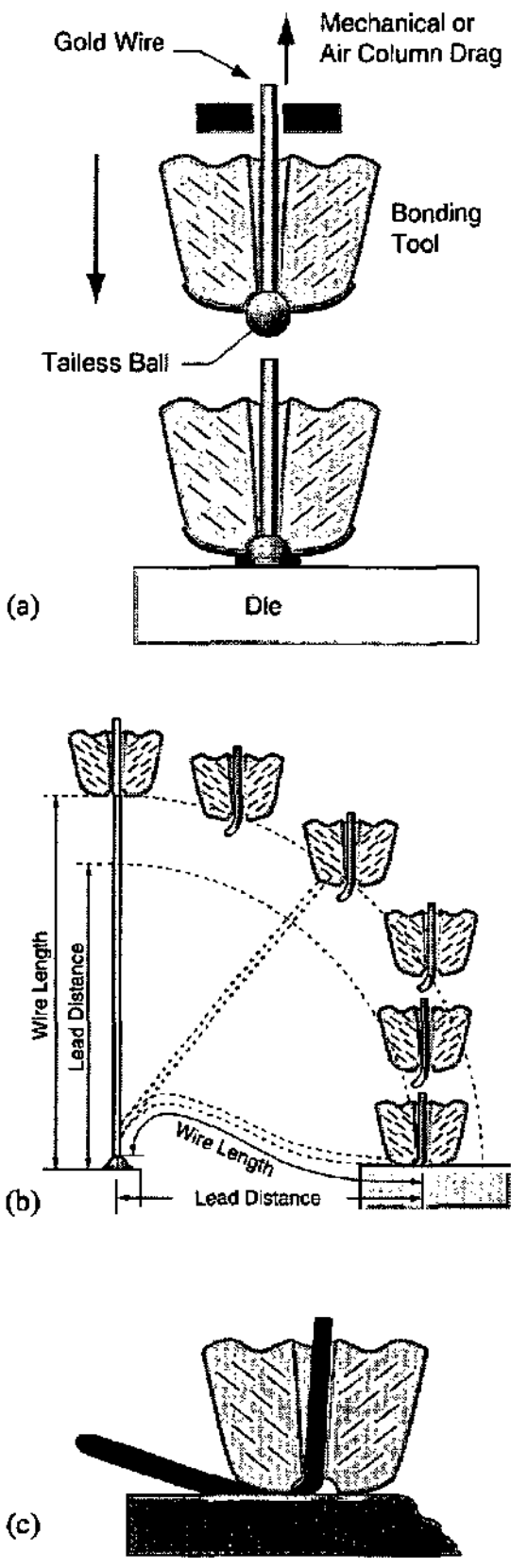


Fig. 2. Thermosonic bonding process: (a) tailless ball bonding, (b) loop formation, and (c) stitch bonding.

This instrument is a development of an earlier ultramicrohardness tester [4] which is based on existing technology [5]. The main advantage of this instrument is its differential measurement of the sample surface, made possible by a sapphire reference ring which remains in contact with the sample during the loading/unloading cycle, giving exact positioning of the Vickers indenter tip relative to the sample surface. Thus the elasticity of the sample and holder is compensated, as is thermal drift during measurement.

The combined optical/SFM system allows a specific sample area to be located under the optical microscope and then relocated precisely under the SFM in order to carry out high resolution microscopy of the same area. The actual SFM used was a CSEM Atomic Scale Tribometer [6,7], a stand-alone instrument having sub-nanometer lateral and vertical displacement resolution.

4.2. Experimental procedure

Four different IC bonding pad types were selected for nanoindentation, each from a different manufacturer but all having the same processing history, i.e., sputtered aluminium to a depth of approximately 1 μm. A series of 10 indentations were carried out on each pad using the NHT and an average value of Vickers hardness calculated. Care was taken to ensure that each indentation was made within a grain of the aluminium microstructure and not on or close to a grain boundary as this might affect the values obtained. A maximum penetration depth of 100 nm (one-tenth of the total pad thickness) was maintained in all cases in order to prevent any substrate effects. The loading rate was kept constant at 5 mN min⁻¹.

Subsequent scanning force microscopy of the indentations was carried out using a silicon cantilever of force constant 0.5 N m⁻¹ in contact mode. Scanning electron microscopy (SEM) was used to gain an overview of the aluminium grain structure and to verify the position of each indentation.

5. Results and discussion

The average Vickers hardness values for each bonding pad type are summarised in Fig. 3. It can be seen that type A has the highest hardness (≈83HV), type D an intermediate hardness value (≈72HV) and types B and C the lowest values (≈64HV). These measurements correlate well with the performance of each pad type in practice when subjected to the probe testing and subsequent thermosonic bonding processes. Type A resisted probe testing the best, leaving only a shallow scrub mark and having the least continuity failures due to poor probe tip alignment and contamination from the Al₂O₃ surface oxide layer. In contrast, types B and C were observed to have much deeper scrub marks, no doubt owing to their reduced hardness, and the tungsten

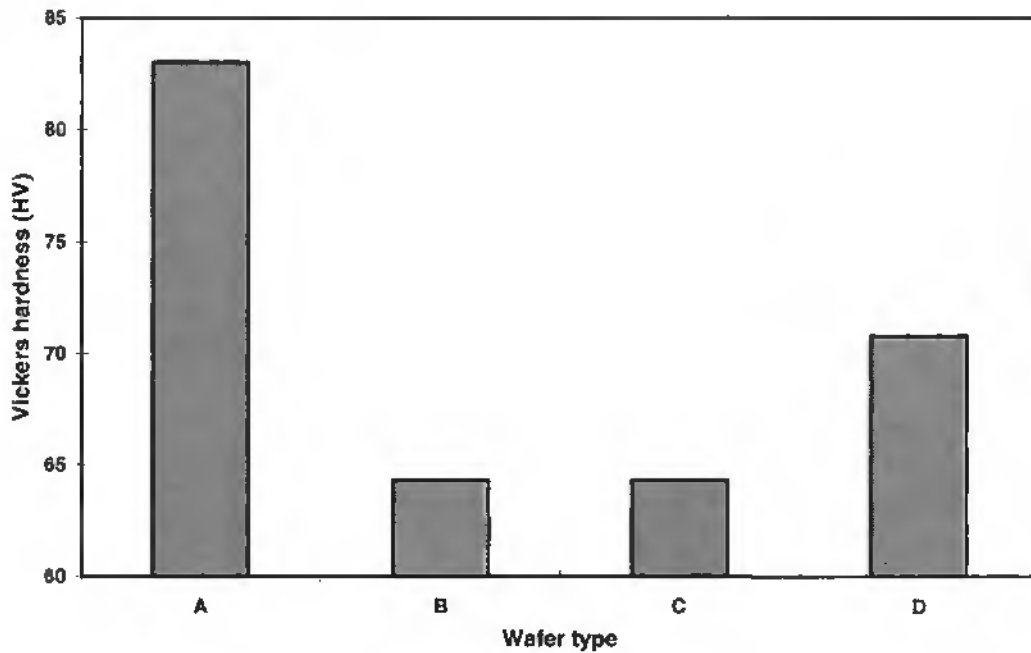


Fig. 3. Vickers hardness of aluminium bonding pads from four different manufacturers.

needle probe tips were more contaminated after testing. Therefore it is clear that the success of the probe testing process can be directly linked to the hardness of the bonding pads.

Fig. 4 shows an optical micrograph of wafer type A in which a typical arrangement of bonding pads can be seen and their position relative to the surrounding circuitry. The SEM micrograph shows the actual pad tested in this study, the scrub mark and the line of nanoindentations being clearly visible. Fig. 5 is a high resolution SEM micrograph of a typical nanoindentation made on bonding pad type D. The sputtered aluminium grain

structure is evident, as is the accurate positioning capability of the NHT in making the indentation precisely in the middle of a grain. Although the SEM is a valid technique for post-indentation surface analysis, it has a number of disadvantages which are worthy of note:

- (1) An idea of the surface morphology can be obtained but no quantitative measurement of surface roughness is possible.
- (2) For indentations with residual depths smaller than 100nm, the resolution limit of the instrument is approached resulting in reduced contrast.

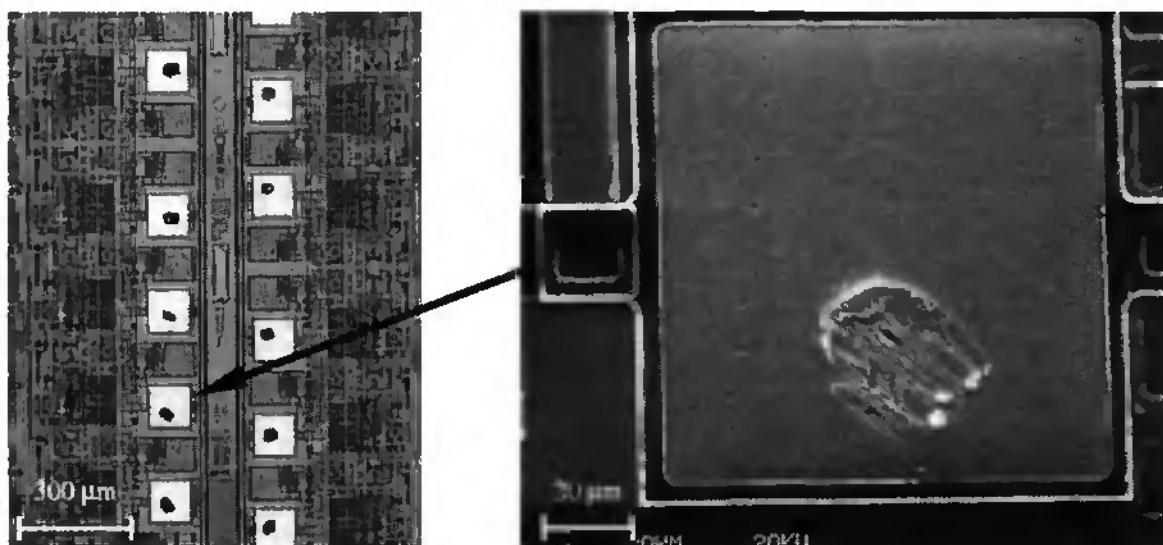


Fig. 4. Optical micrograph (left) of wafer A showing the arrangement of bonding pads and SEM micrograph (right) of the tested pad showing the line of nanoindentations and the scrub mark.

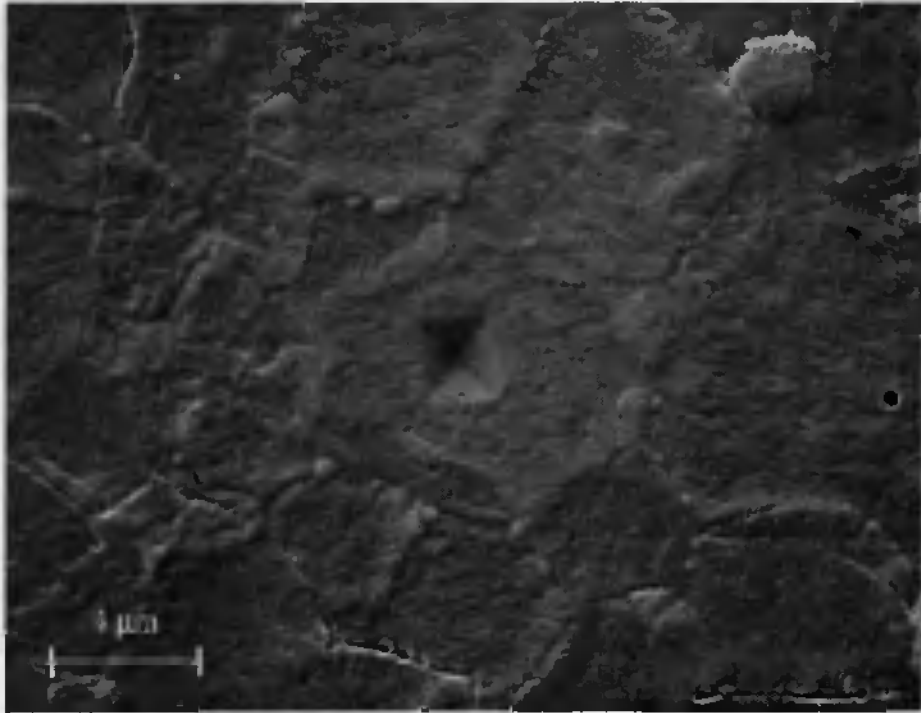


Fig. 5. High-resolution SEM micrograph of a nanoindentation on bonding pad D. Note the grain structure and the ability of the NHT in making an indentation precisely in the middle of a grain.

- (3) The location of an indented area may prove time-consuming if it is not accurately known.
- (4) For bonding pads which may be insulated from the substrate wafer material, a thin conducting layer (c.g., gold) may need to be applied prior to imaging.
- (5) With hardness testing being a possibility for on-line quality control of IC bonding pads, a much more efficient surface imaging technique is required which has a high resolution but does not require a high vacuum environment.

SFM images of nanoindentations on pad types D and A are depicted in Fig. 6, showing the significant difference in surface morphology between the two, regardless of their similar surface roughness values. Similar images were made on all four tested pad types and the root mean square (RMS) roughness of a typical grain was found to be in the range 10-20 nm in all cases. The RMS roughness can be defined as the standard deviation of the distribution of surface heights and was chosen in preference to other roughness parameters because it is the only one with basic significance in describing surface roughness by statistical methods. In the example of Fig. 6 it can be seen that pad A has a regular granular structure whereas pad D has a less defined height variation and so might be less efficient for the energy transfer during thermosonic bonding. A defined surface structure is known to provide a superior key for the soft gold wire.

In discussing the aspects of surface roughness, it should be mentioned that such a parameter is also an important consideration regarding nanoindentation. Variations in

the surface topography of the sample on a small scale compared with the size of the indentation should not have a significant effect because the sample surface is merely forced downward. However, in the present case, where an indentation of depth 100 nm is made on a surface having an RMS roughness of 10-20 nm, it is possible that slight differences may occur in the hardness values obtained. This was observed in practice, thus confirming the importance of surface topographical characterisation before as well as after nanoindentation.

It is interesting to note that the four bonding pad types, produced by separate manufacturers but all conforming to the same quality standard, should have such variation in surface profile and hardness. It is obvious that the processing treatment, the purity of the sputtered aluminium and the processing environment are all contributory factors. Although the need for better quality control has been established and one method found, it is still another problem integrating a combined indentation/SFM instrument as a real on-line industrial process. However, such a system can be envisaged if the measuring components are suitably miniaturised and integrated into one measuring head which is capable of acquiring both hardness and roughness data. One such solution might be a modified SFM whose cantilever tip can be used for indentation as well as surface imaging [8], where the development of diamond coated SFM tips [9] and micromachined actuators [10] would help to solve some of the technical problems. A suitably miniaturised system could be integrated onto the probe testing card so that the bonding pads' mechanical

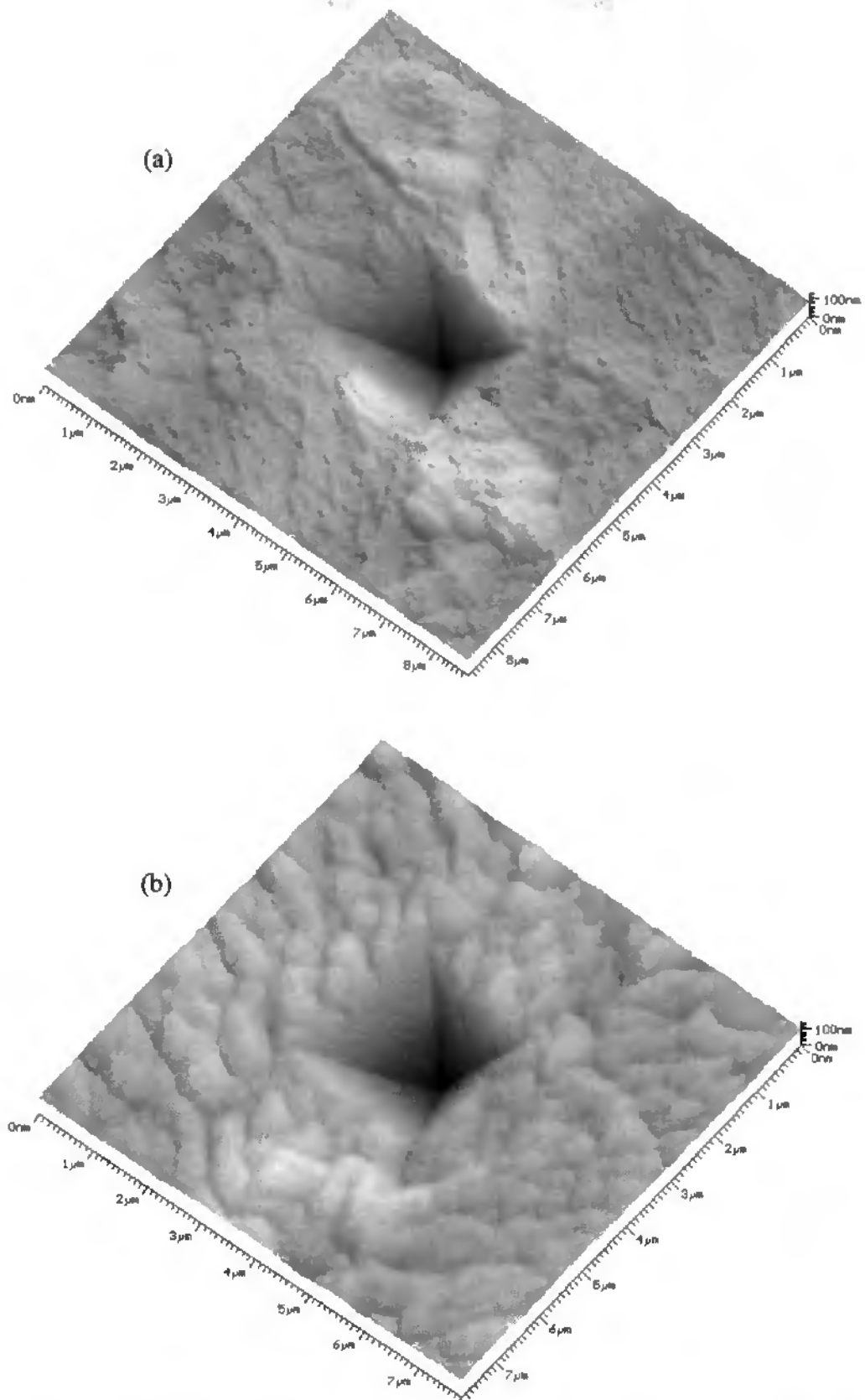


Fig. 6. Three-dimensional SFM images of nanoindentations (depth = 100 nm) on (a) bonding pad D and (b) bonding pad A. Both have approximately the same surface roughness (approx. 20 nm) but significantly different surface morphologies.

properties can be measured at the same time as their electrical properties.

6. Conclusions

This study has shown a clear correlation between the service performance of an IC bonding pad and its surface mechanical properties. The advantages of a nanoindentation instrument combined with SFM have been described, as has its ability to carry out highly localised indentation studies with micrometre positioning accuracy and to measure precisely the corresponding areas with SFM. The need for further development in this field has been established, with the vision of an integrated system able to measure on-line in a modern industrial environment.

Acknowledgements

The authors would like to thank Marco Jorio of Moldinject for providing Fig. 2, Mr. Ketterer for the SEM imaging and Denise Buri for the optical microscopy.

References

- [1] J. Burger, N. Randall, M. Binggeli, R. Christoph, H. Hintermann and M. Jorio, *Proceedings of the 10th meeting of the Societé Suisse des Traitements de Surfaces*, Fribourg, January 1994
- [2] N. X. Randall, C. Julia-Schmutz, J-M. Soro, J. von Stebut and G. Zacharie, *Novel nanoindentation method for characterising multiphase materials*, *Thin Solid Films* (1997) in press
- [3] N. X. Randall, R. Christoph, S. Droz and C. Julia-Schmutz, *Thin Solid Films*, 290-291 (1996) 348-354
- [4] H. E. Hintermann, *Fresenius J. Anal. Chem.*, 346 (1993) 45-52
- [5] W. C. Oliver and G. M. Pharr, *J. Mater. Res.*, 7, No. 6 (1992) 1564-1583
- [6] M. Binggeli, R. Christoph, H. Hintermann and O. Marti, *Surface and Coatings Tech.*, 62 (1993) 523-528
- [7] N. X. Randall, in *Tribology - Solving Friction and Wear Problems* (edited by Wilfried J. Bartz). Proceedings of the 10th International Colloquium on Tribology, Vol. 3 (1996) 1885-1890
- [8] E. T. Lilleodden, W. Bonin, J. Nelson, J. T. Wyrobek and W. W. Gerberich, *J. Mater. Res.*, 10, No. 9 (1995) 2162-2165
- [9] G. J. Germann, G. M. McClelland, Y. Mitsuda, M. Buck and H. Seki, *Rev. Sci. Instrum.*, 63 (1992) 4053-4055
- [10] J. Brugger, V. P. Jaecklin, R. A. Buser, C. Linder and N. F. De Rooij, *NATO ARW on Manipulations of Atoms under High Fields and Temperatures: Applications*, Lyon, France, July 6-10 1992 (Kluwer Academic)

7.7 Nanoindentation and scanning force microscopy as a novel method for the characterisation of tribological transfer films

Paper published in Wear 212 (1997) 18-24

Nanoindentation and scanning force microscopy as a novel method for the characterisation of tribological transfer films

N. X. Randall^a, J. L. Bozet^b

^a Centre Suisse d'Electronique et de Microtechnique S. A., Jaquet-Droz 1, CH-2007 Neuchâtel, Switzerland

^b Université de Liège, Service d'Éléments de Machines et de Tribologie, Rue E. Solvay 21, 4000 Liège, Belgium

Received 5 March 1997; accepted 23 June 1997

Abstract

In conventional pin-on-disk testing of the tribological characteristics of two different materials in sliding contact, the main parameters of interest are notably the friction and wear properties of the material pair. However, when two bodies consisting of hard and soft materials respectively are subjected to such testing, the apparition of a transfer film, or *third body*, which can be a composite mixture of the two, is often observed. Until now the characterisation of transfer films in terms of their mechanical properties has been hampered by their non-homogeneous distribution across a tested surface, their small size, low thickness and the difficulty in accurately positioning a test probe such that the film properties can be measured independently from those of the substrate. In this paper a new method is introduced, consisting of nanoindentation and scanning force microscopy (SFM), which is capable of highly localised indentation testing of a specified sample site with high resolution imaging of the area prior to and after indentation. In this way the hardness and modulus of a transfer film can be obtained, as well as valuable surface topographical information concerning the material response to the indentation. Measurements are presented for the material pair A286/polyimide after testing on a pin-on-disk tribometer in ambient air and liquid nitrogen. Distinct variations in hardness between the transfer films and their contacting bodies have been observed and correlated to the wear behaviour and testing environment.

Keywords: Nanoindentation; Scanning force microscopy; Tribological transfer films

1. Introduction

In recent years, and with the rapid development of rocket engines for aerospace propulsion, the quest for higher specific impulse has led designers to the use of cryogenic fluids such as liquid oxygen (LO_x) and liquid hydrogen (LH₂), the combination of which gives far higher efficiency than more conventional fuels. With such development has come the necessary research into the behaviour of materials when operated in cryogenic environments, in an attempt to aid engineers in the reliable selection of materials capable of withstanding severe operating conditions.

The tribological behaviour of a pair of materials immersed in a cryogenic fluid is substantially different from that observed in ambient air, owing to the variation in thermal, rheological and chemical properties. For laboratory testing purposes, liquid nitrogen (LN₂) is commonly used to replace LO_x or LH₂, not only for safety and cost considerations but also because of its low reactivity and similar thermal behaviour [1]. Simulation of the processes occurring at low temperatures in rocket engines are relevant to the engine feeding system components, e.g., turbopump, expansion joints in the feeding lines, chamber

valves, purge valves and their associated actuating mechanisms [2]. The materials having a sliding or sealing function must remain sufficiently ductile and exhibit a good wear resistance, as well as a low friction coefficient.

Previous work [3] has shown that polyimide resins submerged in a cryogenic fluid exhibit a noticeable increase in hardness which induces a decrease in friction coefficient and wear rate, when compared with a sliding process performed in ambient air. Such a decrease of wear and friction coefficient is believed to be due to the competition between adhesive and deformation phenomena. It was also observed that small residual flakes of a transfer film were evident on both the polyimide pin and the A286 steel disk after testing with a pin-on-disk tribometer. However, the influence of such a third body on the wear process was not investigated.

The recent development of depth-sensing indentation techniques at a nanometric scale, commonly known as nanoindentation, has allowed highly localised hardness and modulus measurements to be performed on very small material volumes. The motivation for the present study is therefore based on the use of such a new technique for the

characterisation of transfer films created between polyimide and A286 steel disks during sliding contact. Other analysis techniques are not appropriate owing to the large sample size (typical disk diameter is 8 cm) and the difficulties in locally characterising such thin films.

Nanoindentation has become widely accepted as the logical solution to microindentation, the latter being limited by the resolution of an optical microscope as this is used to determine the imprint diagonal and thus the hardness of the tested material. The nanoindentation principle relies on the continuous measurement of force and displacement as an indenter, of known geometry, is pressed into a sample material [4-9]. The force is usually applied via an electromagnet, in which case the current in the coil determines the load, or by a piezoelectric load cell where the inherent inaccuracies in such a system are corrected by interferometry. The displacement is measured, in most cases, by a capacitive sensor. With instruments now having microNewton force and nanometer depth resolutions it is possible to produce load-displacement curves representative of the material response in terms of hardness, modulus and elastic recovery [10], although a true understanding of the elastic/plastic interactions occurring at the indenter/sample interface is not possible solely from such data.

Additional surface topographical information has become increasingly important for characterising surface deformation in and around the indentation area. Various methods have been proposed, including SEM [11], TEM [12] and STM/SFM [13], with scanning probe techniques being one of the few able to quantitatively measure interfacial effects, such as material pile-up around indentations, with nanometric precision and three-dimensional imaging capability. Furthermore, SFM does not have the inconveniences of tedious sample preparation, does not require a vacuum environment and in a stand-alone configuration can measure samples of unlimited size [14]. Some previous work [15] has already shown the net advantages of combining nanoindentation with SFM and this paper aims to introduce such a method for the characterisation of tribological transfer films.

2. Experimental details

2.1. Instrumental set-up

The apparatus consists of two separate instruments, a Nano Hardness Tester (NHT) [16] and a combined optical/scanning force microscope (SFM) system [15], both developed by CSEM Instruments. The NHT comprises two distinct components, a measuring head for performing indentations and an optical microscope for selecting a specific sample site prior to indentation and for checking the location of the imprint after indentation. Both components are directly linked by an electro-mechanical positioning system which allows movement in two perpendicular horizontal axes with a lateral displacement resolution of 1 μm . This instrument is a development of an earlier ultramicrohardness tester [17] which is based on existing technology [18]. The main advantage of this instrument is its differential measurement of the sample surface, made possible by a sapphire reference ring which remains in contact with the sample during the loading/unloading cycle, giving exact positioning of the Vickers indenter tip relative to the sample surface. Thus the

Table 1
Summary of pin-on-disk test conditions and sample nomenclature

Sliding speed (ms^{-1})	Test environment	
	Liquid nitrogen (LN_2)	Ambient air
0.2	4	2
2.0	3	1

elasticity of the sample and holder is compensated, as is thermal drift during measurement.

The combined optical/SFM system allows a specific sample area to be located under the optical microscope and then relocated precisely under the SFM in order to carry out high resolution microscopy of the same area. The actual SFM used was a CSEM Atomic Scale Tribometer [19-20], a stand-alone instrument having subnanometre lateral and vertical displacement resolution.

2.2. Experimental procedure

Four identical samples of the material pair A286/polyimide were subjected to sliding wear experiments using an automated ISMCM-CNES pin-on-disk tribometer [21] in LN_2 and ambient air ($\sim 20^\circ\text{C}$) environments. Sliding speeds of 0.2 and 2 m s^{-1} were used and the contact pressure was maintained at 15 MPa. The contact mode was a flat-on-flat conformal contact, and the pin and wear track diameters were 6 mm and 65 mm respectively. The disks used for testing were machined from forged bars of A286 austenitic stainless steel which had been precipitated for 16 h at 725°C , and their hardness was 330 HV. The pins consisted of a commercially available, 15% graphite-filled, polyimide resin. The test conditions and sample nomenclature are summarised in Table 1.

The average roughness (R_a) was measured for the disk wear surface before and after testing using a Surfscan three-dimensional stylus profilometer. The residual transfer films which had accumulated on both the pin and the disk were then analysed using nanoindentation, and their Vickers hardness (HV) compared to that of the A286 and polyimide virgin materials. All measurements were performed in ambient air conditions. The maximum force and the loading rate were varied in the ranges 5-50 mN and 10-100 mN s^{-1} respectively. The smallest force value was used when indenting on the transfer films in order to keep substrate effects to a minimum. A series of 5 measurements were made on each sample area and an average value calculated. Subsequent scanning force microscopy of the indentations was carried out using a silicon cantilever of force constant 0.5N m^{-1} in contact mode.

3. Results and discussion

After pin-on-disk testing of the four samples, the presence of a dark-coloured compound was observed on both the pin and disk wear surfaces, this being a direct result of the wear process. It was also observed that the two disks tested in

Table 2

Summary of pin-on-disk test results for the A286/polyimide material pair (the weight and volume values are for the pin)

Sample	Initial weight (g)	Final weight (g)	Weight difference (g)	Volume lost (mm ³)	Sliding distance (m)	Force (N)	Wear rate (mm ³ N ⁻¹ m ⁻¹)
1	2.65732	2.65528	0.00204	1.43662	2000	424.12	1.694×10^{-6}
2	2.65169	2.65082	0.00087	0.61268	500	424.12	2.889×10^{-6}
3	2.66068	2.66043	0.00025	0.17606	2000	424.12	2.076×10^{-7}
4	2.65224	2.65212	0.00012	0.08451	500	424.12	3.985×10^{-7}

ambient air had a far greater amount of this transfer film than those tested in LN₂. The calculated wear rates for the pins are summarised in Table 2 and show that, for tests performed in ambient air, the wear rate is a factor of ten greater than that for tests performed in LN₂. In addition, the wear rate is higher for a sliding speed of 0.2 m s⁻¹ than for a speed of 2 m s⁻¹ in both environments.

The stylus profilometry measurements on each disk confirmed that abrasion had taken place, owing to the equidistant and concentric scratches present on each wear track surface. The notable increase in surface roughness as a result of the wear process is summarised in Table 3 for the A286 disk. Scratches were visible on the wear surface, the deepest of which were of the order 20–25 µm. Scratches were observed to be deeper for tests performed in LN₂, this being presumably due to hardening of the polyimide pin at such lower temperatures.

Fig. 1 shows the Vickers hardness of the polyimide pin, transfer film and A286 disk for the four tested material pair samples. In all cases the hardness of the pin and disk were found to be 93–97 HV and 332–345 HV respectively, these values being in agreement with those found in the literature for the polyimide resin and A286 austenitic stainless steel. However, the hardness values obtained on the transfer film were found to vary by up to 15% in some cases. This substantial variation may have been due to one or more of the following factors:

1. The transfer film can be considered as a thin film adhered to a harder substrate (A286). It is now common knowledge that if the indentation depth exceeds one tenth of the film thickness then the hardness of the substrate will start to contribute to the value measured for the film. In the present experimental case the average thickness of the transfer film was estimated to be in the range 3–4 µm, which meant that a maximum penetration depth of 100 nm was well within the prespecified limit.

Table 3

Average roughness (Ra) values for the disk wear surface before and after testing; profiles were measured with a stylus profilometer in ambient air

Sample	Average roughness of A286 disk (µm)	
	Before testing	After testing
1	0.04	0.76
2	0.03	0.10
3	0.05	0.96
4	0.04	0.17

However, it is clear that variations in the thickness of the transfer film did exist, as did variations in the substrate surface morphology as a result of the wear process.

2. The transfer film is an inhomogeneous mixture of steel wear particles produced by abrasion combined with polyimide resin particles which may be at differing stages of chemical modification with the atmosphere.
3. The contact pressure between pin and disk may vary greatly if the pin is not mounted exactly vertically and if only part of the pin is in sliding contact with the disk at certain times. This leads to higher shear stresses in some areas which, in turn, leads to higher hardness of the third body agglomerate.
4. Relatively shallow indentation depths may result in the measured hardness value being different to that of the bulk material due to the near-surface region being more prone to atmospheric oxidation and higher contact temperatures.

In practice, several indentations were made on different transfer film areas and the values of hardness averaged in order to reach one representative value in each case, as represented in Fig. 1. Although variations do exist, the main trend is that transfer films produced in ambient air have a higher hardness (196–217 HV) than those produced in a LN₂ environment (138–152 HV). This can be accounted for by the hardening effect resulting from a low temperature atmosphere; the contact temperature at the pin-disk interface may well exceed –500°C in ambient air but not in the LN₂ atmosphere, this being the temperature above which the hardness of an austenitic stainless steel begins to decrease.

Surface topographical characterisation of the residual imprints by SFM gave significant additional information about the material response to the indentation as well as to surface morphological changes resulting from the sliding wear process. Fig. 2 shows an image of an indentation on a transfer film produced at a sliding speed of 0.2 m s⁻¹ in ambient air. A large amount of pile-up is visible around the indented region, the extent of which is seen better in the three-dimensional representation of Fig. 3(b) with the corresponding cross-section through the indent. The shape of the Vickers diamond imprint has become distorted due to elastic relaxation of material around the imprint and possibly by adhesion of matter between the indented region and the diamond tip during unloading. The surface of the transfer film itself is quite obviously made up of sheared particles which can clearly be seen in both images, as well as shallow pits on the surface where fragments have been ripped out during the abrasion process.

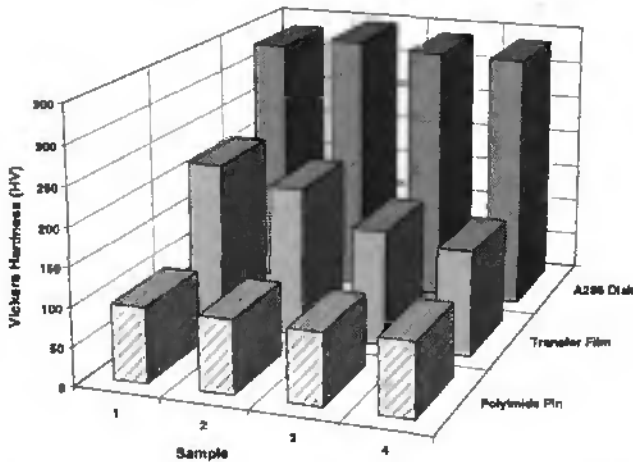


Fig. 1. Vickers hardness of polyimide pin, transfer film and A286 disk for the four tested material pairs.

In contrast, the image shown in Fig. 3(a) shows an indent on the A286 disk on an area where no transfer film is present. Little pile-up is observed and the shape of the Vickers indenter is maintained, this being a typical example of an indentation in which plastic deformation is dominant. It should be noted at this stage that austenitic stainless steel is a multiphase material and that, without etching the surface prior to indentation, it is not possible to distinguish on which phase the indentation is made. Thus the hardness value obtained is likely to vary depending on which grain type has been measured. In practice this was taken into account by making a large number of indentations across a chosen region of the surface and taking an average value. The SFM image also shows the extent of nanometer-scale scratches across the surface. Obviously, the roughness of this surface cannot be compared to values obtained with stylus profilometry because of the different scales being measured; as an example, the image in Fig. 3(a) has a surface area of approximately $9 \times 9 = 81 \mu\text{m}^2$, whereas a typical profilometer measurement is made over an area of approximately 9 mm^2 . Clearly, the SFM is able to investigate a chosen surface with far higher resolution than with a profilometer and so the two methods are complementary for gaining a better understanding of the surface topography at two different scales [20].

Figs. 4(a) and 4(b) show SFM images of indentations made on polyimide pins which have been worn in different environments. In contrast to indentations on the steel disk, elastic deformation is dominant in such a polymeric material causing huge elastic recovery during the unloading of the indenter tip. This is confirmed by the fact that the maximum penetration depth for all indentations on the polyimide pins was $\sim 1300 \text{ nm}$, but the residual indentation depth (see cross-sections) is only $\sim 300 \text{ nm}$. Such elastic nature of polyimide and plastic nature of A286 steel helps to explain the mixed elastic/plastic behaviour of the transfer film and hence its intermediate hardness value.

The two images in Fig. 4 exhibit different surface structures which can be correlated to their wear environment: pin 4 has a relatively smooth, but slightly scratched surface whereas pin 2 has a very dimpled surface. The latter is probably due to much higher contact temperatures causing a modification in topography.

To summarise, it is evident that SFM is a particularly useful tool because the effects of an indentation can be accurately quantified and the surface topography investigated, both from the same image. In addition, the surface roughness of an area can be measured prior to indentation, so as to be able to judge whether such an area is suitable or not. Variations in the surface topography of a sample material, if small compared with the size of the indentation, should not have an adverse effect because the sample surface is simply forced downwards. However, when indenting down to nanometric scales, surface roughness may play an increasingly important role, and thus its prior measurement becomes extremely important.

Regarding the wear of a material pair such as A286/polyimide in a cryogenic liquid such as LN_2 , the aforementioned results correlate well with previous work by Fusaro [22] who observed a transition from high friction to low friction depending on the temperature, caused by a gradual softening of the polymer surface followed, under more severe sliding conditions, by the formation of a viscoelastic film which develops at the interface. It has also been shown by Bozet and Gras [3], for the same material pair, that the wear rate is about 10 times less in LN_2 than in ambient air. They also observed that in ambient air the sliding of polymers over a metallic counterface is governed, in a cryogenic fluid, by adhesion more than by deformation phenomena.

4. Conclusions

It has been shown that for the A286/polyimide material pair in dry sliding, an increase in the hardness of the transfer film which is inevitably produced corresponds to an increase in the wear rate. The wear rate itself is dependant on the testing atmosphere and on the resultant temperature at the metal/polymer interface, as well as on the roughness of the mating surfaces.

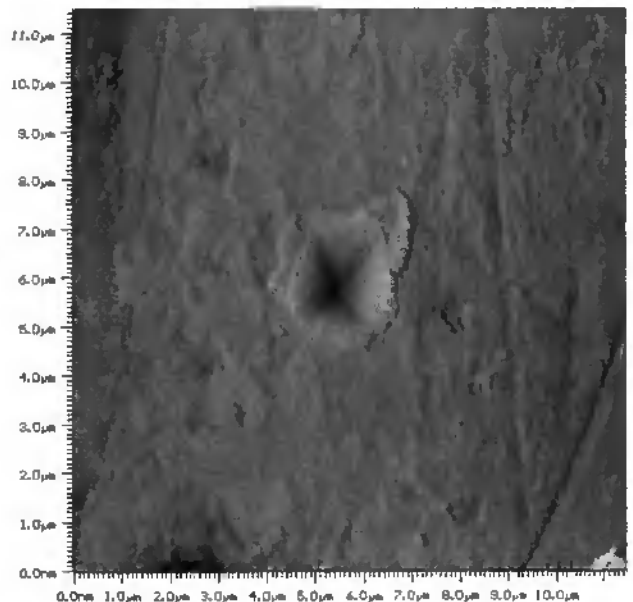


Fig. 2. SFM image of an indentation on the sample 2 transfer film.

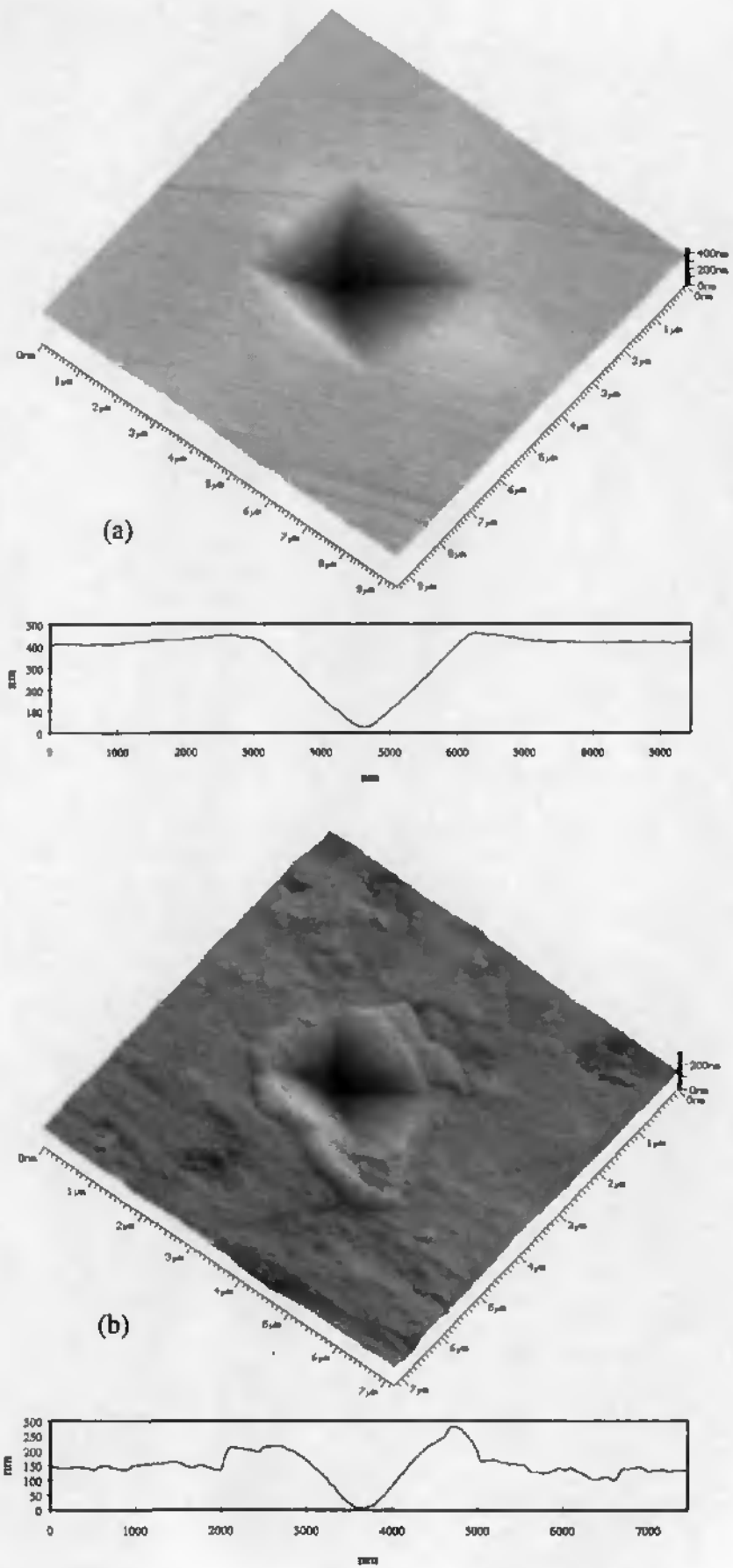


Fig. 3. Three-dimensional SFM images and cross-sections of indentations made on (a) A286 stainless steel disk and (b) transfer film.

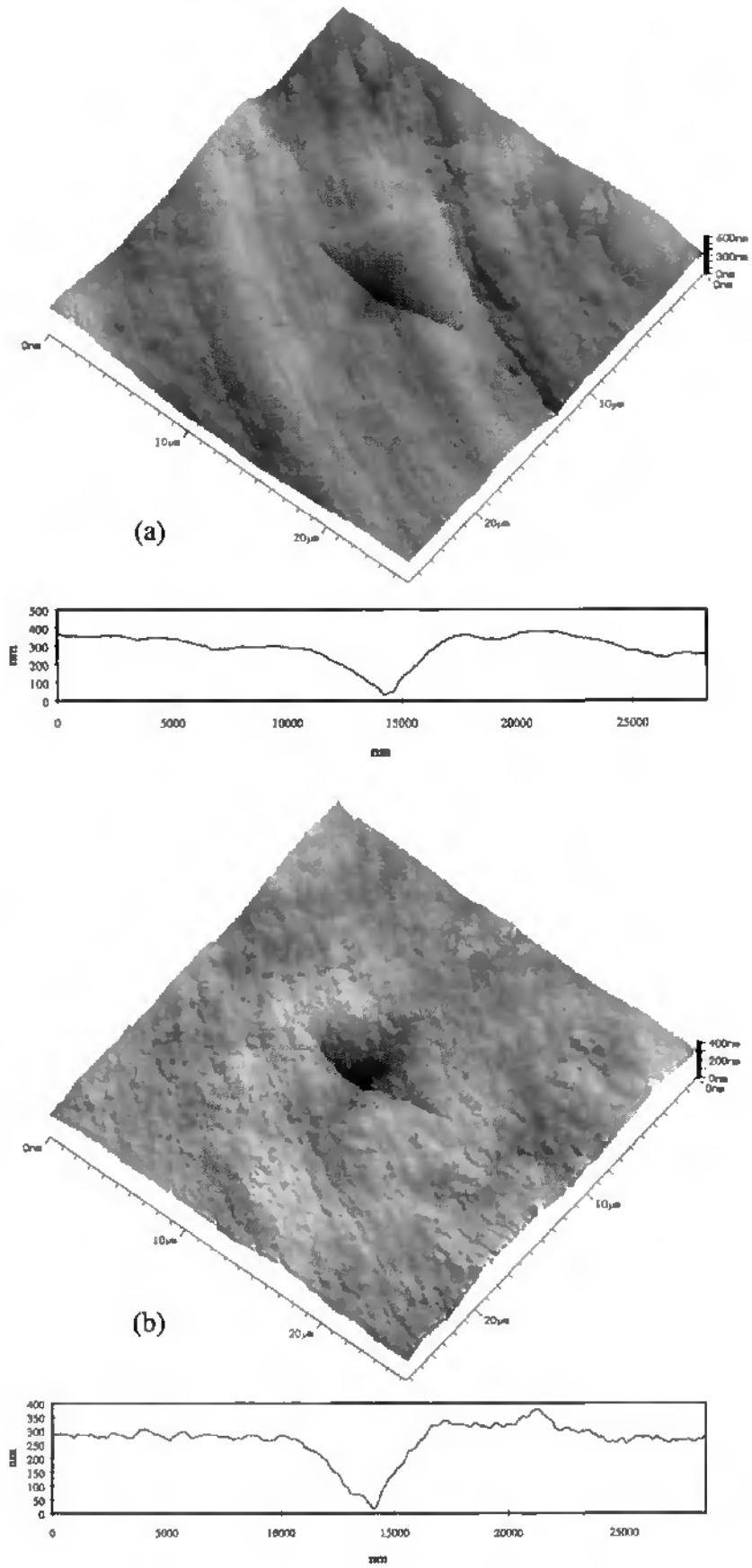


Fig. 4. Three-dimensional SFM images and cross-sections of indentations made on (a) sample 4 and (b) sample 2 polyimide pins. Note the difference in surface morphology.

Nanoindentation has been introduced as a valid method for measuring the hardness of ultra-thin transfer films and, by combining it with high resolution SFM, for investigating differences in material response and surface topography, and correlating them to the wear process. The present study should help to predict the maximum contact energy above which polyimide and similar polymers begin to wear unacceptably when operated in cryogenic fluids. Future work will include more extensive mapping of the hardness gradients present in transfer films in order to gain further information concerning the thermal history endured by the friction track in various different service environments. It is hoped that such a fast-developing technique will find application in many other tribology-related and materials research problems, and pave the way for a better understanding of materials properties at the nanometer scale.

Acknowledgements

The authors gratefully acknowledge Techspace Aero and the Walloon Regional Government for their sponsorship. More particularly, Mr. E. de Lamotte of Techspace Aero is thanked for helpful discussions and comments.

References

- [1] J. F. Cretegy and R. Gras, Cryotechnical tribology analysis and characterisation of couples, Proc. 1st Vulcain Material Symposium, Vernon (1990)
- [2] J. M. Drapier, E. de Lamotte and J. L. Bozet, Tribological problems related to cryotechnic valves of the Vulcain engine, Proc. 1st Vulcain Material Symposium, Vernon (1990)
- [3] J. L. Bozet and R. Gras, Tribological behaviour of fluorinated resins and polyimide resins sliding over a metallic surface in liquid

nitrogen, Proc. 5th European Space Mechanisms and Tribology Symposium, Noordwijk, The Netherlands (ESA SP-334, April 1993)

- [4] J. B. Pethica, R. Hutchings and W. C. Oliver, *Philos. Mag. A*, 48 (1983) 593-606
- [5] J. Loubet, J. M. Georges, D. Marchesini and G. Meille, *J. Tribology*, 106 (1984) 43-48
- [6] T. F. Page, W. C. Oliver and C. J. McHargue, *J. Mater. Res.*, 7, No. 3, Mar 1992
- [7] B. Bhushan, V. S. Williams and R. V. Shack, *Trans. ASME J. Tribol.*, 110 (1988) 563-571
- [8] M. Nishibori and K. Kinoshita, *Thin Solid Films*, 48 (1978) 325-331
- [9] H. M. Pollock, ASM Handbook, Vol. 18, ASM International, Ohio (1992) 419-429
- [10] W. C. Oliver, *MRS Bulletin*, Oct. 1986, 15-19
- [11] H. M. Pollock, ASM Handbook, Vol. 18, ASM International, Ohio (1992) 419-429
- [12] M. F. Doerner and W. D. Nix, *J. Mater. Res.*, 1, No. 4 (1986) 601-609
- [13] E. T. Lilleodden, W. Bonin, J. Nelson, J. T. Wyrobek and W. W. Gerberich, *J. Mater. Res.*, 10, No. 9 (1995) 2162-2165
- [14] P. Niedermann, J. Burger, M. Binggeli, R. Christoph, H. Hintermann and D. Marti, A stand-alone scanning force and friction microscope, Proc. NATO ARW on The Ultimate Limits of Fabrication and Measurements, Cambridge, England (April 1994)
- [15] N. X. Randall, R. Christoph, S. Droz and C. Julia-Schmutz, *Thin Solid Films*, 290-291 (1996) 348-354
- [16] N. X. Randall, C. Julia-Schmutz, J.-M. Soro, J. von Stebut and G. Zacharie, *Novel nanoindentation method for characterising multiphase materials*, *Thin Solid Films* (1997) in press
- [17] H. E. Hintermann, *Fresenius J. Anal. Chem.*, 346 (1993) 45-52
- [18] W. C. Oliver and G. M. Pharr, *J. Mater. Res.*, 7, No. 6 (1992) 1564-1583
- [19] M. Binggeli, R. Christoph, H. Hintermann and O. Marti, *Surface and Coatings Tech.*, 62 (1993) 523-528
- [20] N. X. Randall, in *Tribology - Solving Friction and Wear Problems* (edited by Wilfried J. Bartz), Proceedings of the 10th International Colloquium on Tribology, Vol. 3 (1996) 1885-1890
- [21] J. L. Bozet, Type of wear for the pair Ti6Al4V/PTFE in ambient air and in liquid nitrogen, *Wear*, 162-164 (1993) 1025-1028
- [22] R. L. Fusaro, Effect of atmosphere and temperature on the wear, friction and transfer of polyimide films, *ASLE Trans.*, 21 (1978) 125-133

Summary and Outlook

The goal of this thesis was to develop an integrated instrument which combines nanoindentation with scanning force microscopy. To this end, a working prototype has been completed and its virtues demonstrated before subsequently refining it into a more user-friendly and viable proposition. In addition, the applicability of the SFM to alternative modes of operation, such as indenting and scratching, has been explored and successfully realised. The end result is a powerful system for the more complete characterisation of surface mechanical properties.

The implications of such a development to the field of tribology and materials testing are numerous and will help to bridge the gap between fundamental research at a nanometric scale and more routine quality control in the modern industrial environment. Within the field of nanoindentation, a certain speculation has existed for several years as to the actual modes of deformation occurring at the nanoscale when an indenter penetrates either a bulk or a coated material. This has existed owing to the lack of suitable techniques for imaging residual indentation sites and the difficulties in easily locating them. The use of the SFM has permitted a direct quantitative measurement of imprint dimensions as well as other important information concerning material response. The routine inspection of imprints will help to tailor the indentation apparatus for specific applications, such as indentation creep, stress relaxation and simple fatigue experiments. In addition, the short transfer time between making an indentation and subsequently imaging it will create new possibilities in the research of materials which exhibit time-dependent, viscoelastic properties, e.g., polymers. As with conventional hardness testing, where the residual contact area is calculated from optical microscopic observation, the SFM allows the same principle to be applied to nanoscale indentation, by measuring the residual contact area directly from an image. Thus, nanoindentation hardness values can be accurately compared to those of conventional testing instruments, thus bridging the gap between these two complimentary disciplines.

The application of a combined nanoindentation/SFM apparatus to a wide variety of industrial and research fields has been covered in detail in Chapter 7. For certain examples, namely tribological

transfer films, IC bonding pads and nitrided surface layers, this still remains one of the only methods presently available for characterising the properties of such ultrasmall material volumes.

The future outlook for this kind of apparatus is particularly promising, especially since the application of local probe techniques is still in its infancy and many exciting developments are yet to come. The constant refinement of scanning force microscopies and their complimentary modes, e.g., pulsed force, tapping, magnetic force, friction force, electrostatic force, etc, will significantly broaden the range of surface properties which can be directly measured. The continuing evolution of local optical spectroscopies, such as is scanning near field optical microscopy (SNOM), will provide additional, yet unprecedented nanomechanical information. Furthermore, the combination of such disciplines will pave the way for a more global knowledge of materials, of how they respond to external factors, and of how they can be influenced by different processes and conditions.

The continuing trend of miniaturisation regarding instrumental methods, local environments and measurable scales will allow molecular and even atomic level characterisation in a routine manner. This is of importance, for example, in the study of lubrication and friction in the microelectromechanical systems (MEMS) of tomorrow and the optimisation of mating surfaces in regular sliding contact. Simulation of the light loads involved at these scales will stimulate great strides forward in materials research. The modelling and measurement of energy dissipation mechanisms will significantly contribute to another yet unsolved problem: the accurate prediction of friction coefficients. In the field of biocompatible materials the surface chemical and mechanical properties will be measurable *in-situ* in their native environments.

One of the main problems with modern research is that the gap between the atomic scale and the macroscopic scale has yet to be fully overcome, if a true knowledge of processes occurring over the whole range of scales is to be gained. As with all challenges of this kind, only much time and effort from future generations will unlock the secrets which at this moment have not yet even been discovered.

References

1. J. M. Hutchings, *Tribology: Friction and Wear of Engineering Materials*, Arnold, London, 1992
2. B. Bhushan, *Handbook of Micro/Nanotribology*, CRC Press, Florida, USA, 1995
3. G. Binnig, H. Rohrer, C. Gerber and E. Weibel, *Phys. Rev. Lett.*, 49 (1982) 57-61
4. D. Sarid, *Scanning Force Microscopy*, Oxford University Press, New York, 1991
5. D. Rugar and P. K. Hansma, *Phys. Today*, 43 (1990) 23-30
6. D. W. Pohl, W. Denk and M. Lanz, *Appl. Phys. Lett.*, 44 (1984) 651
7. U. Hartmann, *J. Appl. Phys.*, 64 (1988) 1561
8. C. M. Mate, G. M. McClelland, R. Erlandsson and S. Chiang, *Phys. Rev. Lett.*, 59 (1987) 1942-1945
9. M. Binggeli, R. Christoph, H. E. Hintermann, J. Colchero and O. Marti, *Nanotechnology*, 4 (1993) 59-63
10. R. Wiesendanger and H. J. Güntherodt, *Scanning Tunnelling Microscopy and related techniques*, Springer, Berlin, 1992
11. K. Wickramasinghe in 'Scanning Probe Microscopes', *Scientific American*, Oct. 1989
12. G. Binnig, C. F. Quate and C. Gerber, *Phys. Rev. Lett.*, 56 (1986) 930-933
13. O. Marti, B. Drake and P. K. Hansma, *Appl. Phys. Lett.*, 51 (1987) 484-486
14. M. Binggeli, *Nanotribology at the Solid-Liquid Interface*, PhD Thesis, University of Neuchâtel, Switzerland, 1994
15. N. A. Burnham, D. D. Domiguez, R. L. Mowery and R. J. Colton, *Phys. Rev. Lett.*, 64 (1990) 1931-1934
16. G. Meyer and N. M. Amer, *Appl. Phys. Lett.*, 53 (1988) 1045-1047
17. H. J. Hug, A. Moser, T. Jung, O. Fritz, A. Wadas, I. Parashikor and H. J. Güntherodt, *MRS Bulletin* (January 1993) 41-49
18. M. D. Kirk, T. Albrecht and C. F. Quate, *Rev. Sci. Instrum.*, 59 (1988) 833-835
19. J. B. Pethica, R. Hutchings and W. C. Oliver, *Philos. Mag.*, A48 (1983) 593-606
20. D. Tabor, *The Hardness of Metals*, Clarendon Press, Oxford, England, 1951
21. T. W. Wu, A. L. Shull and R. Berriche, *Surf. Coat. Tech.*, 47 (1991) 696-709
22. P. A. Steinmann, Y. Tardy and H. E. Hintermann, *Thin Solid Films*, 154 (1987) 333-349

23. B. Bhushan in 'Overview of Coating Materials, Surface Treatments and Screening Techniques for Tribological Applications', *Testing of Metallic and Inorganic Coatings* (W. B. Harding and G. A. DiBari, eds.), STP 947, ASTM, Philadelphia (1987) 310-319
24. N. A. Stilwell and D. Tabor, *Proc. Phys. Soc.*, 78 (1961) 169-179
25. P. J. Blau and B. R. Lawn (eds.), *Microindentation Techniques in Materials Science and Engineering*, STP 889, ASTM, Philadelphia, 1986
26. J. C. Bravman, W. D. Nix, D. M. Barnett and D. A. Smith (eds.), *Thin Films: Stresses and Mechanical Properties*, Symp. Proc., Vol. 130, Materials Research Society, Pittsburgh, 1989
27. M. F. Doerner and W. D. Nix, *J. Mater. Res.*, 1 (1986) 601-609
28. G. M. Pharr and W. C. Oliver, *MRS Bulletin* (July 1992) 28-33
29. P. H. Townsend, T. P. Weihs, J. E. Sanchez and P. Borgesen (eds.) *Thin Films: Stresses and Mechanical Properties IV*, Vol. 308, Materials Research Society, Pittsburgh, 1993
30. B. Bhushan, B. K. Gupta and M. H. Azarian, *Wear*, 183 (1995) 743-758
31. M. F. Doerner, D. S. Gardner and W. D. Nix, *J. Mater. Res.*, 1 (1986) 845-851
32. W. C. Oliver and G. M. Pharr, *J. Mater. Res.*, 7 (1992) 1564-1583
33. B. D. Fabes, W. C. Oliver, R. A. McKee and F. J. Walker, *J. Mater. Res.*, 7 (1992) 3056-3064
34. W. D. Nix, *Metall. Trans. A*, 20A (1989) 2217-2245
35. D. Stone, W. R. LaFontaine, P. S. Alexopoulos, T. W. Wu and C. Y. Li, *J. Mater. Res.*, 3 (1988) 141-147
36. K. L. Mittal (ed.), *Adhesion Measurements on Thin Coatings, Thick Coatings and Bulk Coatings*, STP 640, ASTM, Philadelphia, 1978
37. W. R. LaFontaine, C. A. Paszkiet, M. A. Korbonen and C. Y. Li, *J. Mater. Res.*, 6 (1991) 2084-2090
38. W. B. Li, J. L. Henshall, R. M. Hooper and K. E. Easterling, *Acta Metall. Mater.*, 39 (1991) 3099-3110
39. M. Nastasi, D. M. Parkin and H. Gleiter (eds.), *Mechanical Properties and Deformation Behaviour of Materials having Ultra-Fine Microstructures*, Kluwer Academic Publishers, Dordrecht, 1993
40. B. Lawn, *Fracture of Brittle Solids*, Second Edition, Cambridge University Press, 1993
41. J. C. M. Li and S. N. G. Chu, *Scr. Metall.*, 13 (1979) 1021-1026

42. S. V. Hainsworth, H. Sjöström, T. F. Page and J. E. Sundgren, *Thin Films: Stresses and Mechanical Properties VI*, Vol. 436, Materials Research Society, Pittsburgh, 1996
43. N. A. Stelmashenko, M. G. Walls, L. M. Brown and Y. V. Milman, *Acta. Metall. et Mater.*, 41 (10) (1993) 2855-2865
44. W. C. Oliver, *MRS Bulletin* (October 1986) 15-19
45. Y. Martin, C. C. Williams and H. K. Wickramasinghe, *J. Appl. Phys.*, 61 (1987) 4723
46. D. Rugar, H. J. Marnin and P. Güthner, *Appl. Phys. Lett.*, 55 (1989) 2588
47. R. Erlandsson, G. M. McClelland, C. M. Mate and S. Chiang, *J. Vac. Sci. Tech. A*, 6 (1988) 206
48. M. Tortonese, R. C. Barrett and C. F. Quate, *Appl. Phys. Lett.*, 62 (1993) 834
49. P. Maivald, H. J. Butt, S. A. C. Gould, C. B. Prater, B. Drake, J. A. Gurley, V. B. Elings and P. K. Hansma, *Nanotechnology*, 2 (1991) 103-106
50. M. Salmeron, G. Neubauer, A. Folch, M. Tomitori, D. F. Ogletree and P. Sautet, *Langmuir*, 9 (1993) 3600-3611
51. O. Marti, J. Colchero and J. Mlynek, *Nanotechnology*, 1 (1990) 141
52. B. Bhushan and A. V. Kulkarni, *Thin Solid Films*, 278 (1996) 49-56
53. R. Lüthi, E. Meyer, H. Haefke, L. Howald, W. Gutmannsbauer and H. J. Güntherodt, *Science*, 266 (1994) 1979
54. M. Hipp, H. Bielefeldt, J. Colchero, O. Marti and J. Mlynek, *Ultramicroscopy*, 42-44 (1992) 1498
55. P. Niedermann, J. Burger, M. Binggeli, R. Christoph, H. E. Hintermann and O. Marti in 'A scanning force and friction microscope', *Proc. of the NATO-ASI on Ultimate Limits of Scanning Probe Microscopy*, Cambridge, England, April 1994
56. O. Marti, S. Hild, J. Staud, A. Rosa and B. Zink in 'Nanomechanical interactions of SFM tips with polymer surfaces', *Proc. of the NATO-ASI on Micro/Nanotribology and its Applications*, Sesimbra, Portugal, June 1996
57. N. X. Randall in 'Surface characterisation of bearing components', *Proc. of the 10th Int. Colloquium on Tribology – Solving Friction and Wear Problems*, Esslingen, Germany, January 1996
58. A. Leijala, *Micro- and Nanotribological Surface Measurements*, Licentiate Thesis, Helsinki University of Technology, Finland, 1996
59. J. F. Song and T. V. Vorburger in 'Surface Texture', *ASM Handbook on Friction, Lubrication and Wear Technology*, ASM International, 18 (1995) 334-345

60. B. B. Mandelbrot, *The Fractal Geometry of Nature*, W. H. Freeman, New York, 1982
61. G. Dietler and Y. Zhang, *Physica A*, 191 (1992) 213
62. A. Majumdar and B. Bhushan, *ASME J. Tribol.*, 112 (1990) 205-216
63. M. W. Mitchell and D. A. Bonnell, *J. Mater. Res.*, 5 (1990) 2244-2254
64. F. E. Talke, *Wear*, 190 (1995) 232-238
65. B. Bhushan and V. N. Koinkar, *Tribol. Trans.*, 38 (1995) 119-127
66. B. Bhushan and V. N. Koinkar, *Wear*, 183 (1995) 360-370
67. B. Bhushan and V. N. Koinkar, *Wear*, 180 (1995) 9-16
68. R. Kaneko and E. Hamada, *Wear*, 162-164 (1993) 370-377
69. E. Hamada and R. Kaneko, *Ultramicroscopy*, 42-44 (1992) 184-190
70. O. M. Leung and M. C. Goh, *Science*, 255 (1992) 64-66
71. W. Shen, C. Ji, F. N. Jones, M. P. Everson and R. A. Ryntz, *Surf. Coat. Int.*, 6 (1996) 253-256
72. R. Kaneko, T. Miyamoto, Y. Andoh and E. Hamada, *Thin Solid Films*, 273 (1996) 105-111
73. H. O'Neill, *The hardness of metals and its measurement*, Chapman and Hall, London, 1934
74. A. Wahlberg, *J. Iron & Steel Inst.*, 59 (1901) 243
75. R. Smith and G. Sandland, *J. Iron & Steel Inst.*, 1 (1925) 285
76. G. R. Anstis, P. Chantikul, B. R. Lawn and D. B. Marshall, *J. Am. Cer. Soc.*, 63 (1980) 574
77. K. L. Johnson, *Contact Mechanics*, Cambridge University Press, Cambridge, England, 1985
78. A. E. Giannakopoulos, P. L. Larsson and R. Vestergaard, *Int. J. Solids Struct.*, 31 (1994) 2679
79. T. A. Larsen and J. C. Simo, *J. Mater. Res.*, 7 (1992) 618
80. A. Bolshakov, W. C. Oliver and G. M. Pharr, *J. Mater. Res.*, 11 (1996) 760
81. T. J. Bell, J. S. Field and M. V. Swain, *Thin Solid Films*, 220 (1992) 289-294
82. T. Y. Tsui, W. C. Oliver and G. M. Pharr, *Thin Films: Stresses and Mechanical Properties VI*, Materials Research Society, Pittsburgh, 436 (1997) 147-152
83. J. Boussinesq, *Applications des Potentiels à l'étude de l'équilibre et du mouvement des solides élastiques*, Gauthier-Villars, Paris, 1885
84. H. Hertz, *J. Reine und Angewandte Mathematik*, 92 (1882) 156
85. A. E. H. Love, *Philos. Trans. A*, 228 (1929) 377
86. I. N. Sneddon, *Int. J. Eng. Sci.*, 3 (1965) 47
87. J. W. Harding and I. N. Sneddon, *Proc. Cambridge Philos. Soc.*, 41 (1945) 12

88. D. Tabor, *Proc. R. Soc. A*, 192 (1948) 247
89. S. I. Bulychev, V. P. Alekhin, M. Kh. Shorshorov, A. P. Ternovskii and G. D. Shnyrev, *Zavod. Lab.*, 41 (1975) 1137
90. M. Kh. Shorshorov, S. I. Bulychev and V. P. Alekhin, *Sov. Phys. Dokl.*, 26 (1982) 769
91. G. M. Pharr, W. C. Oliver and F. R. Brotzen, *J. Mater. Res.*, 7 (1992) 613
92. D. L. Callahan and J. C. Morris, *J. Mater. Res.*, 7 (1992) 1614-1617
93. N. X. Randall, R. Christoph, S. Droz, C. Julia-Schmutz, *Thin Solid Films*, 290-291 (1996) 348-354
94. A. Bolshakov, W. C. Oliver and G. M. Pharr, *Thin Films: Stresses and Mechanical Properties VI*, Materials Research Society, Pittsburgh, 436 (1997) 141-146
95. N. A. Burnham, R. J. Colton and H. M. Pollock, *Nanotechnology*, 4 (1993) 64-80
96. P. Maivald, H. J. Butt, S. A. C. Gould, C. B. Prater, B. Drake, J. A. Gurley, V. B. Elings and P. K. Hansma, *Nanotechnology*, 2 (1991) 103-106
97. S. M. Hues, C. F. Draper, K. P. Lee and R. J. Colton, *Rev. Sci. Instrum.*, 65 (1994) 1561-1565
98. P. Niedermann, W. Hänni, N. Blanc, R. Christoph and J. Burger, *J. Vac. Sci. Technol. A*, 14 (1996) 1233-1236
99. Jean-Michel Soro, *Contribution à l'étude du vieillissement et de la fragilisation d'aciers inoxydables austénoferritiques. Mise en oeuvre de l'essai de microindentation instrumentée*, PhD Thesis, Ecole des Mines de Nancy, France, 1997
100. E. Hecht, *Optics*, 2nd Edition, Addison-Wesley Publishing Company, Massachusetts, 1987
101. G. Reichardt, F. Eggenstein, U. Flechsig, R. Follath, F. Schäfers, J. Schmidt and F. Senf, *Groove profiles of soft X-ray diffraction gratings: AFM measurements, efficiency simulations and measurements*, European Workshop on Microtechnology and Scanning Probe Microscopy, 1997
102. E. R. Weppelmann, J. S. Field and M. V. Swain, *J. Mater. Res.*, 8 (1993) 830-840
103. T. F. Page and S. V. Hainsworth, *Surf. Coat. Tech.*, 61 (1993) 201-208
104. N. M. Jennet, G. Shafirstein and S. Saunders in 'Comparison of indenter tip shape measurement using a calibrated AFM and indentation into fused silica', *Proc. of the 9th Int. Symposium on Hardness Testing in Theory and Practice*, Dusseldorf, 1995 (Publ. VDI-Verlag GmbH, Dusseldorf, Vol. 1194, 201-210)

Publications

C. Biselli, D. G. Morris and N. X. Randall, *Mechanical alloying of high-strength copper alloys containing TiB₂ and Al₂O₃ dispersoid particles*, Scripta Metallurgica et Materialia, 30, No. 10 (1994) 1327-1332

J. Burger, N. X. Randall, M. Binggeli, R. Christoph, H. E. Hintermann and M. Jorio, *Surface morphology of ceramic bonding tools investigated with Atomic Force Microscopy*, Proceedings of the 10th meeting of the Societé Suisse des Traitements de Surfaces, Fribourg, Switzerland January 1994

J. Burger, N. X. Randall, R. Christoph, L. Yan and O. Parriaux, *Characterisation of short period gratings by a stand-alone Atomic Force Microscope*, Proceedings of the International Symposium on Integrated Optics, Lindau, Germany, April 1994

N. X. Randall, *Surface characterisation of bearing components*, Proceedings of the 10th International Colloquium on Tribology – Solving Friction and Wear Problems, Technisches Akademie Esslingen, Germany, January 1996

A. Leijala, A. S. Korhonen, R. Christoph, N. X. Randall, M. Quintus, S. Hild and O. Marti, *Elasticity/adhesion measurement based phase separation of spin-finished PP fibers by pulsed force mode*, Proceedings of the Nordic-SPM96 workshop, Lund, Sweden, May 1996

N. X. Randall, R. Christoph, S. Droz and C. Julia-Schmutz, *Localised micro-hardness measurements with a combined scanning force microscope/nanoindentation system*, Presented at ICMCTF, San Diego, 1996 and published in Thin Solid Films 290-291 (1996) 348-354

D. S. Finch, J. Franks, N. X. Randall, A. Barnetson, J. Crouch, A. C. Evans and B. Ralph, *Diamond-like carbon, a barrier coating for polymers used in packaging applications*, Packaging Technology and Science, 9 (1996) 73-85

J. A. Anna Selvan, H. Keppner, U. Kroll, J. Cuperus, A. Shah, T. Adatte and N. X. Randall, *The fiber texture growth and the surface roughness of ZnO thin films*, Presented at Materials Research Society (MRS) Symposium, San Francisco, March 1997 and published in the proceedings

N. X. Randall, *Characterisation of DLC multilayers by nanoindentation and scanning force and friction microscopy*, Presented at the Journées Internationales Francophones de Tribologie (JIFT97), Neuchâtel, Switzerland, March 1997 and published in Tribologie et Précision, Actes des Journées Internationales Francophones de Tribologie 1997 (editor M. Maillat)

N. X. Randall, N. Renevier, H. Michel and P. Collignon, *Correlation between processing parameters and mechanical properties as a function of substrate polarisation and depth in a nitrided 316L stainless steel using nanoindentation and scanning force microscopy*, Vacuum 48 (10) (1997) 849-855

N. X. Randall, E. Holländer and C. Julia-Schmutz, *Characterisation of integrated circuit aluminium bonding pads by nanoindentation and scanning force microscopy*, Surface and Coatings Technology 99 (1997) 111-117

F. Sanchette, E. Damond, L. Henry, P. Jacquot, N. X. Randall and P. Alers, *Single cycle plasma nitriding and hard coating deposition in a cathodic arc evaporation device*, Presented at ICMCTF, San Diego, April 1997 and published in Surface and Coatings Technology 94-95 (1997) 261-267

N. X. Randall, C. Julia-Schmutz, J. M. Soro, J. von Stebut and G. Zacharie, *Novel nanoindentation method for characterising multiphase materials*, Presented at ICMCTF, San Diego, 1997 and published in Thin Solid Films 308-309 (1997) 297-303

N. X. Randall and J. L. Bozet, *Nanoindentation and scanning force microscopy as a novel method for the characterisation of tribological transfer films*, Wear 212 (1997) 18-24

Acknowledgements

I would like to thank Prof. Nico de Rooij from the Institute of Microtechnology at the University of Neuchâtel for his guidance, enthusiasm and support during the last three years, as well as for accepting academic responsibility for this work. Prof. Bharat Bhushan from Ohio State University is acknowledged for several useful discussions and for kindly agreeing to being an examiner for this thesis.

Prof. H. E. Hintermann is thanked for his active interest and useful advice, as well as for being an examiner. Dr. Jürgen Burger is kindly thanked for introducing me to scanning force microscopy and for being an examiner.

I would particularly like to thank Dr. Rainer Christoph for giving me the opportunity to carry out this PhD thesis and for broadening my horizons, both professionally and socially! His ability to make even the most negative seem positive is gratefully acknowledged, as is his friendship and encouragement.

None of this would have been possible without the dedication and technical expertise of the team at CSEM Instruments, notably Serge Droz, Jean-Pierre Jeanneret, Pierre-André Feuz, Willy Bettex, Francis Brandt, Jacques Béguin, Stephan Schäfer, Bertrand Bellaton and Gerald Besson. Claudine Julia-Schmutz (alias *Schmutzy!*) is particularly thanked for her software skills and for many useful discussions. Other CSEM coworkers who are gratefully thanked include Denise Buri, Pierre Voumard, Hans Boving, Werner Hänni, Jean Luprano and Pierre Sixt for the circular-etched calibration gratings. In addition, Philippe Niedermann and Cynthia Beuret (IMT) are thanked for providing me with diamond-coated cantilever tips.

Prof. Othmar Marti and Dr. Michael Hipp are thanked for allowing me to pass a very stimulating research stay in their department at Konstanz University and for helping me to develop the nanoscale scratching technique.

Michel Jeandin and Jean-Dominic Bartout are thanked for their support during my research stay in their department at the Centre de Materiaux, Ecole des Mines de Paris, where the combined system prototype was successfully demonstrated and first results produced.

Prof. Jean-Luc Bozet (Université de Liège, Belgium), Egon Holländer (Philips Semiconductors, Zürich), Lukas Knoblauch (EMPA, Dübendorf), Pierre Juliet (CENG, Grenoble), Prof. Frank Talke (University of California, San Diego), and Dr. Youmin Liu (Stormedia Inc., Santa Clara) are acknowledged for providing samples.

Jean-Michel Soro (Ecole des Mines, Nancy) is acknowledged for an interesting collaboration, for his dedication to data transfer by email and for his patience during the long evenings spent imaging residual indentations!

Nathalie Renevier (Balzers A.G., Liechtenstein) is thanked for a fruitful collaboration, for remaining (just....!) within the boundaries of Anglo-French etiquette, for her culinary skills, support and friendship, as well as her shared passion for a well-tuned guitar.....

I would like to thank my family in Neuchâtel, La Chaux-de-Fonds and Lucern for their encouragement over the years. I gratefully thank all those who stood by me during the good and the bad times, particularly Tanja Novosad, Valerie Jeanneret, Marie Munoz and Sarah Mitchell. Nat, Jen and Kev in New York are thanked for their extreme kindness and generosity.....and for helping to relieve the stress during many 'passing-through' visits!

Finally, no words can truly express my gratitude towards my parents, Anthony and Anne-Marie, and my brother Julian, for their guidance, encouragement, moral support and for providing the close-knit family of which I am proud.

Curriculum Vitae

Name	RANDALL Nicholas Xavier
Date/Place of birth	4 th February, 1971 in Birmingham
Nationalities	British & Swiss
Education	<ul style="list-style-type: none">- Birmingham King Edward VI Camp Hill Grammar School for boys (Sept. 82 – June 86) - Cavendish School, Eastbourne (Sept. 86 – June 87) - Eastbourne Sixth Form College (Sept. 87 – June 89) - Lewes Tertiary College (Sept. 89 – June 90) - Brunel University, London (Sept. 90 – June 94); BSc. degree in 'Materials Technology and Management'
Work Experience	<ul style="list-style-type: none">- Industrial placement at the Royal Naval Engineering College, Plymouth, England (May – Sept. 91) - Industrial placement at the Institut de Métallurgie Structurale, Neuchâtel, Switzerland (April – Sept. 92) - Industrial placement at the Centre Suisse d'Electronique et de Microtechnique (CSEM), Neuchâtel, Switzerland (April – Sept. 93) - Full-time employment as R&D Engineer at CSEM Instruments (Nov. 94) whilst working on this PhD, leading to promotion as head of Customer Services (July 96)
Hobbies	Snowboarding, Squash, Cycling, Travelling, Music (guitar)